

This document has been
digitized by the Oil Sands
Research and Information
Network, University of
Alberta, with the permission
of Syncrude Canada Ltd.

ENVIRONMENTAL RESEARCH MONOGRAPH 1979-1

A Public Service of

Syncrude Canada Ltd.

WIND TUNNEL SIMULATION OF PLUME DISPERSION AT SYNCRUDE MILDRED LAKE SITE

D. J. Wilson
University of Alberta

F O R E W O R D

Syncrude Canada Ltd. is producing synthetic crude oil from a surface mine in the Athabasca Tar Sands area of North-eastern Alberta. This present report was commissioned to assess the influence of tailings pond dike height on plume dispersion. The study results will be especially useful for atmospheric dispersion modellers concerned with terrain effects.

Syncrude's Environmental Research Monographs are published verbatim from the final reports of professional environmental consultants. Only proprietary technical or budget-related information is withheld. Because we do not necessarily base our decisions on just one consultant's opinion, recommendations found in the text should not be construed as commitments to action by Syncrude.

Syncrude Canada Ltd. welcomes public and scientific interest in its environmental activities. Please address any questions or comments to Syncrude Environmental Affairs, 10030-107 Street, Edmonton, Alberta, T5J 3E5.

WIND TUNNEL SIMULATION
OF PLUME DISPERSION
AT SYNCRUDE MILDRED LAKE SITE

final report of
Contract 98-0117 EA
for
Syncrude Environmental Affairs Department

by
D.J. Wilson
Department of Mechanical Engineering
University of Alberta
Edmonton, Alberta T6G 2G8

TABLE OF CONTENTS

	<u>PAGE</u>
LIST OF TABLES	iv
LIST OF FIGURES	v
NOMENCLATURE	ix
SUMMARY	xiii
CHAPTER 1	
INTRODUCTION AND STUDY OBJECTIVES	1
Why a Wind Tunnel Simulation?	1
Source Inventory	2
Study Objectives	5
1. Low Level Sources in the Dike Wake	5
2. Main Stack Plume Dispersion	6
3. Plume Rise in Shear Flow	7
CHAPTER 2	
ATMOSPHERIC WIND SIMULATION	9
Wind Tunnel System	9
Mean Wind and Turbulent Structure	12
Flow Uniformity	18
Concentration Modeling and Tracer Gas System	19
Modeling Buoyant Plumes	23
Effect of Stack Gas Turbulence on Plume Rise	30
CHAPTER 3	
FLOW IN THE WAKE OF THE TAILINGS POND DIKE	37
Water Channel Flow Visualization	37
Reynolds Number Effects on Flow Separation	40
Previous Investigations of Recirculation Cavities	43
Wind Tunnel Measurement of Dike Wake Recirculation	45
Separation Behind a Sharp Edged Wall	47

	<u>Page</u>
CHAPTER 3	continued
	Dike Recirculation Cavity in the Wind Tunnel 48
	Flow Deflector for Wind Tunnel Dike 52
CHAPTER 4	DISPERSION FROM LOW LEVEL SOURCES 53
	Wind Tunnel Measurements 53
	Converting From Model to Full-Scale 55
	Vertical and Crosswind Concentration Profiles 56
	Effective Source Height 57
	Ground Level Concentration Without Dikes 58
	Effect of Dikes on Ground Level Concentration 67
	Conclusions and Recommendations 74
CHAPTER 5	PLUME RISE AND DISPERSION WITH FLAT TERRAIN 76
	Vertical and Crosswind Concentration Profiles 77
	Averaging Time and Plume Drift 79
	Combined Momentum and Buoyancy Rise 81
	Predicting Final Rise 87
	Stack Wake Downwash 90
	Wind Shear Effects on Plume Rise 93
	Vertical and Crosswind Plume Spread 102
	Plume Spread Measurements 107
	Comparison with Full Scale Spreading 113
	Vertical Plume Spread for Ground Level Concentrations 116
	Summary 117

	<u>Page</u>	
CHAPTER 6	DIKE EFFECTS ON GROUND LEVEL CONCENTRATIONS IN THE MAIN STACK PLUME	119
	Test Conditions	119
	"Critical" and "Realistic" Dike Configurations	120
	Gaussian Plume Influenced by Dike Wake Turbulence	126
	Turbulent Stack Gas Measurements - Test Series II	132
	Maximum Ground Level Concentration	136
CHAPTER 7	CONCENTRATION FLUCTUATIONS	140
	Detecting Fluctuating Concentration	140
	Experimental Techniques	144
	The Log-Normal Probability Distribution	146
	Ground Level Fluctuation Measurements	148
	Peak-to-Mean Ratios	148
	Dike Effects on Fluctuation Intensity	153
REFERENCES		158
APPENDIX A	WIND TUNNEL FACILITY	164
APPENDIX B	SCALE MODELING TECHNIQUES	175
APPENDIX C	GAUSSIAN PLUME DISPERSION EQUATIONS	193

LIST OF TABLES

<u>TABLE</u>		<u>PAGE</u>
1-1	Inventory of Continuous Sources/Syncrude Mildred Lake Plant Site.	3
2-1	Comparison of Wind Tunnel Boundary Layer with Full Scale Atmospheric Data of Counihan (1975).	17
2-2	Velocity Scale Factors for Flux Modeling.	25
2-3	Main Stack Conditions for Full and Model Scale Test Series I - Stack Open - SYN 057 to SYN 128.	27
2-4	Main Stack Conditions for Full and Model Scale Test Series II - Stack with Plug - SYN 129 to SYN 207.	28
4-1	Operating Conditions for Low Level Sources A and B.	54
4-2	Vertical and Crosswind Plume Spread.	62
4-3	Comparison of Model and Full Scale Plume Spreads for Low Level Sources with No Dike.	63
5-1	Comparison of Measured and Predicted Final Rise for the Syncrude Plume*.	91
5-2	Effective Plume Radius for Self-Generated Spreading*.	106
6-1	Measured Equivalent Full Scale Maximum Ground Level Concentrations*.	138
7-1	Concentration Fluctuation and Peak to Means at Ground Level.	152

LIST OF FIGURES

<u>FIGURE</u>		<u>PAGE</u>
1-1	Location of Source Emissions.	4
2-1	Spikes-Barrier and Roughness for Atmospheric Wind Simulation (North Wind - 150' Tailings Pond Dike).	11
2-2	Helium Detector and Tracer Gas Injection System.	11
2-3	Mean Velocity and Turbulence in the Simulated Atmospheric Boundary Layer.	13
2-4	Power Law Fits to Mean Velocity Profiles.	15
2-5	Surface Roughness Z_0 from Log-Law Profile Fit.	16
2-6	Positioning Low Level Source on 800:1 Scale Model (Arrows: Source and Ground Level Sample Probe).	21
2-7	Adjusting Sampling Probe on Vertical Traversing System.	21
2-8	Tracer Gas Injection and Detector System.	22
2-9	Measured Model Stack Exit Velocity Profiles Compared with Full Scale and Idealized Shapes.	32
2-10	Effect of Stack Exit Conditions on Plume Trajectory.	34
2-11	Plume Rise for Laminar and Turbulent Stack Gases at Constant Volume Emission Rate.	36
3-1	Water Channel and Dye Injector for Flow Visualization.	38
3-2	Dye Injection into Recirculation Zone Marks High Turbulence Dike Wake.	38
3-3	Mean Velocity Profile for Water Channel Flow Visualization Tests.	39
3-4	Scale Cross-Sections of Model Dikes Tested in the Water Channel.	41
3-5	Cavity and Wake Boundaries for Flow Visualization over Large Dike Model in Water Channel.	42
3-6	Results of Previous Studies of Cavity Length Behind Obstacles (Adapted from Huber et al. (1976)).	44
3-7	Helium Trace Flow Direction Detector System.	46
3-8	Cavity and Wake Boundaries for Flow Visualization Over a Sharp Edge Wall in the Water Channel.	49

<u>FIGURE</u>		<u>PAGE</u>
3-9	Reynolds Number Effect of Recirculation Cavity Length.	50
4-1	Vertical Concentration Profile at 28 Source Heights Downwind with 45.7 m Dike Height.	60
4-2	Crosswind Concentration Profile at 28 Source Heights Downwind with 45.7 m Dike Height.	61
4-3	Comparison of Gaussian Plume Model to Measured Plant Site Ground Level Concentrations.	64
4-4	Comparison of Gaussian Plume Model to Measured Plant Site Ground Level Concentrations.	65
4-5	Effect on Ground Level Concentration of Tailings Pond Dike Located 850 m Upwind of Low Level Source on Plant Site.	68
4-6	Effect on Ground Level Concentration of Tailings Pond Dike Located 850 m Upwind of Low Level Source on Plant Site.	69
4-7	Effect on Ground Level Concentration of Tailings Pond Dike Located 850 m Upwind of Low Level Source on Plant Site.	70
4-8	Effect on Ground Level Concentration of Tailings Pond Dike Located 850 m Upwind of Low Level Source on Plant Site.	71
4-9	Effect on Ground Level Concentration of Tailings Pond Dike Located 850 m Upwind of Low Level Source on Plant Site.	72
4-10	Effect on Ground Level Concentration of Tailings Pond Dike Located 850 m Upwind of Low Level Source on Plant Site.	73
5-1	Comparison of Measured Vertical and Crosswind Concentration Profiles with a Gaussian Model.	78
5-2	Vertical Concentration Profiles for 100 sec. Time Averages.	80
5-3	Vertical Concentration Profiles for 400 sec. Time Averages.	80
5-4	Contribution of Momentum and Buoyancy to Plume Rise for the Syncrude Plume at 120% of Full Load with 13.4 m/s Wind at Stack Height.	84
5-5	Approach to Final Rise of Plumes in Turbulent Shear Flow.	86

<u>FIGURE</u>		<u>PAGE</u>
5-6	Rise of the Syncrude Plume at $U_s = 13.4$ m/s and Effect of Downwash at $U_s = 26.8$ m/s for Operation at 120% of Rated Load.	92
5-7	Mean Wind Speed Profiles for Turbulent Shear Flow and Grid Turbulence.	94
5-8	Along-wind Decay of Turbulence Intensity Behind the Grid.	96
5-9	Vertical Profiles of Turbulence Intensity in Shear Flow and Grid Turbulence.	97
5-10	Predicted and Measured Plume Trajectories With and Without Vertical Wind Shear - Syncrude Plume at 120% Load with $U_s = 13.4$ m/s.	101
5-11	Combined Momentum and Buoyant Rise of the Syncrude Plume in Uniform Wind and with Shear Flow for Operation at 120% Load with $U_s = 13.4$ m/s.	103
5-12	Vertical Plume Spread Corrected for Self-Induced Jet and Buoyant Mixing.	108
5-13	Crosswind Plume Spread Corrected for Self-Induced Jet and Buoyant Mixing.	109
5-14	Predicted and Measured Total Vertical Spread.	111
5-15	Predicted and Measured Total Crosswind Spread.	112
5-16	Comparison of Model Vertical Spread with Full Scale Correlations for 800:1 Length Scale.	114
5-17	Comparison of Model Crosswind Spread with Full Scale Correlations for 800:1 Length Scale.	115
6-1	Ground Level Concentrations With Flat Terrain for $U_s = 16.7$ m/s and 33.4 m/s with Plant at 197% Load.	123
6-2	Ground Level Concentration With 45.8 m Dike Upwind and Downwind of Stack. $U_s = 16.7$ m/s, Plant at 197% Load.	124
6-3	Ground Level Concentration With 45.8 m Dike Upwind and Downwind of Stack. $U_s = 33$ m/s, Plant at 197% Load.	125
6-4	Ground Level Concentration With 94 m Dike Upwind and Downwind of Stack. $U_s = 16.7$ m/s, Plant at 197% Load.	127
6-5	Ground Level Concentration With 94 m Dike Upwind and Downwind of Stack. $U_s = 33.4$ m/s, Plant at 197% Load.	128

<u>FIGURE</u>		<u>PAGE</u>
6-6	Effective Vertical Spread Ratio $\eta = \sigma_z / \sigma_{z, \text{dike}}$ for Downwind Effect of Dikes on Ground Level Concentration.	131
6-7	Comparison of Ground Level Concentration With and Without a 45.8 m Dike Downwind of Stack. $U_s = 13.4$ m/s Plant at 120% Load.	134
6-8	Comparison of Ground Level Concentration With and Without a 94 m Dike Upwind of Stack. $U_s = 26.8$ m/s Plant at 120% Load.	135
6-9	Predictions for Effects of Dikes under "Most Critical" Conditions with 94 m Upwind Dike and "Most Realistic" Conditions with 45.8 m Downwind Dike Plant at 120% Load.	137
7-1	Concentration Fluctuations at Ground Level from Low Level Source in Dike Wake.	142
7-2	Probability Density and Observed Concentration Fluctuations from Main Stack Plume with 94 m High Dike Upwind.	149
7-3	Ground Level Concentration pdf for Main Stack Plume with Flat Terrain.	150
7-4	Ground Level Concentration pdf for Main Stack Plume with 94 m High Dike Upwind.	151
7-5	Variation of Concentration Fluctuation Intensity with Wind Speed and Dike Configuration.	154
7-6	Decay of Fluctuation Intensity at Ground Level with Normalized Downwind Distance for Flat Terrain.	155

NOMENCLATURE

C	= volume fraction of contaminant in ambient air
\bar{C}	= time mean concentration
C_f	= concentration exceeded a fraction "f" of the time (see Eq. 7-7)
C_p	= base pressure coefficient of stack wake
C_s	= volume fraction of contaminant in stack gas
$\overline{C^2}$	= variance of concentration fluctuations about mean \bar{C}
C_{50}	= median concentration (see Eq. 7-6)
$C_{o \max}$	= maximum ground level concentration for a given wind speed
d	= internal stack diameter (m)
F	= buoyancy flux (see Eq. 5-3) (m^4/s^3)
F_m	= stack momentum flux (see Eq. 5-5) (m^4/s^2)
g	= acceleration of gravity (m/s^2)
H	= dike crest height (m)
h	= effective source height, ($h_s + \Delta h$), (m)
Δh	= combined buoyant and momentum plume rise (m)
Δh_B	= buoyant plume rise (m)
Δh_{Bf}	= final buoyant plume rise (m)
Δh_M	= momentum plume rise (m)
i_c	= concentration fluctuation intensity (see Eq. 7-4)
L_B	= buoyancy length (see Eq. 5-1), (m)
L_C	= length of recirculation cavity (m)
L_M	= momentum length (see Eq. 5-4), (m)
\dot{m}_s	= contaminant release rate from stack (kg/s)
n	= wind velocity profile power law exponent
$p(c)$	= probability density function of concentration c
Q	= contaminant volume emission rate at stack conditions (m^3/s)

- Re_H = $U_H H / \nu$ Reynolds number based on dike height
 Re_θ = $U_\delta \theta / \nu$ Reynolds number based on boundary layer momentum thickness
 R_s = stack inside radius $d/2$ (m)
 t = averaging time for a sample, or time, (s)
 T_a = ambient temperature ($^\circ K$)
 T_s = stack gas temperature ($^\circ K$)
 U_H = approach wind speed at dike crest height $Z = H$, (m/s)
 U_h or $U_{\Delta h}$ = wind speed at local height of plume centerline (m/s)
 U_s = wind speed at stack height h_s (m/s)
 U_{ref} = wind speed at height Z_{ref} (m/s)
 $-\overline{uw}$ = Reynolds stress (m^2/sec^2)
 $\overline{u^2}$ = mean square x direction turbulent velocity fluctuation
 U_* = friction velocity $(\tau_o/\rho)^{0.5}$ (m/s)
 U_δ = wind speed at edge of boundary layer (m/s)
 $\overline{v^2}$ = mean square y direction turbulent velocity fluctuation
 $\overline{w^2}$ = mean square Z direction turbulent velocity fluctuation
 w_s = mean vertical stack exit velocity (m/s)
 X = downwind distance from source (m)
 X_f = downwind distance to final rise (m)
 X_{max} = downwind distance to C_o max
 Y = crosswind distance from plume centerline (m)
 Z = height above ground (m)
 Z_o = surface roughness in log-law velocity profile (m)
 Z_{ref} = reference height for wind profile (m)

Greek Symbols

- α = kinetic energy correction factor (see page B3)
 β_1 = momentum jet entrainment constant
 β_2 = buoyant bent over plume entrainment constant
 δ_* = boundary layer displacement thickness (m)
 δ = thickness of atmospheric boundary layer (m)
 ϵ = turbulent dissipation rate of kinetic energy (m^2/s^3)
 Λ_x = Eulerian integral scale of turbulence for $\overline{u^2}$ (m)
 λ_x = Taylor microscale of turbulence for $\overline{u^2}$ (m)
 ρ_s = stack gas density (kg/m^3)
 ρ_a = ambient air density (kg/m^3)
 μ = ambient air dynamic viscosity ($n-s/m^2$)
 ν = ambient air kinematic viscosity (m^2/s)
 ϕ_M = stack exit momentum parameter (see Eq. 5-7)
 χ = mass concentration of contaminant (kg/m^3)
 σ_y = plume crosswind spread (m)
 σ_z = plume vertical spread (m)
 η = vertical spread ratio with and without a dike
 ϕ_B = buoyancy flux parameter (see Eq. B 15)
 θ = momentum thickness of atmospheric boundary layer (m)
 λ = ratio of wind velocity at plume height to source height (see Eq. 5-19)
 $\Omega(c)$ = cumulative probability distribution of concentration less than c
 ξ = ratio of effective plume radius "R" to self-induced spread σ_{self}
 σ_{self} = self-induced plume spread from jet and buoyant mixing (m)

Subscripts

m = model scale

f = full scale

s = stack

o = ground level

B = buoyant

M = momentum

dike = with a tailings pond dike

SUMMARY

The wind tunnel simulation of atmospheric dispersion on the Syncrude plant site encompassed four different problem areas: low level sources within the plant itself, the main stack plume, peak levels of time varying concentration, and the effect of wind shear on plume rise. For all of these studies the major variable was the location and height of the tailings pond dike, which will affect plume dispersion by the turbulence generated in its wake. All of these effects were studied using an 800:1 scale model of the plant site located in a simulated neutrally stable atmospheric boundary layer generated in a large wind tunnel. The model study was validated by comparing the measurements for flat terrain with established full scale correlations of atmospheric dispersion parameters such as plume rise and spreading rate.

The following full scale results were obtained:

1. Low Level Sources in the Dike Wake

Velocity and flow visualization measurements in the wake of the tailings pond dikes indicate that the flow will remain attached to the downwind side of the tailings pond dike, minimizing the influence of the dike on mean wind speed and turbulence in its downwind wake. Measurements for two typical low level sources in the wake of the dike confirmed its small influence on plume dispersion. For these two sources with effective plume source heights of 40 m and 44 m ground level concentrations and vertical and crosswind profiles were measured for flat upwind terrain and with dike heights of 22.9 m, 45.8 m and 94 m with wind from plant north.

The flat terrain measurements were in good agreement with the Gaussian plume model recommended in the Alberta Dispersion Guidelines. Only the highest dike height caused a measureable change from flat terrain ground level concentrations. For this largest dike height, the ground level concentration was reduced about 10 percent, indicating that the dike turbulence increases crosswind spreading more than vertical plume spread. These measurements indicate that if the tailings pond dike has any effect on downwind low level sources it will be to reduce their maximum ground level concentration.

2. Main Stack Plume Dispersion

Vertical and crosswind concentration profiles were made at several downwind locations to assess the plume spreading rate and plume rise of the main stack plume. The plume trajectory was in good agreement with combined momentum and buoyancy rise predictions. The buoyant plume entrainment constant was found to be $\beta_2 = 0.87$ for uniform wind, and $\beta_2 = 1.40$ if vertical wind shear effects are lumped with entrainment and wind speed at stack height is used.

The background atmospheric turbulence causes the plume to break up and level off at a downwind distance of $X_f = 2200 F/U_s^3$ which corresponds to about 1.8 km when the plant is operated at 120 percent of load and $U_s = 13.4$ m/s. This leads to a final plume rise of $155 F/U_s^3$ in neutral stability. This is only about one half the plume rise predicted by Briggs (1975), but is in reasonable agreement with estimates of Slawson and Csanady (1971) for final rise location.

The ground level concentration profiles in flat terrain were in good agreement with predictions from the Gaussian plume model using power-law vertical and crosswind spreading rates corrected for self-induced mixing from buoyancy and jet momentum.

The same ground level concentration profiles were observed for winds perpendicular to the dike crest, and at 45° to it. The effect of tailings pond dikes upwind and downwind from the main stack were to locally increase ground level concentrations due to increased turbulent mixing in their wakes. This increase amounted to only a few percent change from flat terrain values for a dike height of 45.8 m. For the 94 m dike height ground level concentrations were about 20 percent higher than their flat terrain counterparts. These measurements correspond to the "most realistic" and "most critical" situations. The "most realistic" condition was taken as a 45.8 m dike located downwind from the main stack with wind from the plant south direction. The "most critical" case was taken as a 94 m dike located upwind from the main stack (with wind from the plant north direction). For the most realistic case the wind speed at stack height was 13.4 m/s and for the most critical case 26.4 m/s, at which the significant plume downwash completely suppressed all buoyant plume rise.

A simple theoretical model was developed to predict the effect on ground level concentration of dike height and location. With this simple correction to the Gaussian plume model, the effect of dikes of arbitrary height and location can be accurately predicted.

3. Peak to Mean Concentration Fluctuations

Concentration fluctuations were measured using a probability analyzer to determine density function distributions and peak to mean concentrations. It was found that the fluctuation intensity decreases with downwind distance. Probability analysis indicated that extreme values of concentration, above about 1.5 times the mean concentration may be well represented by a log-normal probability density. Using the measured correlation for decay of concentration intensity and this log-normal model, accurate predictions of peak to mean concentration ratios were obtained.

The influence of both the "most realistic" and "most critical" tailings pond dike and wind configuration were to reduce the fluctuation intensity and the peak to mean concentration. Thus, although the tailings pond dike causes a somewhat larger mean concentration due to enhanced turbulent mixing, this same mixing process reduces the peak to mean ratio. Peak to mean ratios exceeded 10 percent of the time were reduced from about 2.0 to 1.8 by the tailings pond dikes. Combined with the increased mean concentrations observed for the dikes, these results indicate that peak concentrations will not increase significantly due to the influence of the tailings pond dikes.

4. Plume Rise in Shear Flow

Because plume rise is a critical factor in determining maximum ground level concentrations, a series of experiments were carried out to determine the effect of vertical wind shear on plume rise. Measurements were carried out in the simulated atmospheric boundary

layer with a $n = 0.28$ wind speed power law in the plume layer and a uniform wind with height. Both had background along-wind turbulence intensities of about 10 percent in the plume layer.

The plume rise observations showed that the final rise height will be overestimated by about 20 percent if wind shear effects are not accounted for. The theoretical model of Djurfors and Netterville (1978) for buoyant plume rise in shear flow gave an accurate prediction for the effect of wind shear on plume trajectory. Other simple corrections for wind shear effects are discussed, and found to be less satisfactory in predicting the plume trajectory.

Recommendations

Because the wind remains attached to the downwind side of the tailings pond dike, avoiding a large flow separation and high turbulence levels, the tailings pond dike should have a negligible effect both on low level sources and on the main stack plume. In general, terrain effects will be much less important on determining maximum ground level concentrations than the trajectory and final rise of the buoyant jets which form low level and main stack plumes. In particular, further study is required to determine the plume break-up and final rise heights in neutral and unstable atmospheric conditions.

CHAPTER 1

INTRODUCTION AND STUDY OBJECTIVES

At the Syncrude plant site the tailings pond containment dike is located about 1.2 km north of the main stack. This containment dike may in time reach a height of 50 meters, about 25 percent of the main stack height. Eventually, the dike will become the predominant topographical feature in the neighborhood of the plant site. The effect of this dike on the dispersion from low level sources within the plant itself, and on the trajectory and diffusion of the plume from the main stack form the basis for the present investigation.

Why a Wind Tunnel Simulation?

The complex interaction of local terrain features on plume dispersion has not yet been successfully modelled mathematically. For this reason, the only viable alternative was an experimental simulation (using a physical model of the tailings pond dike) of atmospheric dispersion in the neighborhood of the plant. This study was carried out in the large atmospheric boundary layer wind tunnel in the Department of Mechanical Engineering at the University of Alberta. The advantage of such a laboratory simulation is that it is possible to generate any terrain feature that may exist in the future. At the same time, the simulated atmospheric conditions are easily reproducible from day to day, allowing the relative effects of various parameters such as wind speed, dike height, and source location to be easily evaluated. A further advantage of wind tunnel simulation is that the events in the wind tunnel occur 20 to 30 times more rapidly than their full scale counterparts. This acceleration of events in the physical model allows long time averages to be generated in a relatively short period of time.

At the same time, laboratory simulations suffer from several disadvantages. The foremost among these is that it is not possible in the present wind tunnel facility to simulate the effects of atmospheric stability, or to generate the turning of wind direction with height caused by Coriolis forces in the full scale atmosphere. These limitations restricted the present study to neutrally stable atmospheric boundary layers, and downwind travel distances of about 5 km.

Wind tunnel modelling of stack gas dispersion provides a specific answer for the particular configuration tested. Because decision making for future planning often requires the extrapolation of such data to new and untested configurations, the present study attempts to generalize specific results using simple mathematical theories of turbulent dispersion. In this way, the specific results of the wind tunnel simulation should be applicable to other situations as well.

Source Inventory

Before beginning a wind tunnel simulation of the effect of the tailings pond dike heights on low level source dispersion, an inventory was carried out to determine the location and relative importance of each of the low level sources on the plant site. This inventory is summarized in Table 1-1, and the locations of these sources are shown on the map in Fig. 1-1. The emission levels shown on the source inventory Table 1-1 represent maximum expected values taken at 120 percent of nominal design conditions. Under average operating conditions, the emission rates from these sources are expected to be somewhat less than these maximum design levels.

All of the distances in Table 1 are relative to an origin at the main stack. The compass directions are nominal Plant North and Plant East

TABLE 1-1. INVENTORY OF CONTINUOUS SOURCES/SYNCRUDE MILDRED LAKE PLANT SITE

Unit Description	Location			Source Height ft	Source Diameter ft	Exit Temp °F	Exit Velocity ft/sec	Fuel Heat Release 10 ⁶ BTU/HR	Emission Rate**, lb/hr		
	Map	North ft	East ft						Total	SO ₂	NO _x
Main Stack 8F-4	1	0 ref.	0 ref.	600	26.0	450	93.4	2930	7,498,000	26,767	6400
Steam Superheater 8-1F-6A&B	2	388	293	130	7.0	580	30.9	125.3	157,800	9.8	28
Steam Superheater 8-2F-6A&B	2	388	-37								
Bitumen Column Feed Heater 7-1F-1	3	1020	320	175	14.4*	440	20.9	523.8	520,080	32.4	145
Bitumen Column Feed Heater 7-2F-1	3	1150	320								
Diluent Preparation Column Reboiler 14F-1	4	1140	483	100	3.75	515	21.3	33.5	33,240	2.1	6
Hydrogen Heater 15-1F-1A&B	5	667	1090	150	5.2	325	19.5	77.4	72,840	4.5	14.8
Hydrogen Heater 15-2F-1A&B	5	792	1190								
Fractionator Reboiler 15-1F-2	6	645	1175	150	6.0	700	22.2	74.9	74,440	4.7	14.5
Fractionator Reboiler 15-2F-2	6	1180	1105								
Reformer Furnace 9-1F-1	7	597	1310	76	13.5	415	36.7	846	839,880	43.4	247
Reformer Furnace 9-2F-1	7	1228	1504								
Bitumen Heater 21F-1	8	2605	1760	20	1.0	1050	85.0	18.0	6,115	None	2.9
Bitumen Heater 21F-2	8	2605	1805								
Bitumen Heater 21F-3	8	1895	1760								
Bitumen Heater 21F-4	8	1895	1805								

*Single stack diameter equivalent to two stacks 10.17 ft diameter
 **Calculated for operation at 120% of design capacity

3

coordinates. "Plant North" is oriented 17.2 degrees west of true north. Fig. 1-1 shows that the crest of the tailings pond containment dike is located about 4,000 feet (1.2 km) in the Plant North direction from the main stack. The only other significant change in surface elevation on the plant site is the 80 foot high (24.4 m) containment dike which runs parallel to the tailings pond dike at a distance of about 2,000 feet (0.6 km) in the Plant South direction from the stack.

Study Objectives

The wind tunnel simulation of atmospheric dispersion on the Syncrude plant site dealt with three interrelated problem areas: low level sources, the main stack plume, and the effects of wind shear on plume rise. All of these studies were carried out using an 800:1 scale model of the plant site in a simulated neutrally stable atmospheric boundary layer.

Considerable care was taken in the test program to establish confidence in the use of laboratory simulation techniques for atmospheric diffusion. The boundary layer simulation was carefully adjusted to produce a neutrally stable atmospheric wind profile with speed variations and turbulent structure typical of the wind approaching the Syncrude plant site. Further general tests in this simulated boundary layer were conducted to confirm that buoyant plume rise, and vertical and horizontal dispersion were properly modelled in the wind tunnel system. Once this preliminary fine-tuning of the wind tunnel system had been completed, a test program was carried out to investigate the main study objectives as follows:

1. Low Level Sources in the Dike Wake

In order to assess the effect of the turbulence generated in the

wake of the tailings pond dike on low level emissions, a series of tests were conducted for a wind direction from Plant North. In this configuration the wind passed first over the tailings pond dike, and then passed over the low level sources. The required measurements were:

- a. To map the extent of the reverse flow recirculation zone on the downwind side of the tailings pond dike using flow visualization techniques in a water channel, and measurements in the wind tunnel.
- b. For two "typical" source locations A and B on Fig. 1-1, to measure the ground level concentration profiles downwind from a low level source. These measurements were to consider a base line case with no tailings pond dike, and for three other dike heights.
- c. To measure crosswind and vertical profiles of concentration from one of these low level sources to determine the effect of the tailings pond dike wake on general mixing characteristics.

2. Main Stack Plume Dispersion

The main stack is the major emission source on the plant site. To provide an accurate model for predicting ground level concentrations from the main stack, the following measurements were required:

- a. Measurements of crosswind and vertical plume spread, and plume rise with no tailings pond dike present were made to provide a basis of comparison, and to investigate the approach to final rise height in a neutrally stable atmosphere.
- b. To establish "most critical" and "most realistic" conditions two wind speeds were studied, equivalent to full scale winds at stack height of 13.4 and 26.8 meters per second. Ground level concentrations were measured for four different wind directions which corresponded to the dike located both upwind and downwind from the stack. For each of

these wind directions a base-line case with no tailings pond dike, and two dike heights were studied. From these 16 different combinations of wind direction, dike height, and wind speed a "most critical" and "most realistic" case were established.

- c. For the "most critical" and "most realistic" cases, measurements of plume rise and vertical spread were used to develop corrections to the base-line case with no dike to account for the effects of dike wake turbulence on plume dispersion from the main stack.
- d. Measurements of the time-varying fluctuating concentrations at ground level were taken to determine the probability distributions of concentration fluctuations, and to predict peak to mean concentration ratios.

3. Plume Rise in Shear Flow

All of the previous measurements were carried out in a single simulated atmospheric shear flow. On the full scale plant site the wind shear with height varies greatly from day to day, occasionally even producing negative shears where wind speed decreases with height above ground. Plume rise is determined by the wind profile in the region above the top of the main stack, and in turn the ground level concentrations are very sensitive to changes in plume rise. To assess the effect of wind shear on plume rise, the following measurements were made:

- a. Turbulence was generated using a symmetric grid to produce a uniform mean profile above stack height, with turbulence levels comparable to those in the simulated atmospheric boundary layer. Vertical concentration profiles at several downwind locations were measured to determine plume rise and spreading rates. These measurements were compared with the base-line case with no dike in the simulated atmospheric shear flow

to determine the effects of wind shear.

- b. Measurements of plume rise were also carried out in a bare tunnel, with a laminar approach flow. In this case, both turbulence and wind shear are no longer present, and by comparing with the wind shear measurements and the grid turbulence measurements, the combined effects of turbulence and shear could be distinguished.

Like most reports prepared in retrospect, the objectives outlined above appear to be concise and logical. In practice, many surprises awaited the investigators along the way. The two most noteworthy of these were the very small effect produced by the tailings pond dike wake on both the low level and main stack plumes, and the very long sample times, corresponding to about three hours in full scale, required to obtain reproducible concentration measurements.

CHAPTER 2
ATMOSPHERIC WIND SIMULATION

Particular care is required in establishing the accuracy of any laboratory simulation of the full scale atmosphere in order to establish confidence in the results of tests in that simulation situation. The foremost liability of any wind tunnel simulation is that if (and usually when) such studies produce unusual and unexpected results it is often difficult to ascertain whether these observations are caused by some inadequacy in the wind tunnel modeling technique, or by some mechanism that would actually exist in the full scale atmosphere. Such uncertainties can greatly impair the usefulness of wind tunnel simulation data, particularly in making expensive or difficult decisions.

The first objective in this study was to accurately simulate a neutrally stable atmospheric boundary layer in 800:1 geometric scale which would be typical of the Mildred Lake plant site. The data for selecting this typical profile were reported by Murray and Morrow (1977), who carried out full scale site tests using single theodolite balloon tracking techniques. For the "unlimited mixing" atmospheric stability situation they found a power law of $n = 0.19$ using $Z_{ref} = 183$ m (600 ft). Their data analysis indicated that the value of the power n increased with increasing values of the reference height Z_{ref} .

In addition, they found that low level jets, in which the wind speed decreases with increasing height above some limit occurred 46% of the time. For this reason, considerable caution must be used in applying the adjective "typical" to any power law wind profile chosen for wind tunnel simulation.

Wind Tunnel System

The general capabilities of the wind tunnel system used for atmospheric simulation are described in detail in Appendix A. The investigation

for the Syncrude plant site was carried out in the lower wind tunnel test section which had a cross section 1.2 m high, 2.4 m wide, and a total section length of 11 m.

The scale modeling criteria for simulating wind flow around terrain obstacles is discussed in detail in Appendix B. The results of this detailed study of simulation criteria are that the wind tunnel is capable of simulating only neutrally stable atmospheric conditions, and is incapable of modeling the turning of wind direction with height caused by Coriolis forces in the full scale atmosphere.

As pointed out in Appendix B, all of the differences between full scale and wind tunnel conditions can be traced to differences in Reynolds number. In the present study a geometric scale of 800:1 and a velocity scale necessary for buoyant modeling of about 30:1 cause the Reynolds numbers of the full scale plant site to be about 25,000 times higher than that of the model. This severe mismatch in Reynolds number is compensated for by a trial and error adjustment of the wind profile and turbulent structure at tunnel test speeds which are typical of the 30:1 velocity scale reduction required for the test program. By "fine tuning" the simulated boundary layer at this low wind tunnel speed, many of the effects of Reynolds number mismatch can be eliminated by using exaggerated roughness elements, and the correct upwind configuration of turbulence generators. By artificially stimulating the boundary layer in this way, the correct levels of turbulent fluctuation and eddy sizes can be generated to achieve a proper model of the full scale atmosphere.

The photograph in Fig. 2-1 shows the final configuration of truncated triangular vortex generators, a barrier at ground level, and surface roughness used in the present study to generate the correct atmospheric wind

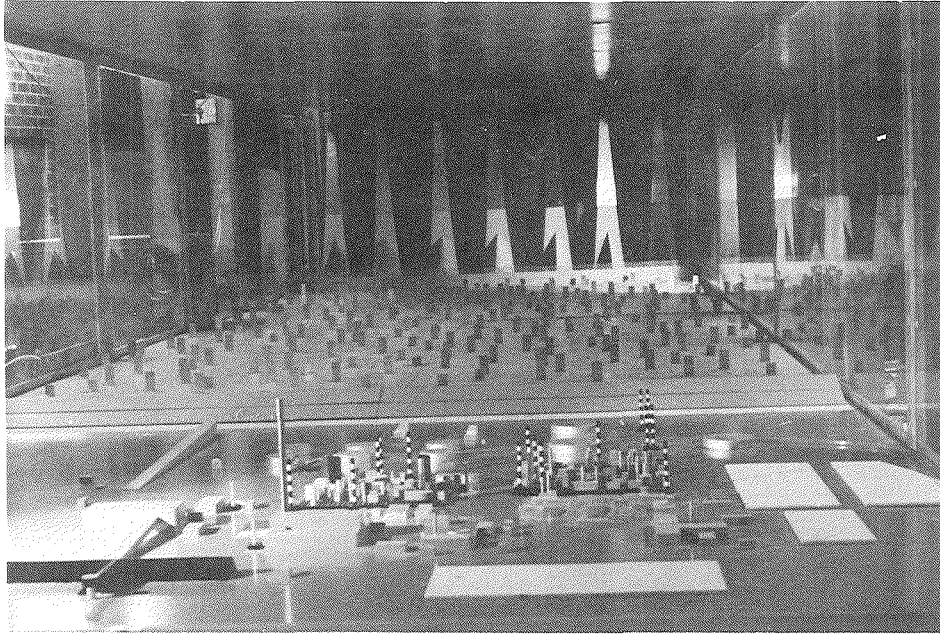


Figure 2-1. Spikes-Barrier and Roughness for Atmospheric Wind Simulation
(North Wind — 150' Tailings Pond Dike)

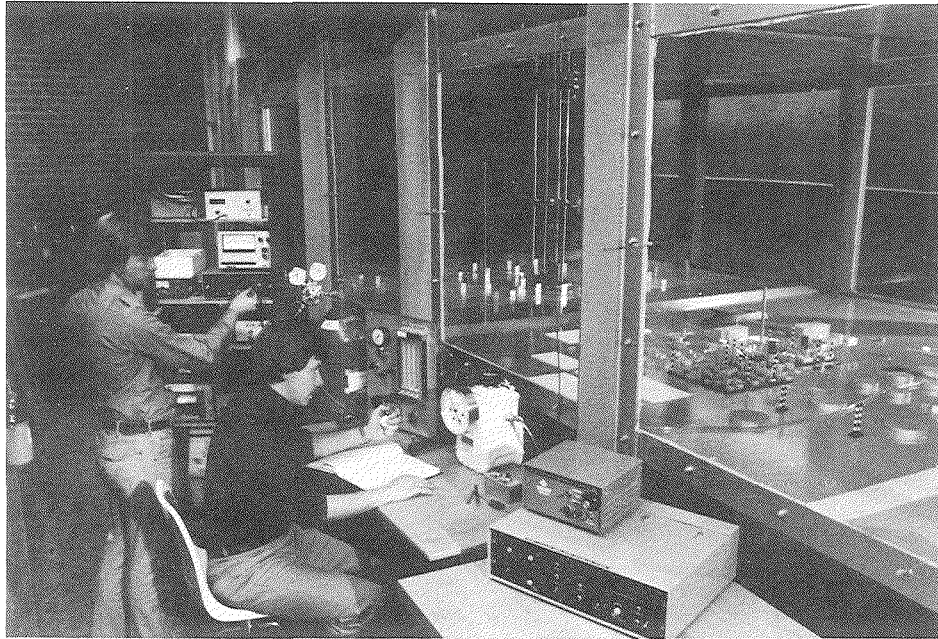


Figure 2-2. Helium Detector and Tracer Gas Injection System

simulation. The detailed techniques for achieving this simulation are discussed in Appendix A.

However, even after the boundary layer has been adjusted to provide the correct turbulent structure at the very low Reynolds numbers used in the model tests, there are still some problems caused by Reynolds number mismatch. One of these is that even when the large scale structure has been correctly modeled there will always be a deficiency in the number of small scale eddies available in the model atmosphere as compared to the full scale. Fortunately, as shown by an analysis in Appendix B, atmospheric dispersion is not particularly sensitive to the scale of eddy motions, and the small scale eddies which are missing in the model wind do not contribute significantly to the dispersion process.

Another problem caused by the different Reynolds numbers is that rounded obstacles, such as the main stack and storage tanks may experience a change in flow regime around them at the low Reynolds numbers used for testing. In particular, flow separation points, and downwash patterns in the wake of such rounded obstacles will often be significantly different in the low Reynolds number wind tunnel model. This effect is discussed in detail in Appendix B, and is not expected to be a significant problem in the present study.

Mean Wind and Turbulent Structure

The vertical variation of mean wind speed and turbulence parameters of the simulated neutrally stable atmospheric boundary layer were measured using single and X hot wire anemometers at a wind speed typical of the required tunnel operating speed for buoyant model tests. These profiles are shown in Fig. 2-3 where it can be seen that the mean wind follows a power law profile $n = 0.18$ for $Z < 20$ cm (160 m full scale) and $n = 0.30$ for

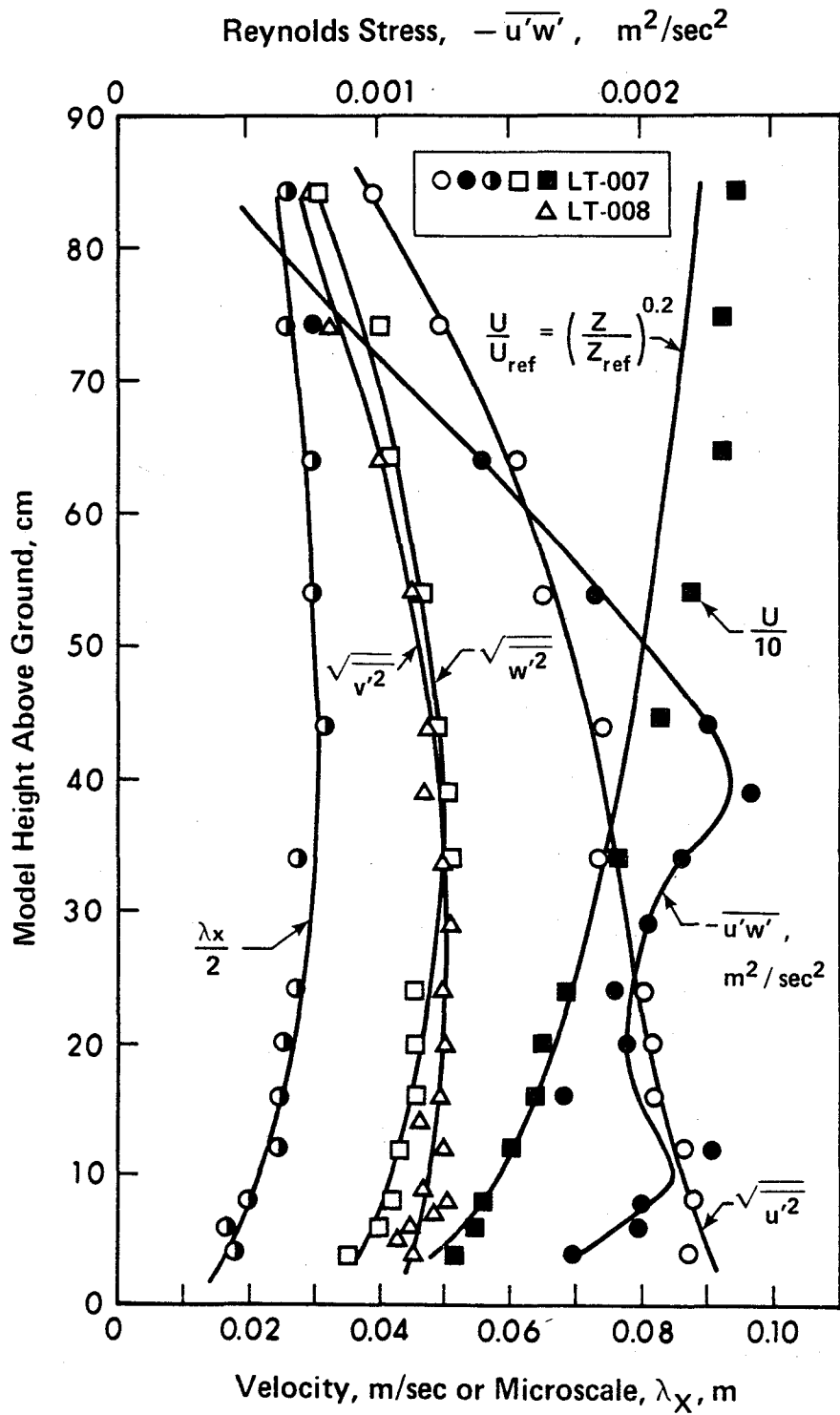


Figure 2-3. Mean Velocity and Turbulence in the Simulated Atmospheric Boundary Layer

$Z > 20$ cm (160 m full scale). The accuracy of this power law approximation to the mean wind profile may be more easily evaluated using the logarithmic plot of Fig. 2-4. This figure also shows that the chosen boundary layer thickness $\delta \cong 75$ cm (600 m full scale) is somewhat arbitrary.

Because many of the characteristics of full scale atmospheric boundary layers are characterized by the surface roughness length Z_0 , Fig. 2-5 shows a semi-logarithmic plot which was used to obtain this roughness parameter. The friction velocity U_* was evaluated from the measured Reynolds stress of $U_*^2 = \overline{-uw} = 0.002$ shown in Fig. 2-3. Fig. 2-5 shows that as expected, the logarithmic law holds only for $Z < 25$ cm (200 m full scale), and breaks down near the wall where the wakes from roughness elements begin to influence the local flow.

The value $Z_0 = 0.05$ cm (0.4 m full scale) obtained in this way was used to compare the turbulent structure of the simulated layer with Counihan's (1975) compilation of full scale adiabatic boundary layer data. This comparison is shown in Table 2-1 using full scale data for the same roughness length Z_0 . Panofsky (1976) in a discussion of Counihan's review data notes that the use of a single power law parameter n is not reasonable, and that in the region where the logarithmic law holds (in our case $Z < 25$ cm) the best fit power law should be approximately

$$\frac{1}{n} = \ln \left(\frac{0.5 Z_{\text{ref}}}{Z_0} \right) \quad (2-1)$$

In our case this gives a value of $n = 0.182$ for the data below 20 cm, in perfect agreement with the experimental observations. Equation 2-1 also shows that the power law should increase gradually as the reference height is raised. This is in agreement with the present study which showed a value of $n = 0.30$ in the upper regions of the boundary layer, and the full scale results of Murray and Morrow (1977) who also found that n increased with

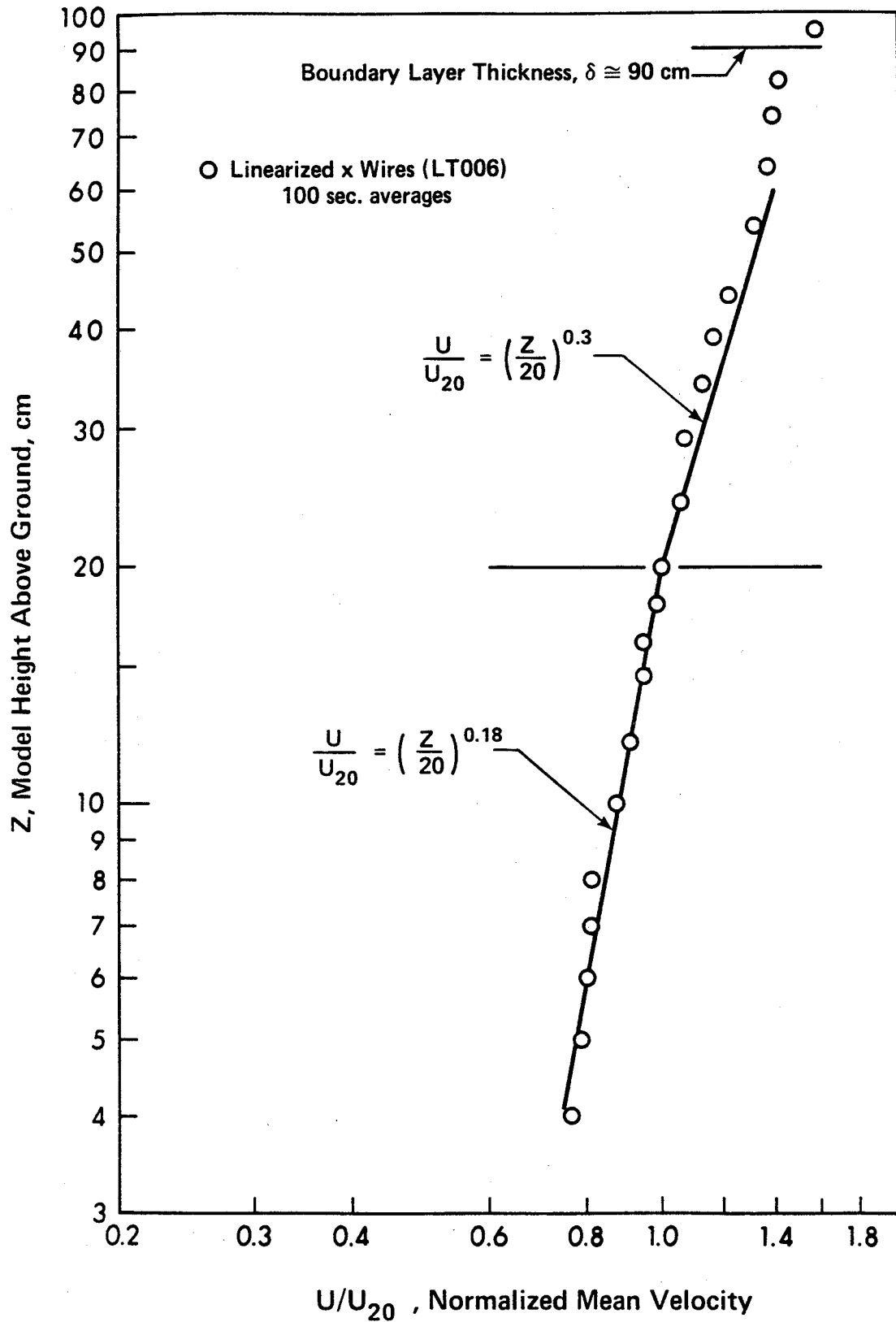


Figure 2-4. Power Law Fits to Mean Velocity Profiles

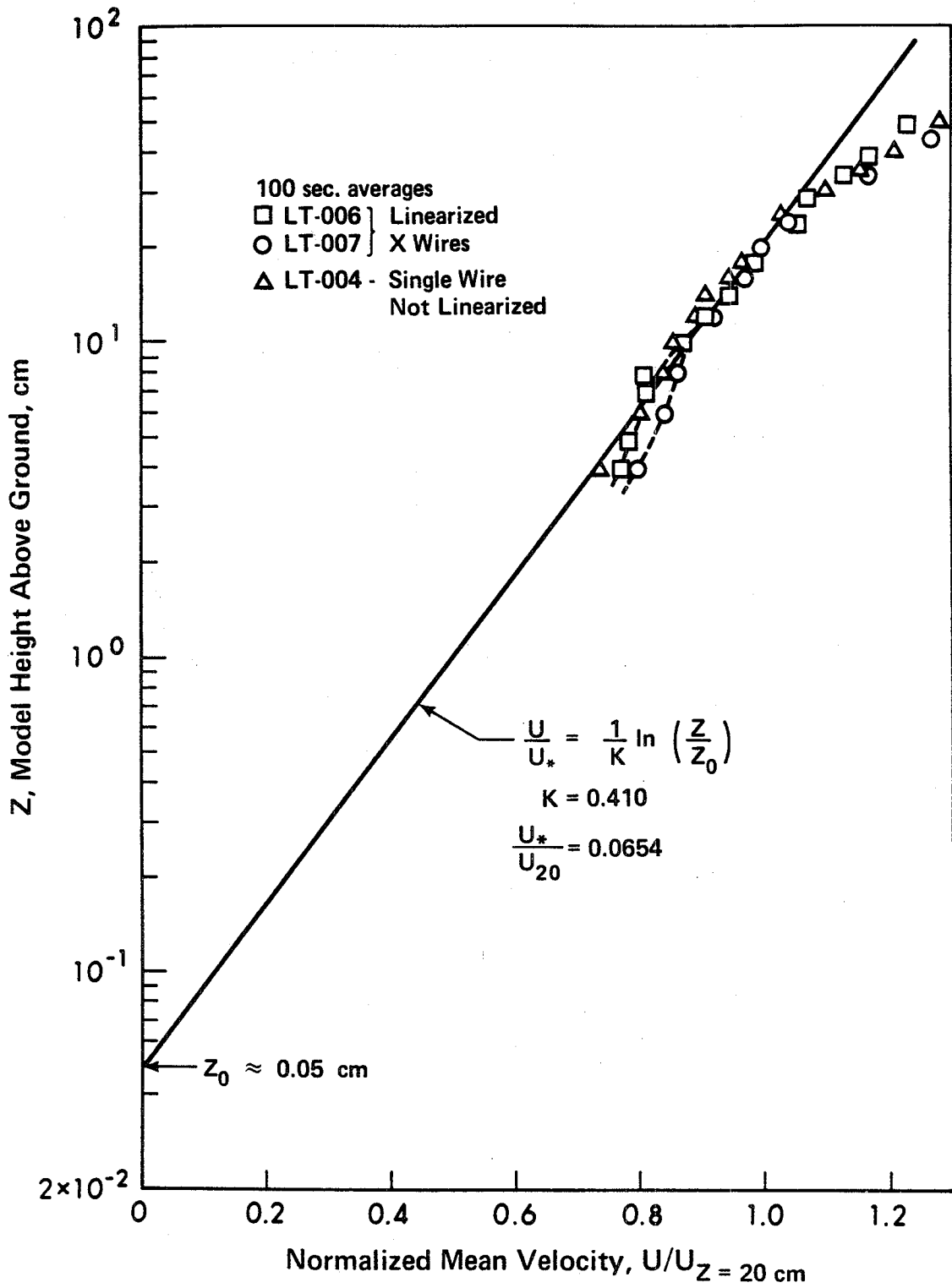


Figure 2-5. Surface Roughness Z_0 from Log-Law Profile Fit

TABLE 2-1

COMPARISON OF WIND TUNNEL BOUNDARY LAYER
WITH FULL SCALE ATMOSPHERIC DATA OF COUNIHAN (1975)

Parameter	Wind Tunnel 800:1 Scale	Full Scale Neutral Stability with same Z_0
Roughness height, Z_0	0.4m	Fixed at 0.4m
Mean velocity power, n	0.18 $Z < 160m$ 0.30 $Z > 160m$	0.20 ± 0.03
Boundary layer thick- ness, δ	650 - 750m	600m (approx.)
$\left(\frac{\overline{u^2}}{UW}\right)^{0.5}$ @ 30m	1.94	1.9
$\left(\frac{\overline{v^2}}{u^2}\right)^{0.5}$ @ 30m	0.53	0.75 ± 0.15
$\left(\frac{\overline{w^2}}{u^2}\right)^{0.5}$ @ 30m	0.41	0.50 ± 0.1
$\frac{C_f}{2} = \frac{\overline{uw}}{U_\delta^2}$ @ 30m	0.00236	0.00251 ± 0.0005
$\sqrt{\frac{\overline{u^2}}{U}}$ @ 30m	0.17	0.20 ± 0.03
Integral Scale, Λ_x	150m @ $Z = 30m$ 180m @ $Z = 160m$	$130m \pm 50$ $200m \pm 50$
$\frac{\overline{uw}}{u^2 + v^2 + w^2}$ @ 100m	0.17	$0.14^* \pm 0.01$

* - Data from Hinze (1975) p. 643, p. 729.

reference height Z_{ref} .

The comparison in Table 2-1 shows excellent agreement between the simulated and full scale atmospheric boundary layers with one notable exception. The simulated boundary layer appears to have a deficiency in cross wind fluctuation levels as evidenced from the low values of the ratio $(\overline{v^2}/\overline{u^2})^{0.5}$ and the high value of the structure function $\overline{uw}/(\overline{u^2} + \overline{v^2} + \overline{w^2})$. To some extent low values of the cross wind fluctuation level are expected in any wind tunnel model because of the restraining influence of the tunnel side walls in preventing the low frequency fluctuations in wind direction which contribute to long term turbulent diffusion. In the present case, however, this value for cross wind turbulence level is somewhat lower than would be expected even including the influence of the tunnel side walls. Fortunately, these lower values of turbulence intensity did not appear to have any significant influence on vertical and cross wind plume spread, as will be seen later.

Flow Uniformity

In modeling diffusion processes and plume rise it is essential that the mean wind speed and turbulent structure remain constant in the downwind direction. In the present study the requirement for both longitudinal and cross wind flow uniformity was taken into consideration during the adjustment and fine tuning of the surface roughness, barrier and vortex generators. Longitudinal and lateral uniformity was measured with the entire tunnel floor covered with random roughness. The later introduction of the scale plant site model caused some longitudinal variations, but these were natural, in that they would also occur over the flat cleared plant site area in the full-scale system.

Both the longitudinal and cross wind uniformity were very good in the final flow configuration. In the cross wind direction the mean wind

profile showed the typical saddle shape with a minimum velocity on the tunnel centerline rising by about 1.5% at the position midway between the centerline and the tunnel side walls. The cross wind uniformity of mean velocity was $\pm 6\%$ of the centerline value over a distance 1 m on either side of the centerline. In the full scale this provides a useable cross section width of approximately 1.6 km. Cross wind variations of turbulence levels were also relatively small, with both the longitudinal and vertical turbulence intensity levels varying by a maximum of 10% of their centerline values over a width from the centerline to midway to the tunnel side wall.

Longitudinal variations of mean wind speed and turbulence intensity were even smaller than the cross wind variations. Over a 4 m test section length in which all of the dispersion experiments were carried out the turbulence intensity varied by no more than $\pm 10\%$ of its average value. Some of these variations are summarized in the table below.

Height Above Ground, Z	Maximum Range of Turbulence Intensity $\sqrt{u^2}/U$
5 cm (40 m)	0.176 to 0.193
20 cm (160 m)	0.143 to 0.154
50 cm (400 m)	0.072 to 0.090

Concentration Modeling and Tracer Gas System

The modeling of diffusion processes in the simulated atmospheric boundary layer was accomplished by injecting helium, or a helium-air mixture from the test source, and sampling at a downwind position. The concentration of helium tracer gas in the diffusion plume was measured by

aspirating a sample from any desired point in the wind tunnel, and passing it through a heated element four-arm thermal conductivity bridge of the same type used in gas chromatographs. This helium detector and tracer gas injection system is shown in the photograph in Fig. 2-2. To compensate for background concentration levels a reference sample was drawn simultaneously from a point close to the source height and about 1 m upwind of the edge of the plant site model. The imbalance of the thermal conductivity detector bridge was displayed continuously on a chart recorder, and averaged over four consecutive 100 sec samples using a low-noise bridge amplifier coupled with a voltage to frequency converter and counter. By using this long averaging time, and periodically turning off the tracer gas at the source to obtain zero drift readings, a high level of accuracy was maintained. Concentration readings of 400 sec averages were reproducible within $\pm 5\% \pm 5$ ppm, including all sources of error such as variations in tunnel speed and helium tracer flow rate, zero drift, and probe positioning. In the present study the concentration levels were typically 100 to 500 ppm, so that measurements were generally accurate to about 5%. A schematic diagram of the system used to produce helium air mixtures, and the sampling and detection equipment is shown in Fig. 2-8.

Ground level concentration measurements were obtained using a sample aspirating probe as shown in the photograph in Fig. 2-6. Vertical concentration and velocity profiles were measured by attaching probes to a remotely controlled, motor driven vertical traverse mechanism, which is shown in the photograph in Fig. 2-7. Elevated cross-wind concentration profiles could also be measured using the system by rotating it into the horizontal plane, and attaching supports at the ends. To increase the data collection rate

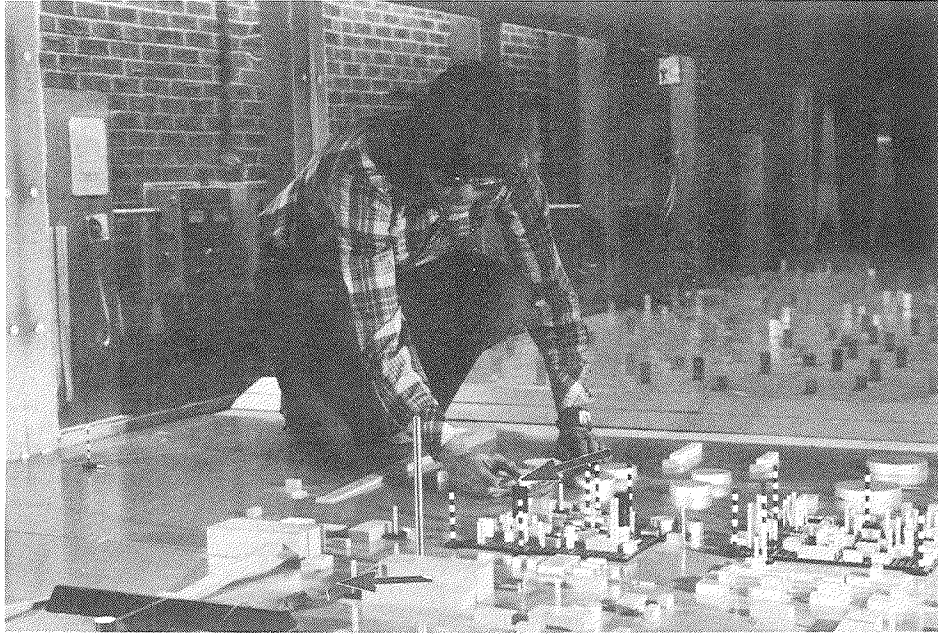


Figure 2-6. Positioning Low Level Source on 800:1 Scale Model
(Arrows: Source and Ground Level Sample Probe)

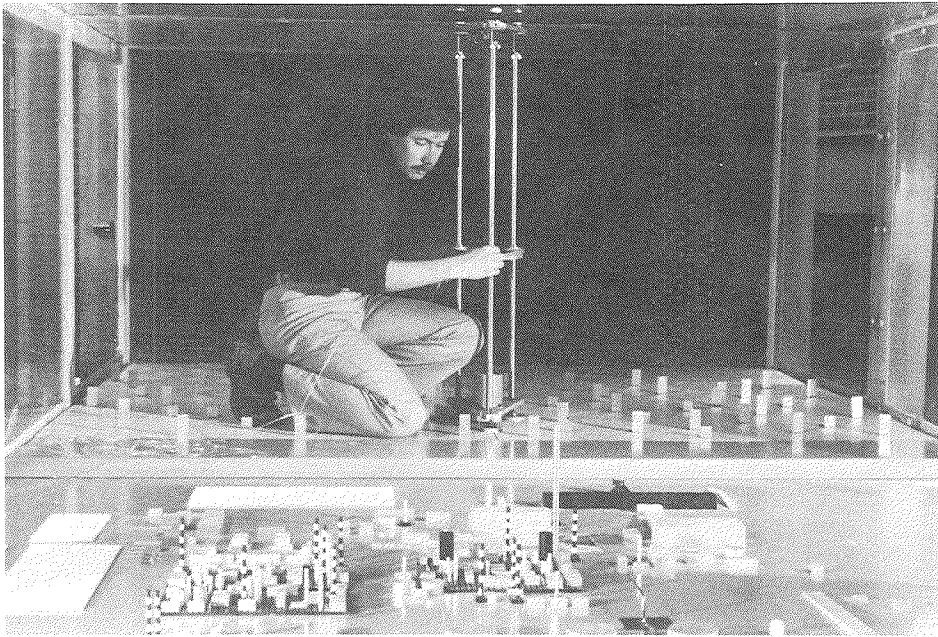


Figure 2-7. Adjusting Sampling Probe on Vertical Traversing System

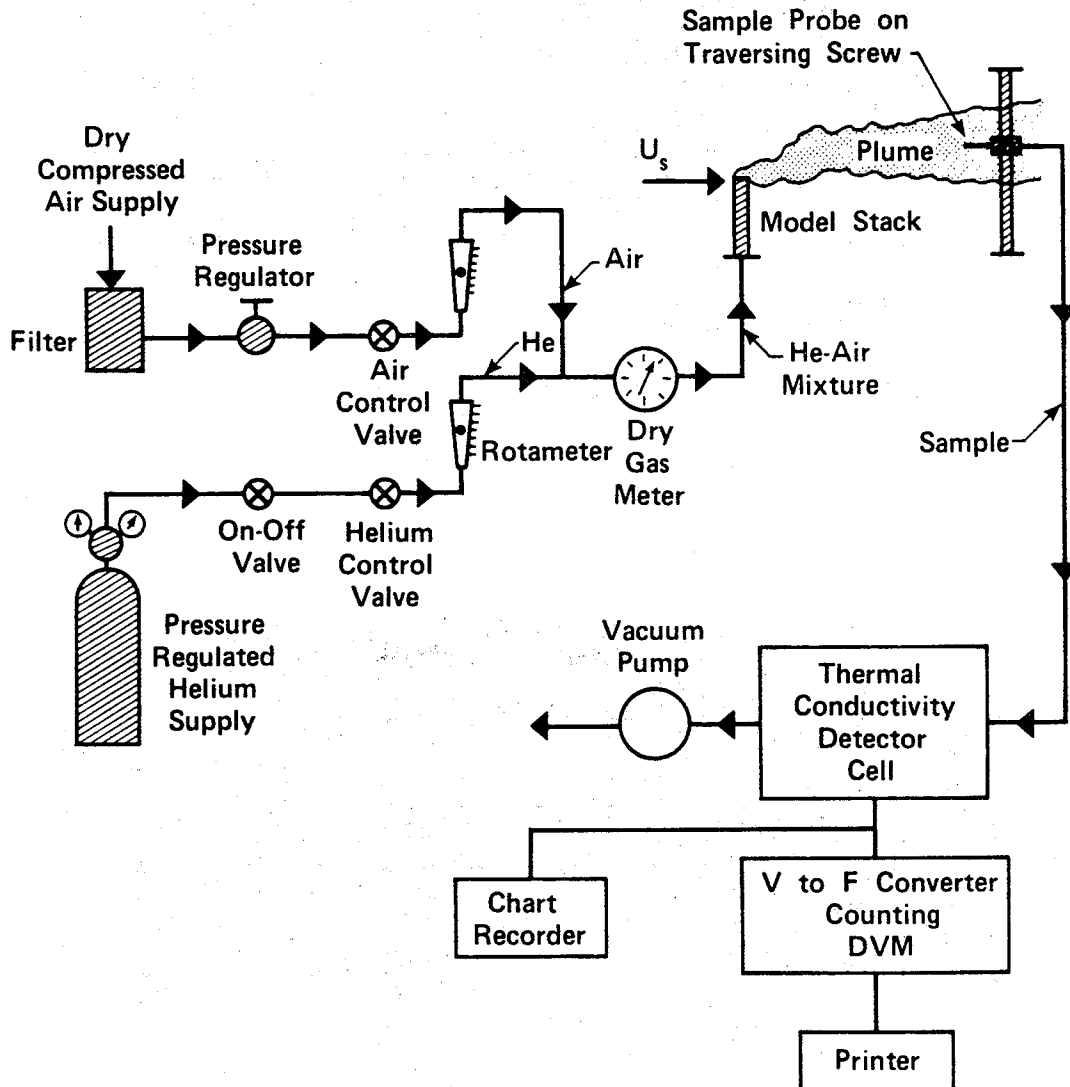


Figure 2-8. Tracer Gas Injection and Detector System

for some profiles, two concentration detectors were operated simultaneously, aspirating samples from probes spaced 5 cm apart.

Modeling Buoyant Plumes

Because the concentration detection system used in the study requires helium as a tracer gas, it was convenient to simulate the buoyancy effects of the stack gas plume using a mixture of helium and air. The air was filtered, pressure regulated and set by a control valve and rotameter to obtain the correct flow rate. Bottled helium gas was also treated in the same way, and the two components were mixed and the final mixture flow rate evaluated on a dry test meter as a double check. This system for tracer gas regulation is shown in the schematic diagram in Fig. 2-8.

The stack gas injection system in Fig. 2-8 was modified during the experimental program by replacing the two rotameters and the dry gas meter with two dry gas meters, one in the helium line and the other in the air line. For both systems the meters were calibrated with a standard wet test meter.

Because the trajectory of a buoyant plume changes with varying wind speed, a wind speed scale factor must be developed to determine the equivalent full scale atmospheric speed which corresponds to a particular wind tunnel test. The necessary conditions to obtain a match between the momentum and buoyancy induced rise of a stack gas plume in model and full scale are derived in Appendix B.

In order to maintain reasonably high wind tunnel operating speeds the stack gas density in the model is generally maintained at a lower value than the full scale. However, in the present study the model was operated with the same stack gas density ratio $\rho_s/\rho_a = 0.554$ as the full

scale stack. By using the same density ratio the effect of fluid property variations on plume entrainment near the stack was properly simulated.

"Flux modeling" was chosen as the criteria for scale modeling of the stack plume. Flux modeling requires that both buoyancy flux, F , and momentum flux F_m are matched in model and full scale. The rationale for this choice is that all plume rise models predict that the buoyancy flux (rather than the buoyancy per unit volume of stack gas) determines the plume rise. Various types of modeling criteria are discussed in Appendix B, and the velocity scales for wind speed and stack exit velocity are given by equations B16 and B17.

Two different full scale conditions were simulated in the present study. In the first test series the model stack was simply a stainless steel tube with no internal roughness or obstructions. Because the model stack internal Reynolds number was about $\rho_s W_s d / \mu = 300$ the flow in the tube was laminar with a kinetic energy factor of $\alpha = 2.0$. This factor α is the ratio of mean stack momentum to the momentum in the average stack velocity W_s , and is discussed in Appendix B. Inside the full scale stack the flow will be turbulent, at a Reynolds number of about 7×10^6 , and with an expected $\alpha = 1.03$. The second test series was carried out with a perforated plug mounted in the stack to flatten the velocity profile and produce $\alpha = 1.27$, to better approximate the full scale turbulent profile. The scaling factors for wind speed and stack velocity for these two test series are listed in Table 2-2.

When both the wind speed and stack gas flow rate are fixed by the scale relationships in B16 and B17, there is a fixed value for the concentration scale given by equation B7 for mass concentrations and C9 for

TABLE 2-2
VELOCITY SCALE FACTORS FOR FLUX MODELING

Parameter	TEST SERIES I STACK OPEN SYN 057 to SYN 128	TEST SERIES II STACK WITH PLUG SYN 129 to SYN 207
Geometric Scale $\frac{d_f}{d_m}$	800	800
Kinetic Energy Factor α	2.0	1.27
Wind Speed Scale eq. (B16) $\frac{U_{sf}}{U_{sm}}$	33.4	29.8
Stack Velocity Scale eq. (B17) $\frac{W_{sf}}{W_{sm}}$	46.5	33.1
Time Scale eq. (2-2) $\frac{t_f}{t_m}$	24.0	26.8
Volume Concentration Scale eq. (C9) $\frac{C_f/C_{sf}}{C_m/C_{sm}}$	0.810*	0.647*

* for $T_{sf} = 505^\circ\text{K}$ and $T_{af} = 294^\circ\text{K}$

volume concentrations in Appendix B. The time scale factor may be determined from

$$\frac{t_f}{t_m} = \frac{X_f}{X_m} \cdot \frac{U_m}{U_f} \quad (2-2)$$

where the subscripts "m" and "f" indicate model and full scale values. The concentration and time scales computed from equation 2-2 and C9 are tabulated in Table 2-2.

Using the scale factors from Table 2-2 the equivalent full scale conditions for the two test series were computed, and are presented in Tables 2-3 and 2-4. The standard 100% load conditions for the full scale plant are given in the table below

FULL SCALE 100% LOAD CONDITIONS

Stack SO ₂ Volume Concentration	1553 ppm
Total Stack Volume Flow	1170 m ³ /sec
Stack Exit Velocity W _s	23.75 m/sec

The 400 second averaging times for concentration measurements were obtained by averaging 4 consecutive 100 second averages. This 400 second interval corresponds to about 3 hours in the full scale, emphasizing the very long time averages under constant wind speed necessary to determine stable mean values.

All of the previous discussion has related to Flux modeling in which buoyancy flux is matched between model and full scale. Froude

TABLE 2-3
MAIN STACK CONDITIONS FOR FULL AND MODEL SCALE
TEST SERIES I - STACK OPEN - SYN 057 TO SYN 128

Parameter	Full Scale	800:1 Model
Stack Height, h_s	183 m	22.9 cm
Inside Diameter, d	7.92 m	0.99 cm
Gas Molecular Weight, M_s	27.6	16.07
Exit Temperature, T_s	505°K	294°K
Standard Ambient Temperature, T_a	294°K	294°K
Stack Gas Density Ratio ρ_s/ρ_a	0.554	0.554
Contaminant Concentration C_s	1553 ppm sulphur dioxide	5.173×10^5 ppm helium
Kinetic Energy Factor α	1.03	2.0
Exit Velocity w_s	46.8 m/sec	1.006 m/sec
% Rated Load	197%	197%
Wind Speeds at Stack Height U_s	16.7 and 33.4 m/s	0.50 and 1.00 m/sec
Concentration Sample Time	160 min	400 sec

TABLE 2-4
MAIN STACK CONDITIONS FOR FULL AND MODEL SCALE
TEST SERIES II - STACK WITH PLUG - SYN 129 TO SYN 207

Parameter	Full Scale	800:1 Model
Stack Height, h_s	183 m	22.9 cm
Inside Diameter, d	7.92 m	0.99 cm
Gas Molecular Weight, M_s	27.6	16.07
Exit Temperature, T_s	505°K	294°K
Standard Ambient Temperature, T_a	294°K	294°K
Stack Gas Density Ratio ρ_s/ρ_a	0.554	0.554
Contaminant Concentration C_s	1553 ppm sulphur dioxide	5.173×10^5 ppm helium
Kinetic Energy Factor α	1.03	1.27
Exit Velocity w_s	28.5	0.8604 m/sec
% Rated Load	120%	120%
Wind Speeds at Stack Height U_s	13.4 and 26.8 m/sec	0.45 and 0.90 m/sec
Concentration Sample Time	179 min	400 sec

number modeling is an alternate condition, in which the non-dimensional buoyancy force on an individual parcel of stack gas is held constant in model and full scale. The Froude Modeling equations are developed in Appendix B as B-11 and B-12. Using these equations the wind speed scale ratio for Test Series II is 28.3 instead of 29.8 for Flux modeling. The stack exit velocity scale in Test Series II is 34.9 for Froude modeling compared to 33.1 for Flux modeling.

To see the relative difference between Flux and Froude modeling we can use the buoyancy length $L_B = F/U_s^3$ to define a dimensionless downwind distance X/L_B for plume rise. Using Flux modeling criteria, X/L_B is the same in model and full scale at corresponding points on the site model. However, with the different velocity scales for Froude modeling, the non-dimensional lengths X/L_B in the model will be 23% larger (for Test Series II) than their full scale values at the same site location. Because transitional plume rise is proportional to $L_B^{0.66}$ and final rise to $L_B^{1.0}$ the use of Froude modeling may underestimate plume rise in this case, because Froude scaling will produce model L_B value smaller by a factor of 0.815 than model values from Flux modeling. The basic reason for choosing Flux modeling for the present study is that all physically realistic mathematical models of plume rise use the buoyancy flux rather than the densimetric Froude number.

Downwash effects in the stack wake were properly simulated in the experiments. For a typical test speed of $U_s = 1$ m/sec the Reynolds number for flow around the model stack was about 800, corresponding to a value of 2×10^7 for the full scale stack. Both of these values lie outside the transitional region of 3×10^4 to 3×10^6 , discussed in

Appendix B, where variations in wake pressure coefficients occur. This indicates that for long (2-dimensional) cylinders the wake pressure coefficients will be properly modelled. However, near the top of the stack there may still be some mismatch between model and full scale base pressure coefficients. This mismatch is possible because full scale measurements of base pressure on short cylinders with length to diameter ratios of about 3.0 show no evidence of an upper transition Reynolds number and its associated decrease in base pressure. In the absence of an upper transition Reynolds number near the stack top, the base pressure coefficient on the model of $C_p \approx -0.8$ is not a good simulation of the expected full scale value of $C_p \approx -0.5$. In this case the model tests may somewhat overestimate stack wake downwash effects on the plume.

Effect of Stack Gas Turbulence on Plume Rise

In the previous section it was pointed out that two distinctly different test series were carried out to model the Syncrude plume. The first test series used a laminar stack gas, while the second test series inserted a plug in the stack to cause the exit flow to be turbulent. This change from a laminar to turbulent stack gas was made during the course of the study when it was discovered that the effect of the velocity profile in the stack gas could not be entirely corrected for through the kinetic energy correction factor α .

The use of a laminar stack gas in the first test series was justified by noting that most of the turbulence responsible for entrainment in a plume is either self-generated from buoyancy, or contained in atmospheric turbulence. The velocity profile shape was accounted for by including the kinetic energy correction factor α in the modelling equations. After completing part of the

experimental program, there was some concern that all of the initial conditions at the stack exit could not be accounted for by α . To investigate the effect of stack velocity profile and turbulence a series of tests were carried out using a perforated plug in the stack to produce a turbulent velocity profile at the stack exit. Velocity and turbulence profiles were measured at the stack exit, and are shown in Fig. 2-9. Because the internal stack Reynolds number with a helium-air mixture was only about 300, the perforated plug could only produce an approximately fully developed turbulent profile. As shown in Fig. 2-9 both the turbulence level and the kinetic energy factor α were both somewhat higher than expected in full scale. The measured velocity profiles in Fig. 2-9 were determined using pure air as the stack gas, with a Reynolds number of 600, twice as high as that of the helium-air mixture used in the wind tunnel tests. Plume rise curves determined from measured vertical concentration profiles are shown in Fig. 2-10. The data with solid triangles and open circles show the effects of inserting the turbulence generating plug in the stack while maintaining all other parameters such as stack gas volume flow rate and wind velocity constant. It is clear from these two curves that changing the velocity profile shape at the stack exit has a measurable effect on plume rise. The lower value of kinetic energy factor α for the turbulent stack gas leads, as expected, to a lower plume rise.

To examine whether the flux modelling equations in Appendix B could account for the differences between laminar and turbulent stack gases solely through kinetic energy factor α , a third experiment was carried out. In this test the approach wind speed and stack gas flow rate were adjusted according to the scale relationships in the modelling equations B16 and B17

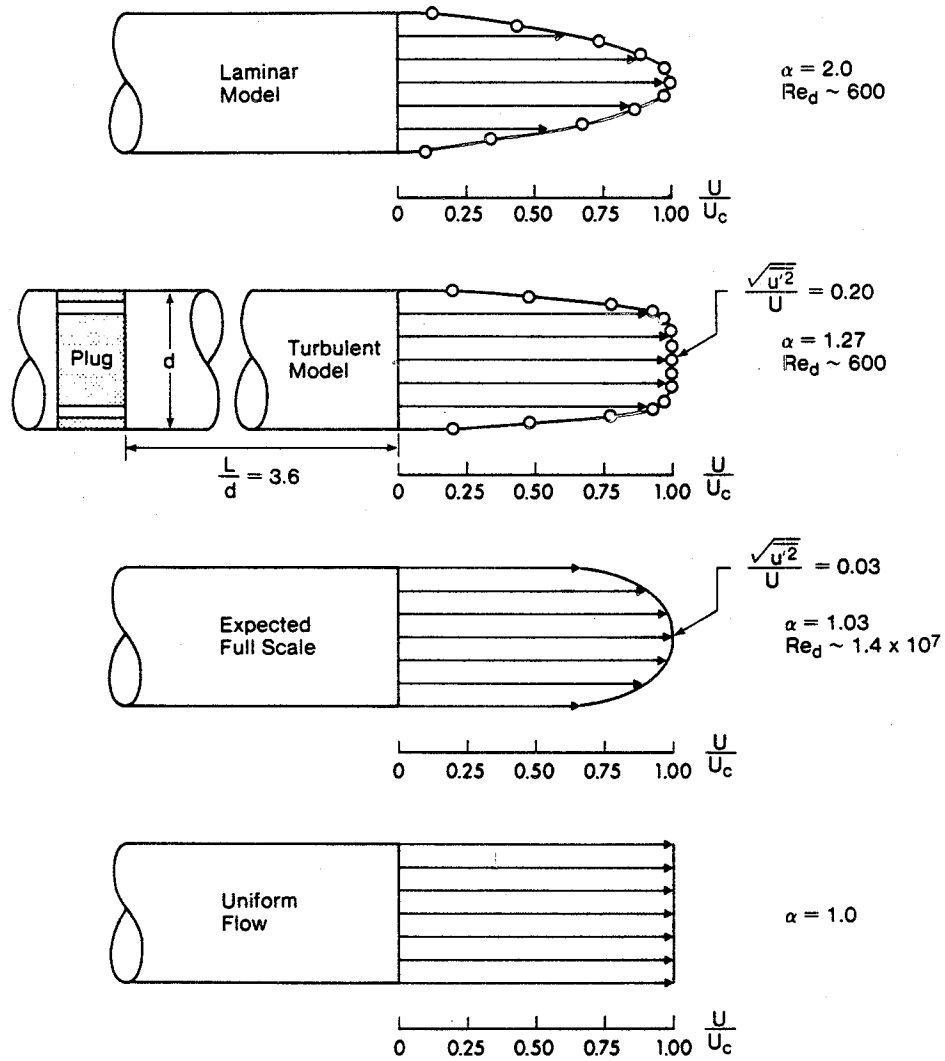


Fig 2-9 Measured Model Stack Exit Velocity Profiles Compared with Full Scale and Idealized Shapes

to produce the same conditions as experienced by the turbulent stack gas. If the modelling equations B16 and B17 are valid for both laminar and turbulent stack gases the data in Fig. 2-10 with solid circles should fall on top of the data for turbulent stack gas shown with open circles. This is obviously not the case. The explanation for the difference between the laminar and turbulent stack gas conditions lies in the effect of stack wake downwash. For both the solid and open circles the downwash parameter $\sqrt{\phi_M} = 1.6$, which lies close to the value of 1.5 where turbulent stack gas will experience significant downwash effects into the stack wake. It is apparent from Fig. 2-10 that laminar stack gases are more susceptible to downwash effects, probably because of the lower stack exit velocity at the outer edges of the jet. For the laminar stack gas trajectory shown by the solid triangles in Fig. 2-10, the higher kinetic energy factor α combined with the same volume flow rate used for the turbulent stack gas experiments resulted in a downwash parameter of $\sqrt{\phi_M} = 2.0$. This was high enough to avoid downwash effects, even with a laminar stack gas exit condition.

The differences between the plume trajectories for the laminar and turbulent stack exit conditions shown in Fig. 2-10 cannot be blamed entirely on failure of the flux-momentum model scale relationships in equations B16 and B17. However, these results do show that plume trajectories, and particularly plume downwash, cannot be accounted for through a single kinetic energy correction factor α . With this in mind, all of the remaining tests in the experimental program were carried out with the turbulence generating plug in the stack. With a turbulent stack exit condition assured, it was felt that the small differences in kinetic energy factor α for the model and full scale conditions could be adequately accounted for by its inclusion in the scaling equations.

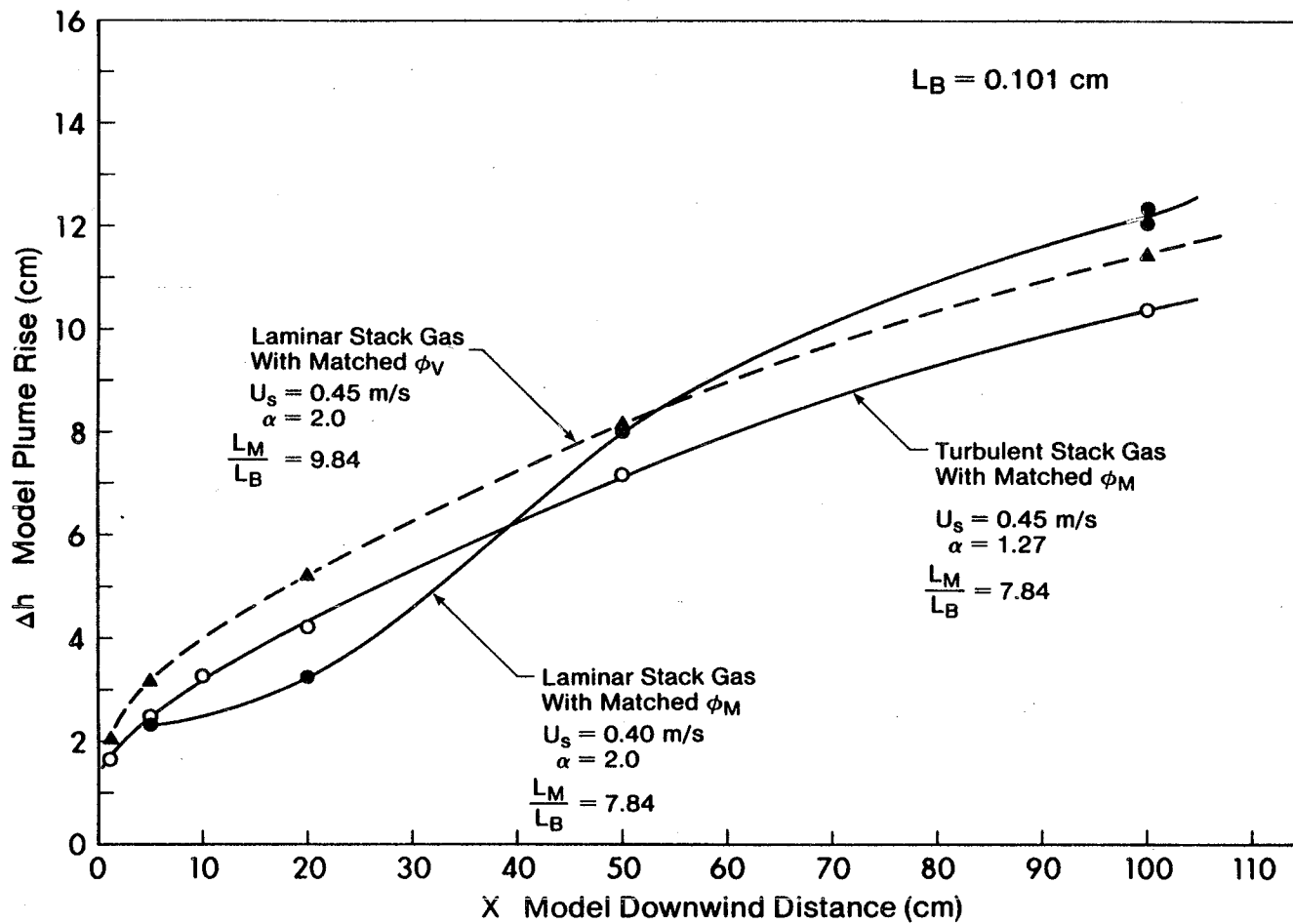


Fig 2-10 Effect of Stack Exit Conditions on Plume Trajectory

The change from laminar to turbulent stack gas not only affects down-wash in the stack wake, but also has a significant effect on the entire plume entrainment process. This is illustrated in Fig. 2-11 where laminar and turbulent stack gas conditions with the same volume flow rate are compared. As expected, the higher momentum in the laminar stack gas causes a greater momentum rise of the plume. However, the stack exit conditions also have a significant effect on the buoyant plume entrainment constant β_2 . Because most of the entrainment in the plume is due to self-induced turbulent mixing, changing the exit conditions from laminar to turbulent flow should only marginally increase the entrainment constant β_2 . Fig. 2-11 shows that the entrainment constant experiences a significant increase, changing from 0.74 to 1.4 as the stack gas conditions are changed from laminar to turbulent. The implication of this result is that plume rise is far more sensitive to initial conditions than we at first thought. From this result it is apparent that considerable care must be taken in modelling the stack exit conditions to assure a proper simulation of full scale plume trajectory.

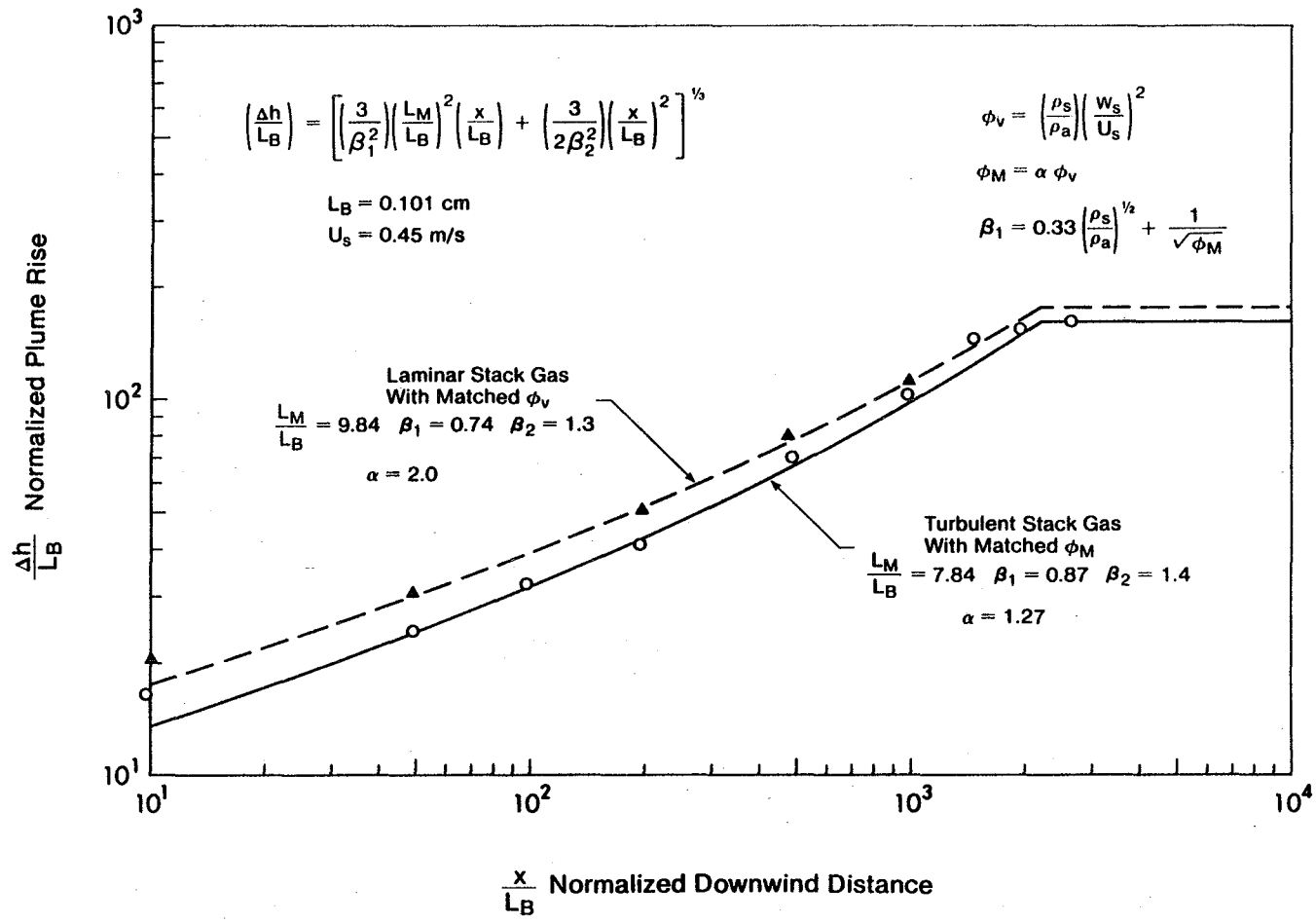


Fig. 2-11 Plume Rise for Laminar and Turbulent Stack Gases at Constant Volume Emission Rate

CHAPTER 3
FLOW IN THE WAKE OF THE TAILINGS POND DIKE

Water Channel Flow Visualization

It is particularly important to establish the point of reattachment of any separated flow downwind of the dike wake to determine if low level sources on the plant site may be entrained into this highly turbulent reverse flow region, and be dispersed upwind of their point of emission. To determine the streamline trajectories near the tailings pond dike, flow visualization techniques were employed using the water channel system shown in Fig. 3-1.

This system was specifically designed to allow flow patterns to be mapped around obstacles immersed in turbulent boundary layers. Because the rate of mixing in the dike wake depends to some extent on the mean velocity profile and turbulence level approaching the dike, it was necessary to simulate typical atmospheric mean velocity profiles and turbulence levels in the approach flow. As shown in Fig. 3-1 this was accomplished by the use of a row of two-dimensional spikes followed by distributed surface roughness in the form of "Leggo" baseboard. The final configuration chosen was a result of a long and tedious program of trial and error measurements, which resulted in the mean velocity profile shown in Fig. 3-3. Measurements of the turbulence intensity were not made because of a lack of suitable instrumentation, however experience has shown that the simulation of the correct mean flow profile usually results in a proper distribution and intensity of turbulence.

With this particular roughness configuration the lateral uniformity in mean velocity was within $\pm 5\%$ of the centerline value at $z = 5$ cm and excluding the outer 10 cm at each side of 66 cm channel width. The mean velocity profile in Fig. 3-3 was measured on the centerline and could be well represented with power laws of $n = 0.2$ for $0.5 < Z < 7$ cm and $n = 0.3$ for $7 < n < 28$ cm. Only this latter profile is shown in Fig. 3-3.



Figure 3-1. Water Channel and Dye Injector for Flow Visualization

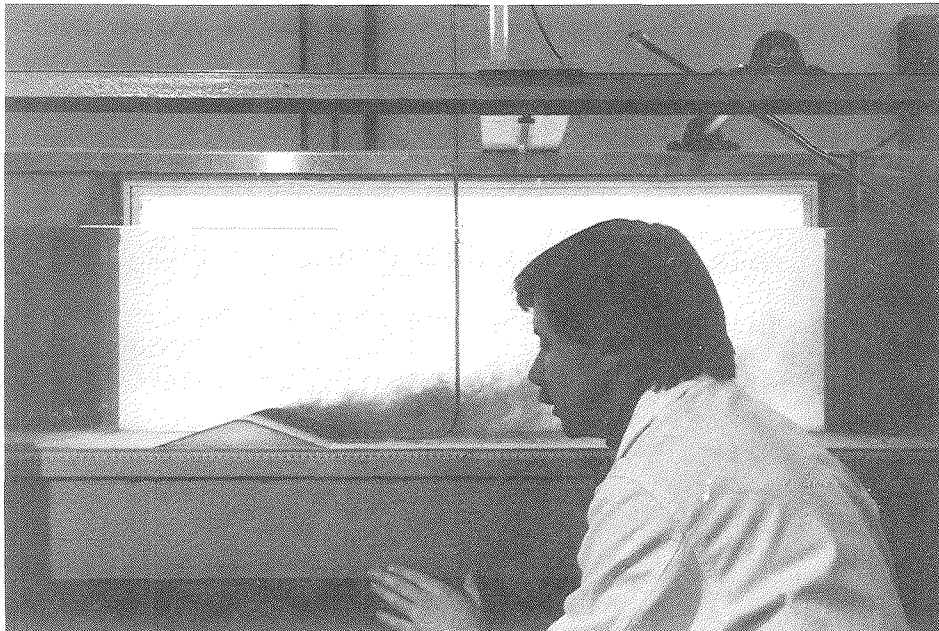


Figure 3-2. Dye Injection into Recirculation Zone Marks High Turbulence Dike Wake

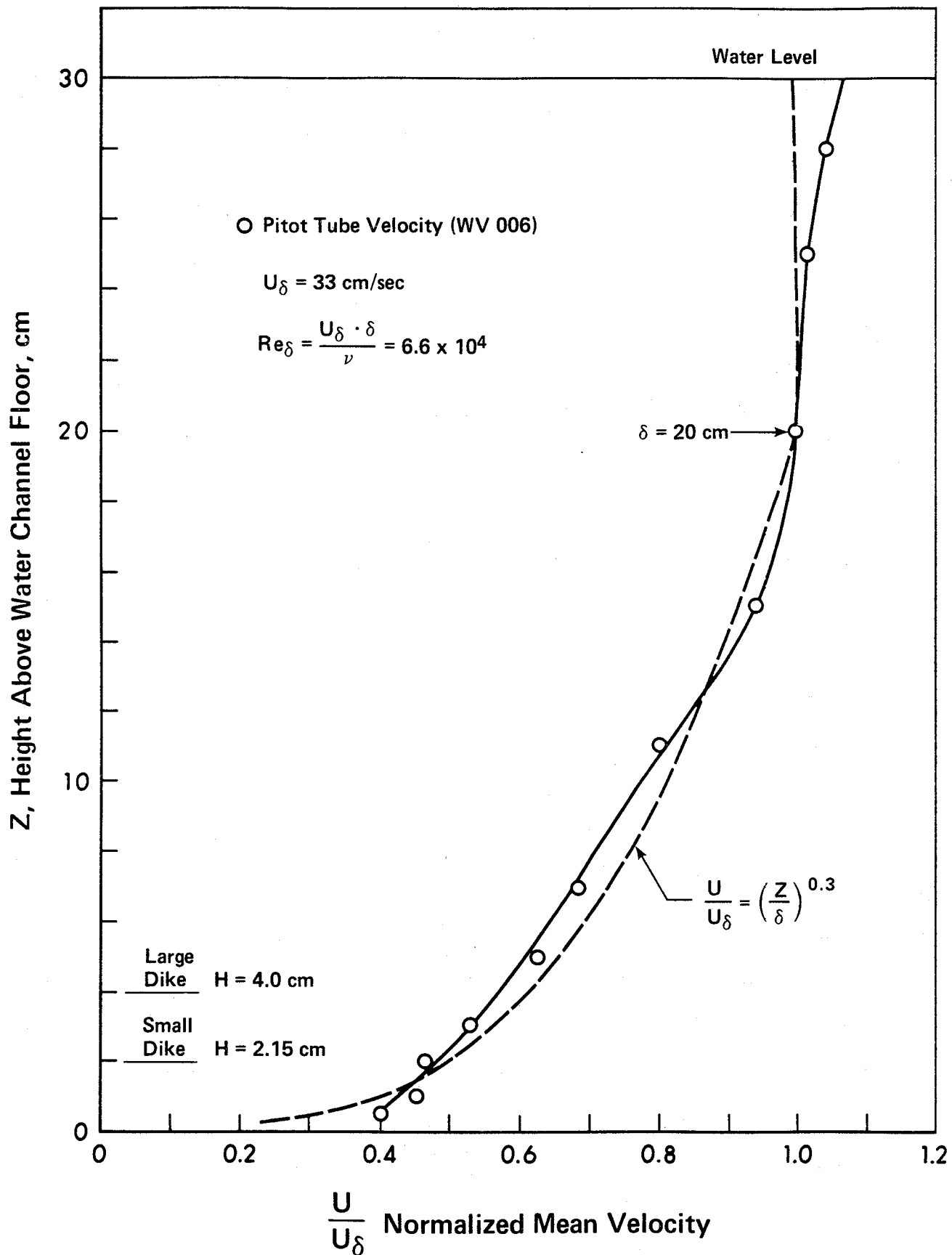


Fig. 3-3. Mean Velocity Profile for Water Channel Flow Visualization Tests

Scale models of the tailings pond and containment dikes were fabricated from sheet metal, and are shown in their final dimensional configuration in Fig. 3-4. A typical flow visualization measurement with dye injection into the recirculation zone behind the large dike is shown in Fig. 3-2.

Water channel measurements were made by releasing a stream of dye from a moveable probe to determine the flow direction, and the intensity of turbulent mixing. The results of this investigation are shown in Fig. 3-5, where the dike wake recirculation zone was observed to have a length of approximately 5 hill heights. As expected, this flow reattachment point fluctuated over a range of about 1 hill height as shown in the figure.

The presence of water in the tailings pond was simulated using a smooth metal sheet which extended approximately 23 hill heights upstream from the model dike. The recirculation patterns in Fig. 3-5 show that the presence of this water level on the upwind side of the dike had very little effect on the flow patterns in the downwind wake.

Reynolds Number Effects on Flow Separation

All of the flow visualization experiments were carried out at a constant water channel speed $U_\delta = 33$ cm/sec at $z = \delta = 20$ cm above the water channel flow. This results in Reynolds numbers based on dike height and velocity at the dike crest of about $U_H \cdot H/\nu \approx 7300$ for the large dike and 3400 for the small dike. These values are alarmingly small compared to their full scale counterparts which are typically 20,000 times larger.

Hopefully, the existence of high levels of turbulent fluctuation in the approach flow will aid in stimulating the proper development of the turbulent recirculation zone downwind from the dike model. However, some caution must be used in applying the results from the flow visualization study to predict the behavior of the full scale dike wake.

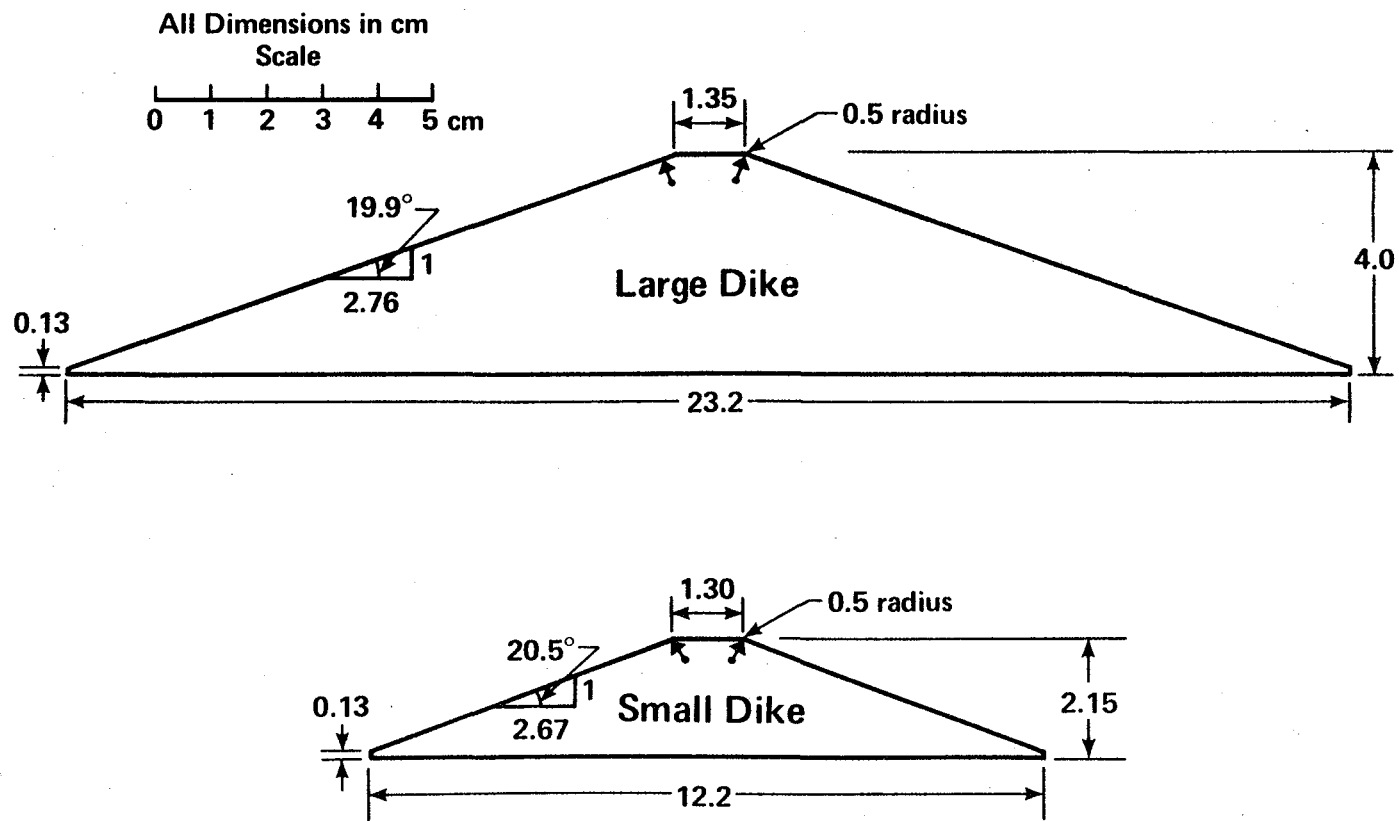


Fig. 3-4. Scale Cross-Sections of Model Dikes Tested in the Water Channel

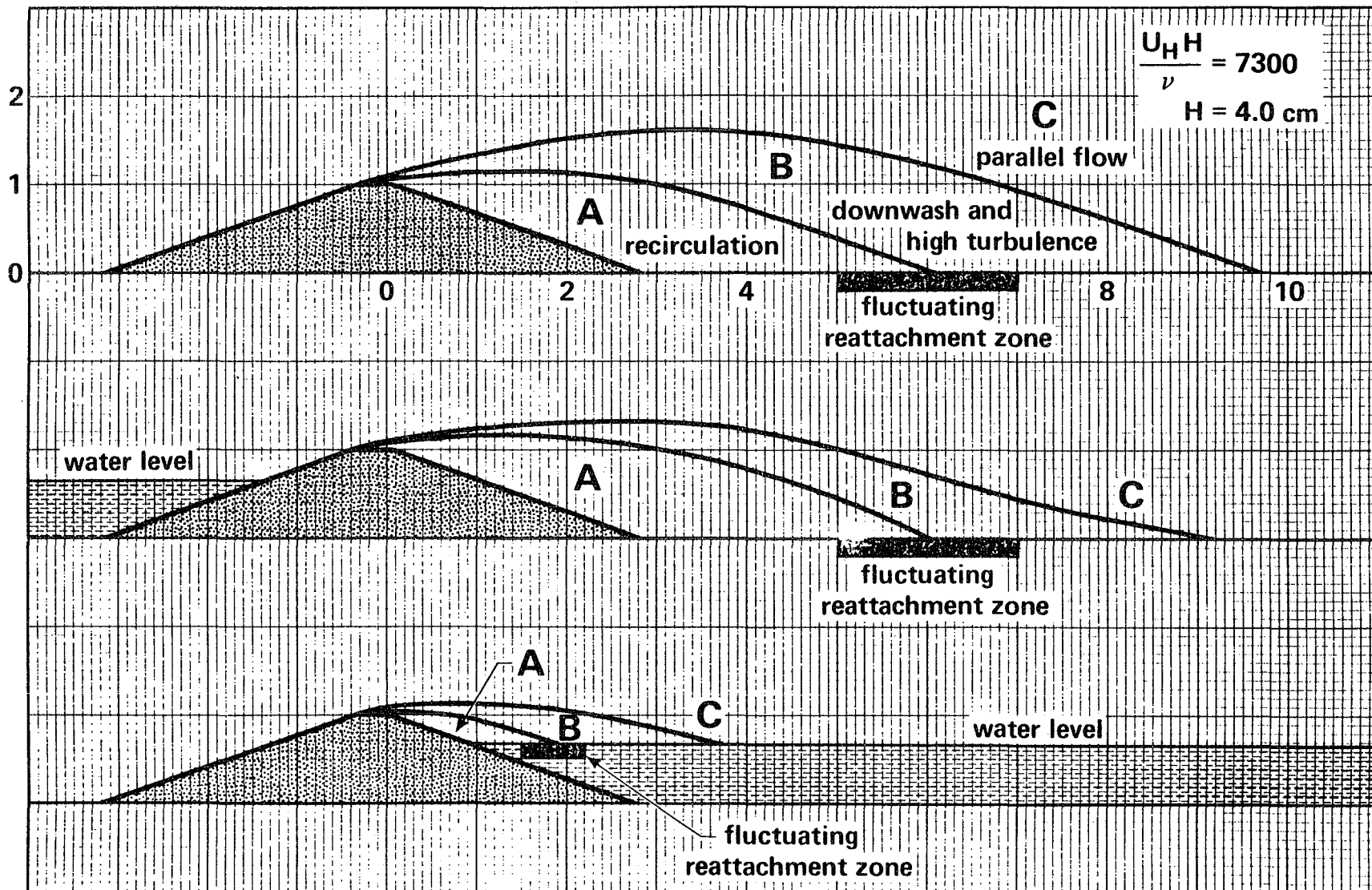


Fig. 3-5. Cavity and Wake Boundaries for Flow Visualization over Large Dike Model in Water Channel

In fact, we will find that Reynolds number effects are of crucial importance to interpreting the wind tunnel and water channel model results. We will see that the recirculation cavity which is present in the water channel flow visualization studies, and in the wind tunnel at the low speeds used in the buoyant plume test, will be absent entirely for the non-buoyant low level source studies, and probably absent for the full scale Syncrude dike. This appearance and disappearance of a recirculation zone is due entirely to the effect of flow Reynolds number.

These Reynolds number effects transformed what were to be a few simple experiments into a major experimental study necessary to accurately assess the expected flow in the full scale dike wake, and to properly simulate this flow in the wind tunnel model.

Previous Investigations of Recirculation Cavities

A considerable body of literature exists which describes the flow in the far wake downwind of an obstacle on a wall. The length of the recirculation cavity immediately downwind of such an obstacle is much more poorly documented, full of uncertainties regarding the test Reynolds numbers, and the specific methods used to determine the cavity length.

A summary of previous data on recirculation cavities is presented in Fig. 3-6. In general, the cavities behind sharp obstacles are quite insensitive to variations in Reynolds number, but show considerable variation with body shape and δ/H , the ratio of approach boundary layer thickness to obstacle height. For a gently curved bell-shaped hill with separation fixed at the crest by means of a trip fence, Huber et al. (1976) found that the cavity length increased as the ratio δ/H decreased. In their specific investigation they found that $L_C/H = 9$ for $\delta/H = 2$ and $L_C/H = 11$ for $\delta/H = 1$.

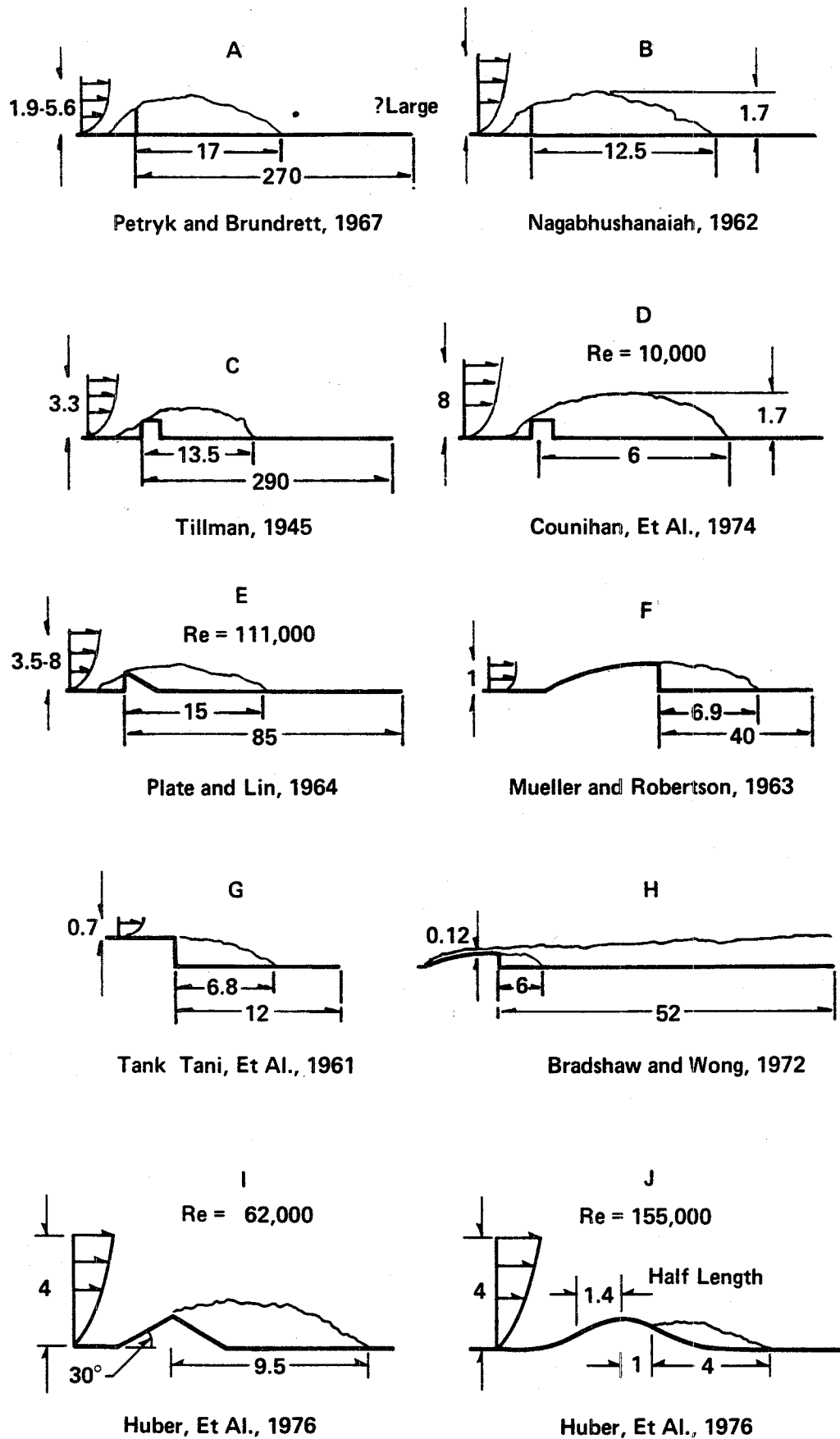


Fig. 3-6. Results of Previous Studies of Cavity Length Behind Obstacles (adapted from Huber et al. (1976))

Based on the experience of testing and designing airfoil profiles, a strong Reynolds number dependence of the location and extent of flow separation on Reynolds number is expected on bodies of gradual curvature. Fig. 3-6 shows one such separation pattern observed over a model hill by Huber et al. (1976), who tried to eliminate these effects by using a sharp edged trip at the crest to fix the point of separation. When this was done the separation cavity increased from $L_C/H = 5$ for natural separation to $L_C/H = 9$ with separation induced at the crest. Both of these observations were made at the same Reynolds number.

Eliseev (1973) carried out a full scale wind study over a 100 m high hill with gradual crest curvature and slopes of 15° to 30° . This full scale study is of interest because the hill contour closely resembled the shape of the Syncrude tailings pond dike. Eliseev's observations, using smoke streamers to visualize instantaneous vertical velocity profiles, showed a separation region of approximately $L_C/H \approx 2$ with a Reynolds number $Re_H \approx 10^7$. Because the downwind slopes of this hill were somewhat more abrupt than that of the Syncrude tailings pond dike, it might be expected that these observations would represent an upper limit on the length of the recirculation cavity behind the tailings pond dike.

Wind Tunnel Measurement of Dike Wake Recirculation

In order to check the results of the water channel experiments a special helium tracer probe was developed to detect surface flow direction in the wind tunnel. A schematic of this probe is shown in Fig. 3-7. Its principle of operation was to use a helium tracer gas signal to determine flow direction by measuring the relative concentration between a point upwind and downwind from a small helium source. These upwind and downwind samples were measured using the helium concentration bridge. The polarity of the signal indicated whether the tracer gas was being aspirated by the reference side or the sample side of the concentration detector.

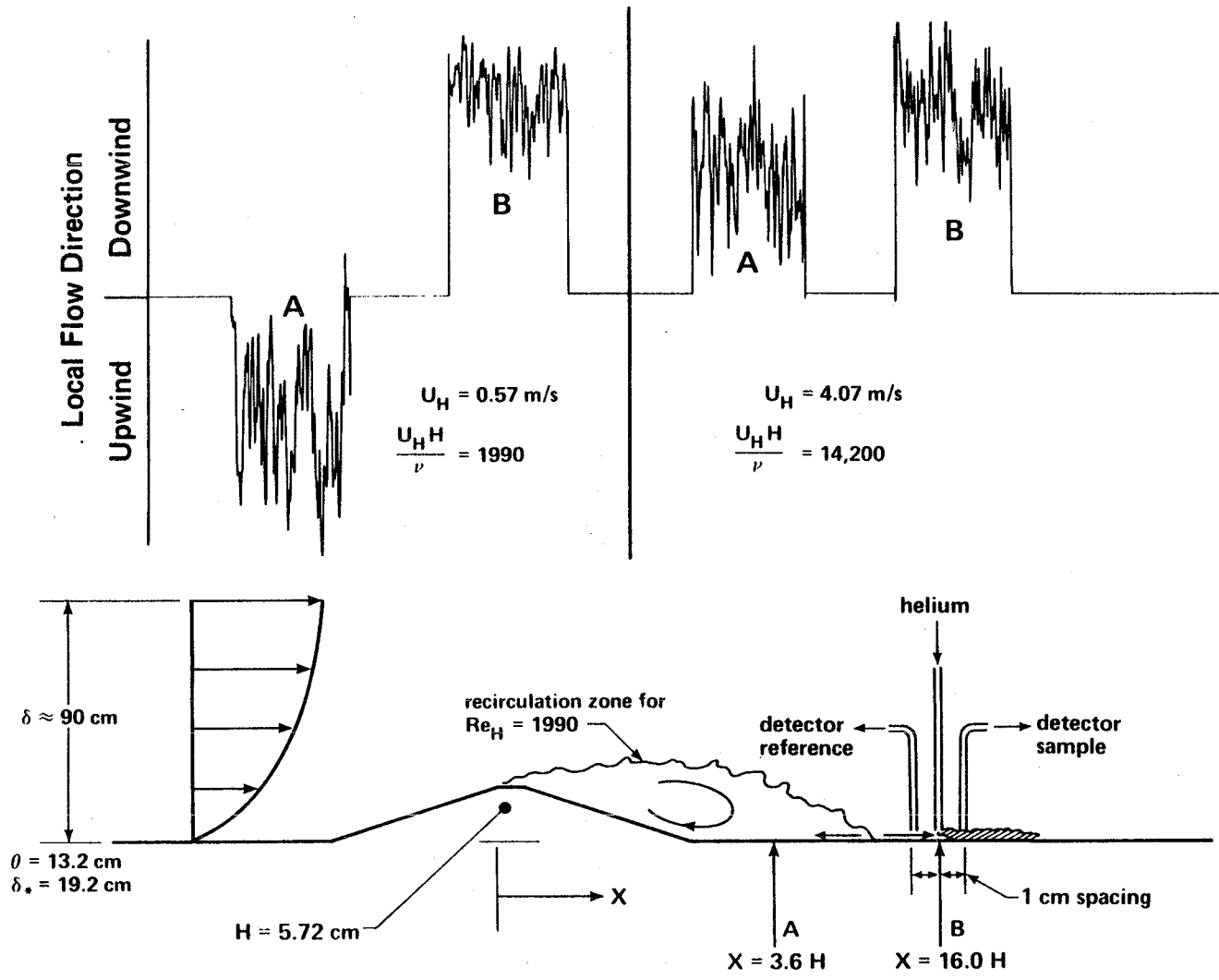


Fig. 3-7. Helium Trace Flow Direction Detector System

The extent of the flow recirculation zone in the wind tunnel model was found to be strongly dependent on Reynolds number. This is illustrated in Fig. 3-7 where the output signals from the flow direction detector are shown at two sampling locations for two different Reynolds numbers. The output of the detector indicates that at sampling location "A" ($X/H = 3.56$) close to the hill there is an upwind (separated) flow at the lower test Reynolds number. In contrast to this, at the higher Reynolds number the same test location shows a downwind (unseparated) flow. For comparison purposes a sample from location "B" ($X/H = 16$) far downwind from the hill is also shown, with its characteristic downwind flow at all Reynolds numbers.

Because the helium tracer system for detecting flow direction was a new development, there was some suspicion that these measurements may have represented some anomaly in the detector operation, or a misinterpretation of the output signal. Some further tests were required to establish confidence in the detector system.

Separation Behind a Sharp Edged Wall

With the doubts raised by the lack of agreement between the water channel and wind tunnel tests of the length of the wake recirculation cavity, an experiment was devised to provide a baseline for comparison. The system chosen for this test was a sharp edged vertical wall, whose point of flow separation is unaffected by Reynolds number.

The flow recirculation zone downwind from this vertical wall was investigated in both the water channel and the wind tunnel. The results are tabulated below.

System	L_C/H	Re_H	δ/H
Water Channel	9.5	7300	4
Wind Tunnel	9.05	63,000	8.6

The length of the recirculation cavity determined by these two independent methods are in excellent agreement, considering the large disparity in Reynolds number and the variation in the ratio δ/H for the two systems. The shape of the flow recirculation cavity and the highly turbulent shear layer above it, are shown in Fig. 3-8, based on the water channel measurements. The excellent agreement between the flow reattachment point determined in the water channel and wind tunnel is even more remarkable considering that Fig. 3-8 shows the fluctuating zone of flow reattachment extends about 2 hill heights upwind and downwind of its average position.

These tests established confidence in the results obtained from the helium tracer gas detector used for flow direction measurements in the wind tunnel.

Dike Recirculation Cavity in the Wind Tunnel

With our confidence restored in the wind tunnel experimental techniques, a series of measurements were performed to determine the effect of Reynolds number on flow reattachment. These results are shown in Fig. 3-9 where they are compared with the water channel measurements. The small differences between the wind tunnel and water channel measurements at the same Reynolds number might be due to the effect of the approach boundary layer ratio δ/H . The increase in cavity length with decreasing values of this ratio are consistent with both the trend and magnitude of the differences observed by Huber et al. (1976), discussed previously.

For the largest dike the reattachment length was consistently about $0.5H$ longer than the two smaller dikes. The reason for this discrepancy may be due to tunnel blockage effects, which amounted to 11% area blockage for the largest dike. Because the wind tunnel test section had a fixed roof with no means of pressure gradient control, the reattachment may have

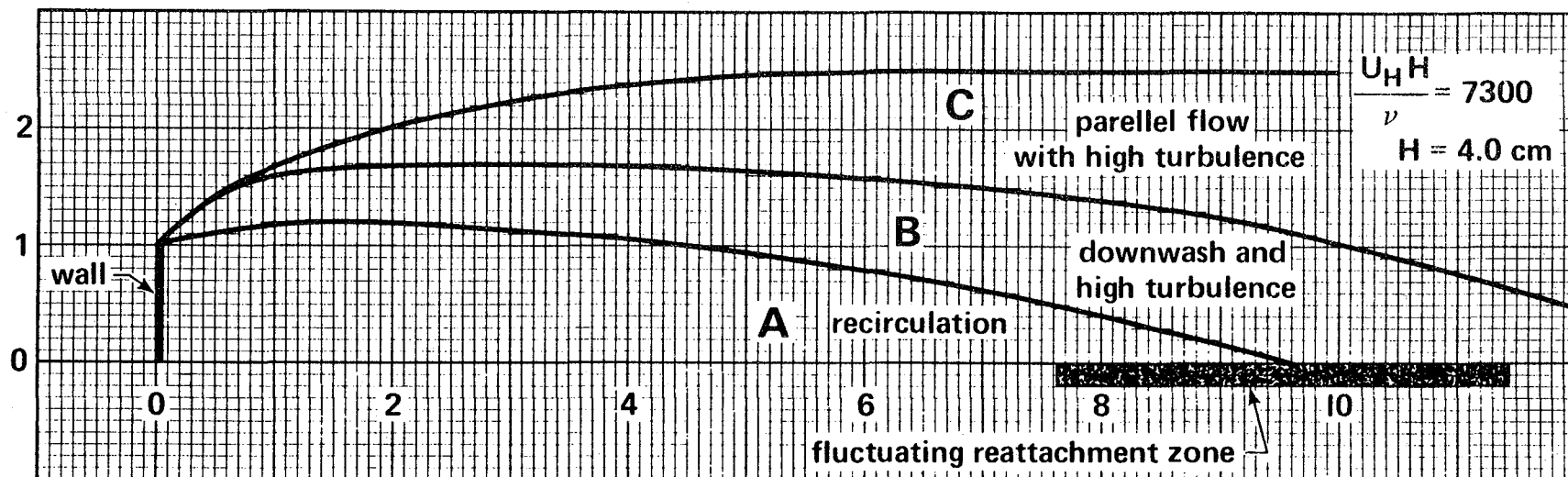


Fig. 3-8. Cavity and Wake Boundaries for Flow Visualization over a Sharp Edge Wall in the Water Channel

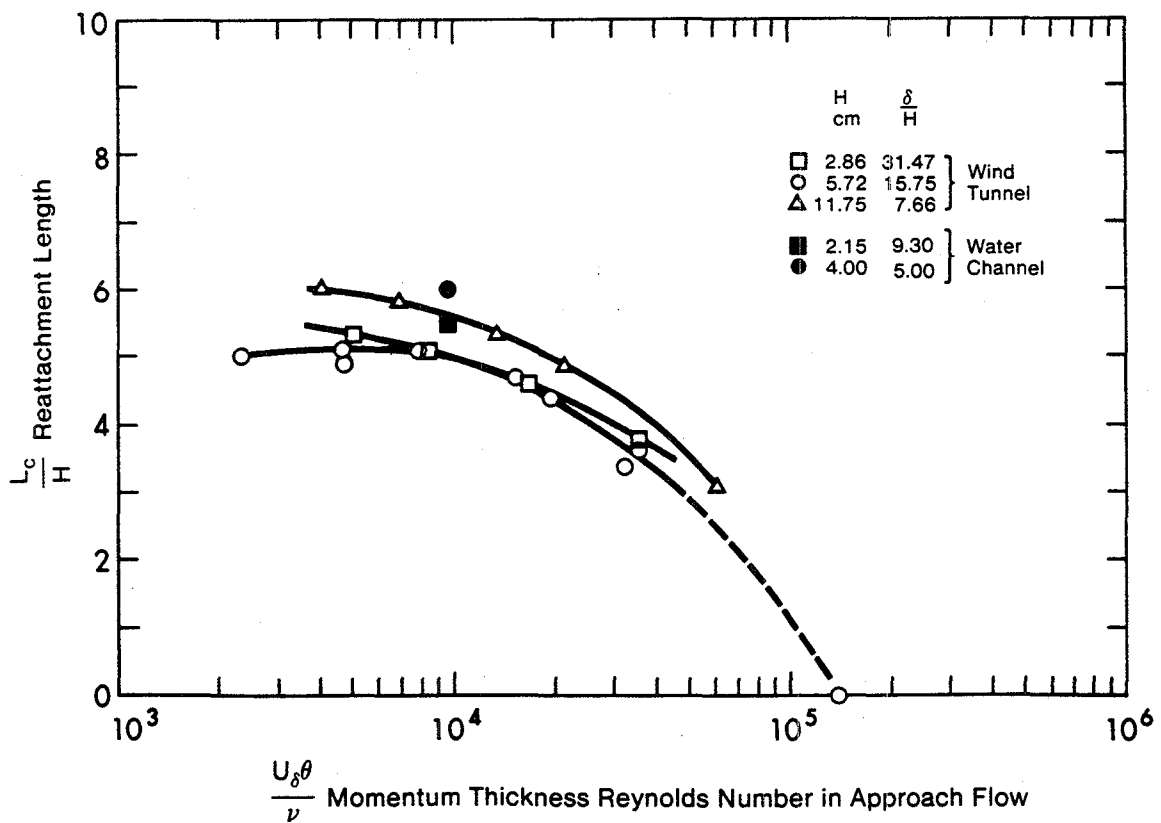
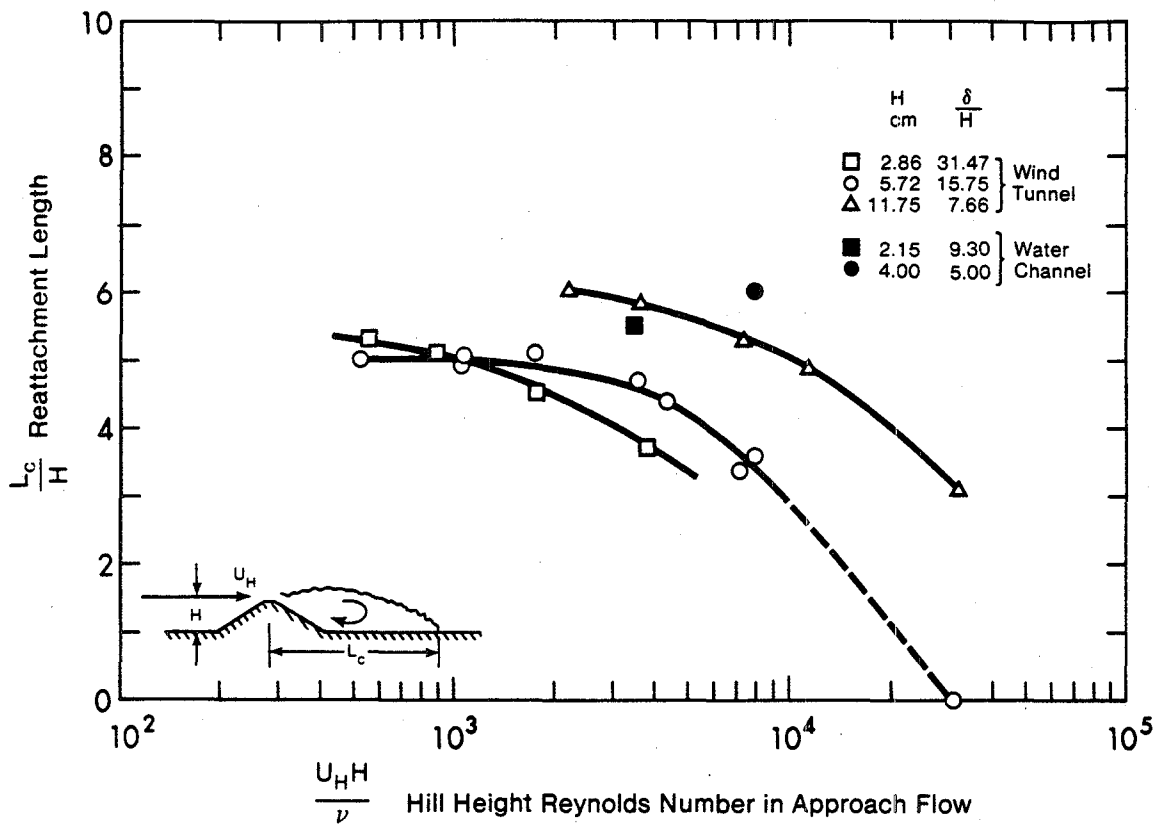


Fig. 3-9. Reynolds Number Effect of Recirculation Cavity Length

been influenced by pressure gradients induced by blockage. This is consistent with results of Good and Joubert (1968) who found that the measurements of base pressure coefficients on walls in turbulent boundary layers with pressure gradients indicated that the rear separation bubble was affected by pressure gradient.

Two different Reynolds numbers are used for correlating the data in Figure 3-9. The local dike crest Reynolds number $Re_H = U_H H / \nu$ and the momentum thickness Reynolds number of the approach flow $Re_\theta = U_\delta \theta / \nu$. The momentum thickness Reynolds number, which is independent of dike height gives a better correlation for different dike heights than the dike crest Reynolds number. However, as H increases, δ/H decreases and the observed changes in L_c/H are consistent with the expected effect of decreasing δ/H . In addition, some of the variation in L_c/H may be due to changes in tunnel blockage for the 3 hill heights. Further studies are required using different approach boundary layers for a constant dike height to determine the appropriate Reynolds number for correlating L_c/H .

The most surprising result of the study was that even for 3:1 dike slopes, which at least visually appear quite steep, the flow recirculation zone disappears at a Reynolds number of about $Re_H \sim 10^5$. Because full-scale Reynolds numbers for dikes are typically 10^7 , wind tunnel measurements at low Reynolds number will not give a true picture of the expected full-scale flow field. The full-scale measurements of Eliseev (1973) support this, indicating that even for relatively steep dikes, flow recirculation zones will be very small.

From the observations summarized in Fig. 3-9 we can draw the following conclusions:

1. The full scale Syncrude dike has a high Reynolds number of about $Re_H = 1.5 \times 10^7$ (for full scale $U_s = 6$ m/sec, $H = 45.7$ m) so that no separation is anticipated in the full scale system.
2. Low Level non-buoyant source experiments which were carried out in the wind tunnel at a Reynolds number $Re_H \approx 31,000$ ($U_s = 12.0$ m/sec) will experience no flow separation downwind from the model dike, in agreement with the full scale expectations.
3. The buoyant plume tests where $0.4 < U_s < 1.0$ m/sec will be typical for our velocity scale factor of about 30:1 will have a separation cavity about 5 hill heights in length. This will not be an accurate simulation of the expected full scale system which should have no separation cavity.

Flow Deflector for Wind Tunnel Dike

To provide an accurate simulation of the dike wake at low tunnel speeds, a flow deflector was mounted on the dike crest. This deflector was positioned by trial and error to direct the flow down the lee side of the dike, thus preventing flow separation. Titanium tetrachloride smoke was used at tunnel speeds in the 0.5 to 1.0 m/sec range to assure that no significant flow separation occurred. The final configuration looked much like the wind deflectors mounted on vehicles to keep the rear window clear.

Mean velocity and turbulence profiles were measured in the dike wake. With the deflector in place the profiles showed that flow separation (with its large wake momentum loss and high turbulence) was almost completely eliminated. This deflector was used in all low speed tests with dikes. The high speed tests at a tunnel speed of about 10 m/sec did not require the use of a deflector because the Reynolds number was high enough to keep the flow attached.

CHAPTER 4DISPERSION FROM LOW LEVEL SOURCES

The effect of the turbulent wake downwind from the tailings pond dike on dispersion from low level sources was investigated for a single wind direction from due plant north. For this wind direction the tailings pond dike lay perpendicular to the wind, and the turbulent wake behind it passed directly over the low level plant sources.

Wind Tunnel Measurements

The low level sources shown on the map in Fig. 1-1 were not simulated on an individual basis. Instead, two low level sources A and B were located a distance of 366 m upwind from the main stack, and at the two crosswind locations shown on the map of Fig. 1-1. These source locations were selected as being the closest typical distances to the dike wake, and therefore the positions which should experience the greatest effect of the tailings pond dike. A standard source height of $h_s = 30.5$ m was selected as typical of an average low level source.

The operating conditions used for the tests are given in Table 4-1 along with a sketch of the source itself, which ejected pure helium tracer gas horizontally to avoid momentum rise. The high tunnel operating speed was chosen to minimize the effects of buoyancy rise. As we shall see later even this large tunnel speed did not completely suppress the rise of the helium tracer gas, which reached an effective source height of about $h = 5$ to 5.5 cm 40 to 44 m. In spite of this small buoyant rise, the tests were typical of dispersion from a non-buoyant source, whose only non-dimensional parameter should be $CU_h h^2/Q$. The reader will recall from the flow visualization studies that at the high tunnel speeds used for these tests, the model, like the full scale dike, will have no flow recirculation region on its downwind side.

TABLE 4-1

OPERATING CONDITIONS FOR LOW LEVEL SOURCES A AND B

Source Height $h_s = 3.81$ cm (30.5 m)

Emission Rate $Q = 101.3$ cm³/sec

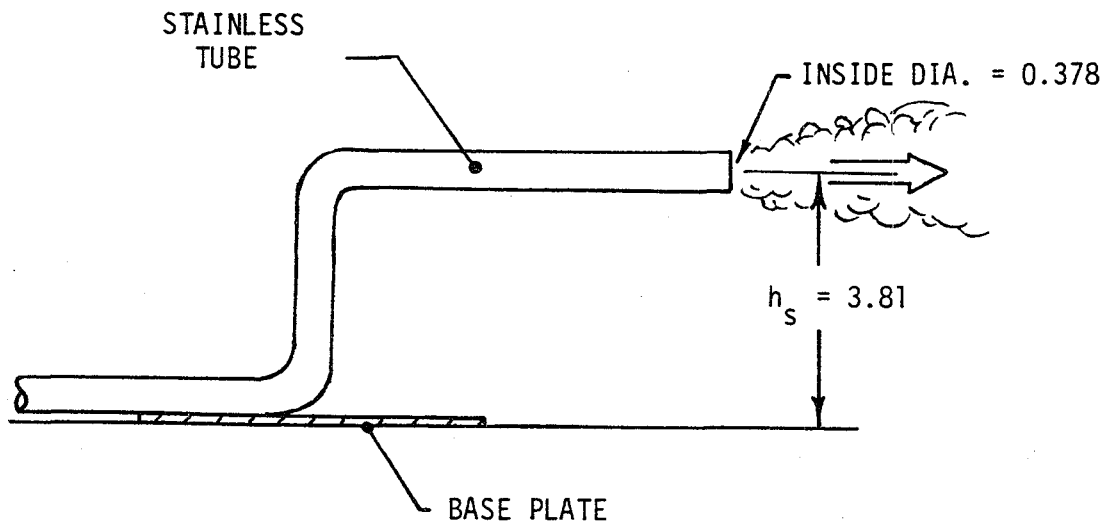
Exit Diameter $d = 0.378$ cm

Density Ratio $\rho_s/\rho_a = 0.138$ (100% helium)

Model Wind Speed at Main Stack Height $U_s = 1183$ cm/sec

Model Wind Speed at Source Height* $U_h = 900$ cm/sec

Upwind Distance From Main Stack = 45.7 cm (366 m) Plant North



*with no upwind dike present

All wind tunnel tests were carried out at a constant speed which was maintained using a reference pitot tube located upstream from the turbulence generator spikes. This reference speed location upwind of the dikes maintained a constant wind speed approaching the dike. At the source locations A and B downwind from the dike, both the turbulence and the mean wind speed may be altered by the presence of the tailings pond dike. With a constant wind speed approaching the dike both of these effects will automatically be included in the observed concentration profiles.

All concentration measurements were made using a 100 second time average, followed by a 10 second reading with no helium injection to compensate for bridge drift. For non-buoyant sources there is no direct time scale ratio between model and full-scale. To determine the full-scale averaging time corresponding to this 100 second wind tunnel measurement, it is necessary to compare the measured plume spreading widths in the wind tunnel to full-scale values determined for various averaging times. We will see later that there is considerable uncertainty determining these full-scale averaging times, which will lead to the same uncertainty in interpreting the full-scale averaging time equivalent to the wind tunnel measurements.

Converting From Model to Full-Scale

The turbulence structure in the approach wind, and the model of the plant site both have a length scale factor of 800:1. This factor can be applied to any of the measured length parameters in the model study, such as x , y , z , σ , h , etc.

The sources A and B used in the wind tunnel study do not represent any specific full-scale source on the Syncrude plant site. For this reason a direct comparison between model and full-scale measurements is neither desirable nor relevant. However, many of the full-scale sources have release heights similar to that chosen for the wind tunnel study, and the dimensionless variable $\frac{C_o U_h^2}{Q}$ should be constant for non-buoyant behavior at high wind speeds. Then, the model (m) and full-scale (f) concentrations are related by

$$\begin{aligned} \left. \frac{C_o U_h}{Q} \right|_f &= \left. \frac{C_o U_h}{Q} \right|_m \cdot \left(\frac{h_m}{h_f} \right)^2 \\ &= 64 \times 10^4 \left. \frac{C_o U_h}{Q} \right|_m \end{aligned} \quad (4-1)$$

Because it is the relative effect of the dike on ground level concentrations that is important, and not the value of the concentration itself, all concentration measurements will be given here in terms of the model concentrations measured in the wind tunnel.

Vertical and Crosswind Concentration Profiles

Vertical profiles of concentration and crosswind concentration profiles at ground level were measured at a single downwind distance of $X = 107$ cm (full scale: 2808' or 856 m) from source location A. The vertical concentration measurements were carried out using the vertical probe traversing system shown in the photograph of Fig. 2-7. Crosswind ground level measurements were obtained simply by moving the ground level sampling probe to the y distance selected. This downwind sampling point was selected to avoid interference with nearby structures. In addition,

this sampling position was located at a point where the ground level concentration profile showed a stable decay rate in the X direction (away from the dips and valleys observed near the point of maximum ground level concentration).

Concentration profiles were measured without a dike, and for two dike heights of 75' and 150'. Figures 4-1 and 4-2 show typical concentration profiles obtained with an upwind dike height of 150'. Plume spreading rates σ_y and σ_z were determined by fitting ground-reflected Gaussians which had the same area under their curves. As can be seen, the observed concentration profiles show excellent agreement with the Gaussian plume model.

The plume spreading ratio σ_z/σ_y at $X = 107$ m (2808 ft., 856 m) for source A was approximately 0.66 to 0.67, in very good agreement with the Brookhaven data of Singer and Smith (1966) who found a value of 0.69 for neutrally stable atmospheric conditions. These values are presented in Table 4-2, and compared with full-scale values in Table 4-3. The high turbulence near ground level causes significantly larger measured plume spread than predicted values for an elevated release.

Effective Source Height

Table 4-2 shows values of vertical and crosswind spreading rates obtained from Gaussian fits to the measured concentration profiles. In addition, using the measured plume spreading ratio σ_z/σ_y and the experimental value of the maximum concentration the effective source heights can be computed by writing equation (C3) as

$$h = \left[\frac{2}{\pi e} \left(\frac{Q}{C_{\text{Omax}} U_h} \right) \left(\frac{\sigma_z}{\sigma_y} \right) \right]^{0.5} \quad (\text{C3})$$

This equation requires that the plume spreading ratio σ_z/σ_y remain constant at all X locations. These effective source heights are shown in Table 4-2, and lead to the conclusion that although the plume was emitted at a height of 3.81 cm above the surface, buoyant plume rise has caused its effective height to be approximately 5.5 cm. This corresponds to a 30.5 m emission height to a final rise of 44 m.

Only part of the plume rise can be attributed to buoyancy effects. Using Briggs (1969) estimate for buoyant rise

$$\Delta h = 1.6 \frac{F^{1/3} X^{2/3}}{U_h}$$

and taking the final rise at 10 source heights downwind, a plume rise of 0.61 cm is predicted. This is less than half of the value predicted using maximum observed ground level concentrations. Because of the uncertainties involved in applying full-scale plume rise predictions to model scale systems, the effective source height deduced from ground level concentration measurements was considered to be a more reliable estimate.

The assumption in Eq. (C3) above that the plume spreading ratio σ_z/σ_y remains constant, was relaxed by assuming different power law functions for σ_z and σ_y . The full-scale spreading rates for 3 minute sampling times recommended by Alberta Dispersion Guidelines were used in Eq. (C13) from Appendix C to predict the effective source height. This more complicated approach gave values within a few percent of the effective source heights predicted by the much simpler equation (C3).

Ground Level Concentration Without Dikes

Ground level profiles were measured by positioning a movable sampling

probe at ground level downwind from each of the source locations. The photograph in Fig. 2-6 shows the source at location A and the ground level sampling probe in position downwind.

Figures 4-3 and 4-4 show the ground level measurements along a line directly downwind from the source. All of the ground level profiles gave fluctuating values of the mean concentration at various positions close to the ground level maximum. The data in Fig. 4-7, taken with a model dike in place, shows that these fluctuations with downwind distance are reproducible, and cannot be attributed to experimental error. The probable source of these variations is a crosswind displacement of the plume axis, which exposes the sampling probe to lower off-axis concentration levels. The dips in ground level concentrations appeared to occur most often when the plume passed near a large building. To account for this plume meandering, the maximum ground level concentration listed in Table 4-2 was determined from a smoothed profile drawn as an envelope around the maximum observed concentrations, with the lower dips and valleys in the profile assumed to represent values off the axis of maximum concentration.

Although the two source locations A and B produced the same qualitative trends for their results, the maximum concentrations for locations B were about 20 percent higher than those for location A. Because the effective source height can only partly be accounted for by buoyancy rise, it is plausible to suppose that the plume from source A may have been deflected upward by about 0.5 cm more than the plume from source B. This slight additional plume rise for source A would account for the difference in both magnitude and downwind location of the ground level concentrations observed for the two sources. Another plausible explanation is that the

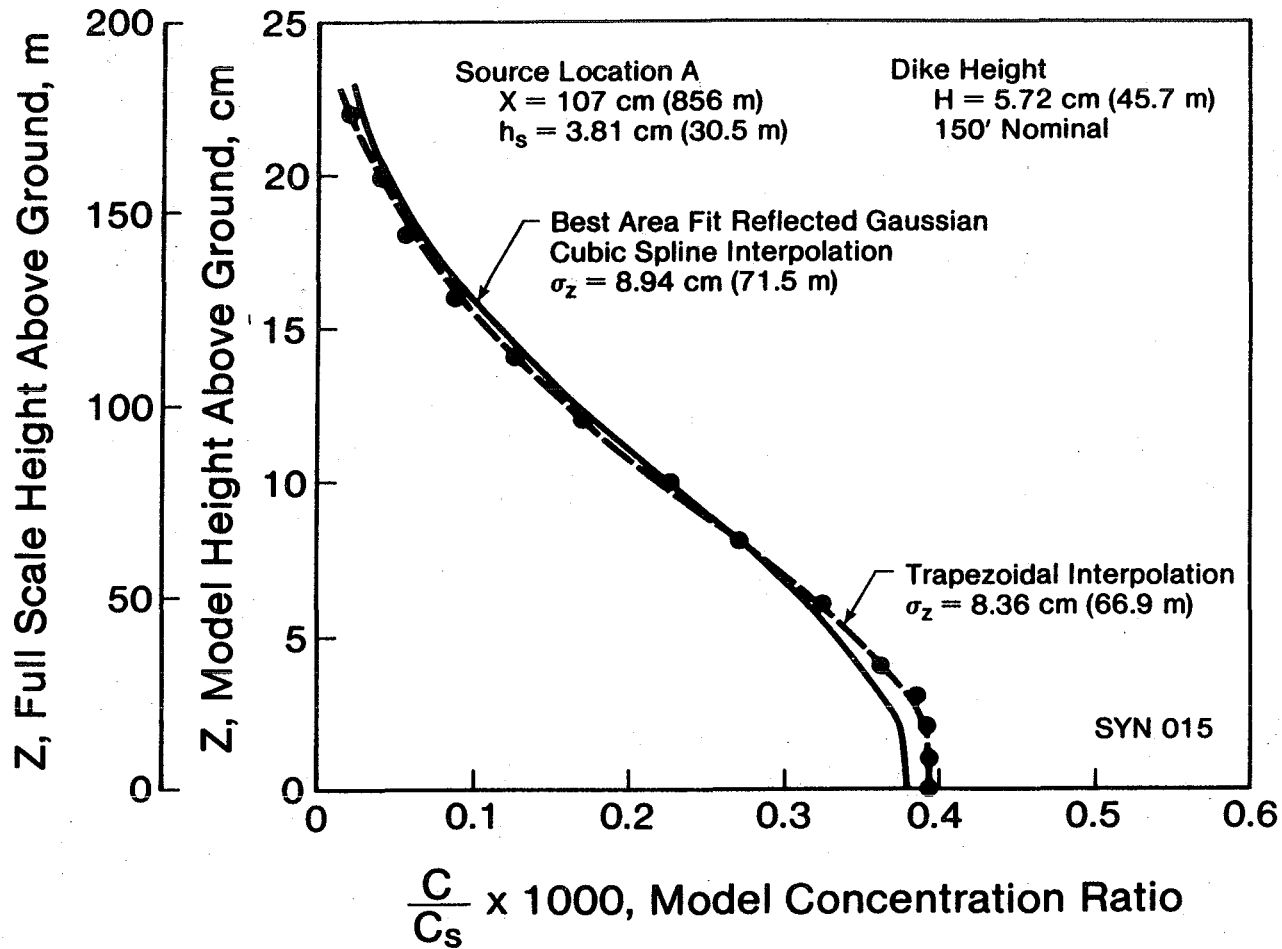


Figure 4-1. Vertical Concentration Profile at 28 Source Heights Downwind with 45.7 m Dike Height

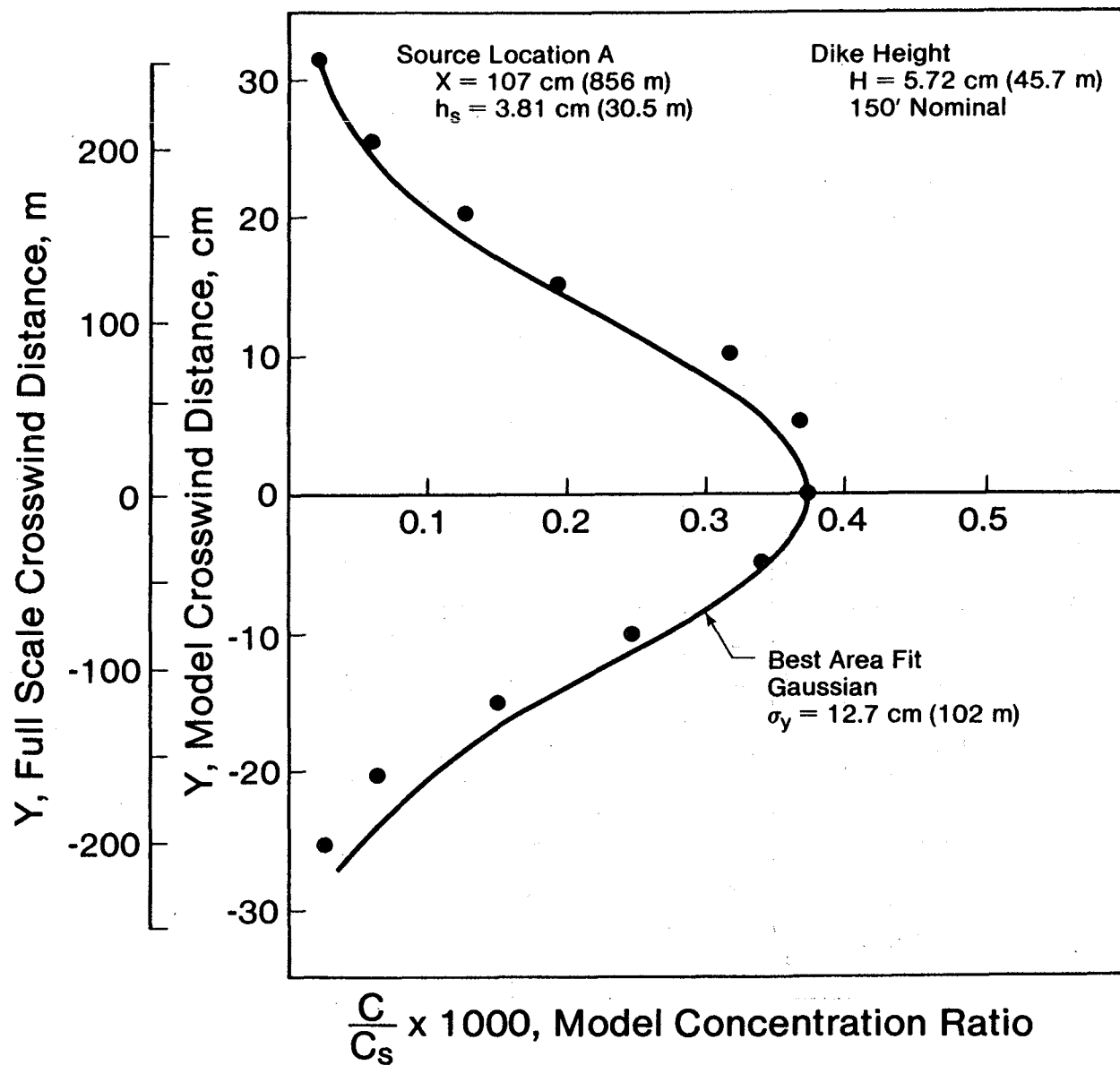


Figure 4-2. Crosswind Concentration Profile at 28 Source Heights Downwind with 45.7 m Dike Height

TABLE 4-2
VERTICAL AND CROSSWIND PLUME SPREAD

Source Location A

$X = 107 \text{ cm}$ (2808 ft, 856 m)

$h_s = 3.81 \text{ cm}$ (100 ft, 30.5 m)

Dike Height H	σ_z^{**} cm	σ_y cm	$\frac{\sigma_z}{\sigma_y}$	Experimental $\frac{C_{0\max} U_h}{Q}$ cm^{-2}	Effective source height h Eq C3 cm
No Dike	7.84	11.65	0.673	.0052*	5.51*
75' (2.86 cm)	7.98	12.05	0.662	.00515	5.49
150' (5.72 cm)	8.34	12.70	0.657	.0050	5.55

*Data from Location B has maximum concentration levels about 20% higher and, if σ_z/σ_y is the same, values of $h \approx 5.0 \text{ cm}$, 10% lower than those shown for Location A

**computed using effective source height $h = h_s = 3.81 \text{ cm}$

TABLE 4-3
 COMPARISON OF MODEL AND FULL SCALE PLUME
 SPREADS FOR LOW LEVEL SOURCES WITH NO DIKE

Source Location A

X = 107 cm (2808 ft, 856 m)

Parameter	σ_z m	σ_y m	$\frac{\sigma_z}{\sigma_y}$
Wind Tunnel scaled up 800:1	62.7	93.2	0.673
Singer and Smith(1966) Brookhaven 1 hour averages	42.6	62.0	0.688
Alberta Dispersion Guidelines (1978) 3 min averages	45.0	74.2	0.606
Alberta Dispersion Guidelines (1978) 1 hour averages	45.0	135.0	0.333

Full Scale Values in Meters

Singer and Smith (1966)
for 1 hour averages

$$\sigma_z = 0.22 x^{0.78}, \quad \sigma_y = 1.45 \sigma_z$$

Alberta Dispersion Guidelines (1978)
for 3 min averages

$$\sigma_z = 0.456 x^{0.68}, \quad \sigma_y = 0.195 x^{0.88}$$

for 1 hour averages

$$\sigma_z, \text{ unchanged, } \sigma_y = 0.355 x^{0.88}$$

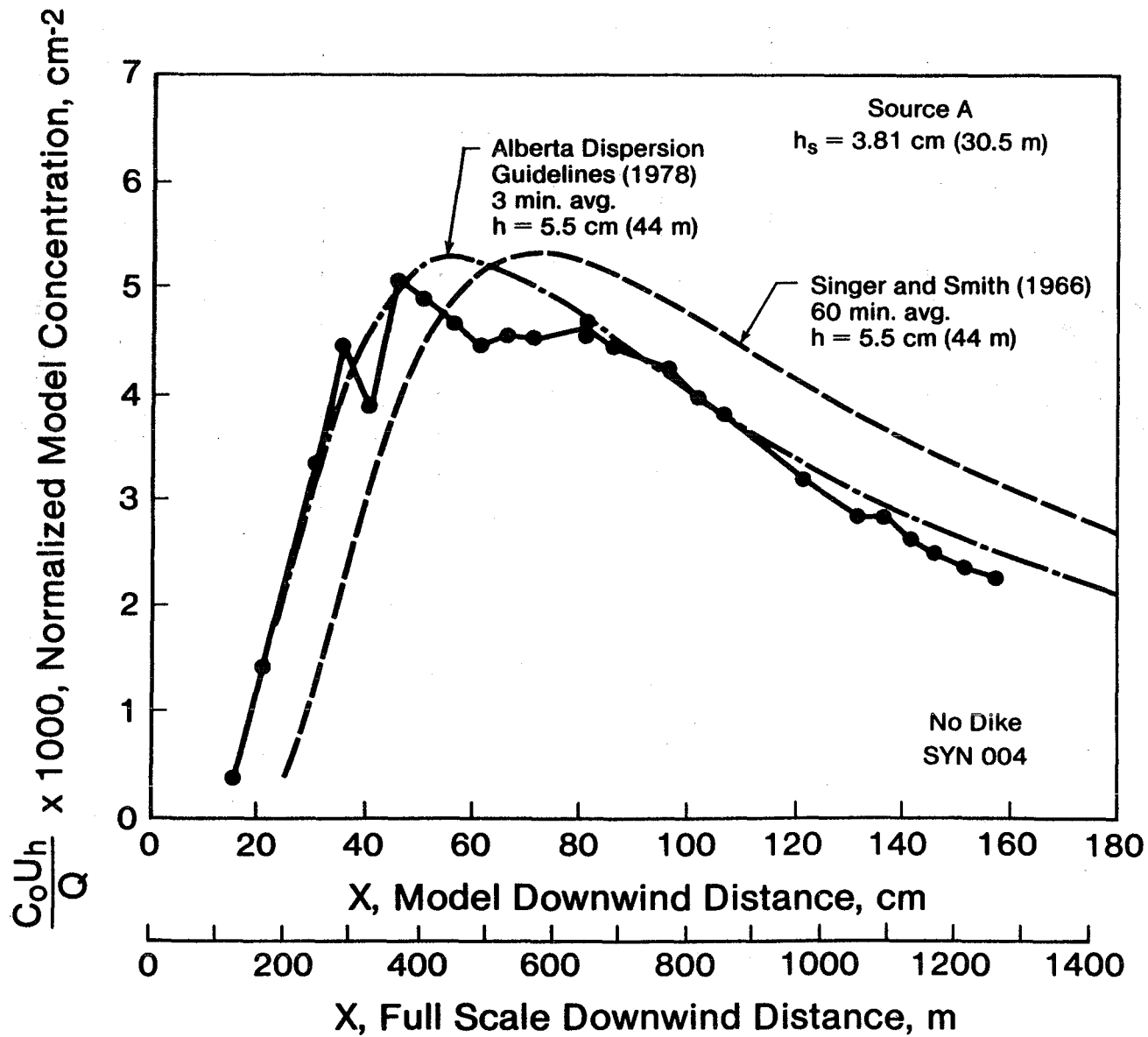


Figure 4-3. Comparison of Gaussian Plume Model to Measured Plant Site Ground Level Concentrations

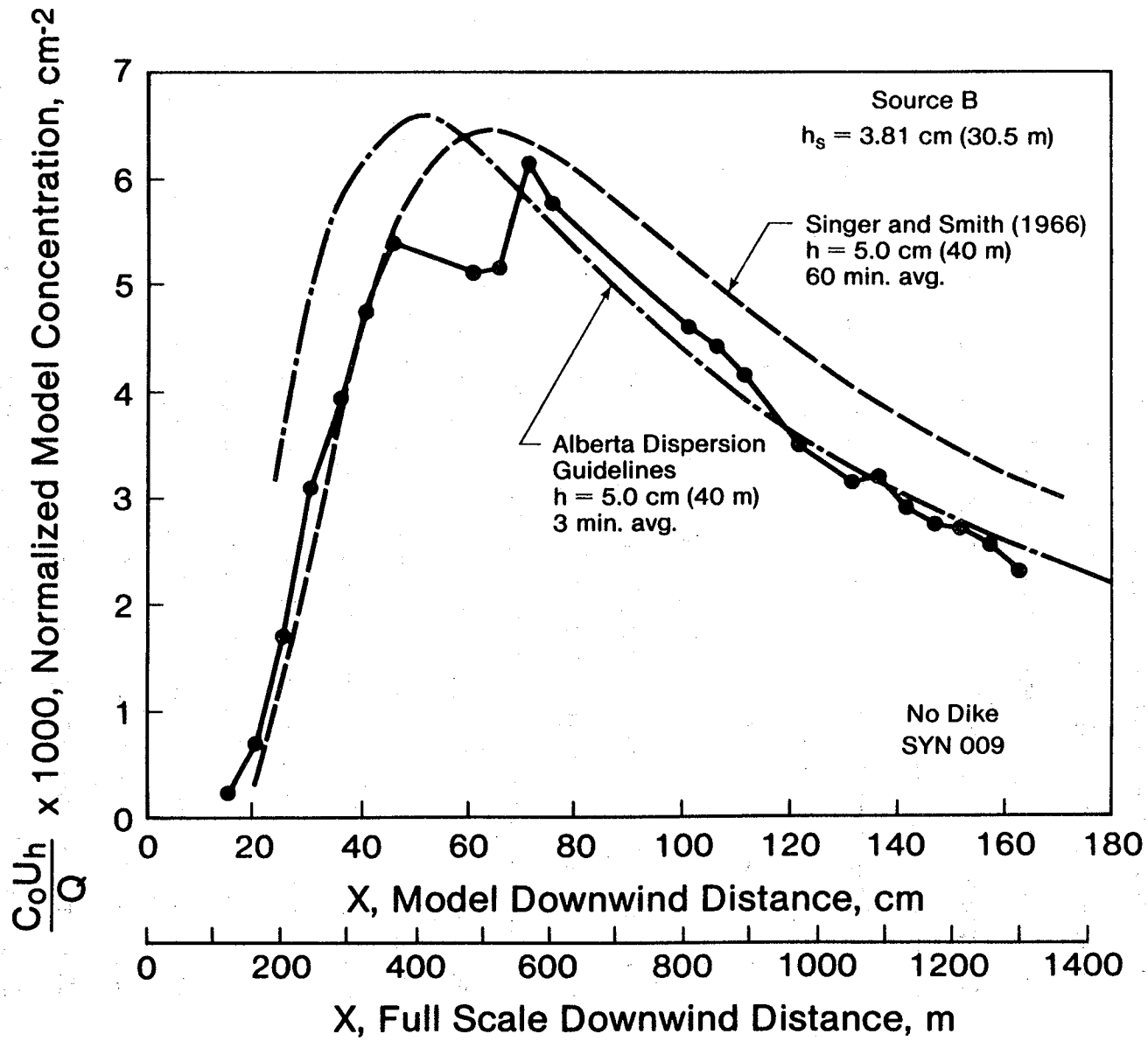


Figure 4-4. Comparison of Gaussian Plume Model to Measured Plant Site Ground Level Concentrations

plume from source A had a larger crosswind spread σ_y than the plume from source B. No direct measurements were made of crosswind spread to support this hypothesis, however it was observed that several large structures, including the main power plant building, lie close to the position of maximum ground level concentration for source location A. These buildings may have locally increased the crosswind plume spreading and/or caused the plume axis to deviate so that the sensor was not placed on the line of maximum concentration.

Theoretical predictions were made for ground level concentration profiles using a Gaussian plume model, with full-scale plume spreading rates from correlations given by Singer and Smith (1966), and Alberta Dispersion Guidelines (1978). For a Gaussian plume the ground level concentration is represented by Eq. (C10) and the spreading rates are given by power law functions shown in Table 4-3.

The predictions in Figs. 4-3 and 4-4 show remarkably good agreement with the experimental measurements, even considering that the effective source heights were adjusted to give the correct value for maximum ground level concentration. The most puzzling aspect in these predictions, is that the concentration profiles claim such widely different averaging times. The Alberta Dispersion Guidelines profile is supposed to represent 3 minute averages, while the curves generated using Singer and Smith's spreading rates are claimed to be for 1 hour averages. Clearly, both of these averaging times cannot be correct. The Alberta Dispersion Guidelines (1978) suggest that only the crosswind spread depends on averaging time according to a relationship $\sigma_y \propto t^{-0.2}$. If the 3 minute crosswind spreads are corrected to 60 minute values using this proportionality, the ground level concentrations decrease by about a factor of 2.

The measured ratio of plume spreading rates σ_z/σ_y shown in Table 4-3 does not help to resolve this dilemma, because its value of 0.67 agrees reasonably well with both the claimed 3 minute and 60 minute averaging times.

Effect of Dikes on Ground Level Concentration

Ground level profiles for both source locations are shown in Fig. 4-5 to 4-10 for dike heights of $H = 75'$, $150'$, and $300'$. For all dike heights the ground level concentrations exhibited the same fluctuations with downwind distance that were observed with no dike present. Fig. 4-7 for the $150'$ dike height shows that these fluctuations are reproducible from day to day, and are almost certainly due to crosswind deflection of the plume axis by nearby structures on the plant site model.

Both source locations showed consistent trends, with increasing dike height causing a slight decrease in maximum ground level concentration. Concentrations closer to the source than the ground level maximum tended to increase slightly, while concentrations downwind from the ground level maximum position showed a significant decrease with increasing dike height. These two observations indicate that the position of maximum concentration moves somewhat closer to the source as dike height increases. This movement toward the source of the maximum concentration point with increasing dike height must be inferred, because fluctuations with downwind distance make it difficult to accurately locate this maximum concentration position. The movement of the ground level maximum closer to the source is consistent with a high rate of vertical plume spread σ_z that will occur when the dike increases the turbulence in its wake, see Table 4-2.

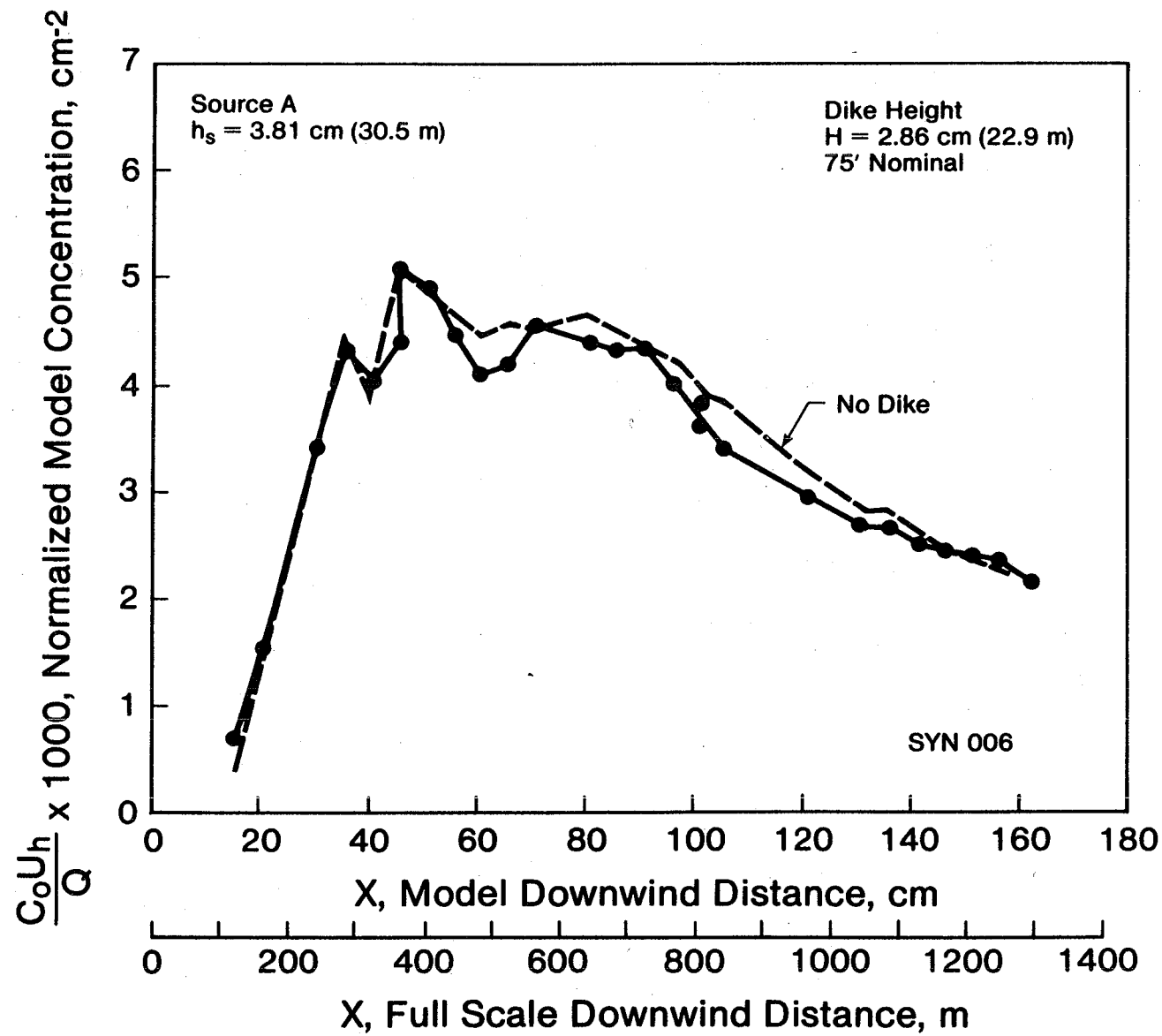


Figure 4-5. Effect on Ground Level Concentration of Tailings Pond Dike Located 850 m Upwind of Low Level Source on Plant Site

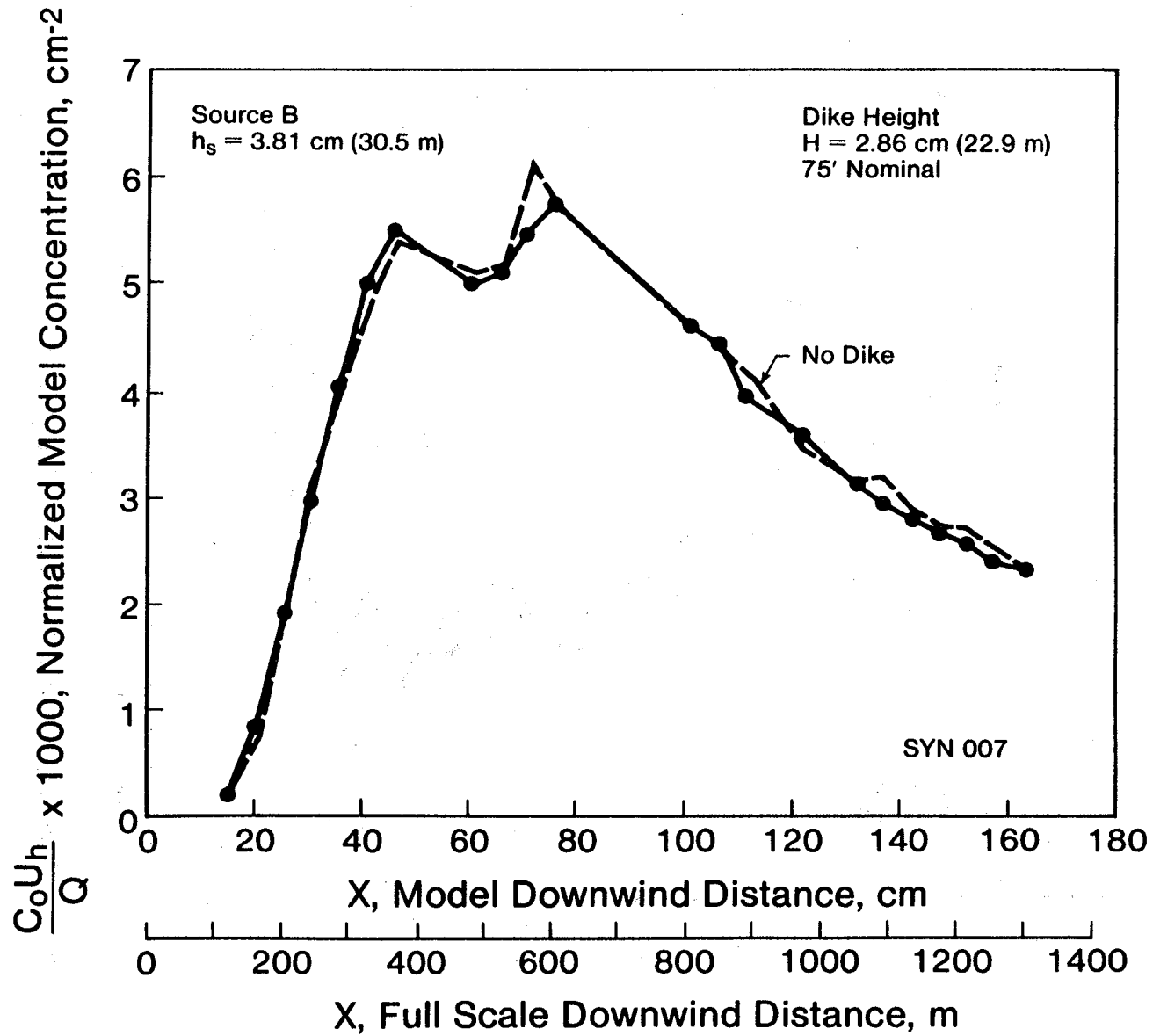


Figure 4-6. Effect on Ground Level Concentration of Tailings Pond Dike Located 850 m Upwind of Low Level Source on Plant Site

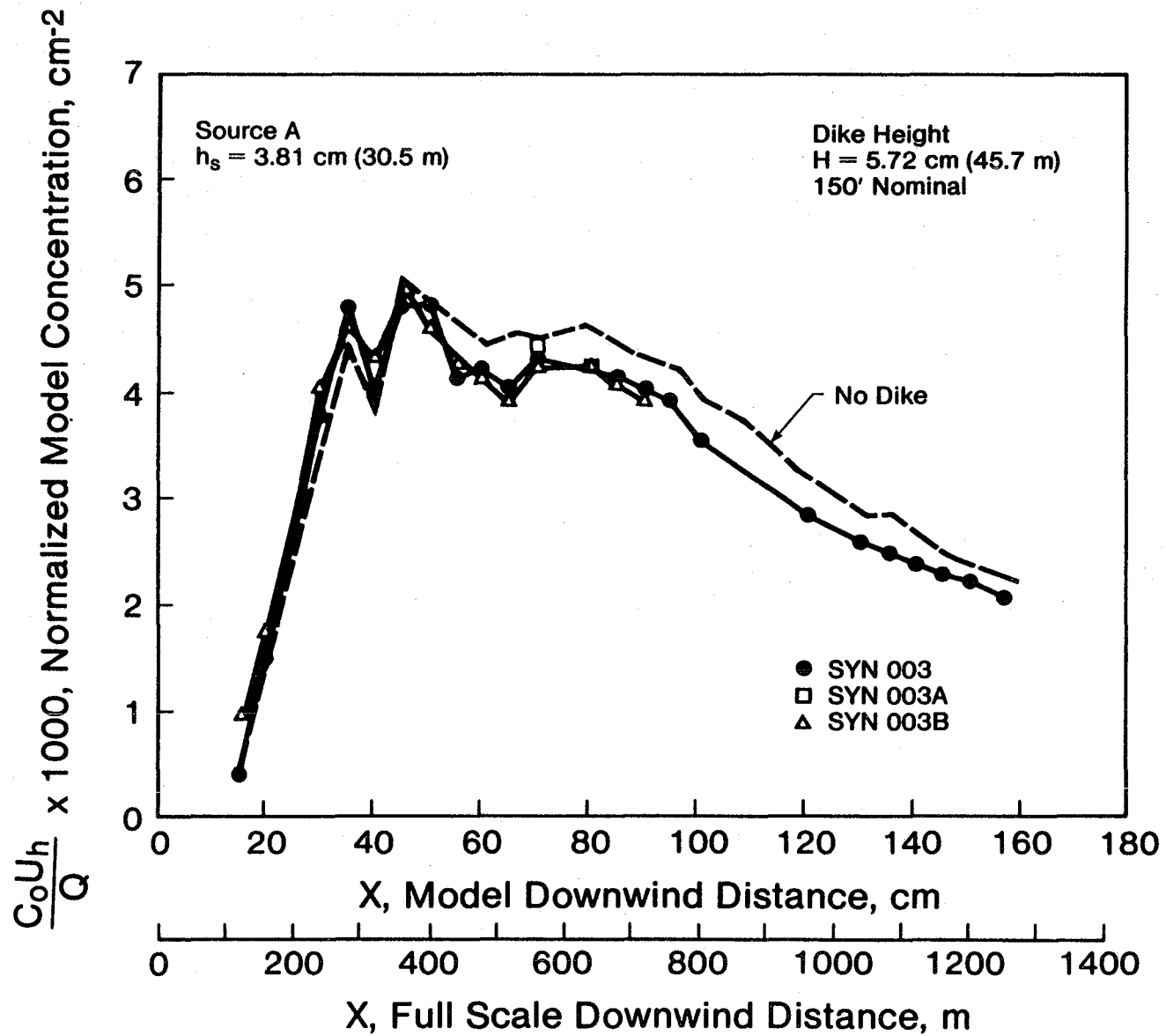


Figure 4-7. Effect on Ground Level Concentration of Tailings Pond Dike Located 850 m Upwind of Low Level Source on Plant Site

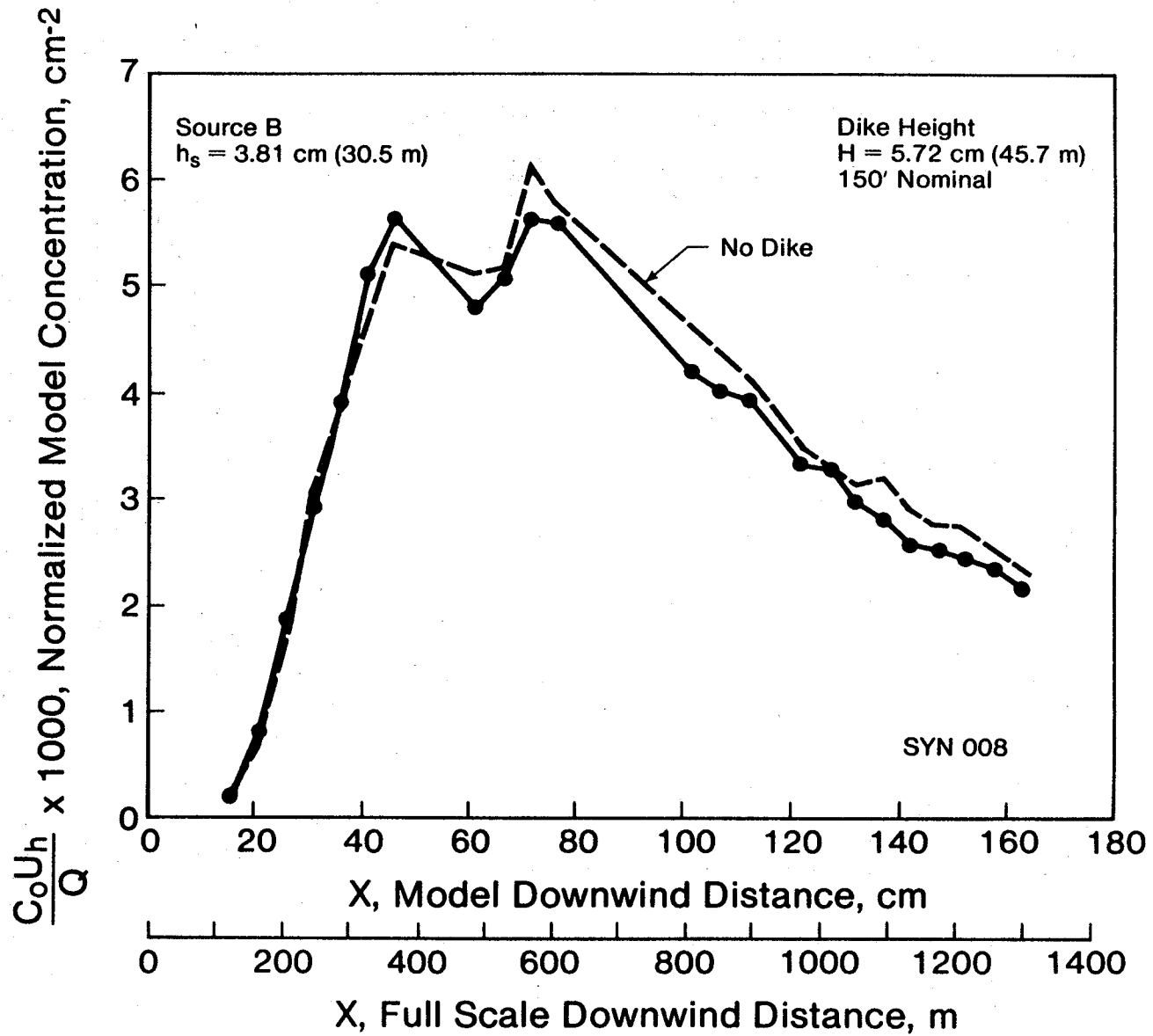


Figure 4-8. Effect on Ground Level Concentration of Tailings Pond Dike Located 850 m Upwind of Low Level Source on Plant Site

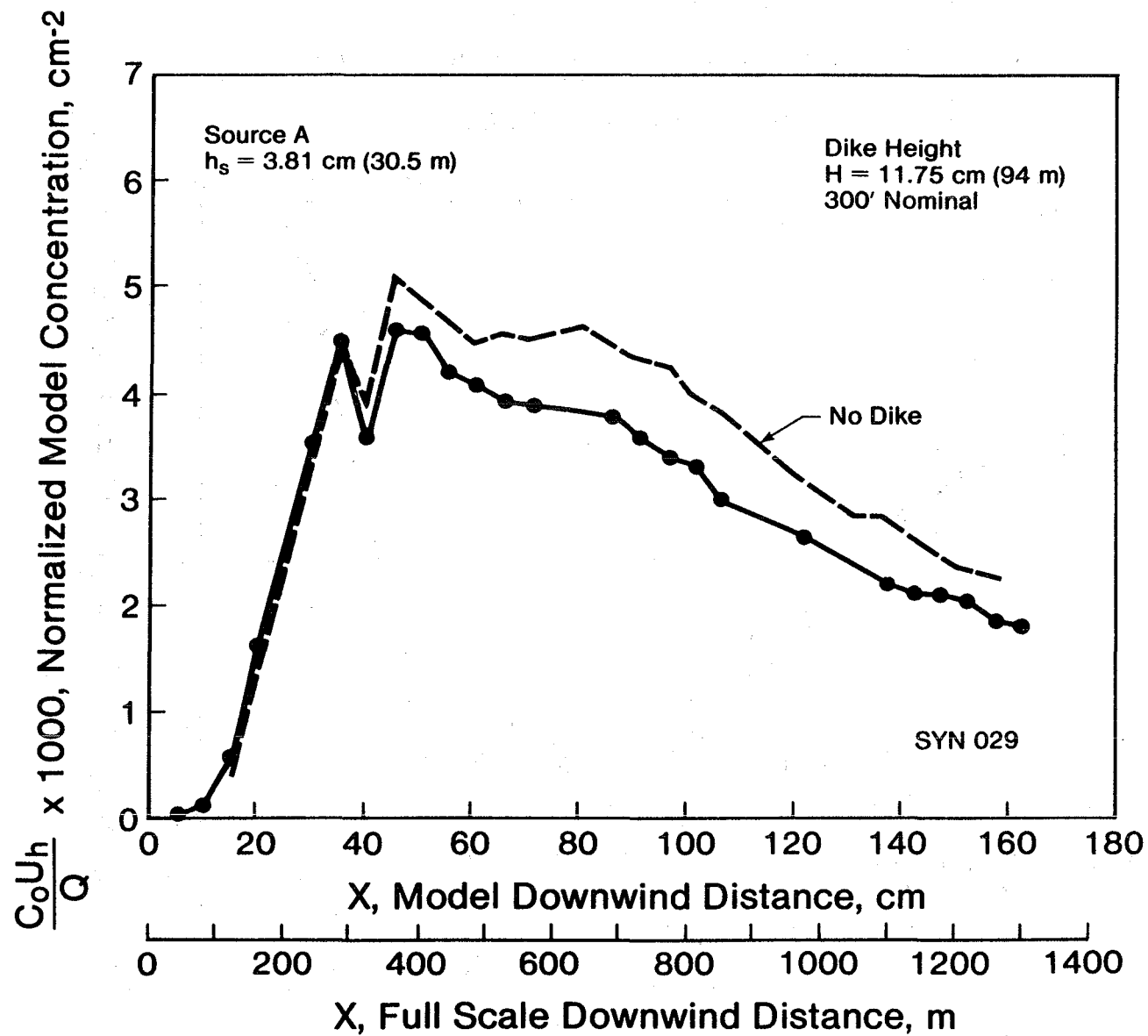


Figure 4-9. Effect on Ground Level Concentration of Tailings Pond Dike Located 850 m Upwind of Low Level Source on Plant Site

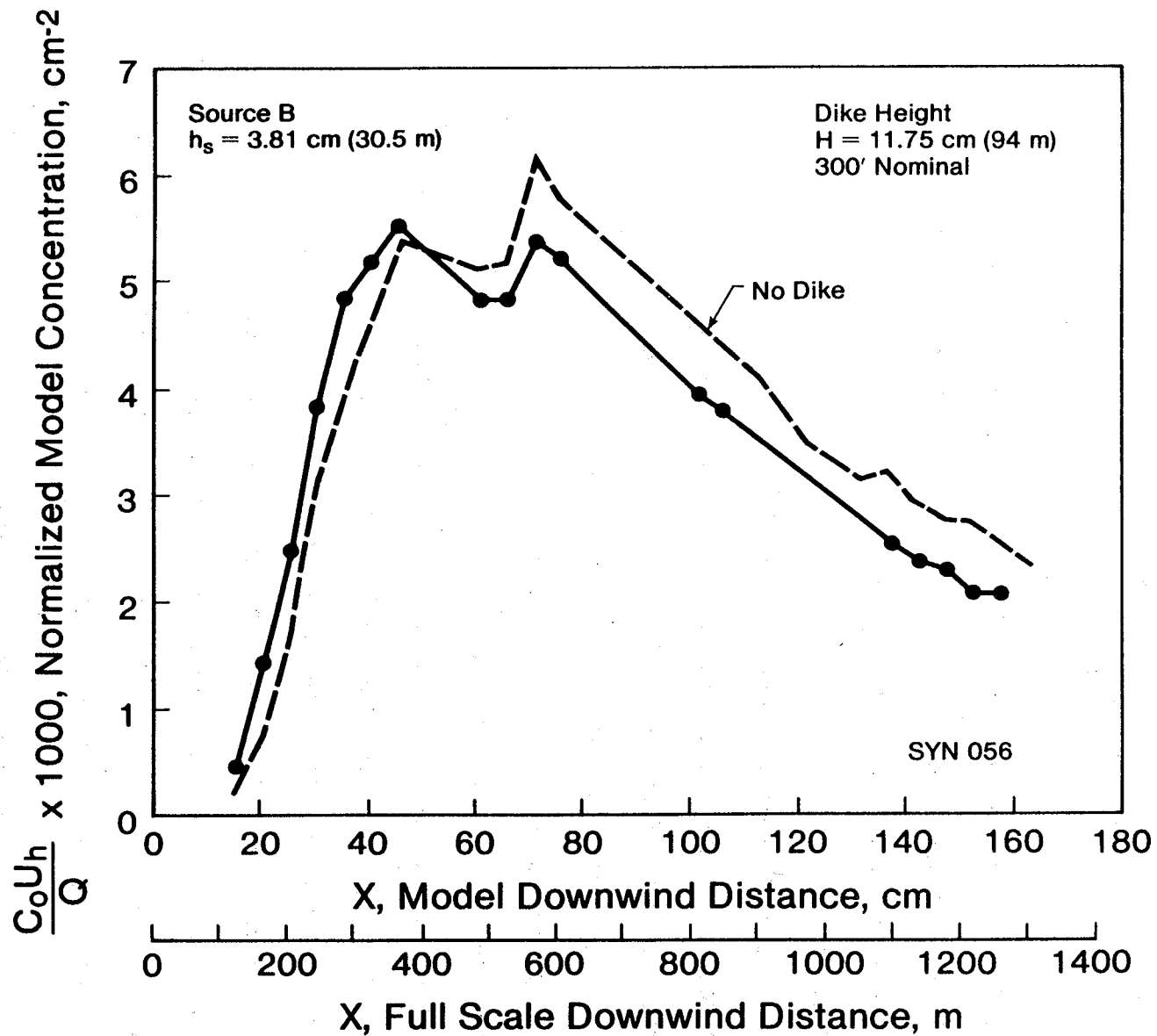


Figure 4-10. Effect on Ground Level Concentration of Tailings Pond Dike Located 850 m Upwind of Low Level Source on Plant Site

The Gaussian plume model described in Appendix C provides a rational explanation for all of the observed effects of the dike wake on ground level concentrations. Writing equation (C3) in the form

$$\frac{C_{o \max} U h^2}{Q} = \frac{2}{\pi e} \left(\frac{\sigma_z}{\sigma_y} \right)$$

The decrease in maximum ground level concentration observed in the dike wake implies that the turbulence generated by the dike produces a larger increase in crosswind spread σ_y than it does to increase the vertical spread σ_z .

The most remarkable observation of the effect of the dike on the source is not that it causes a change in concentration, but how little effect it has. Even for the 300' dike height, Figs. 4-9 and 4-10 show that the sources located about 10 dike heights downwind experience only a 10 percent change in their maximum ground level concentration due to the dike wake turbulence. Even more surprising is the observation that this change represents a decrease and not an increase in concentration.

The reason for the small effect of the dikes on downwind sources is that the flow over the model dike does not separate and produce a high turbulence recirculation zone on its downwind side. This lack of flow separation and recirculation observed in the model, and described in Chapter 3, should also occur for the full-scale tailings pond dike which will experience much high Reynolds numbers due to its larger size.

Conclusions and Recommendations

The following conclusions can be drawn from the wind tunnel experiments using low level sources in the wake of the tailings pond dike:

1. The effect of increasing the tailings pond dike height, if any, will be to lower the ground level concentration from low level sources. This is consistent with an increased crosswind spread caused by turbulence in the dike wake.
2. Simple Gaussian models, such as that recommended in the Alberta Dispersion Guidelines, are capable of providing an accurate prediction of ground level concentration when care is taken to properly estimate the effective source height. For low-level sources it is particularly important to determine the plume rise, because this can represent a significant fraction of the total effective source height.
3. Full-scale correlations of plume spread are not consistent in their specification of averaging time. The Alberta Dispersion Guidelines (1978) and the Brookhaven correlations of Singer and Smith (1966) both predict the same value of maximum ground level concentration. However, the Alberta Dispersion Guidelines claim that this concentration represents a 3 minute average, while the Brookhaven spreading rates claim that the average is for 60 minutes. Further investigations of full-scale plume spreading rates are required to resolve this discrepancy.

CHAPTER 5

PLUME RISE AND DISPERSION WITH FLAT TERRAIN

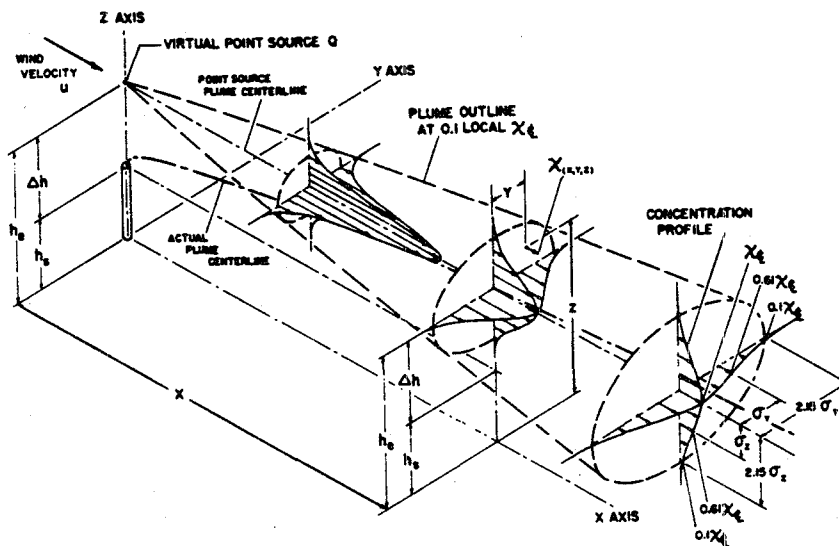
The plume rise Δh and plume spread σ_y and σ_z are important not only for developing a model for ground level concentration of the main stack plume, but also they are important to determine if the wind tunnel is correctly modelling the full scale situation. The plume rise Δh is a sensitive indicator of stack gas conditions and mean speed. Measured values of plume spread with downwind distance are indicators of the background turbulence scale and intensity. In addition, it is only through a comparison of the plume spread σ_y and σ_z with full scale values that we can obtain an estimate of the appropriate full scale averaging time corresponding to the model measurements.

We will show in this chapter that not only does the tunnel accurately model plume rise and dispersion, but it is also able to simulate such effects as stack wake downwash, combined rise due to momentum and buoyancy, and wind shear effects on plume rise. Finally, the wind tunnel model is able to demonstrate that plumes in neutral stability do have a final rise height caused by plume break-up by atmospheric turbulence.

Most of the data presented in this chapter were measured using a turbulent stack gas condition, with the mixing plug inserted in the stack. For this configuration the operating conditions are summarized in Table 2-4, which shows that two different approach wind speeds were for these tests. The low speed tests were carried out at a tunnel speed of 0.45 m/s (13.4 m/s full scale), while the high speed tests in which stack downwash was the dominant factor were carried out at exactly twice this speed.

Vertical and Crosswind Concentration Profiles

Vertical and crosswind concentration profiles were necessary to determine plume rise Δh , vertical spread σ_z and crosswind spread σ_y . Each of these measured profiles also presented the opportunity of examining the validity of the Gaussian plume model in turbulent shear flow. The Gaussian plume model with a single parameter to describe the plume spread in any given direction is the simplest of all models for atmospheric dispersion. The governing equations for this Gaussian model are described in detail in Appendix C, and summarized schematically in the diagram below.



In the presence of non-homogeneous atmospheric shear flow, mean wind speed variations with height, and self-induced turbulence from buoyant mixing, the validity of the Gaussian plume model is often questioned. The crosswind and vertical profiles shown in Figure 5-1 close to the stack show an excellent agreement with a Gaussian shape. At this point close to the stack, a significant fraction of the measured plume spread is due to self-induced mixing by momentum and buoyancy effects.

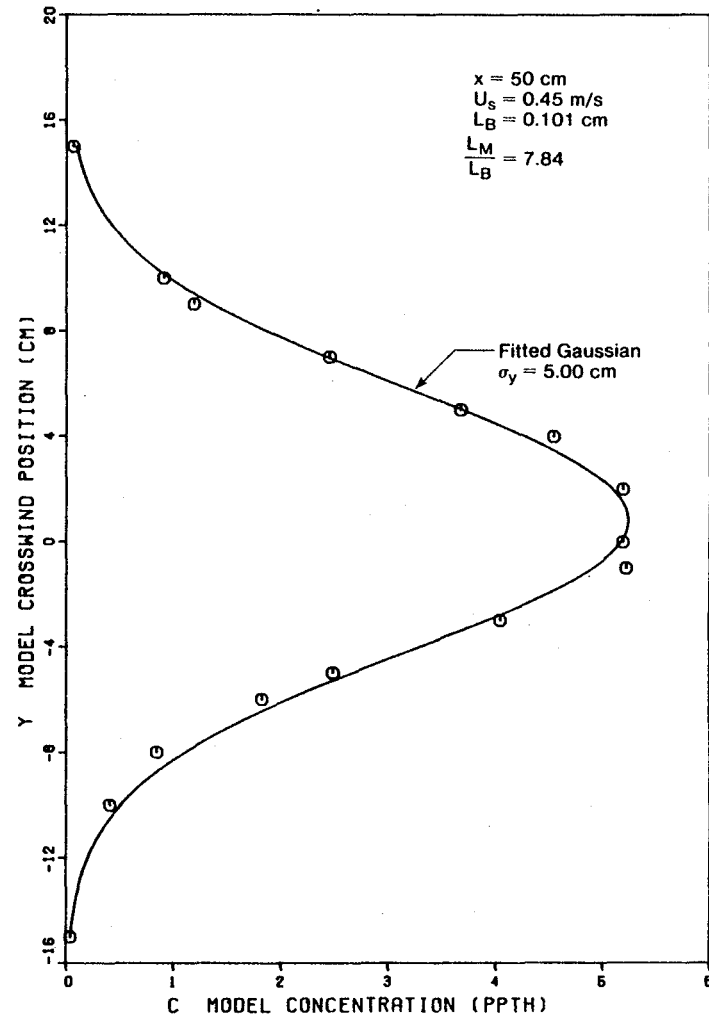
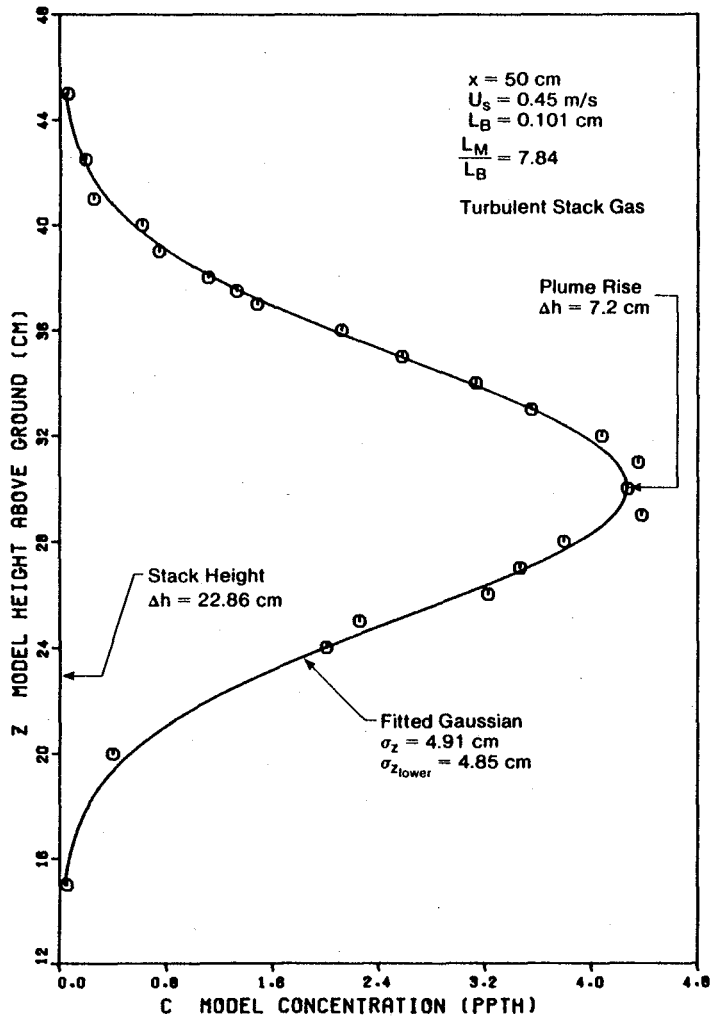


Figure 5-1. Comparison of Measured Vertical and Crosswind Concentration Profiles with a Gaussian Model

Further downwind, where ground level reflection causes the concentration profiles to lose their symmetry, Figure 5-2 shows that a ground-reflected Gaussian is still an excellent approximation to the measured concentration profiles. For all measured profiles, the plume spread σ_y or σ_z was adjusted to obtain a best-fit to the observed data. The profiles shown in Figures 5-1 and 5-2 are generated from these best-fit values.

Averaging Time and Plume Drift

Figure 5-2 shows graphically the necessity of using sufficiently long time averages to define the concentration. Four consecutive 100 second time averages are shown along with the 400 second mean values in Figure 5-3 from these consecutive samples. Note that even with 400 second model scale averages, the plume rise Δh is very difficult to establish with a precision greater than about $\pm 10\%$.

Buoyancy modelling scales developed in Appendix B and discussed in Chapter 2 indicate that the 100 second model time averages correspond to about 45 minute full scale values. Thus, the 400 second averages should correspond in full scale to about 3 hour averages. However, the reader should not place too much reliance on this time scaling from buoyancy modelling. Because the wind tunnel does not accurately simulate the plume meandering that influences full scale averages over times longer than about 1 hour, a direct scale factor cannot be directly established for the wind tunnel model. In the wind tunnel the spreading of the plume eventually approaches an asymptotic value as averaging time increases, while the full scale plume indicates increasing spread with longer averaging times. We will pursue this point later when full scale values are compared to the measured model plume spreads.

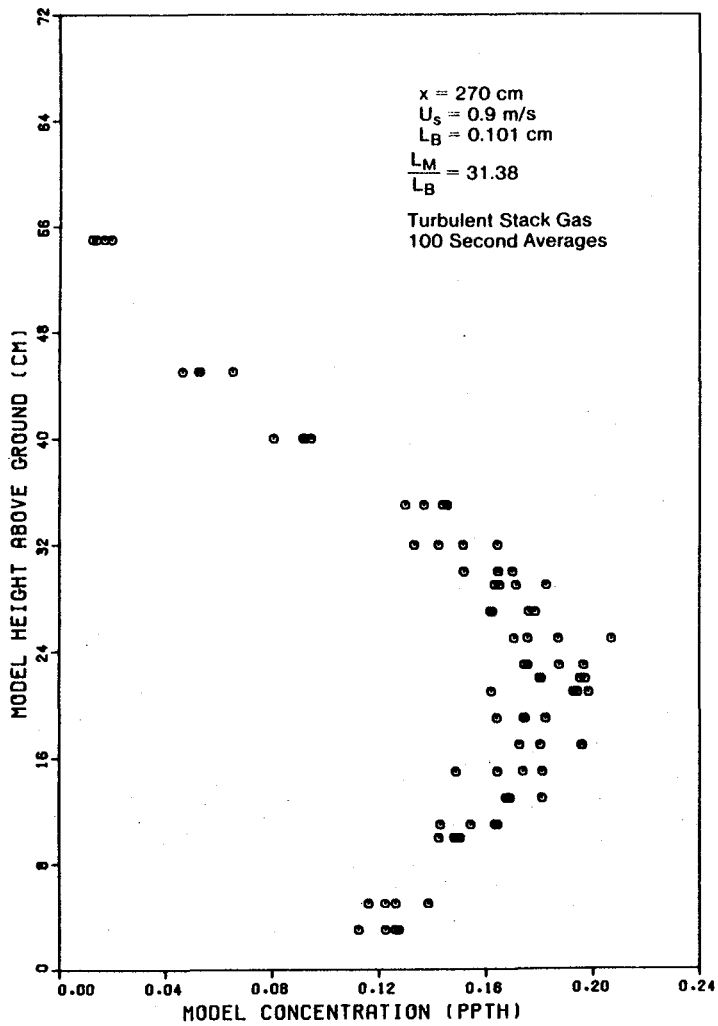


Fig 5-2 Vertical Concentration Profiles for 100 sec Time Averages

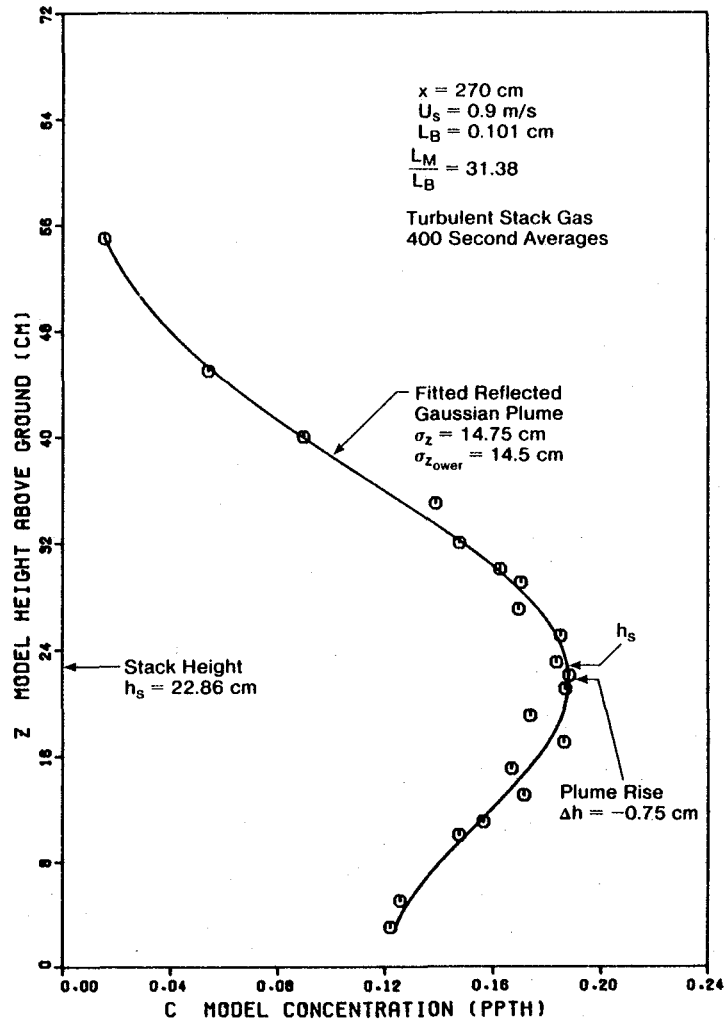


Fig 5-3 Vertical Concentration Profiles for 400 sec Time Averages

In the crosswind concentration profiles it was observed that the plume drifted slightly to the right or left as it moves downwind. This drift is probably due to local variations in the flow, and it was always less than 1° from the nominal wind direction. However, the drift did appear to be systematic, and at the end of the test section $X = 290$ cm (2320 m full scale) the plume was always to the right of the tunnel centerline (looking downwind). At this point the drift was less than 5 cm in the negative y direction.

Combined Momentum and Buoyancy Rise

The rise of a plume due to momentum and buoyancy effects from a source of finite radius R_s has been developed by many investigators for both stable and neutrally stable atmospheric conditions, see for example Briggs (1975) p. 78. For neutrally stable conditions, such as those in the wind tunnel, the plume rise is given by

$$\frac{\Delta h}{L_B} = \left(\frac{3}{\beta_1^2} \left[\frac{L_M}{L_B} \right]^2 \frac{X}{L_B} + \frac{3}{2\beta_2^2} \left[\frac{X}{L_B} \right]^2 + \left[\frac{R_s}{\beta_1 L_B} \right]^3 \right)^{1/3} - \frac{R_s}{\beta_1} \quad (5-1)$$

R_s is the stack radius and β_1 is the momentum entrainment constant; β_2 is the buoyancy entrainment constant, and L_B is the buoyancy length defined by

$$L_B = \frac{F}{U_s^3}$$

which is defined in terms of the buoyancy flux

$$F = g \left(1 - \frac{\rho_s}{\rho_a} \right) W_s R_s^2 \quad (5-3)$$

The momentum length L_M is

$$L_M = \frac{F_M^{0.5}}{U_s} \quad (5-4)$$

defined in terms of the momentum flux

$$F_M = \alpha \frac{\rho_s}{\rho_a} W_s^2 R_s^2 \quad (5-5)$$

from which we see the ratio

$$\frac{L_M}{L_B} = \frac{\sqrt{\alpha}}{g R_s} \left[\frac{\left(\frac{\rho_s}{\rho_a} \right)^{0.5}}{1 - \frac{\rho_s}{\rho_a}} \right] U_s^2 \quad (5-6)$$

For most practical problems, including the Syncrude stack, the terms involving the source radius $R_s = d/2$ in Equation 5-1 are negligible. The entrainment constants β_1 and β_2 are of primary importance and must be fixed by comparing measured plume trajectories to the predictions of Equation 5-1. Briggs (1970, 1975) after an extensive review of literature on momentum rise suggests on purely empirical grounds that the entrainment constant should be

$$\beta_1, \text{ Briggs} = 0.33 + \frac{U_s}{W_s}$$

However, this is not consistent with the measurements of Ricou and Spalding who found that the entrainment constant is proportional to $(\rho_s/\rho_a)^{0.5}$. In addition, all of the present measurements show that it is the momentum parameter

$$\phi_M = \alpha \left(\frac{\rho_s}{\rho_a} \right) \frac{W_s^2}{U_s^2} \quad (5-7)$$

and not the velocity ratio that is important. Keeping the general form of Briggs' expression the present study suggested the form

$$\beta_1 = 0.33 \left(\frac{\rho_s}{\rho_a} \right)^{0.5} + \left(\frac{1}{\phi_M} \right)^{0.5} \quad (5-8)$$

Because it represents an average from several investigators, Briggs' constant of 0.33 has been retained in preference to Ricou and Spalding's value of 0.25.

The entrainment constant β_2 for buoyant mixing is generally set at a constant value, more from our state of ignorance of the mixing processes than for any good reason. Briggs (1975) suggests the value of $\beta_2 = 0.6$ based on correlation of full-scale plume rise measurements. In the present study, data which will be presented later will suggest a value of $\beta_2 = 0.87$ in a uniform wind.

Equation 5-1 is only strictly valid when the wind speed is constant with height above the stack. When the wind speed varies with distance above the stack top, some simple corrections can be applied to Equation 5-1 to compensate for the effect of wind speed variations. One method is to adjust the effective wind speed U_s at each downwind position to compensate for the higher wind speeds encountered by the plume as it rises through the shear flow. Another simple but purely empirical correction is to adjust the buoyancy entrainment constant β_2 to account for wind shear. When this is done for the measurements in the present study we will find that β_2 will increase from $\beta_2 = 0.87$ to values as high as $\beta_2 = 1.4$.

The character of Equation 5-1 for combined rise is illustrated in Figure 5-4. The values of the entrainment constants and the ratio of momentum to buoyancy length are those that we will later find appropriate

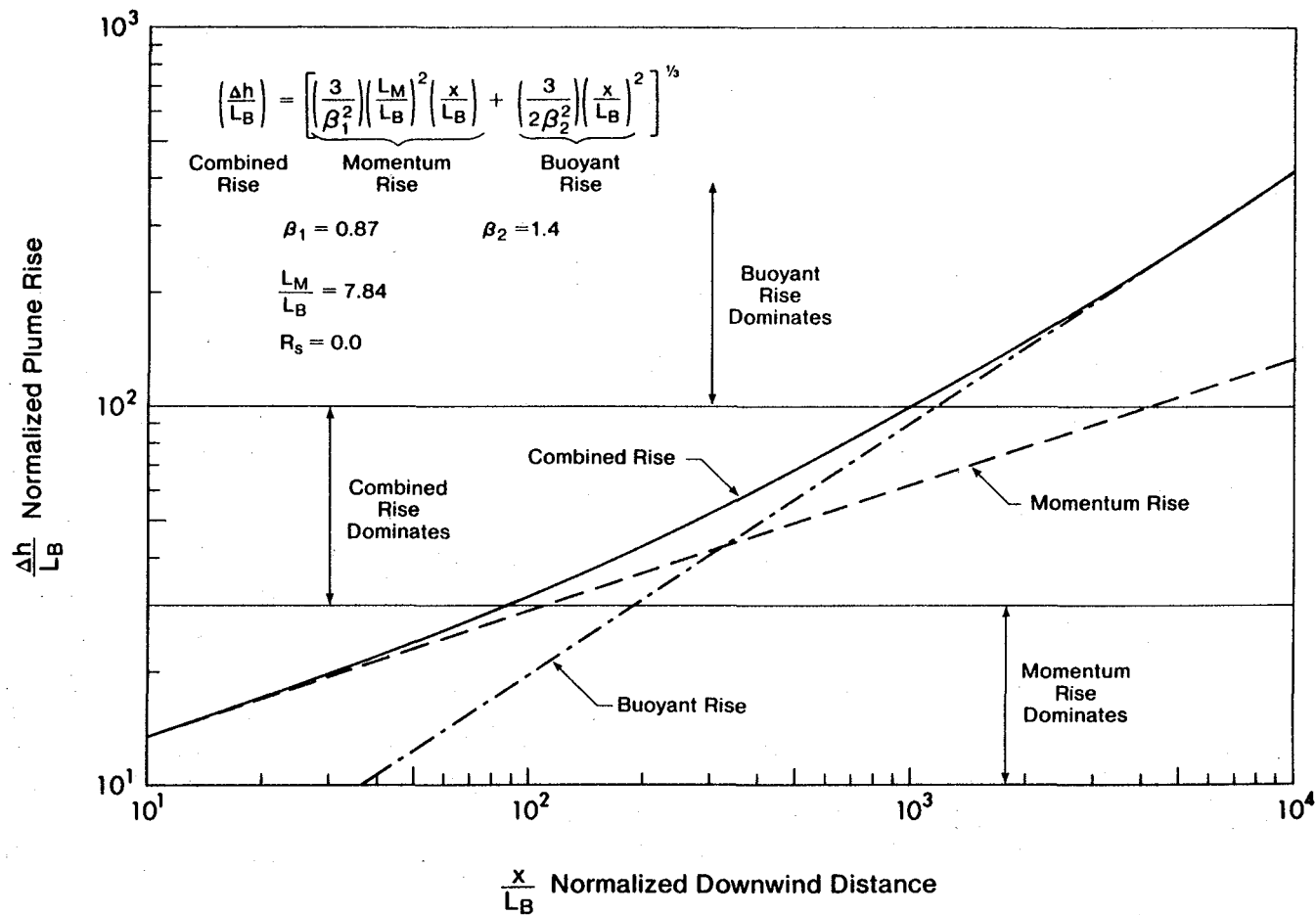


Fig 5-4 Contribution of Momentum and Buoyancy to Plume Rise for the Syncrude Plume at 120% of Full Load with 13.4 m/s Wind at Stack Height

for the Syncrude plume at 120 percent of nominal rated load and a wind velocity at stack height of $U_s = 0.45$ m/s (13.4 m/s full scale). It is apparent that the momentum rise only contributes significantly close to the stack. Terms involving the initial source size are small, and have been neglected, except where specifically noted.

Data taken for several momentum to buoyancy length ratios are shown in Figure 5-5 for one specific set of entrainment constants. All of the measurements were made in turbulent shear flow with $\sqrt{\phi_M} > 1.6$, to avoid stack wake downwash effects. In this case the momentum entrainment constant β_1 is computed from Equation 5-8. Data for the measured Syncrude plume at $U_s = 0.45$ m/s (13.4 m/s full scale) had a momentum length ratio of 7.84 and is included with the open circles. Several general observations may be made:

1. The value of $\beta_2 = 1.2$ in Figure 5-5 gives the best overall fit to the data. It is exactly twice as large as the value suggested by Briggs (1969, 1975) as an average of full scale measurements. We will show later that this high value is mostly due to the presence of shear flow which causes the plume to bend over and decreases its rise. However, even for a uniform approach flow the value of β_2 is about 0.9 in the wind tunnel.
2. The measurements show that there is definitely a final rise for plumes in neutral stability. Even for high momentum plumes this final rise appears to be governed only by the buoyancy length, and occurs at about $X_f = 2200 L_B$. Because of the uncertainty in fixing this point, the choice for final rise position was based mostly on convenience for fitting ground level concentration

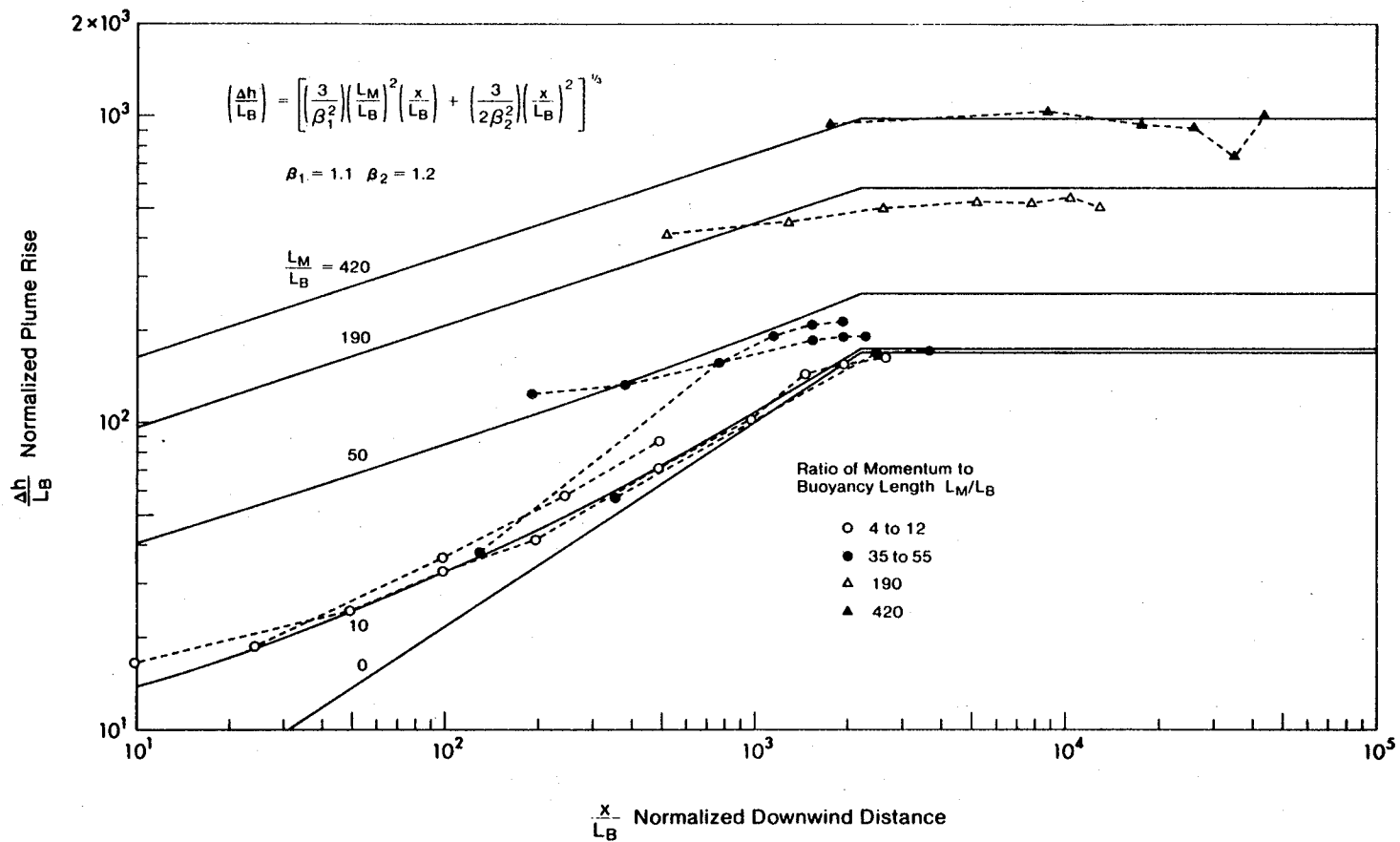


Figure 5-5. Approach to Final Rise of Plumes in Turbulent Shear Flow

profiles, rather than any rational assessment of the data scatter in Figure 5-5.

3. The contribution of momentum to final rise is not significant for the Syncrude plume at the test speed of $U_s = 0.45$ m/s (13.4 m/s full scale). However, Equation 5-6 shows that the momentum to buoyancy length ratio varies as the square of the wind speed, and for higher wind speeds the momentum to buoyancy length ratio may be as large as 30, giving significant contribution from momentum. Because it is precisely these higher speeds that are critical in determining whether the stack complies with government standards, it is recommended that momentum rise be included in all plume rise calculations.

Predicting Final Rise

One of the most significant results of this study was the discovery that distance to final rise was scaled according to buoyancy length L_B . Because the buoyancy length in Equation 5-2 is inversely proportional to the wind speed cubed, the distance from the stack to the point of final rise rapidly decreases as wind speed increases. This in turn causes drastic decreases in final plume rise, which must be taken into account to determine a realistic model for ground level concentrations at high wind speeds. If we assume a buoyancy dominated plume at the position of final rise, and insert the final rise position as $X_f = 2200 L_B$ the final rise for the Syncrude plume should be about

$$\Delta h_{Bf} = \frac{194}{\beta_2^{0.67}} \frac{F}{U_s^3} \quad (5-9)$$

Using the best fit value of $\beta_2 = 1.4$ which includes wind shear effects, the final rise of the Syncrude plume should be

$$\Delta h_{Bf} = 155 \frac{F}{U_s^3} \quad (5-10)$$

if momentum effects can be neglected.

Unfortunately, the downwind position of final rise of $X_f = 2200 L_B$ is applicable only for the specific atmospheric shear flow used in the Syncrude model studies. However, Briggs (1975) in Equations 79 and 80 derives the final rise of a purely buoyant plume by setting buoyant turbulent dissipation equal to the atmospheric turbulent dissipation. From this he obtains the final buoyant rise height as

$$\Delta h_{Bf} = \frac{0.47}{\beta_2^2} \left[2.5 \ln \left(\frac{h_s + \Delta h}{Z_0} \right) \right]^2 \left[1 + \frac{h_s}{\Delta h} \right]^{2/3} \frac{F}{U_s^3} \quad (5-11)$$

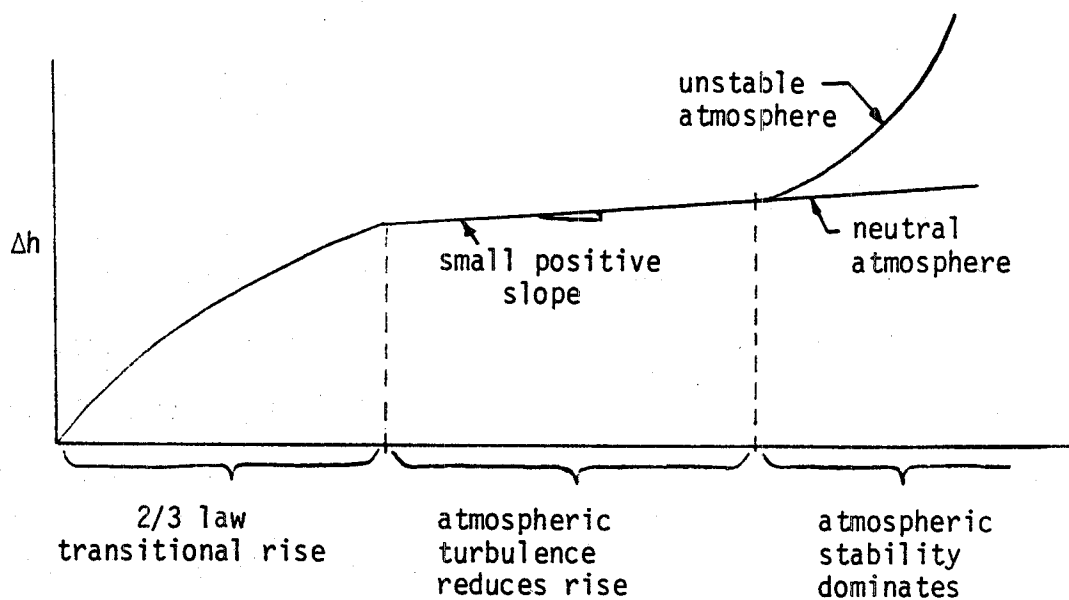
Inserting this in the transitional 2/3 law for buoyant rise gives

$$\frac{X_f}{L_B} = \frac{0.263}{\beta_2^2} \left[2.5 \ln \left(\frac{h_s + \Delta h}{Z_0} \right) \right]^3 \left[1 + \frac{h_s}{\Delta h} \right] \quad (5-12)$$

This shows that distance to final rise depends on atmospheric turbulence properties contained in the surface roughness Z_0 and in the height of the plume ($h_s + \Delta h$).

Slawson and Csanady (1971) consider the problem of departures from the 2/3 law for buoyant plumes. They include the effects of both atmospheric turbulence and stability. Their hypotheses are supported by full scale measurements. They find that for unstable air the plume rise is enhanced, and the transitional rise Equation 5-1 may grossly underestimate the plume

rise. In contrast to this, background atmospheric turbulence causes the plume rise to flatten as shown in the sketch below.



Here we are concerned only with the effect of atmospheric turbulence in neutral stability. We will identify the first transition point where the slope of plume rise changes sharply as the position of "final rise." Slawson and Csanady (their equation 19a) find this transition point as

$$\frac{x_f}{L_B} = \frac{0.565 \beta_2^{0.4}}{L_B^{0.6}} \left[\frac{U}{a_1 \epsilon^{0.33}} \right]^{1.8} \quad (5-13)$$

If a log law for velocity applies Briggs (1975) p. 88 has shown the dissipation ϵ is

$$\epsilon = \frac{U_*^3}{0.4 (h_s + \Delta h)}$$

which has the velocity profile

$$\frac{U}{u_*} = \frac{1}{0.4} \ln \left(\frac{h_s + \Delta h}{z_0} \right)$$

Combining these equations and applying them to Equation (5-13) yields

$$\frac{x_f}{L_B} = 0.565 \beta_2^{0.4} \left[\frac{2.5}{a_1} \ln\left(\frac{h_s + \Delta h}{z_o}\right) \right]^{1.8} \left[\frac{0.4(h_s + \Delta h)}{L_B} \right]^{0.6} \quad (5-14)$$

Slawson and Csanady give no hint for the value of a_1 . It should be of the order of unity, and we will take it as $a_1 = 1.0$ for all our estimates here.

Table 5-1 presents a comparison of these predictions for final rise with observations in the wind tunnel. The rationale for using $\beta_2 = 0.87$ for determining the distance to plume break-up is that this entrainment constant was determined for a uniform approach wind, and does not contain any extra compensation for plume deflection by vertical wind shear. On the other hand, the entrainment constant $\beta_2 = 1.4$ is used in estimating the final rise height, because this final rise is influenced by wind tunnel shear. Considering the approximations made in developing the final rise predictions, the agreement in Table 5-1 is reasonably good.

Stack Wake Downwash

The true perils of wake downwash are seldom appreciated by stack designers. Some downwash will begin to be noticeable when the stack momentum parameter defined by Equation 5-7 is $\phi_M < 2$ or more crudely $W_s/U_s < 1.5$.

Most stack designers either ignore downwash completely, or compensate by reducing the plume rise by a few stack diameters to account for a lower virtual origin of the buoyant source. Figure 5-6 shows the effects of downwash on plume trajectory. At the high wind speed the plume is sucked down into the stack wake, never to rise again. The shaded region shows the predicted rise heights for a range of entrainment constants determined from other measurements.

Table 5-1
Comparison of Measured and Predicted
Final Rise for the Syncrude Plume*

Investigator	Distance to Breakup $\frac{x_f}{L_B}$ $\beta_2 = 0.87$	Final Buoyant Rise $\frac{\Delta h_f}{L_B}$ for $\beta_2 = 1.4$ (with shear effects)
Present Study	2200 \pm 500	155 \pm 25
Briggs (1975)	3884 (eq. 5-12)	225 (eq. 5-11)
Slawson and Csanady (1971) for $a_1 = 1.0$	1730 (eq. 5-14)	130 (eq. 5-1, $L_M = 0$)

* computed for $U_s = 0.45$ m/s (13.4 m/s full scale)

with $\Delta h = 16$, $h_s = 22.86$, $Z_0 = 0.05$, $L_B = 0.101$, all in cm

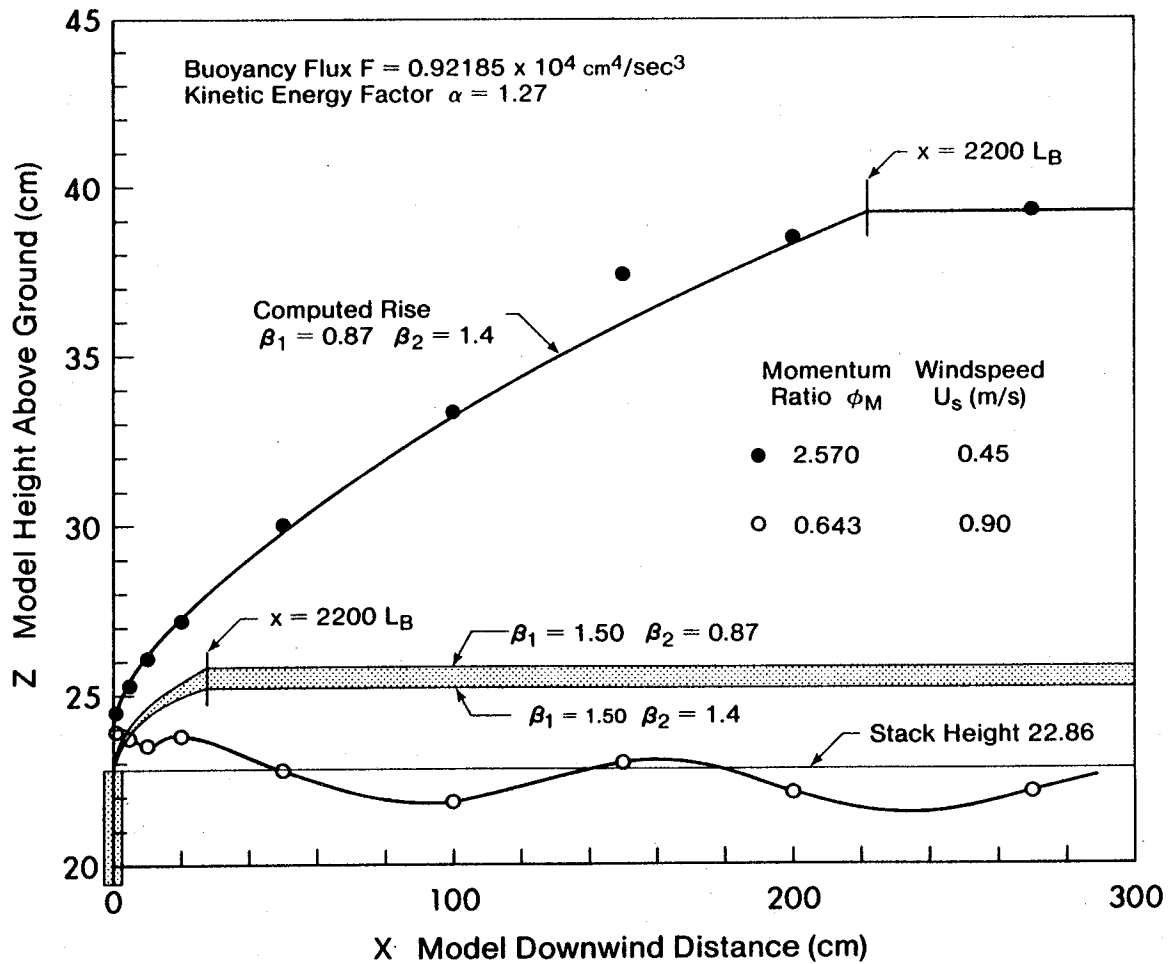


Figure 5-6. Rise of the Syncrude Plume at $U_s = 13.4 \text{ m/s}$ and Effect of Downwash at $U_s = 26.8 \text{ m/s}$ for Operation at 120% of Rated Load

On Figure 5-7 we can clearly see that the low pressure region in the stack wake applies a downward vertical force to the plume near the stack and overcomes its momentum, sucking the plume downward into the wake. As if this downward displacement were not enough of a disaster, the high turbulence in the wake increases entrainment not only close to the stack but, apparently far downwind as well. That is, its contact with the highly turbulent stack wake changes the character of plume entrainment at all downwind locations, drastically reducing plume rise.

Because the critical wind speed to determine compliance with government regulations often is high enough to cause significant stack wake downwash, some correction must be applied for this effect. Based on the present data in Figure 5-7, and on other similar experiments, it is recommended that the plume rise Δh computed with no downwash be corrected using the following factors.

$$\begin{aligned} &= \Delta h && \text{for } \phi_M > 2 \\ \Delta h_{\text{with}} &= \Delta h (1 - \phi_M) && \text{for } 1.0 < \phi_M < 2.0 \\ \text{downwash} &= 0 && \text{for } \phi_M < 1.0 \end{aligned} \quad (5-15)$$

Wind Shear Effects on Plume Rise

One of the specific objectives of this experimental study was to evaluate the effect of wind shear on plume rise. To do this, a special set of experiments had to be devised. Three different conditions were simulated, all with a turbulent stack gas:

1. A "bare" tunnel was used to provide a uniform wind speed with height, with no turbulence in the approaching wind.

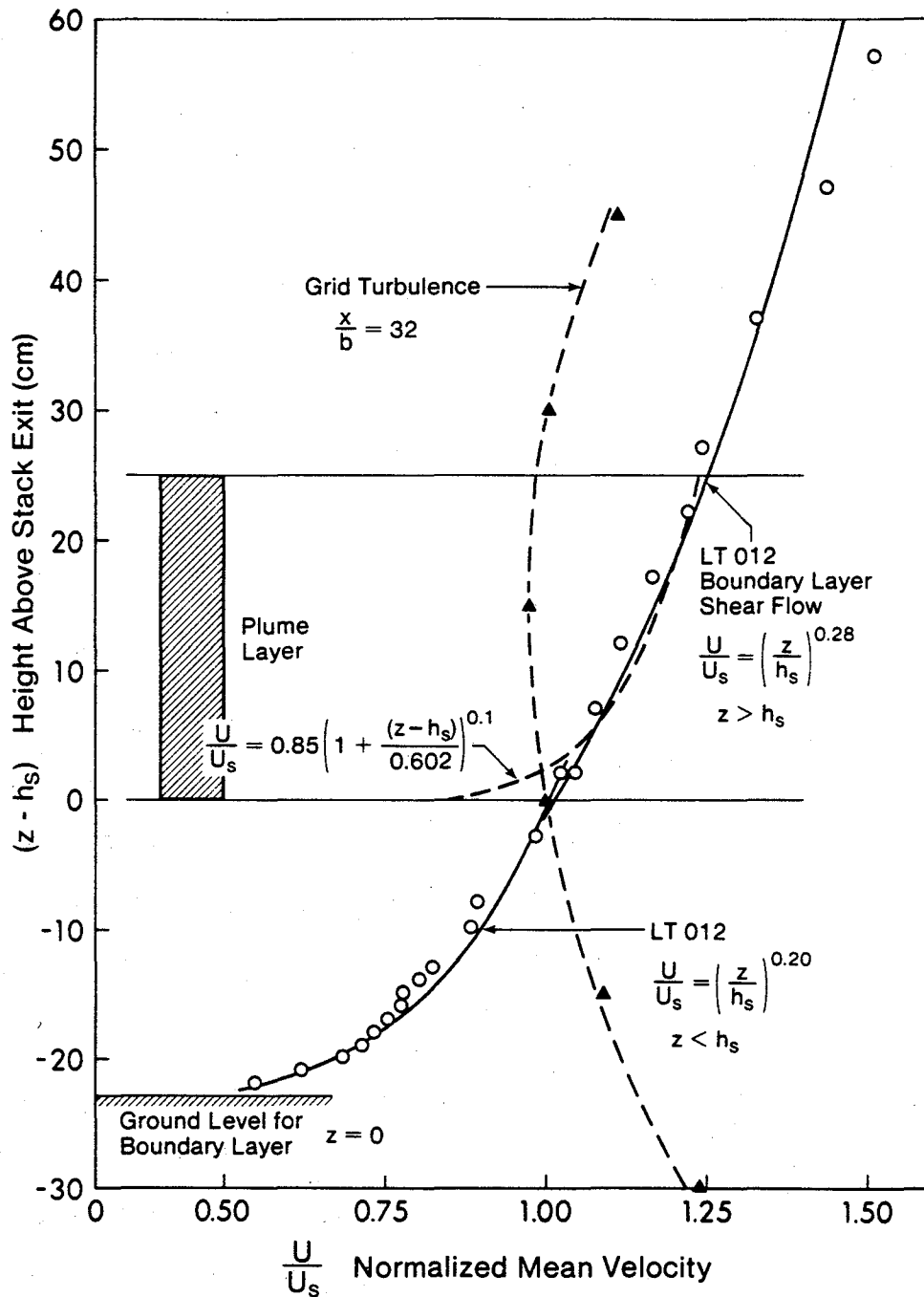


Figure 5-7. Mean Wind Speed Profiles for Turbulent Shear Flow and Grid Turbulence

2. A rectangular bar grid was inserted in the tunnel to produce turbulence levels about the same as those of the simulated atmospheric shear flow, but with uniform mean speed with height.
3. The simulated atmospheric shear flow provided a base-line of data influenced by wind shear.

The mean wind profiles are shown in Figure 5-7 for the grid turbulence and boundary layer shear flow. For the laminar flow obtained with the turbulence grid removed, the mean velocity varied by 1 percent or less throughout the plume layer. The empirical curve-fits to the velocity profile in the plume layer are also shown on Figure 5-7, and will be used later in theoretical predictions for shear effects.

Figure 5-8 shows the turbulence intensity downwind from the grid measured at stack height. These measured values were in good agreement with the data of Baines and Peterson (1951). In the absence of mean wind shear to provide turbulence production, a decay of intensity with downwind distance is inevitable. This downwind decay was in contrast to the constant turbulence level with downwind distance obtained in the simulated atmospheric shear flow.

The vertical variation of turbulence intensity in the shear layer and grid turbulence are shown in Figure 5-9. The downwind decay of turbulence intensity with the grid was exploited by locating the grid far enough upwind of the stack to produce the same turbulence intensity for the grid turbulence and boundary layer shear flow at the stack location. An added bonus was that as the plume rose above stack height it would encounter lower levels of turbulence intensity in the boundary

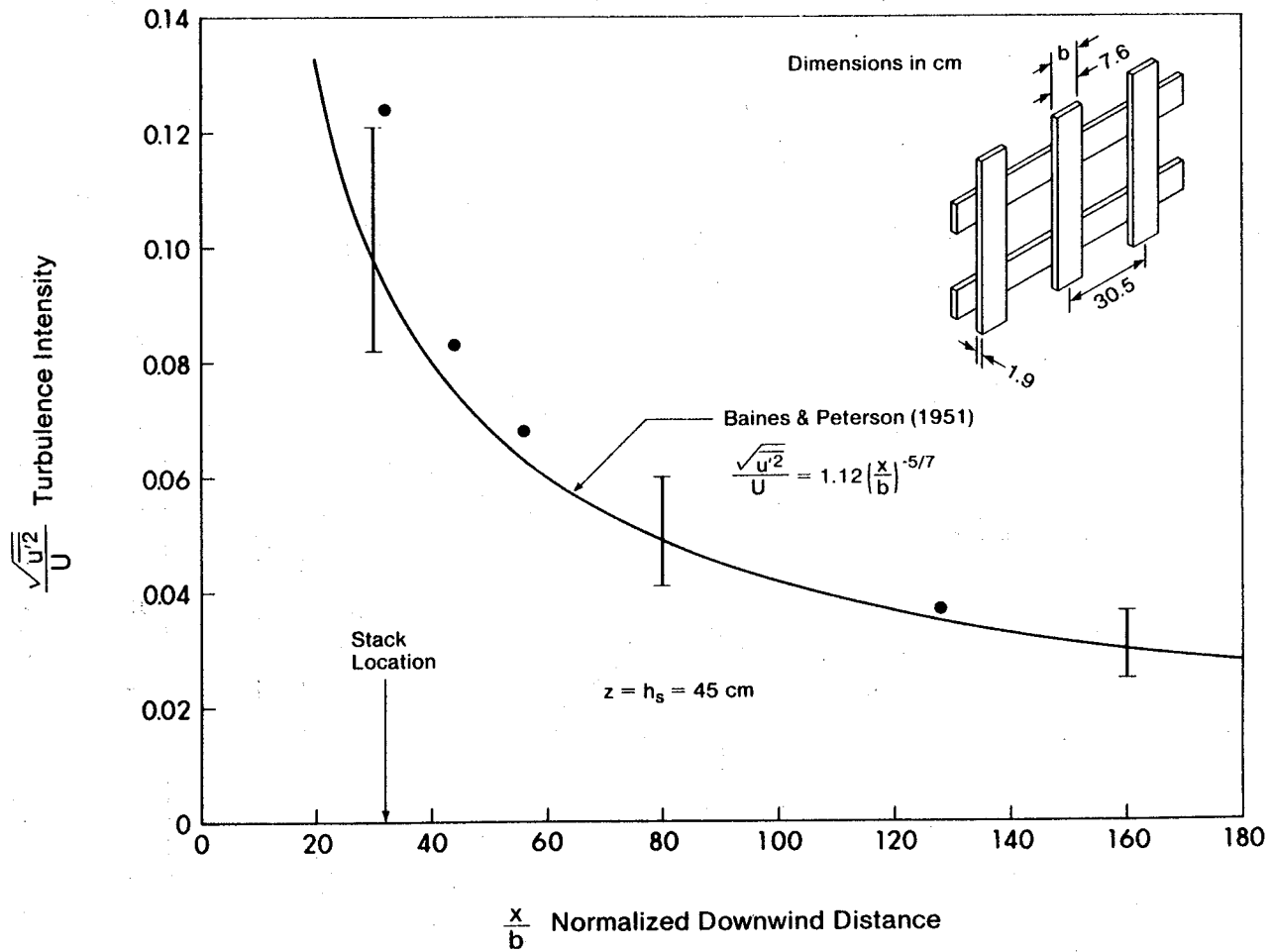


Figure 5-8. Along-wind Decay of Turbulence Intensity Behind the Grid

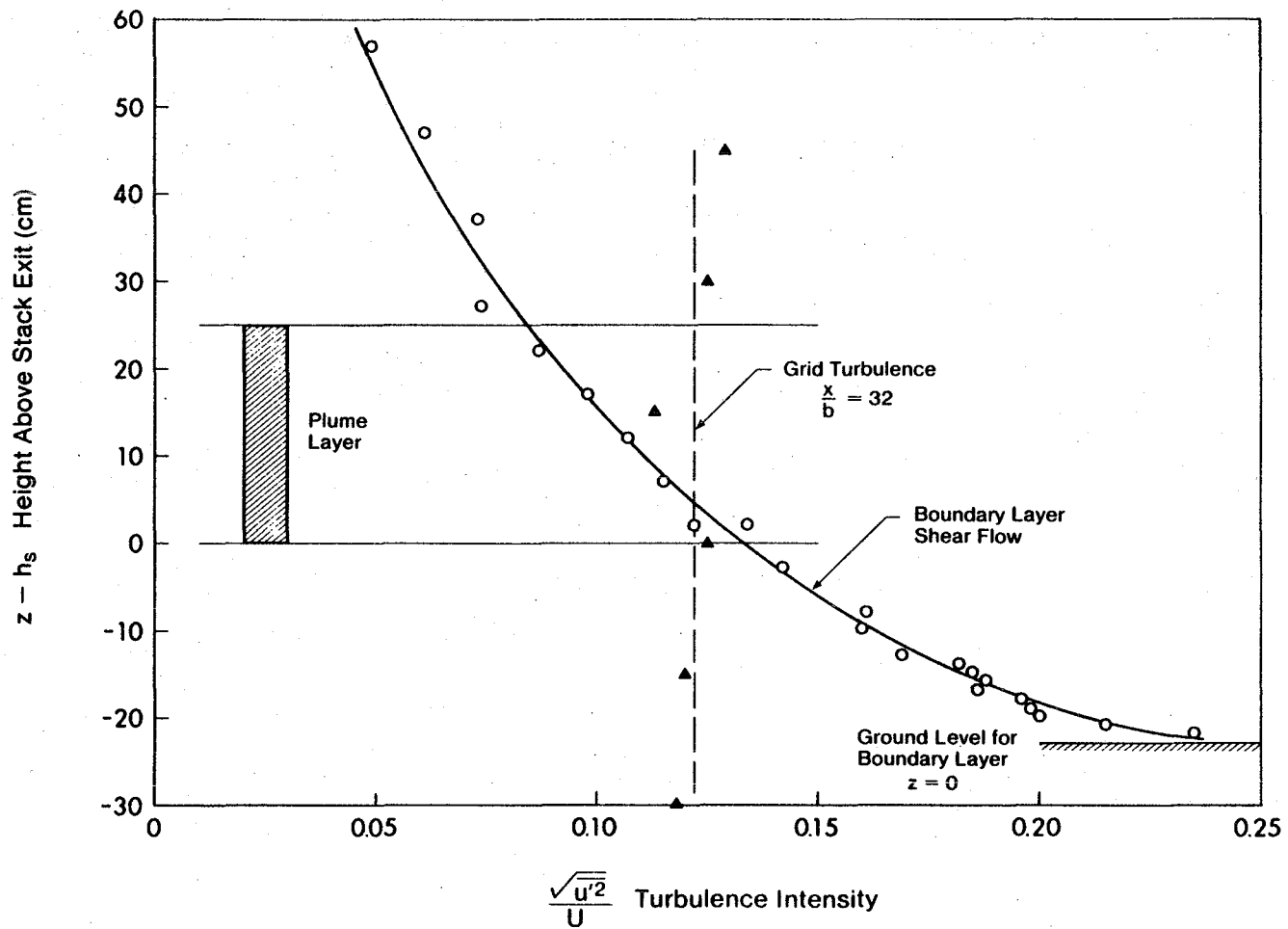


Figure 5-9. Vertical Profiles of Turbulence Intensity in Shear Flow and Grid Turbulence

layer shear flow due to decreasing intensity with height, and at the same time experience this same effect in the grid turbulence due to its downwind decay with distance.

Up to this point in Chapter 5, corrections for wind shear effects have been included directly in the buoyant entrainment constant β_2 . A more realistic approach is to follow the kinematics of the plume as it experiences increasing wind speeds during its travel. Djurfors has extended the solution in Djurfors and Nettekville (1978) for buoyant plume rise in shear flow to include the effects of momentum. Using the present notation, his solution is given by

$$\frac{\Delta h}{L_B} = \left[\frac{(3 + \gamma)}{\beta_{1*}^2} \left(\frac{Z_p}{L_B} \right)^\gamma \left(\frac{L_M}{L_B} \right)^2 \frac{U_s t}{L_B} + \frac{(3 + \gamma)}{2\beta_{2*}^2} \left(\frac{Z_p}{L_B} \right) \left(\frac{U_s t}{L_B} \right)^2 + \left(\frac{Z_p}{L_B} \right)^{3 + \gamma} \right]^{\frac{1}{3 + \gamma}} - \frac{Z_p}{L_B} \quad (5-16)$$

where

$$\beta_* \equiv \frac{\beta}{1 + \frac{\gamma}{2}}$$

$$Z_p \equiv \frac{R_s}{\beta_*}$$

and the velocity profile in the plume layer follows the power law for height Z above ground,

$$\frac{U}{U_s} = \left[\frac{Z - h_s + Z_p}{Z_p} \right]^\gamma \quad (5-17)$$

where $(Z - h_s)$ is the height above the top of the stack. The velocity U_s at stack top is allowed to vary along with γ to obtain a good fit to the observed wind profile.

The plume rise in Equation (5-16) is given in terms of travel time t rather than downwind distance. The downwind distance for any travel time is found by integration

$$X = \int_0^t U dt$$

Using Equation (5-17) and noting $(Z - h_s) = \Delta h$, this becomes

$$X = U_s \int_0^t \left[\frac{\Delta h + Z_p}{Z_p} \right]^\gamma dt \quad (5-18)$$

where $\Delta h = \Delta h(t)$.

Another alternative to integrating Equation (5-18) numerically is to assume that the effective wind speed seen by the plume is the value it is presently experiencing. Fitting the velocity profile by a ground based power law with the stack height as reference, the effective wind speed for rise is U at Δh

$$\lambda \equiv \frac{U \Delta h}{U_s} = \left(1 + \frac{\Delta h}{h_s} \right)^n \quad (5-19)$$

Then for example the effective buoyancy length is

$$\begin{aligned} L_B \text{ eff} &= \frac{F}{U \Delta h} \\ &= \frac{L_B}{\lambda^3} \end{aligned} \quad (5-20)$$

where L_B is defined in Equation (5-2) with U_s .

In the same way using Equation (5-6)

$$\frac{L_M \text{ eff}}{L_B \text{ eff}} = \frac{L_M}{L_B} \lambda^2 \quad (5-21)$$

Inserting these in Equation (5-1), replacing L_M and L_B by their effective values formed with velocity at local plume height yields

$$\frac{\Delta h}{L_B} = \left[\frac{3}{\lambda^2 \beta_1^2} \left(\frac{L_M}{L_B} \right)^2 \frac{X}{L_B} + \frac{3}{2\lambda^3 \beta_2^2} \left(\frac{X}{L_B} \right)^2 + \left(\frac{R_S}{\beta L_B} \right)^3 \right]^{1/3} - \frac{R_S}{\beta L_B} \quad (5-22)$$

which we will call the "local wind speed correction to uniform wind theory." This requires an iterative solution as follows:

- 1.) Compute L_M and L_B based on velocity U_s at stack height.
- 2.) With $\lambda = 1.0$ compute Δh from Equation (5-22).
- 3.) Compute λ using this Δh in Equation (5-19).
- 4.) Using this λ repeat step 2, iterating until Δh converges to its final value.

This procedure usually only requires a few iterations.

This simple method of correction will overestimate the effect of wind shear, because it assumes that the plume has been exposed to the local velocity at its particular height throughout its entire history. In fact, the plume sees a gradually increasing velocity as it rises through the wind shear to a given location.

Figure 5-10 shows a comparison of experimental data with predictions for a uniform wind, and with wind shear. All of the predictions include an initial source size, and both momentum and buoyancy rise. Both wind shear predictions provide a good estimate of the plume rise with shear. In particular, the simple effective distance correction of Equation (5-22)

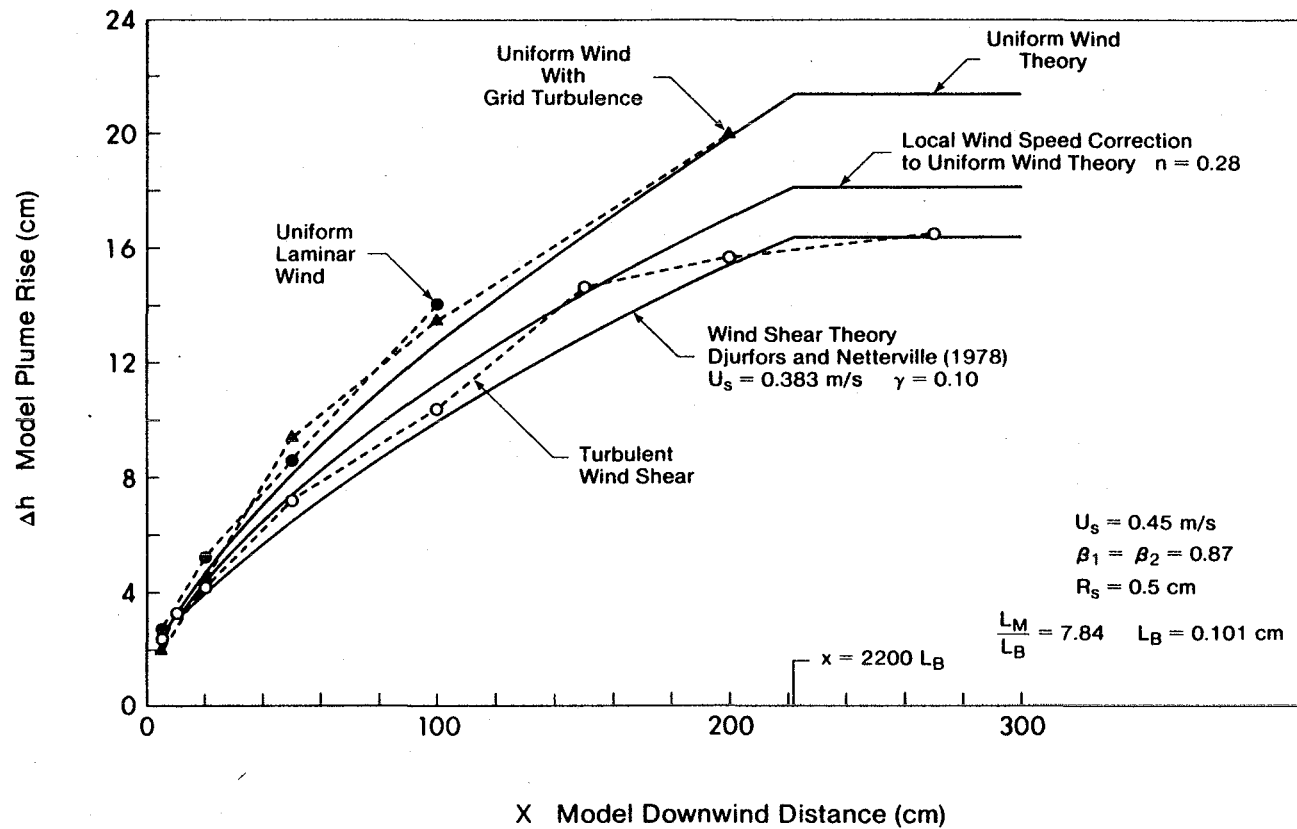


Figure 5-10. Predicted and Measured Plume Trajectories With and Without Vertical Wind Shear - Syncrude Plume at 120% Load with $U_s = 13.4 \text{ m/s}$

gives remarkably good results.

Figure 5-11 presents the same data on a log-log plot to emphasize the change in character from a momentum jet to a buoyant plume. Here only the simple shear correction is shown, along with a uniform wind approximation with all shear effects contained in a larger value of the entrainment constant. We see that to account for shear the entrainment constant must be increased from $\beta_2 = 0.87$ to a value of $\beta_2 = 1.4$.

One puzzling aspect of the local wind speed correction for wind shear is that it underestimates the effect of shear (overestimates plume rise). This is evident in Figure 5-10, where the local speed correction is about 10 percent higher than the observed rise, and the theory of Djurfors and Nettekville (1978). Common sense dictates that using the local wind speed in the plume rise equation should overestimate not underestimate shear effects.

Vertical and Crosswind Plume Spread

The plume standard deviations σ_y and σ_z were evaluated by fitting Gaussian curves to the measured concentration profiles with 400 second time averages. Vertical profiles were fitted using a Gaussian with ground level reflection.

Two curve fitting procedures were used. The first was a purely numerical procedure using a least squares error criteria to minimize error on the percentage deviation from the measured curve. By applying least squares fitting to the percentage deviations extra weight was implicitly given to low concentrations in the "tails" of the profiles. Occasionally, when there was considerable scatter of the data or large ground level concentration reflection, the numerical technique was unable

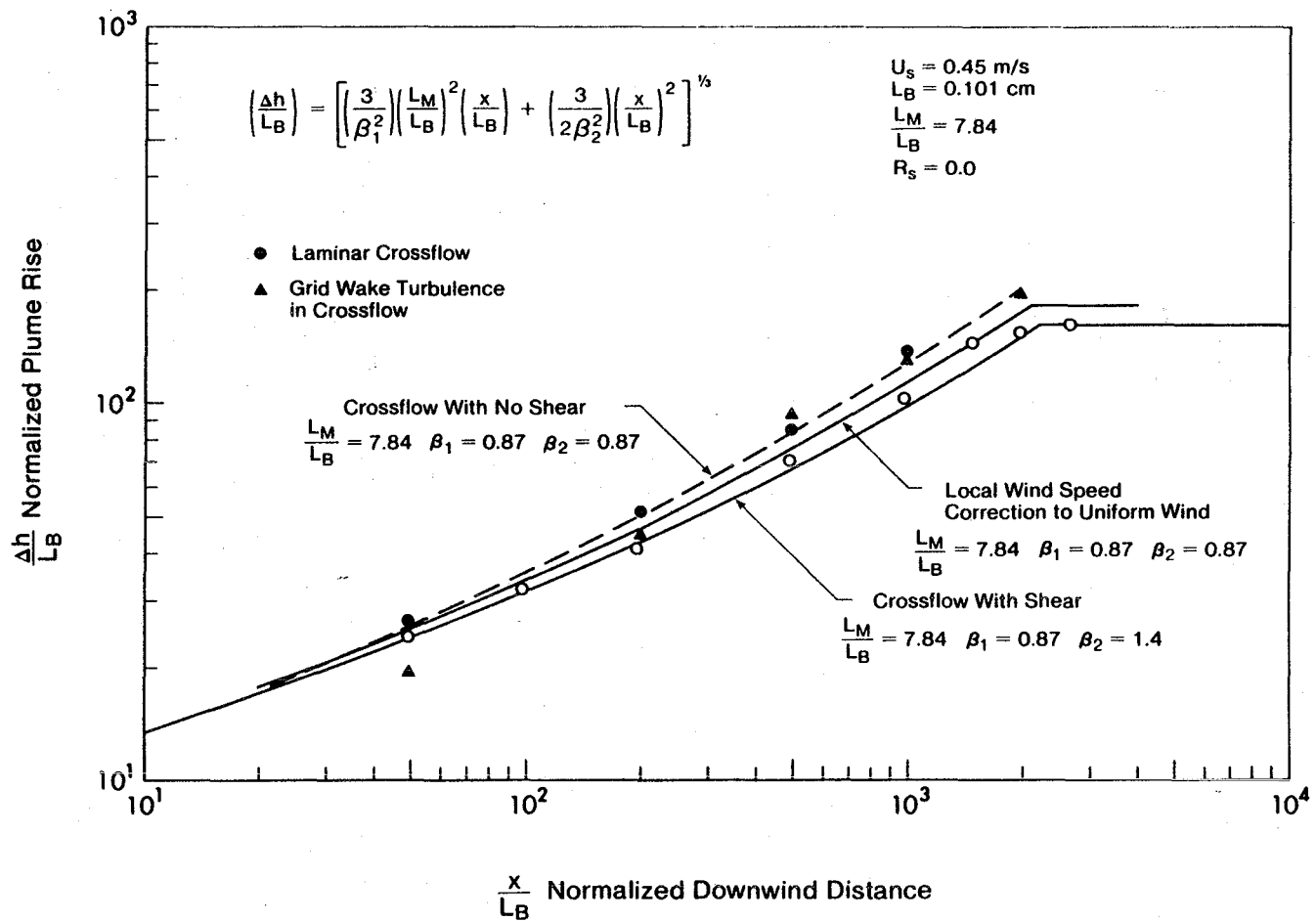


Figure 5-11. Combined Momentum and Buoyant Rise of the Syncrude Plume in Uniform Wind and with Shear Flow for Operation at 120% Load with $U_s = 13.4 \text{ m/s}$

to accurately locate the plume axis, and the overall fit was reduced in accuracy. It was always obvious when this failure occurred, because the fitted profiles simply did not "look right." When this problem arose, the plume axis position and the standard deviation were adjusted slightly using an interactive fitting technique on a CRT computer terminal to improve the curve fit. Usually only very small adjustments were required to dramatically improve the agreement between measurements and the fitted Gaussian profiles.

For a buoyant plume or a momentum jet, the plume standard deviations σ_y and σ_z will be larger than for a passive source dispersed by a turbulent flow. For the self-generated turbulence due to buoyant and jet mixing an estimate of the spread can be obtained from the entrainment constant β_1 or β_2 for a plume rise. For plume rise theories, see for example Briggs (1975). The entrainment constant is related to the plume radius R by

$$R = R_s + \beta \Delta h \quad (5-23)$$

At this point we will assume that the plume behaves as if it issues from a point source, and neglect the source radius R_s . The effective radius "R" of the plume is related to the Gaussian standard deviation σ_{self} from self-generated turbulence by

$$R = \xi \sigma_{self} \quad (5-24)$$

Combining Equation (5-23) and (5-24) the contribution from self-generated spread can be evaluated from the plume rise as

$$\sigma_{self} = \frac{\beta \Delta h}{\xi} \quad (5-25)$$

If the spreading due to self-generated turbulence is statistically independent of spreading σ_z due to turbulence in the wind, we should be able to simply add the variances $\sigma_z^2 + \sigma_{self}^2$ to obtain the variance of the combined spread. In reality, the fields from buoyancy, jet and ambient turbulence will interact in a complicated non-linear way, and will certainly not be statistically independent.

To account for interaction between self-generated and ambient turbulence a factor η will be applied to σ_{self} in adding the variances to obtain for the total spread σ_{zB}

$$\sigma_{zB}^2 = \sigma_z^2 + (\eta \sigma_{z,self})^2 \quad (5-26)$$

with a similar equation for crosswind spread σ_y .

The effective radius ξ in standard deviations in (5-25) was evaluated experimentally by using plume rise and spreading in a laminar crosswind. The plume rise measurements in Figure 5-10 indicated $\beta = \beta_1 = \beta_2 = 0.87$. The plume spreading widths σ_z are summarized in Table 5-2, where the ξ values are computed using plume rise from Equation (5-1) with $R_s \equiv 0$. Based on these measurements we will use a value of

$$\xi = 1.75$$

for future calculations.

The value of η is much more difficult to evaluate. Equation (5-25) with $\xi = 1.5$ was used in Equation (5-26) to correct measured values of σ_{yB} and σ_{zB} at two different tunnel speeds of $U_s = 0.45$ m/s and $U_s = 0.90$ m/s. These two speeds should produce the same spread σ_y and σ_z due to ambient turbulence. It was found by trial and error that a value of

Table 5-2

Effective Plume Radius for Self-Generated Spreading*

X Model Distance (cm)	$\sigma_{z,self}$ Measured (cm)	$\xi = \frac{\beta \Delta h}{\sigma_{z,self}}$ Effective Radius (std. deviations) **
5	1.20	1.88
20	2.6	1.70
50	3.95	1.88
100	7.00	1.63

* turbulent stack gas with laminar crosswind

$$U_s = 0.45 \text{ m/s}$$

$$\frac{L_M}{L_B} = 7.84$$

$$L_B = 0.101 \text{ cm}$$

** Δh computed from Eq. 5-1 with $\beta = \beta_1 = \beta_2 = 0.87$ and $R_s = 0$

$$\eta = 0.577$$

produced the best agreement between the two sets of data. The final form of the self induced spreading correction, using Equation (5-1) for plume rise is,

$$\sigma_B = \left[\sigma^2 + 0.33 \sigma_{\text{self}}^2 \right]^{0.5} \quad (5-27)$$

from Equation (5-25) where "B" refers to total buoyant spread and

$$\sigma_{\text{self}} = \frac{\beta_2}{1.75} \left[\frac{3}{\beta_1^2} \left(\frac{L_M}{L_B} \right)^2 \frac{X}{L_B} + \frac{3}{2\beta_2^2} \left(\frac{X}{L_B} \right)^2 \right]^{0.33} \quad (5-28)$$

Plume Spread Measurements

Using the corrections for self-mixing in Equations (5-27) and (5-28) power laws were fitted to the observed plume spreading rates. The total and corrected spreading rates are shown in Figures 5-12 and 5-13 along with the fitted power laws.

For vertical concentration profiles the correction for self-generated turbulence gives a much better fit to the observations, particularly close to the source. However, the crosswind spreading rates σ_y behave quite differently. Far downwind the spreading rates behave opposite to the expected trend, with the low speed data falling below the high speed spread σ_y . Corrections for self-mixing shown in Figure 5-13 only serve to further separate these data.

One plausible explanation for the behavior of crosswind spreading rates σ_y , is that the high speed case was influenced by the stack wake. Figure 5-6 shows that for the higher approach wind speed the plume is sucked into the stack wake by downwash. Once it is trapped by the stack

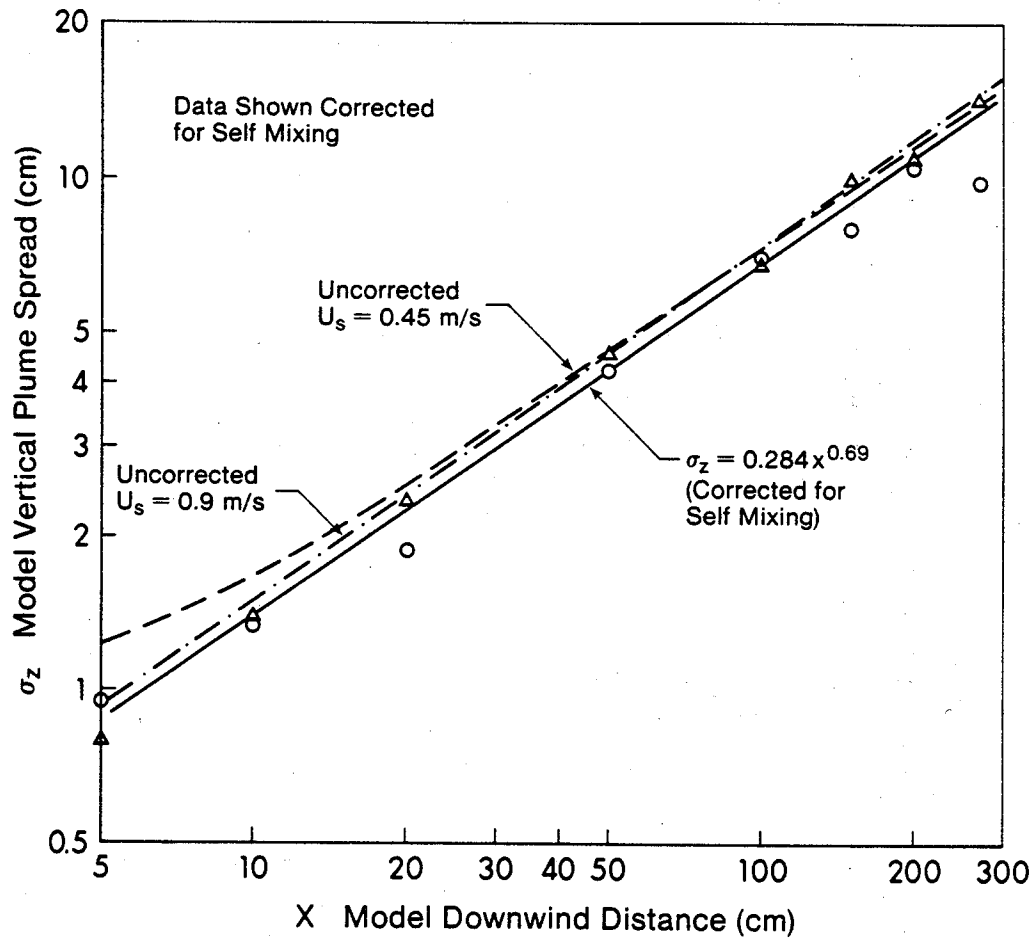


Figure 5-12. Vertical Plume Spread Corrected for Self-Induced Jet and Buoyant Mixing

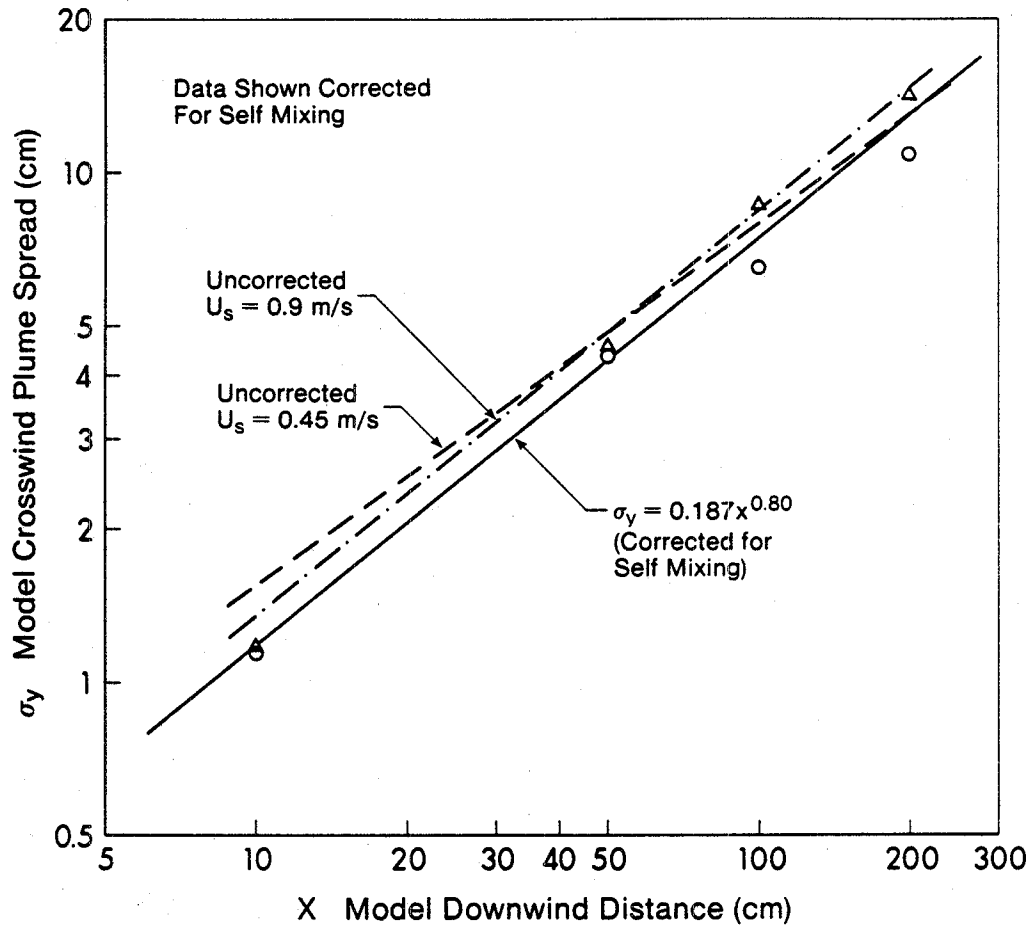


Figure 5-13. Crosswind Plume Spread Corrected for Self-Induced Jet and Buoyant Mixing

wake, the vortex shedding from the stack should increase crosswind spread σ_y much more than vertical plume spread σ_z . This hypothesis (if true) explains the observed behavior of σ_y and σ_z for the high wind speed case.

In the model scale, the fitted power laws for plume spreading were found to be

$$\sigma_z = 0.284 X^{0.69}, \text{ model cm} \quad (5-29)$$

and

$$\sigma_y = 0.187 X^{0.80}, \text{ model cm} \quad (5-30)$$

Using a 800:1 scale factor these correspond to full scale spreads corrected for self-mixing of,

$$\sigma_z = 0.541 X^{0.69}, \text{ full scale m} \quad (5-31)$$

$$\sigma_y = 0.283 X^{0.80}, \text{ full scale m} \quad (5-32)$$

Plume spreading rates are also shown in Figures 5-14 and 5-15. These linear plots show that the correction for self-mixing produces the correct trend for vertical spreading, but exactly the opposite effect required to correlate the results for crosswind spreading. As discussed previously this may be due to the influence of the stack wake on crosswind spreading and for the high wind speed. At the furthest downwind position the measured values of vertical spread are somewhat lower than predicted by the power-law fit. This may be due to the restraining effect of the wind tunnel floor on vertical spread.

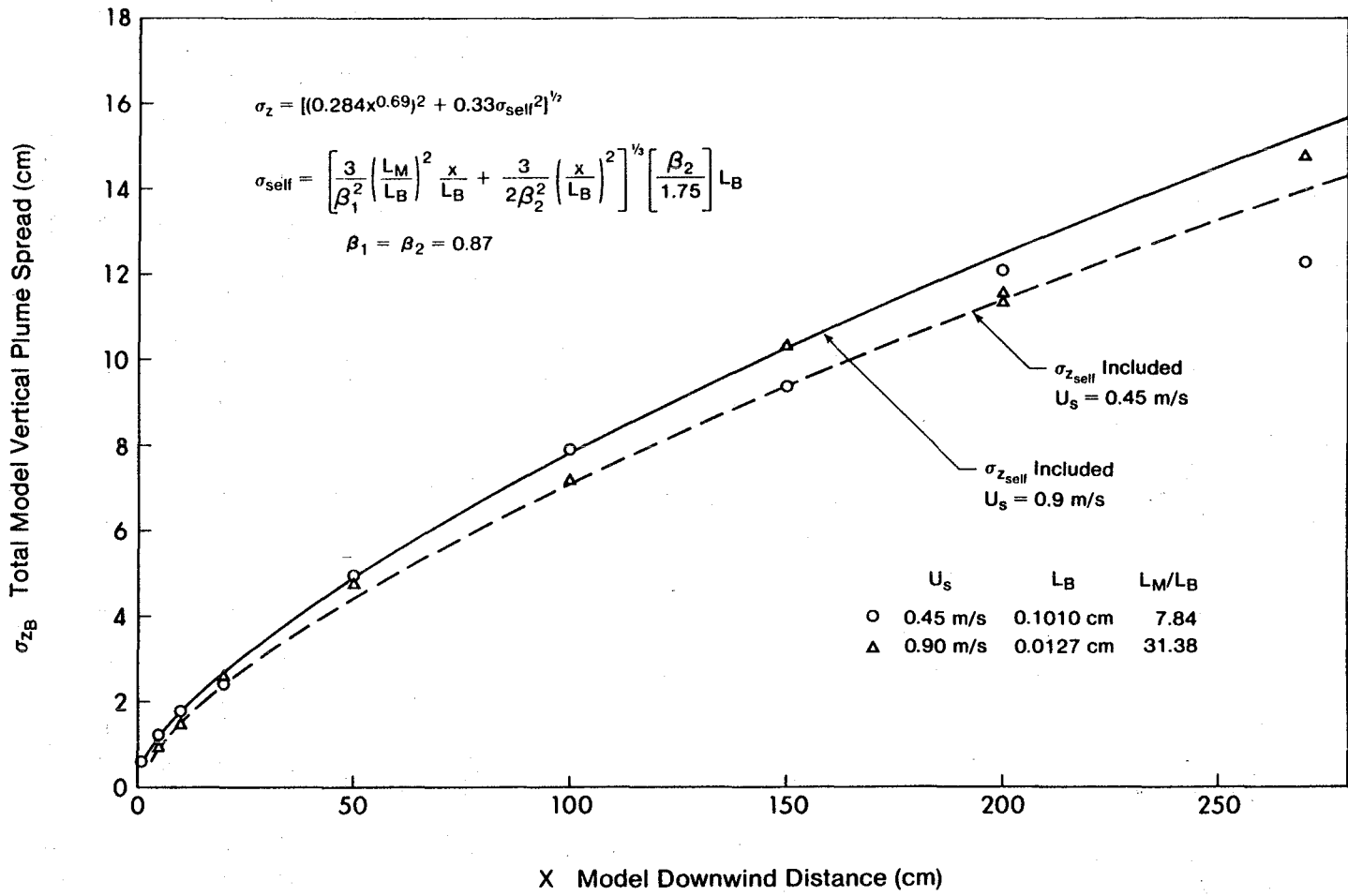


Figure 5-14. Predicted and Measured Total Vertical Spread

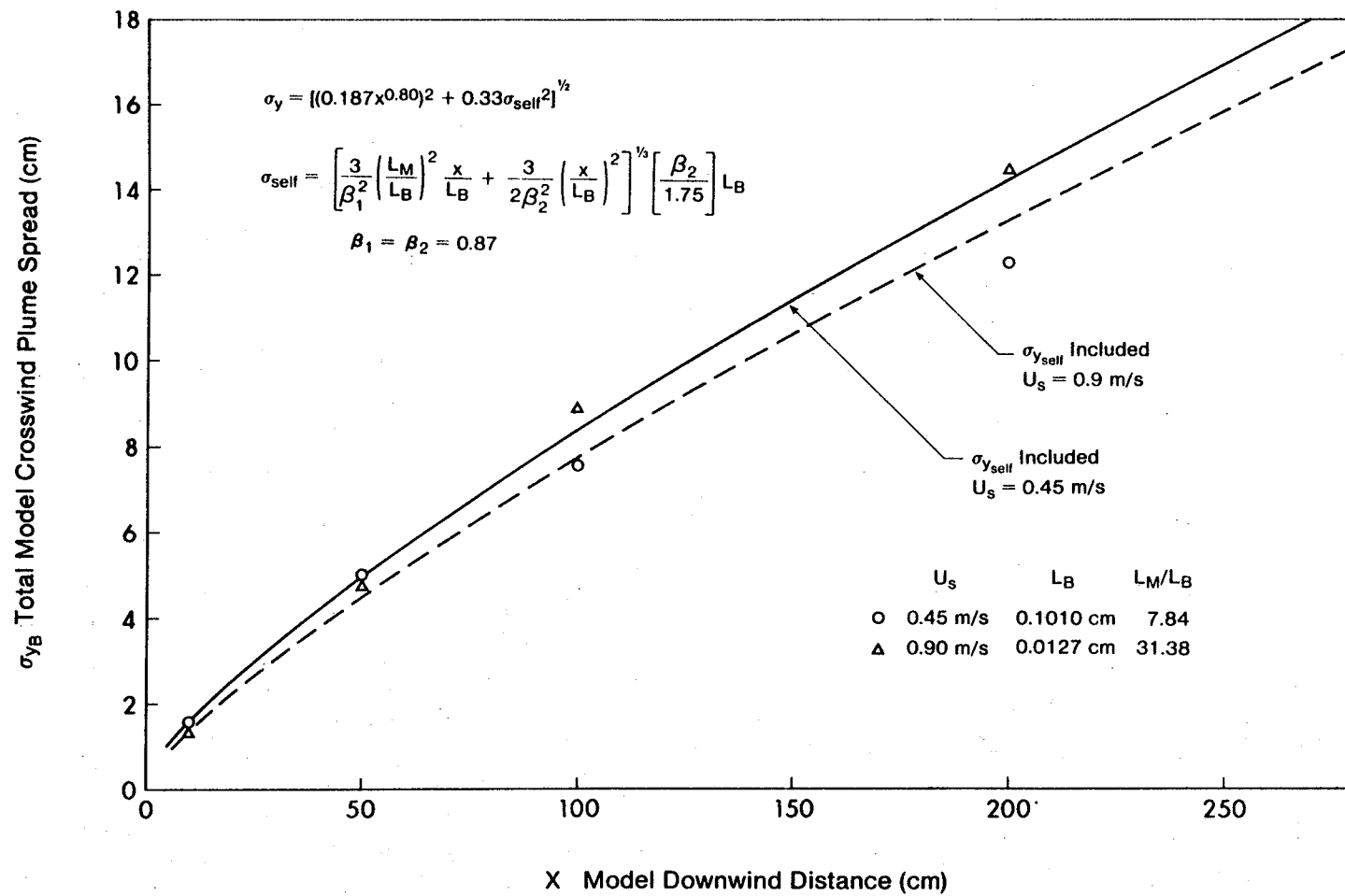


Figure 5-15. Predicted and Measured Total Crosswind Spread

Comparison with Full Scale Spreading

The full scale Brookhaven spreading rates of Singer and Smith (1966) are compared with the measured power laws for vertical and crosswind spread in Figures 5-16 and 5-17. In addition, vertical spreading rates suggested by Smith and Pasquill (1975), and crosswind spreading rates of Gifford (1968) are also shown.

Considering the wide variation in averaging times and surface roughness Z_0 , the measurements are in reasonably good agreement with their full scale counterparts. One particularly vexing problem is caused by the stated averaging times on full scale measurements. For example, in Figure 5-16 the spreading rates of Smith-Pasquill and the Brookhaven curves are almost the same, yet one claims a 30 to 90 minute averaging time while Pasquill states that a 3 minute averaging time is appropriate. With this kind of variation it is difficult to determine the appropriate full scale averaging time equivalent to the 400 second averaging time used in the wind tunnel. About all that can be said is that the model scale measurements are consistent with full scale averaging times ranging from about 30 to 120 minutes. The reader will recall that the buoyancy time scale factor developed in Chapter 2 indicates that the 400 second wind tunnel measurements correspond to 180 minute full scale averages.

Because the wind tunnel walls prevent long time plume meandering, it is difficult to make a direct scaling of wind tunnel averaging times to a full scale equivalent. In the wind tunnel, plume spreading rates will rapidly approach an asymptotic limit as averaging time is increased. However, the full scale measurements continue to show increasing plume spread with averaging time due to plume meandering caused by large scale

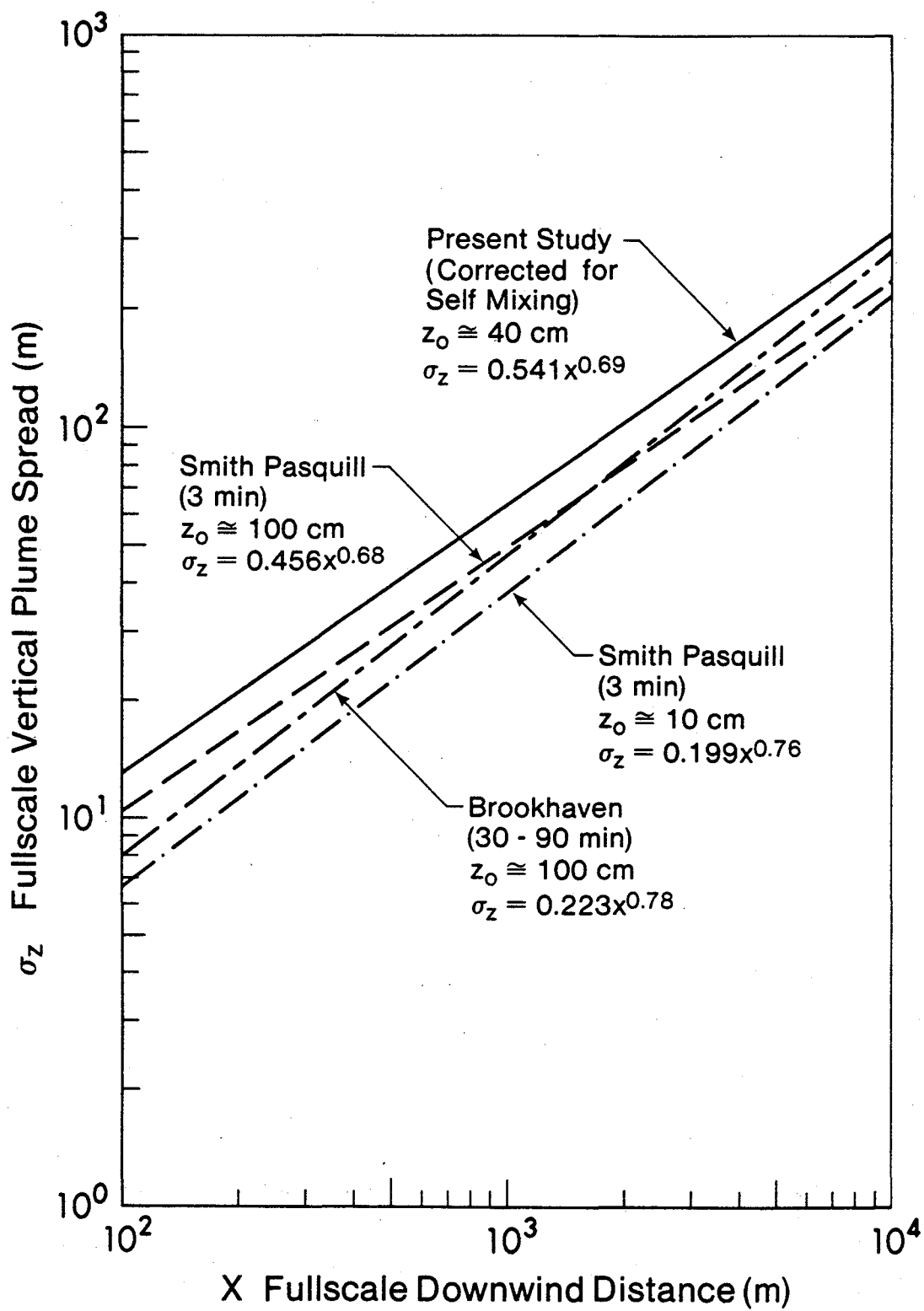


Figure 5-16. Comparison of Model Vertical Spread with Full Scale Correlations for 800:1 Length Scale

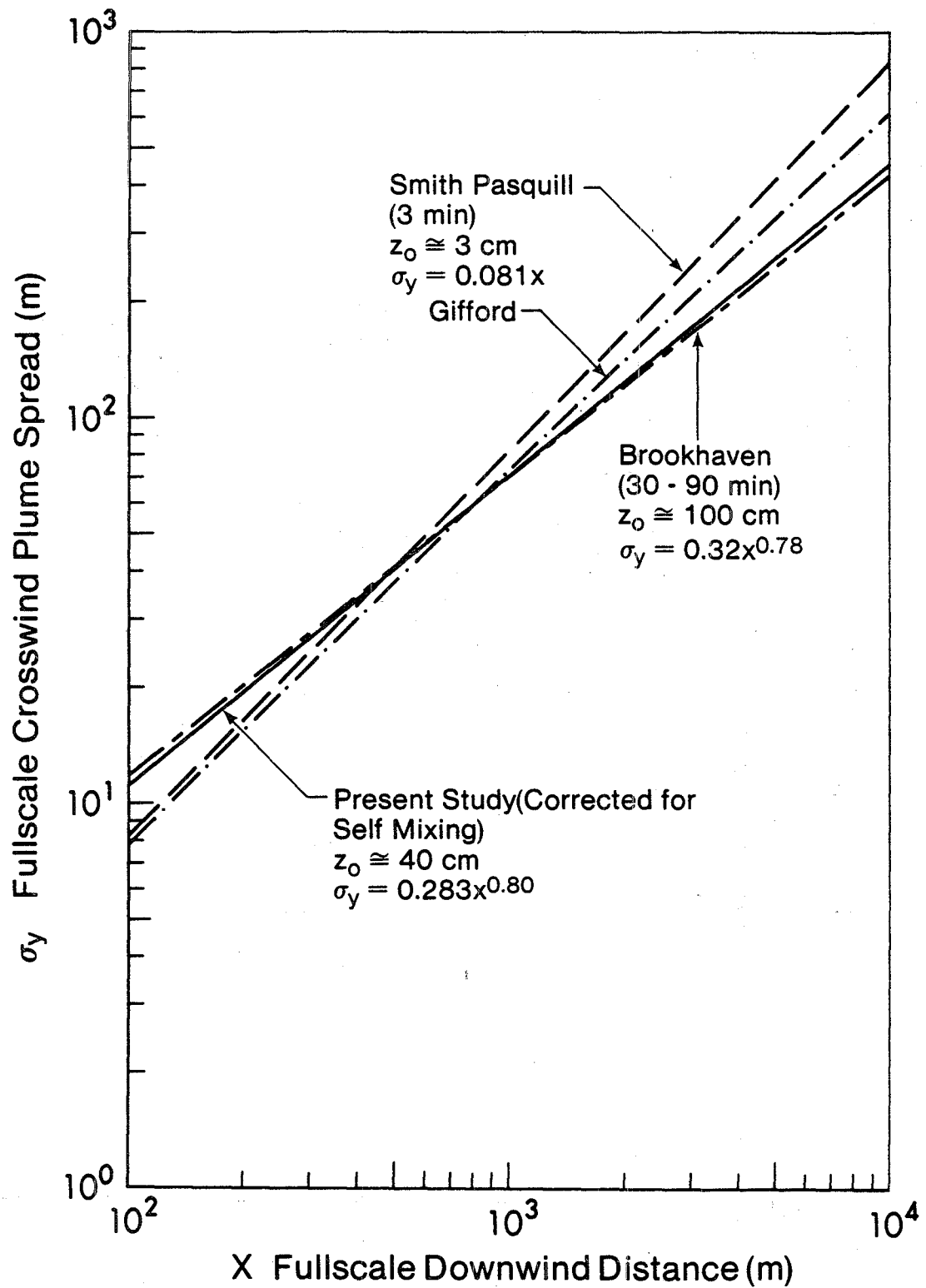
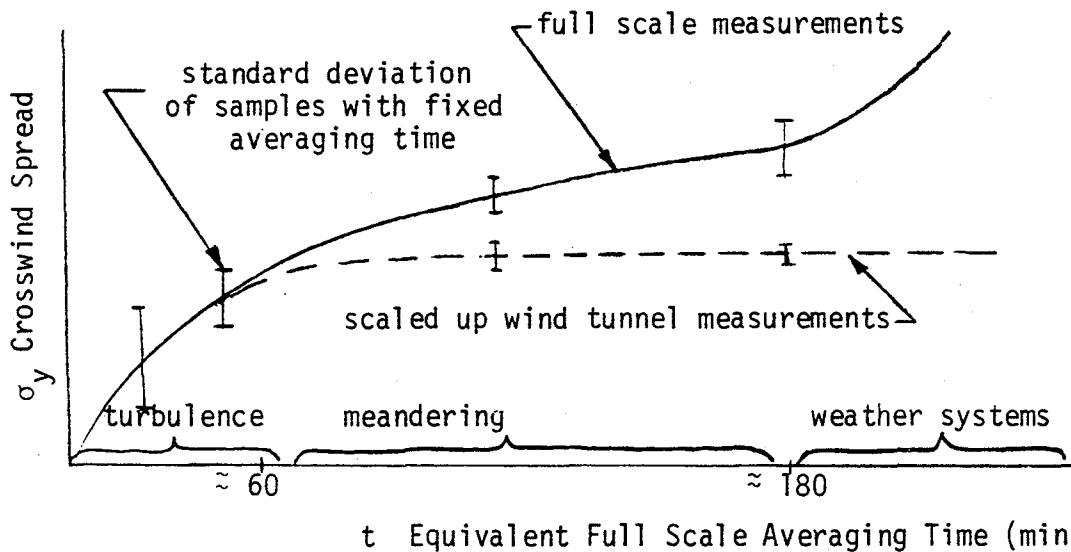


Figure 5-17. Comparison of Model Crosswind Spread with Full Scale Correlations for 800:1 Length Scale

turbulent motions. These effects are illustrated in the sketch below.



The present study, as well as previous experiments indicate that wind tunnel modelling breaks down for time averages longer than about 30 to 60 minutes. Note that even at the limit of the wind tunnel simulation, the standard deviation of successive samples for σ_y and σ_z will still be rather high. The 400 second time averages used in the present study were required to obtain a true mean, by reducing the standard deviation of successive samples. However, these 400 second averages probably do not correspond to 180 minute full scale averages.

Vertical Plume Spread for Ground Level Concentrations

All of the vertical plume spreads σ_y discussed previously were obtained from best-fit curves to the entire vertical concentration profile at a given location. Because both wind speed and turbulence vary throughout the boundary layer in which dispersion takes place, an average plume spread σ_z determined in this way may not be the best for predicting ground level concentrations. To account for this, and hopefully to provide a better estimate of ground level concentrations,

vertical plume spreads were fitted using reflected Gaussian profiles to the measured concentrations below plume centerline.

Surprisingly, considering the non-homogeneity of the shear flow, the values of σ_z based on the lower half of the profile were almost the same as those using the entire profile. Using the same corrections for self-induced spread given in Equations (5-27) and (5-28) the vertical spreading rates based on the lower half of the profile were in close agreement with the power law

$$\sigma_z = 0.271 X^{0.70}, \text{ model cm} \quad (5-33)$$

or in full scale with an 800:1 factor

$$\sigma_z = 0.506 X^{0.70}, \text{ full scale m} \quad (5-34)$$

These equations predict values very close to Equations (5-29) and (5-31) for σ_z values based on the entire profile.

For all computations of ground level concentrations presented in the following chapter, the values of the "lower half" spreading rates in Equations (5-33) and (5-34) were used. We will see that the differences in ground level concentrations predicted by the two different vertical spreading rates is at most a few percent, and for this reason the choice of the "lower half" values for σ_z is mostly a matter of personal preference.

Summary

The measurements reported in this chapter show that the wind tunnel is capable of accurately modelling all of the essential plume dynamics required for atmospheric dispersion measurements. At the inception of this project it was hoped that the wind tunnel would be

capable of simulating the buoyant rise of a hot stack gas. As time progressed and the modelling simulation was found to be good, the expectations and demands placed on the wind tunnel simulation were further increased. Eventually, it was found that with considerable care applied to simulating the initial stack gas conditions, complete confidence could be placed in the accuracy of the wind tunnel simulation.

The only point which could not be adequately explained was the relatively high value for the buoyancy entrainment constant of $\beta_2 = 0.87$. This was about 50 percent larger than the accepted value of $\beta_2 = 0.6$. As with any wind tunnel simulation, there remains the nagging doubt of whether this difference is real, or caused by some effect of the large Reynolds number mismatch between model and full scale. However, with this one exception, the wind tunnel showed a remarkable ability to simulate full scale plume dynamics.

CHAPTER 6

DIKE EFFECTS ON GROUND LEVEL CONCENTRATIONSIN THE MAIN STACK PLUME

In the previous chapter considerable effort was expended in developing reliable models for plume rise, and plume spreading rates. The ultimate purpose of such models is to predict ground level concentrations. However, to properly validate the Gaussian plume model, an extensive experimental program was undertaken to measure ground level concentrations directly in the wind tunnel. We will show in this chapter that a Gaussian plume model provides excellent approximation to behavior of ground level concentration profiles.

The primary objective of the ground level concentration measurements was to determine the effect of various tailings pond dike heights on ground level concentrations. As we saw earlier, the flow remains attached on the downwind side of the tailings pond dike, but the turbulence created in the dike wake can increase vertical and cross-wind spreading rates to cause changes in ground level concentrations. The measurements presented in this chapter will show that these effects are very small for dike heights up to about 50 meters, and increase the ground level concentration by about 20 percent for a dike height of 100 meters. A simple analytical model will be developed to allow terrain effects to be estimated by simple modifications to values predicted for a Gaussian plume on flat terrain.

Test Conditions

The wind tunnel tests were carried out for two different wind speeds. These speeds of 0.45 m/s and 0.90 m/s at stack height in the tunnel

correspond to a "most realistic" full scale value of 13.4 m/s and a "most critical" value of 26.8 m/s. The lower speed represents a typical wind encountered on the plant site, while the higher speed corresponds to conditions at which considerable plume downwash into the stack wake will occur. These two speeds, both with turbulent stack gas using a mixing plug in the stack, are the same as those in Chapter 5 used to determine plume rise characteristics.

An extensive series of preliminary experiments were carried out with a laminar stack gas. For these preliminary experiments the tunnel speeds were 0.5 and 1.0 m/s. From scaling factors in Table 2-3 these speeds with laminar stack gas correspond to 16.7 and 33.4 m/s in full scale. We will see that the change in conditions from laminar to turbulent stack gas, and the adjustment in wind speed, does not significantly alter the character or magnitude of measured ground level concentrations.

"Critical" and "Realistic" Dike Configurations

Ground level concentration measurements were carried out for various dike heights, wind speeds, and directions. All combinations of the following variables (given in full scale units) were used:

- 3 terrain configurations: flat, and dike heights $H = 45.8$ and 94 m.
- 2 wind speeds: $U_s = 16.7$ and 33.4 m/s Test Series I.
- 4 wind directions: north, south, north-west, and south-west (all directions refer to plant co-ordinates).

With the wind blowing from Plant North the dikes were located upwind of the main stack and perpendicular to the flow.

With wind directions from the north-west and south-west directions the dike lay 45° to the wind direction. Ground level concentrations measured with these orientations showed a negligible effect of oblique winds to the dike. That is, ground level concentrations were the same for winds from the south, and the south-west etc. For this reason, only the data for winds from due north and south will be reported here. The stack was operated under the conditions shown in Table 2-3 as Test Series I, with laminar flow at the stack exit.

Ground level concentration profiles are shown in Figure 6-1 for flat terrain with no tailings pond dike and wind from the plant north direction. At the highest wind speed considerable stack downwash suppresses plume rise, and the maximum ground level concentration along the plume centerline occurs within the tunnel test section length. At the lower wind speed increased plume rise causes maximum ground level values to occur beyond the end of the wind tunnel test section. The portion of the ground level profile remaining within the tunnel shows a monotonic rise with downwind distance.

The lines shown on all ground level concentration profiles in this chapter are predictions using the Gaussian plume model. For flat terrain ground level concentrations were generated in the model scale by:

- a.) Computing vertical and crosswind spreads σ_y and σ_z from Equations (5-30) and (5-33).
- b.) Correcting these power-law plume spreads for self-induced spreading using Equations (5-27) and (5-28) with β_1 from Equation (5-8) and $\beta_2 = 0.87$.

- c.) At the lower wind speed of $U_s = 0.5$ m/s (16.7 m/s), computing combined momentum and buoyant plume rise Δh from Equation (5-1) with β_1 computed from Equation (5-8) and $\beta_2 = 1.22$ to include wind shear effects with laminar stack gas. Set final rise at $X = 2200 L_B$. In Test Series II with a turbulent stack gas a value of $\beta_2 = 1.4$ was used, consistent with plume rise observations discussed in Chapter 5.
- d.) At the higher wind speed of $U_s = 1.0$ m/s (33.4 m/s) (or 0.90 m/s (26.8 m/s) in Test Series II) set $\Delta h = 0.0$ due to plume downwash.
- e.) Inserting the above values in the Gaussian plume Equation (C-10) with $T_s = T_a$ in the model scale.

The predicted ground level concentrations shown in Figure 6-1 are in good agreement with the measured values, with one exception. At the lower wind speed the final plume rise which occurs at $X \approx 190$ cm (1520 m) causes an increase in predicted ground level concentration that is not observed experimentally. No satisfactory explanation could be found for this effect. Plume rise measurements confirm without a doubt that final rise does occur, while ground level concentrations behave as though the plume were still rising. At this lower wind speed the power law approximation to crosswind spreading σ_y overestimates the spread. This effect should cause the predicted ground levels to be lower than the observed values, not higher as actually occurs in Figure 6-1.

The effect of wind speed and direction for the lower dike height of 45.8 meters is shown in Figures 6-2 and 6-3. By comparing the measured values in these figures to Figure 6-1, it is apparent that the 45.8 meter

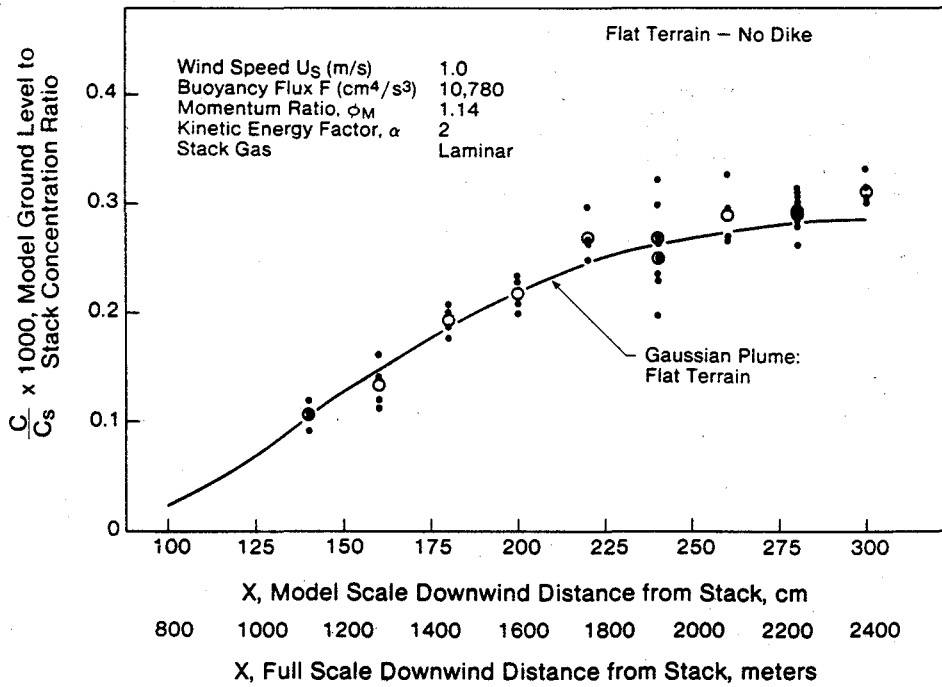
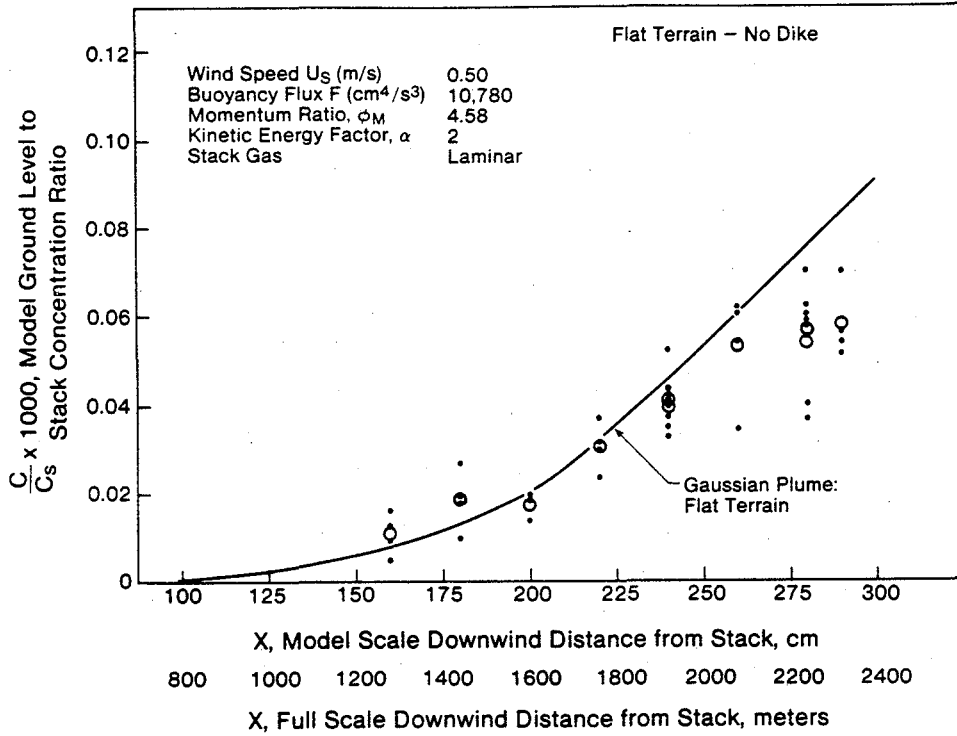


Figure 6-1 Ground Level Concentrations With Flat Terrain for $U_s = 16.7$ m/s and 33.4 m/s with Plant at 197% Load

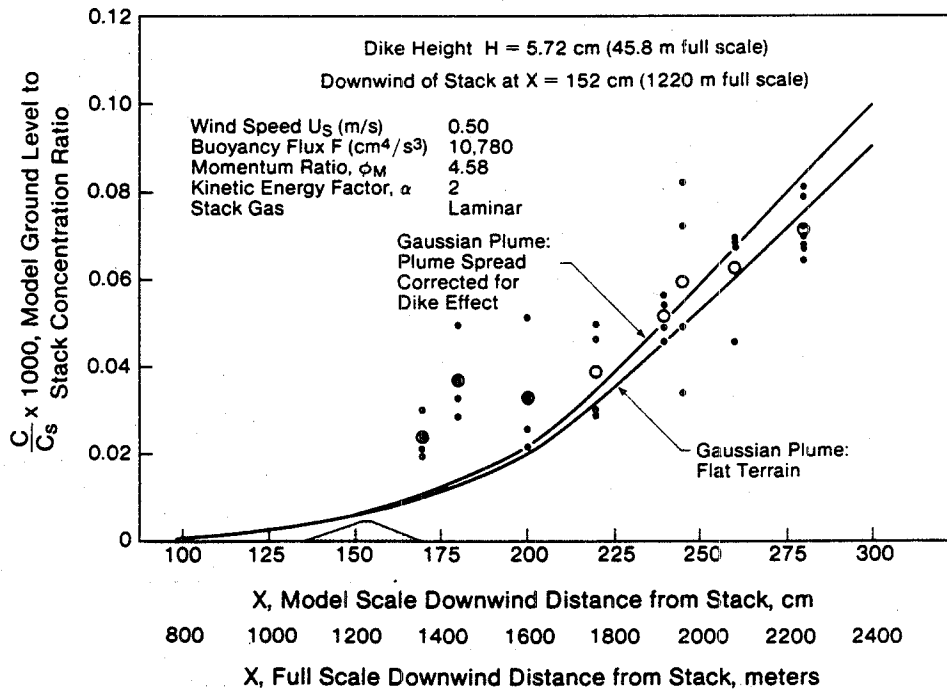
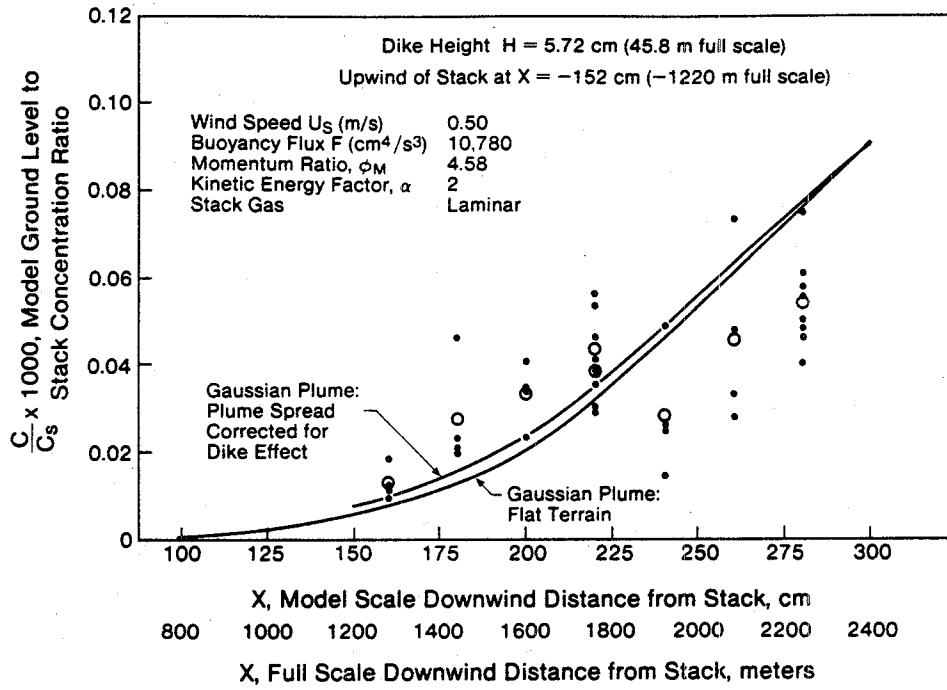


Figure 6-2 Ground Level Concentration With 45.8 m Dike Upwind and Downwind of Stack. $U_S = 16.7$ m/s, Plant at 197% Load

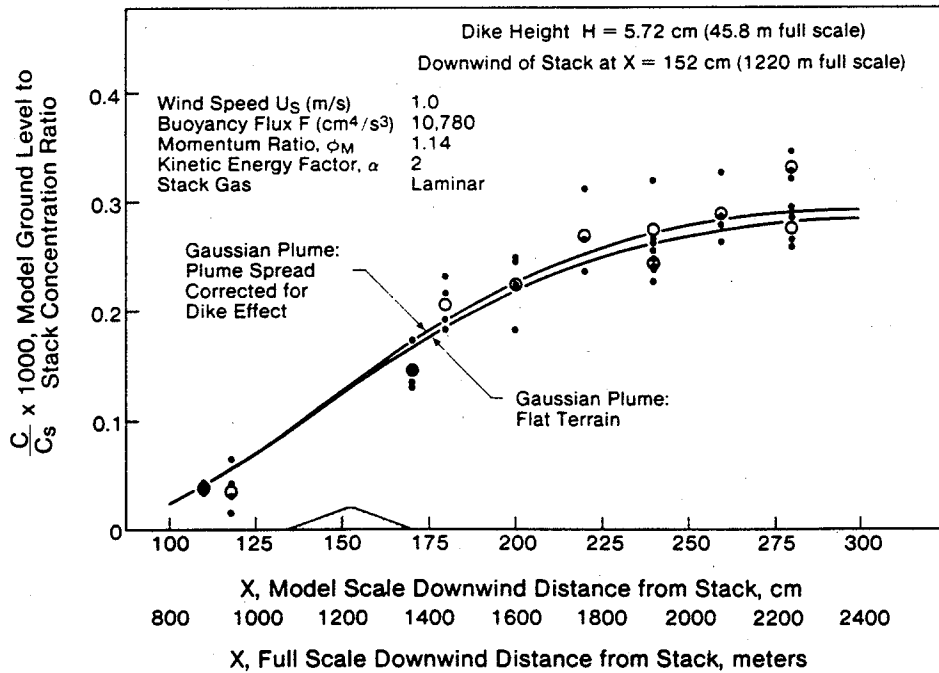
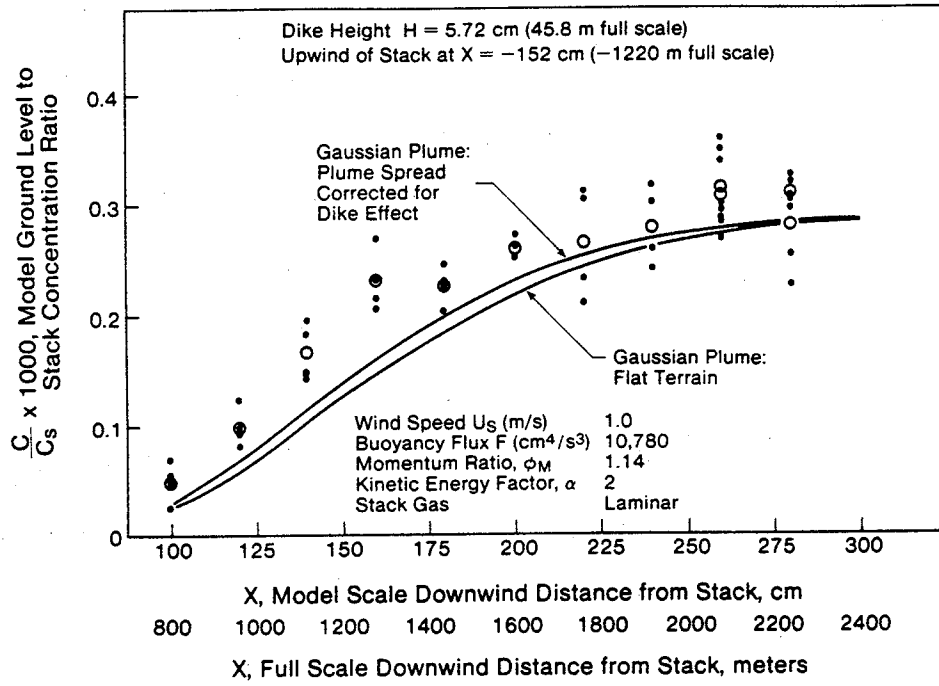


Figure 6-3 Ground Level Concentration With 45.8 m Dike Upwind and Downwind of Stack. $U_s = 33$ m/s, Plant at 197% Load

dike has only a small effect on ground level concentrations. This is not surprising in light of the flow visualization observations which determined that the Reynolds numbers are high enough to maintain attached flow on the downwind side of the dike.

The influence of dike height on ground level concentrations is non linear, increasing more rapidly than the dike height itself. This is evident in Figures 6-4 and 6-5 which show a considerable effect of dike height for the 94 meter dike. The lines shown on Figures 6-2 to 6-5 for the effect of dikes on ground level concentration were computed from a correction to the Gaussian plume model, developed using the measured data in these figures.

Gaussian Plume Influenced by Dike Wake Turbulence

The influence of the dike wake on plume spreading may be considered as an alteration of vertical and crosswind spreading rates σ_y and σ_z , and a change in plume rise in the effective source height h . The volume concentration at ground level for a reflected Gaussian plume is found from Equation (C-10) to be

$$C_o = \frac{Q (T_a/T_s)}{\pi U_s \sigma_y \sigma_z} \exp \left[- \frac{h^2}{2 \sigma_z^2} \right] \quad (6-1)$$

Taking a ratio of GLC with, and without a dike, results in

$$\frac{C_{o \text{ dike}}}{C_o} = \left(\frac{\sigma_y}{\sigma_y \text{ dike}} \right) \left(\frac{\sigma_z}{\sigma_z \text{ dike}} \right) \exp \left[- \frac{h^2}{2 \sigma_z^2} \left(\frac{h_{\text{dike}}^2}{h^2} \cdot \frac{\sigma_z^2}{\sigma_z \text{ dike}^2} - 1 \right) \right] \quad (6-2)$$

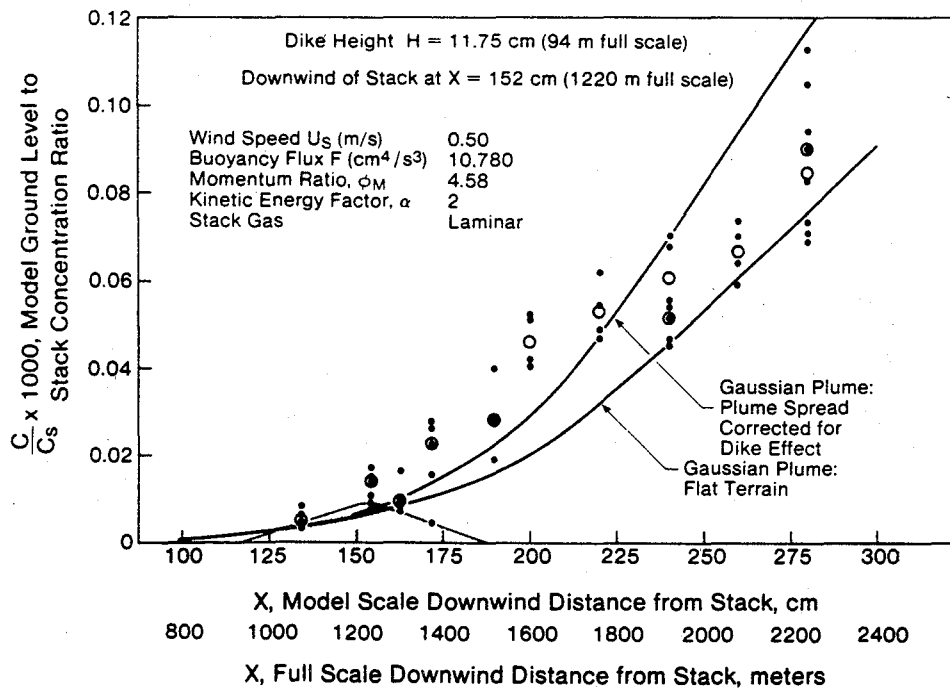
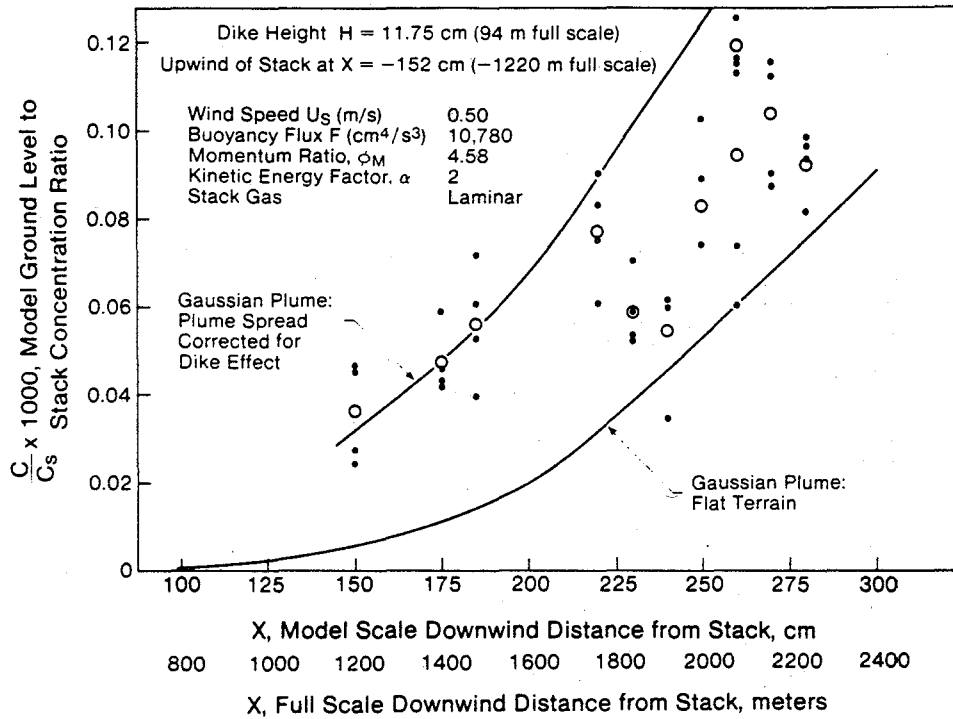


Figure 6-4 Ground Level Concentration With 94 m Dike Upwind and Downwind of Stack. $U_s = 16.7$ m/s, Plant at 197% Load

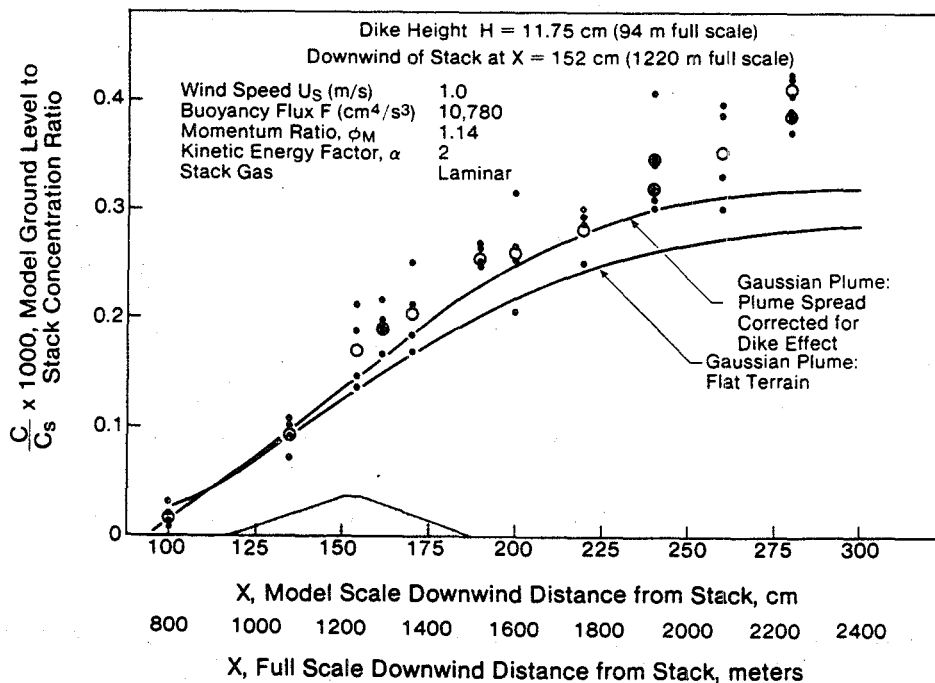
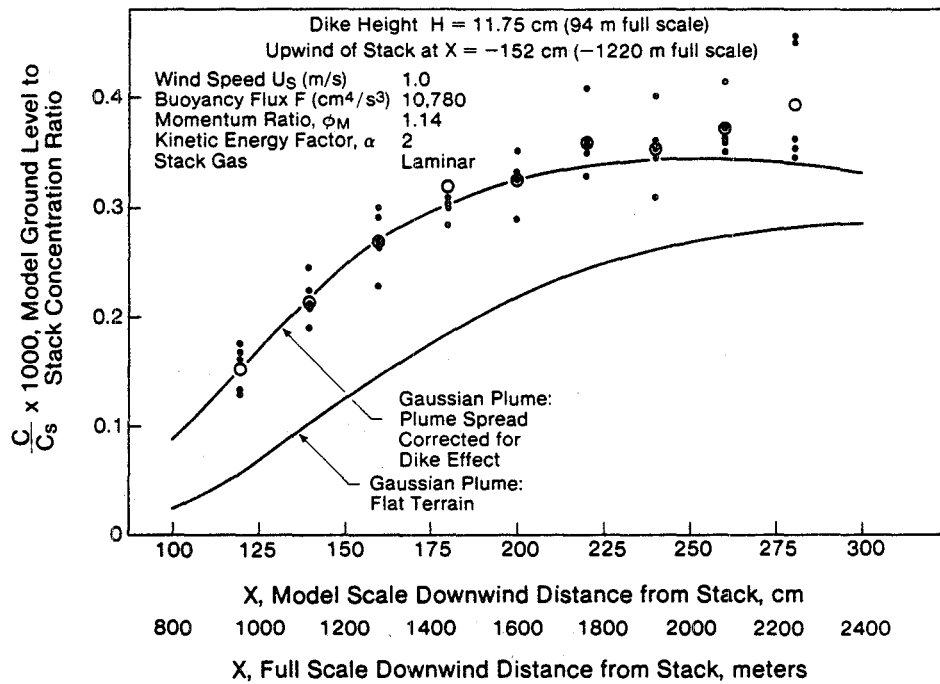


Figure 6-5 Ground Level Concentration With 94 m Dike Upwind and Downwind of Stack. $U_S = 33.4$ m/s, Plant at 197% Load

In order to produce a simple correction we will make the assumptions that:

- a.) The dike does not influence plume rise. From calculations of the effect of obstacles on streamline trajectories this assumption is justified if $h > 2 H$ approximately.
- b.) The dike turbulence has no effect on crosswind spread σ_y . This is certainly not physically realistic. However, other assumptions, such as an equal effect on both σ_y and σ_z were less successful in predicting observed effects. The assumption of constant σ_y used here has also been employed successfully by Huber and Snyder (1976) for the effect of building wakes on elevated plumes.

Using these simplifying assumptions, the effect of the dike is reduced to the form

$$\frac{C_{o \text{ dike}}}{C_o} = \eta \exp \left[- \frac{h^2}{2 \sigma_z^2} (\eta^2 - 1) \right] \quad (6-3)$$

where

$$\eta = \frac{\sigma_z}{\sigma_z \text{ dike}} \quad (6-4)$$

and C_o , σ_z and h are for flat terrain. The parameter η should not be interpreted literally as the ratio of plume spreads. Simplifications in the model, and even the use of a Gaussian plume in a wake may not be physically justified. Thus, η becomes a catch-all for necessary correction effects.

The problem of correcting for the downwind effects of the dike is reduced to specifying a functional form for η . We know that

because of the decaying nature of turbulence in the wake of an obstacle, that η must have a value of unity upwind of the dike, and far downwind from the dike. Because dike wake turbulence will increase vertical plume spreading, the form of Equation (6-4) shows that the dike wake η will be less than unity.

Values of η were experimentally determined using smoothed curves through the measured concentration profiles in Figures 6-1 to 6-5 for Test Series I. In addition, similar data for Test Series II from Figures 6-7 and 6-8 were also used. Ratios of these smooth measured concentrations were used to evaluate the left side of Equation (6-3). Values of η were then determined using computed values for flat terrain effective source height h , and vertical spread σ_z on the right side of Equation 6-3. These η values derived from experiment are shown in Figure 6-6. The values of η show a large scatter, however, it must be kept in mind that the predicted concentrations from Equation (6-3) are quite insensitive to the value chosen for η . Because of this insensitivity the measured η values can be satisfactorily represented by two straight line segments joining a constant value of

$$\eta_{low} = 1 - 1.1 \left(\frac{H}{h_s} \right)^3 \quad (6-5)$$

in the region

$$20 < \frac{X - X_{dike}}{H} < 60 \quad (6-6)$$

The general form of the function used in represent η is shown below

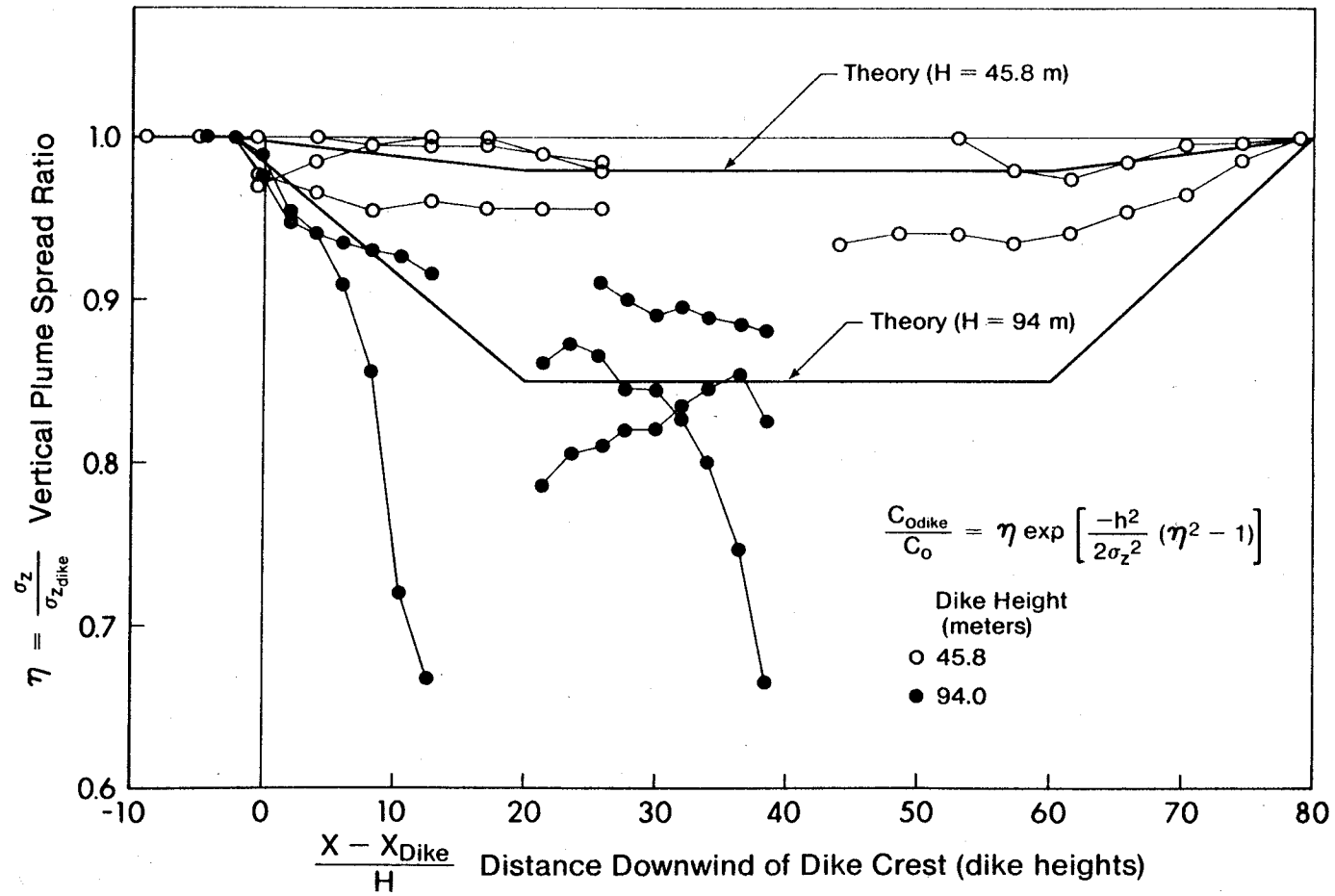
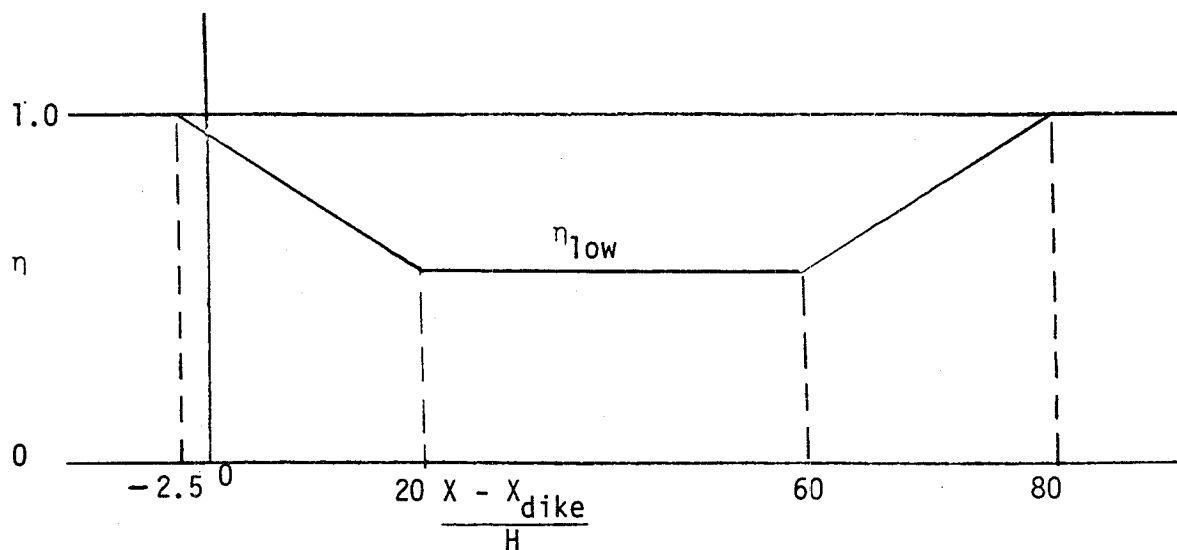


Figure 6-6 Effective Vertical Spread Ratio $\eta = \sigma_z / \sigma_{z \text{ dike}}$ for Downwind Effect of Dikes on Ground Level Concentration



The reader should note that the non-linear relationship between η and dike height H in Equation (6-5) is based on measurements with only two different dike heights. In addition, while the choice of source height h_s is the logical normalizing factor for dike height H in this equation, only a single stack height was actually tested. Equation (6-5) contains a good deal of guess-work in setting its functional form.

The predictions for the effect of dike height on ground level concentrations using Equations (6-3) and (6-5) are shown in Figures 6-2 to Figures 6-5. Considering the simplicity of the correction, it does an adequate job in predicting the effect of dike height on ground level concentrations from the main stack plume.

Turbulent Stack Gas Measurements - Test Series II

In order to more accurately model the plume rise, a second test series was undertaken using a mixing plug to produce turbulent flow at the stack exit. The scale factors appropriate for this second test series are given in Table 2-2, and the operating conditions are described in detail in Table 2-4. With a turbulent stack gas, and lower operating

tunnel speeds, more realistic operating conditions were obtained. For these conditions the stack emitted at 120 percent of rated load.

It was found that ground level profiles with a turbulent stack gas had exactly the same character as those for a laminar stack exit condition. For this reason, only two dike configurations were investigated in this second test series.

The first dike configuration was chosen as a "most realistic case." A full scale wind speed of 13.4 m/s was used, with a 45.8 m dike located downwind from the stack (wind from plant south). Concentration profiles with this dike configuration, and for flat terrain are shown in Figure 6-7. Ground level concentrations predicted using the vertical plume spread σ_z obtained from the entire vertical concentration profile, and from the lower half of the profile are also shown for flat terrain. There is no significant difference in ground level concentrations predicted from vertical plume spreads determined using these two different methods.

The second test configuration was chosen as a "most critical" case. A dike height of 94 m was used, with the dike located upwind of the main stack (wind from plant North). A full scale wind speed at stack height of 26.8 m/s was used to induce plume downwash and suppress plume rise. Ground level concentrations for flat terrain, and with this dike configuration, are shown in Figure 6-8. Comparison of turbulent and laminar stack gas conditions may be seen by comparing this with Figure 6-5. The results show very similar trends, but slightly different magnitudes due to the changes in stack operating conditions and wind speed.

Another interesting experiment was carried out by accident. A series of measurements for ground level concentration were obtained with

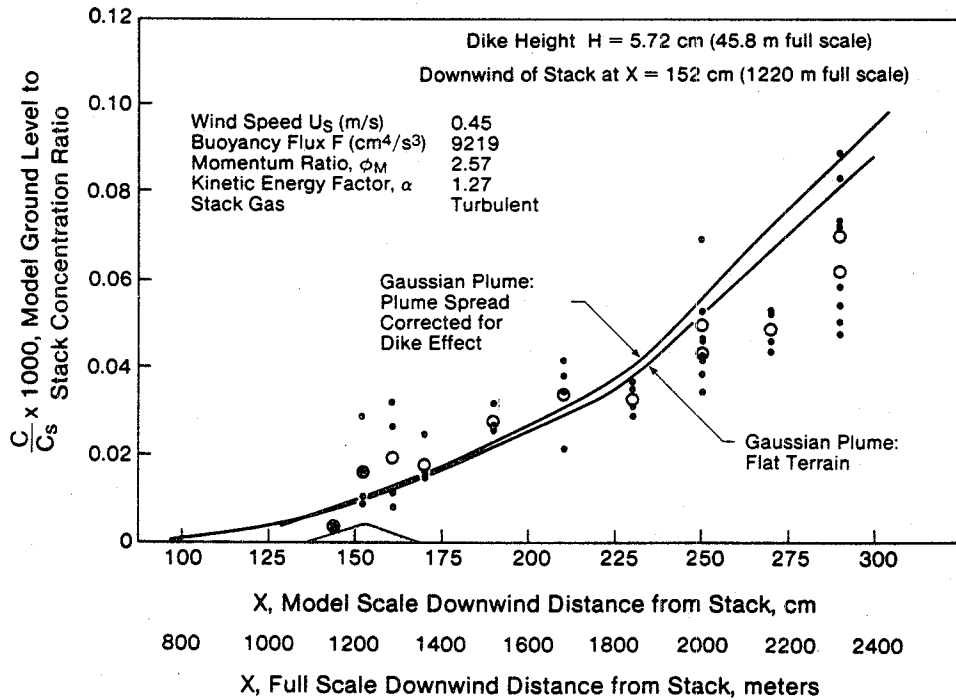
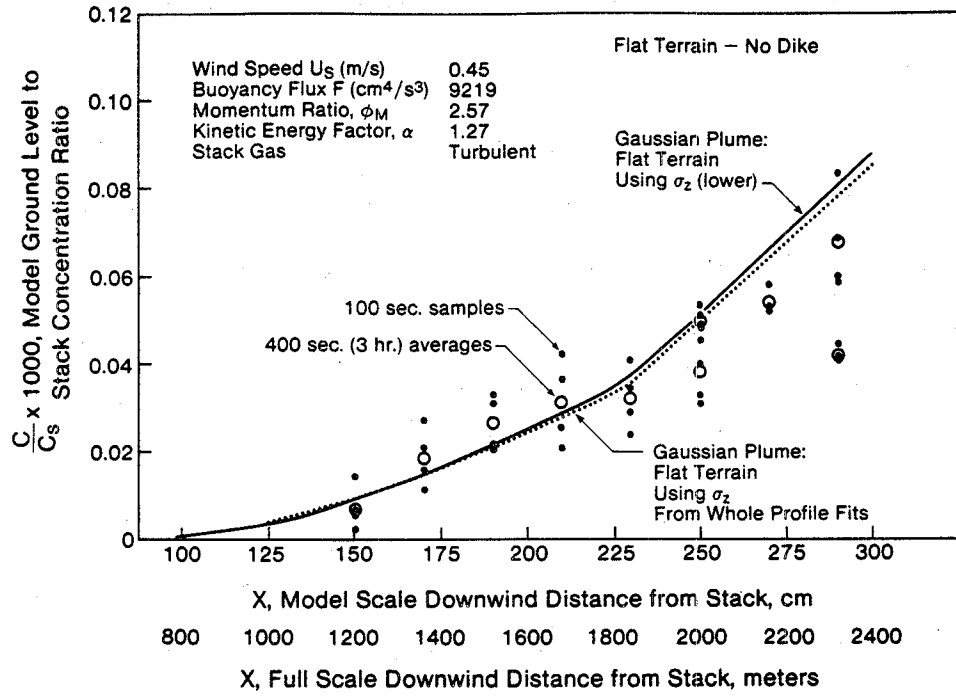


Figure 6-7 Comparison of Ground Level Concentration With and Without a 45.8 m Dike Downwind of Stack. $U_s = 13.4$ m/s Plant at 120% Load

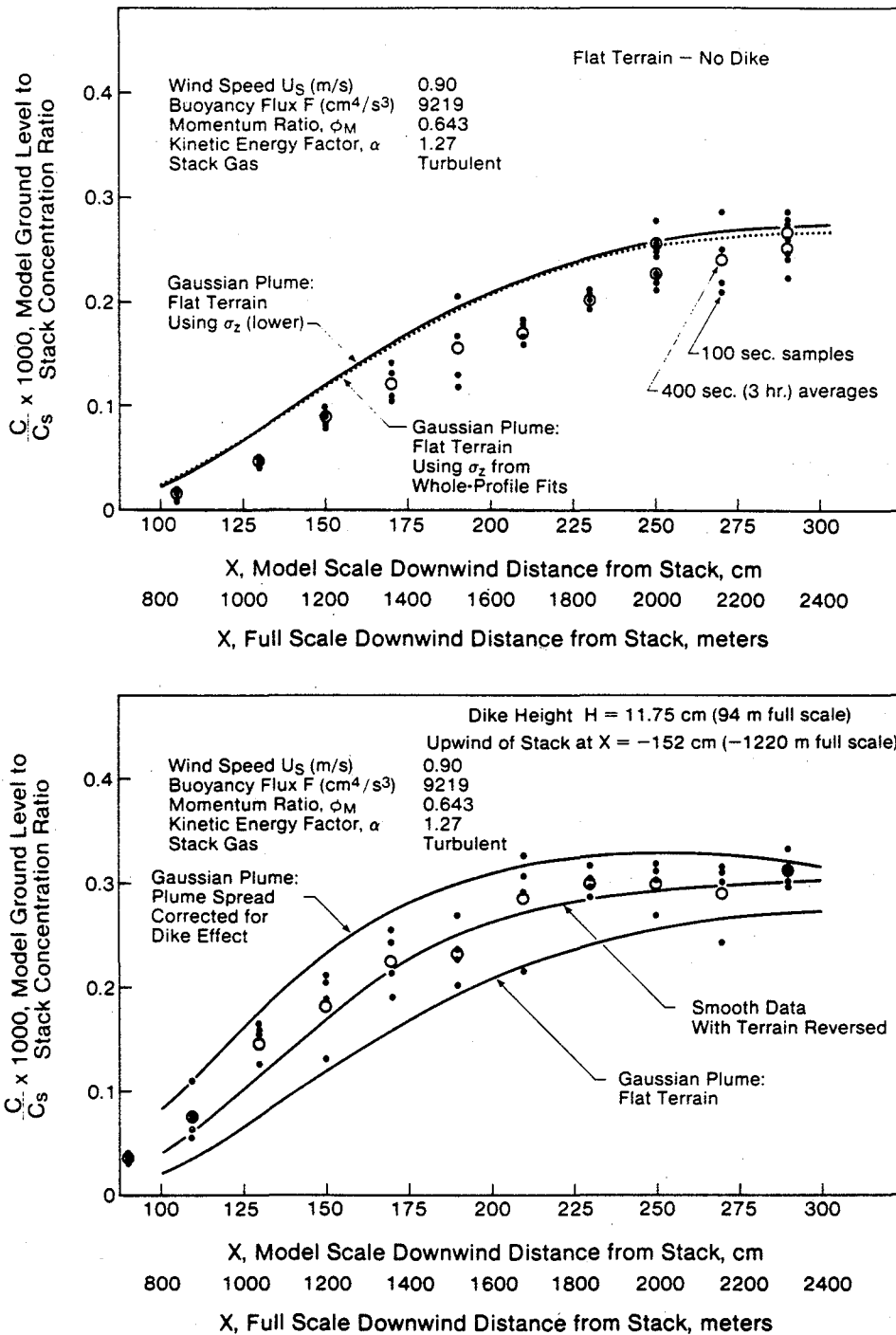


Figure 6-8 Comparison of Ground Level Concentration With and Without a 94 m Dike Upwind of Stack. $U_S = 26.8$ m/s Plant at 120% Load

the dike in the correct location, but the plant reversed. Ground level concentrations taken with the terrain reversed are shown as a smoothed data curve on Figure 6-7. Within the limits of experimental scatter, these measurements produced identical downwind concentrations to those observed with the terrain properly oriented. This invariance shows that the dispersion is not particularly sensitive to the location or orientation of structures on the plant site. For this reason, the results in this study may be applied to any plant site of similar size.

Maximum Ground Level Concentration

Although the present study did not attempt to locate critical wind speeds at which the global maximum ground level concentration would occur, it is interesting to see exactly what concentrations are predicted for the wind tunnel test conditions. We will consider here only Test Series II, which operated the stack at realistic emission rates.

At the lower wind speed of $U_s = 0.45$ m/s (13.4 m/s) the limited length of the wind tunnel test section prevented a direct measurement of maximum ground level concentration. The Gaussian plume model was used to extrapolate beyond the end of the test section to determine maximum concentrations. The predictions from the Gaussian plume model are shown in Figure 6-9. Plume spreading rates, corrections for self-generated spreading, and plume rise are all computed from correlations based on wind tunnel measurements. Figure 6-9 shows clearly that for realistic wind speeds, maximum ground level concentrations will be virtually unaffected by dike heights up to 45.8 meters.

Full scale maximum ground level concentrations are presented in Table 6-1 for the two conditions chosen as "most realistic" and "most

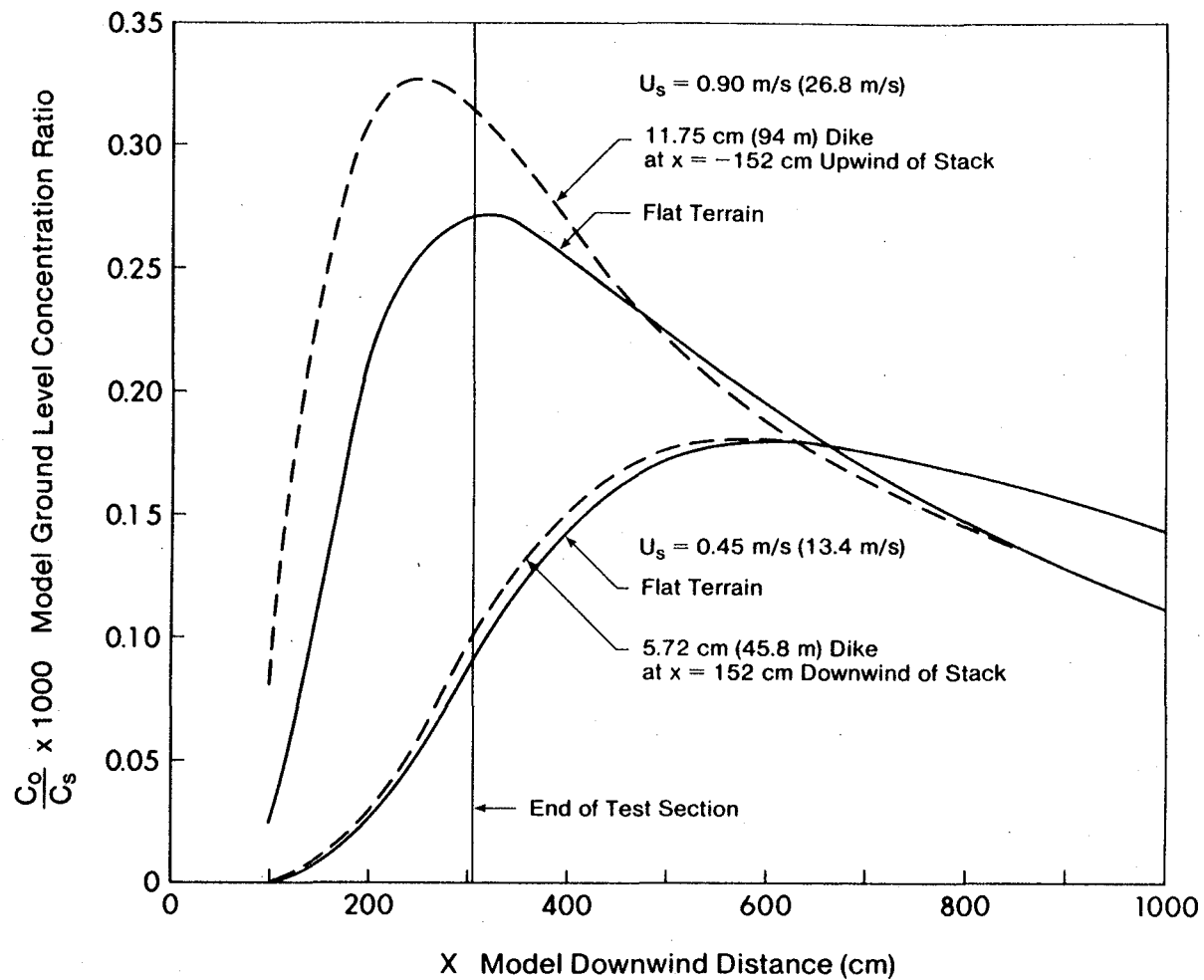


Figure 6-9. Predictions for Effects of Dikes under "Most Critical" Conditions with 94 m Upwind Dike and "Most Realistic" Conditions with 45.8 m Downwind Dike Plant at 120% Load

TABLE 6-1
MEASURED EQUIVALENT FULL SCALE
MAXIMUM GROUND LEVEL CONCENTRATIONS*

Condition	Wind Speed U_s m/s	Max. G.L.C. $C_{O,MAX}$ ppm	X_{max} m	Remarks
Flat terrain	13.4	0.18	4800	Extrapolated from wind tunnel data
45.8 m downwind dike	13.4	0.18	4800	
Flat terrain	26.8	0.27	2300	Measured in wind tunnel
94 m upwind dike	26.8	0.31	2000	

* Test Series II, operating at 120% of rated load with scaling factors from Table 2-2, $C_{sf} = 1553$ ppm at 505°K stack exit temperature.

critical." It must be emphasized that these values may not in fact correspond to the critical wind speed at which the global maximum of ground level concentration occurs. The values presented are based on smoothed experimental data, rather than predictions of the Gaussian plume model. However, these predictions will give values very close to those tabulated.

In summary, the measurements of ground level concentration presented in this chapter are in good agreement with a Gaussian plume model. A simple correction procedure based on a Gaussian plume gives a good estimate of the effect of various dike locations and heights on ground level concentrations.

CHAPTER 7

CONCENTRATION FLUCTUATIONS

The preceding portion of this report has dealt only with the time averaged concentration measured over sampling times which ranged from 100 to 400 seconds in the model, equivalent to 45 minutes to 3 hours full-scale. To properly assess the toxic affects of an emission, it is also necessary to characterize the short term concentration fluctuations which cause high concentration peaks which persist over a period of several minutes.

The measurements of concentration fluctuation described in this chapter were carried out to assess the peak ground level concentrations which would be exceeded a specified fraction of the time. A secondary objective was to establish the validity of a log-normal model for the probability density function. This log-normal distribution can then be used to predict peak-to mean concentration ratios for other sources, and at other positions in a stack plume. All of the measurements reported here were carried out at ground level.

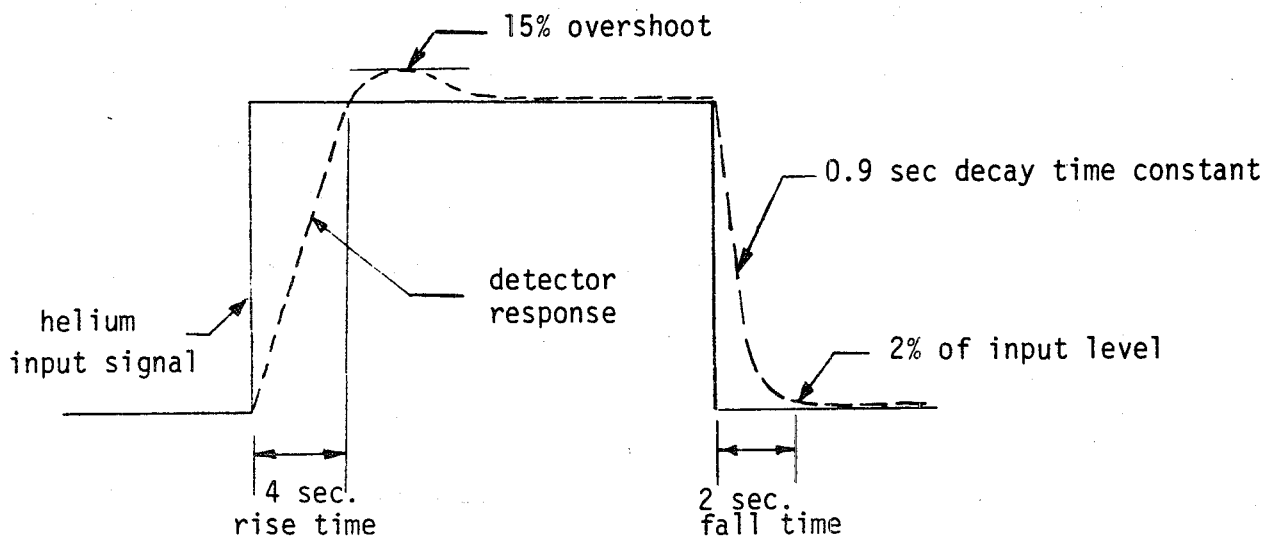
Detecting Fluctuating Concentration

Typical ground level concentrations downwind from the main stack in the wind tunnel model range from 20 to 150 gpm. Accurate measurement of the low mean concentration levels requires the use of a stable low-noise and drift, heated element detector located outside the tunnel in a constant temperature bath.

During measurements of mean concentration, this heated element detector also showed the ability to follow rapid time varying fluctuations. In tests with low level sources, the chart recorder output appeared to

correctly represent the expected trend in peak-to mean concentration ratios. A typical chart recorder output from the mean detector is shown in Fig. 7-1 where it can be seen that, as expected, the peak-to mean concentration decreases as the distance from the source becomes larger. Note that the time axis on the chart recorder outputs in Fig. 7-1 run from right to left on the page.

These measurements of concentration fluctuations suggest that the mean detector may also be suitable for measuring peak values. To determine the feasibility of this, the time response of the detector was measured using a suddenly applied and removed helium tracer gas signal. The results are shown in the sketch below.



From these measurements it is apparent that the rise and fall times of the detector system are not symmetric, with the detector requiring about twice as long to respond to an increasing helium signal, than to a decreasing one. The detector rise time behaves like an underdamped harmonic oscillator, with some overshoot. The decay time for a decreasing helium signal shows no evidence of this overshoot, indicating that it is more

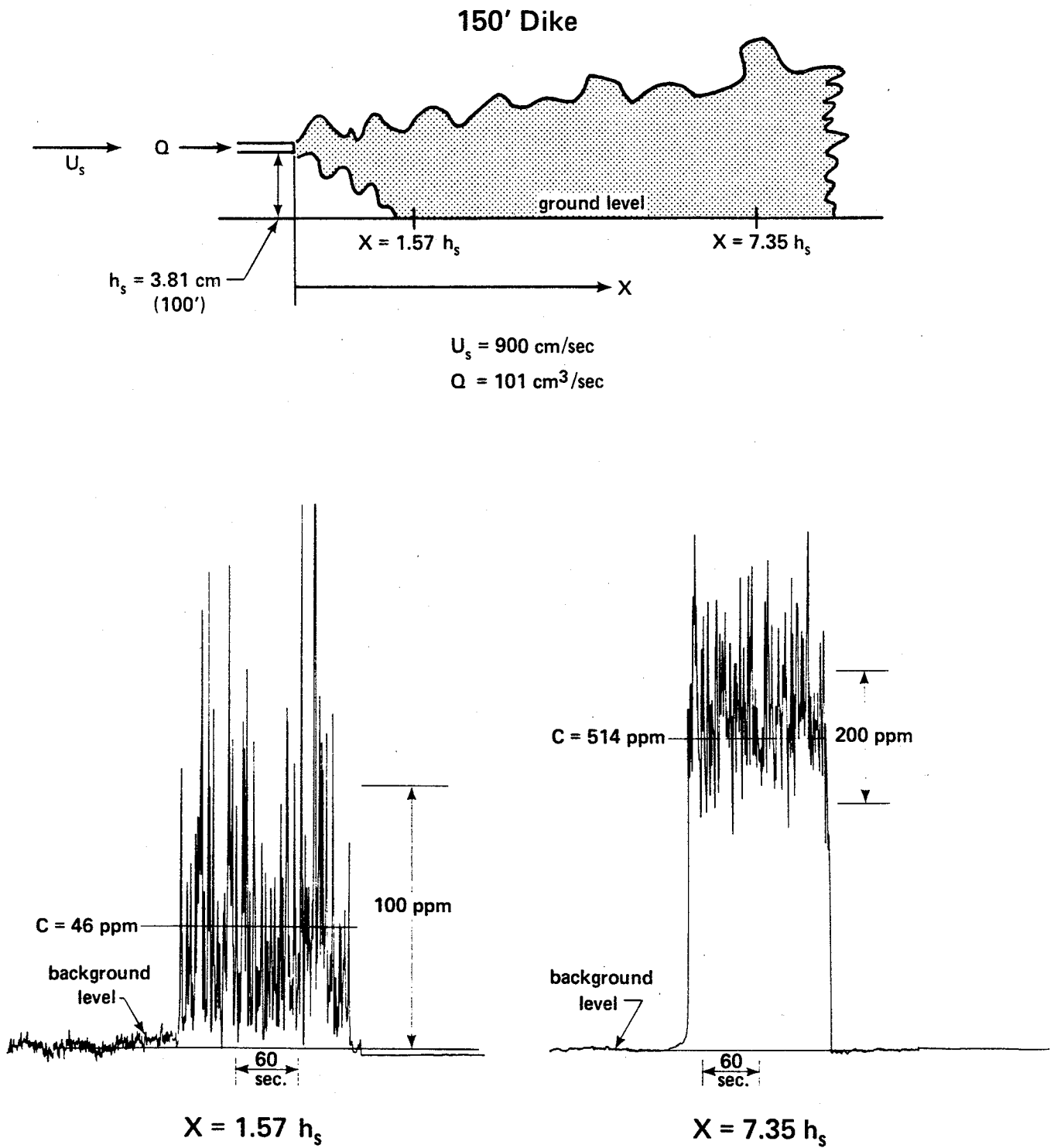


Figure 7-1. Concentration Fluctuations at Ground Level from Low Level Source in Dike Wake

than just the time constant of the system which changes for increasing and decreasing helium signals. This lack of symmetry in time response makes it unlikely that the mean detector would be suitable for quantitative measurements of frequency spectra of concentration fluctuations. On the credit side, the response characteristics show that any fluctuation peak which has a duration longer than 4 seconds in the wind tunnel will be accurately reproduced in amplitude by the mean detector. For the Syncrude buoyant plume study, the wind tunnel model time scale factor is 26.9:1. Applying this factor to the four second time response shows that the mean detector will accurately reproduce peak fluctuation levels which have a full scale duration longer than about 100 seconds. Concentration peaks of shorter duration will be reproduced, but with a reduced amplitude due to detector lag.

At first, it was thought that the slow rise time of the detector was due to the diffusion smearing of concentration fluctuations as they passed down the 7 meter long sample lines to the detector. However, when these lines were shortened to 0.5 meters, there was no measurable effect on the response characteristics. This anomalous result, was eventually explained using the theory of Taylor (1953) who found that the effective diffusion coefficient for longitudinal smearing in laminar tube flow is inversely proportional to the molecular coefficient of diffusion. This effect is caused because increased molecular diffusion prevents the velocity profile across the tube from causing convective smearing in the longitudinal direction. The high molecular diffusion coefficient of the helium tracer gas actually reduces concentration smearing effects in the sampling tubes, contrary to our intuition. Thus,

the time response shown in the previous sketch is due entirely to the detector filaments themselves, and cannot be improved by shortening the sample lines.

Because the mean detector accurately follows concentration fluctuations with time periods larger than a few minutes, this detector was considered to be suitable for concentration fluctuation measurements.

Experimental Techniques

In order to measure peak-to-mean concentration ratios it is necessary to determine the cumulative probability distribution function for concentration. The derivative of this cumulative distribution function is the probability density function, which is particularly useful in verifying analytical models for probability. To measure these distribution functions a Hewlett-Packard 3721A digital correlator was used. This correlator consists of an analog-to-digital convertor with variable sampling rate, and a digital discriminator system to sort measured concentrations into 100 discrete bins for probability analysis. The cumulative distribution function (cdf) and the probability density function (pdf) are displayed directly on a CRT display, and presented in hard copy on an x-y recorder.

The signal from the detector bridge was passed through a two stage amplification to provide an overall gain of 10,000. To provide the necessary low frequency response these amplifiers, and all subsequent signal processing were DC coupled. After amplification the instantaneous concentration signal was averaged using a voltage-to-frequency convertor over a 400 second sample time to determine the mean concentration \bar{C} . This same procedure was used for all mean concentration measurements

reported in previous chapters.

The instantaneous concentration signal was also processed by a DC coupled true RMS circuit, and averaged using a voltage-to-frequency convertor and 400 second sample time. By squaring this true RMS reading, and correcting for background noise and mean detector zero drift, the variance of concentration fluctuation $\overline{c'^2}$ was determined.

For both mean concentration and fluctuating variance, the helium supply to the source was turned off before and after the readings were taken to provide a base line to determine zero drift and background noise. The tests were conducted at two tunnel speeds of $U_s = 0.45$ m/s and 0.90 m/s. For both speeds the zero drift over a 400 second sample fell in the range from 5 to 10 ppm. For the concentration fluctuation measurements, the RMS noise to signal ratio was about 0.5 at the lower tunnel speed, and 0.2 at the high speed.

For probability density measurements the noise signal cannot be easily extracted from the probability measurements. Most of the noise in the concentration signal occurred at higher frequencies than the concentration fluctuations themselves, and a low-pass filter set at 5 Hz was used to remove most of the noise before passing the amplified signal to the digital correlator for measurements of probability density and cumulative distribution functions. For all measurements samples were digitized at intervals of 3.33 milliseconds, and were taken over a 435 second sample time for cumulative distribution functions. Because the probability density functions are the derivative of the cumulative distribution, a longer sample time was required, ranging from 745 to 1068 seconds. These sample times correspond to full scale values

of about 3 hours for cumulative distributions up to 8 hours for stable measurements of probability density functions.

The Log-Normal Probability Distribution

To understand the results of our measurements, and to extrapolate them to other downwind positions, an analytical function for the probability distribution is essential. Csanady (1973) presents a convincing argument for the use of a log-normal distribution for concentration fluctuations. The physical justification for a log-normal distribution is that concentration eddies are diluted by a random multiplicative factor rather than an additive factor. This means that the concentration observed at any instant is the product of many random factors. Thus, the logarithm of this product will produce a sum of random factors, resulting in a Gaussian distribution for the logarithm of concentration.

A realistic description of concentration fluctuations requires the intermittency of concentration to be considered. The intermittency is defined as the fraction of time that concentrations above zero will be measured. For the remaining fraction of the time the concentration remains at zero. Unfortunately, the slow time response of the detector used requires the concentration to fall to zero for several seconds before the detector would indicate an intermittent reading. This seldom occurs, and for all practical purposes the detector time response removes any zero concentration that may actually exist. Intermittent concentrations are certainly present in the wind tunnel, but cannot be dealt with in the present study due to detector limitations. For this reason, we will consider here only a non-intermittent log-normal concentration distribution.

The cumulative probability $\Omega(c)$ of the instantaneous concentration being less than c is from Csanady (1973),

$$\Omega(c) = \frac{1}{2} \left[1 + \operatorname{erf} \left[\frac{\ln\left(\frac{c}{c_{50}}\right)}{\sqrt{2} \sigma_l} \right] \right] \quad (7-1)$$

The derivative of this is the probability density

$$p(c) = \frac{1}{\sqrt{2\pi} \sigma_l c} \exp \left[-\frac{\left[\ln\left(\frac{c}{c_{50}}\right) \right]^2}{2 \sigma_l^2} \right] \quad (7-2)$$

which has the required property that

$$\int_0^{\infty} p(c) dc = 1.0 \quad (7-3)$$

The log standard deviation σ_l and the median concentration c_{50} are related to the mean \bar{c} and variance $\overline{c'^2}$ through the fluctuation intensity i_c

$$i_c = \sqrt{\frac{\overline{c'^2}}{\bar{c}}} \quad (7-4)$$

$$\sigma_l = \sqrt{\ln(1 + i_c^2)} \quad (7-5)$$

$$c_{50} = \bar{c} \exp \left[\frac{-\sigma_l^2}{2} \right] \quad (7-6)$$

Peak to mean ratios for the log-normal distribution are given by

$$\frac{c_f}{\bar{c}} = \exp \left[\sigma_l \left(E - \frac{\sigma_l^2}{2} \right) \right] \quad (7-7)$$

where

$$E = 2 \operatorname{erf}^{-1} \left[1 - 2f \right] \quad (7-8)$$

The concentration c_f is exceeded a fraction "f" of the time.

Ground Level Fluctuation Measurements

A typical probability density function (pdf) and the chart recorder signal output taken over the same time period is shown in Fig. 7-2. These measurements were carried out at a distance of 290 cm, a full scale equivalent of 2320 meters downwind from the main stack. At low concentrations this measured pdf does not follow a log-normal distribution. No explanation could be found for the appearance of the second maximum in the measured pdf. This maximum did not appear on other measured probability density functions. Note that the averaging time for the measured probability density in Fig. 7-2 was 1068 seconds, equivalent to a full scale time of about eight hours.

A comparison of measured probability distributions with and without the dike are shown in Figs. 7-3 and 7-4. The zero drift over 435 second sampling times used for the cumulative distribution function was about 4% of the mean concentration for the data shown in these two figures. Zero drift was always positive throughout a sample interval.

Peak-To-Mean Ratios

Median and peak concentrations, exceeded 5% and 10% of the time were extracted graphically from the measured cumulative distribution functions. Table 7-1 summarizes all of the results, and shows that although the

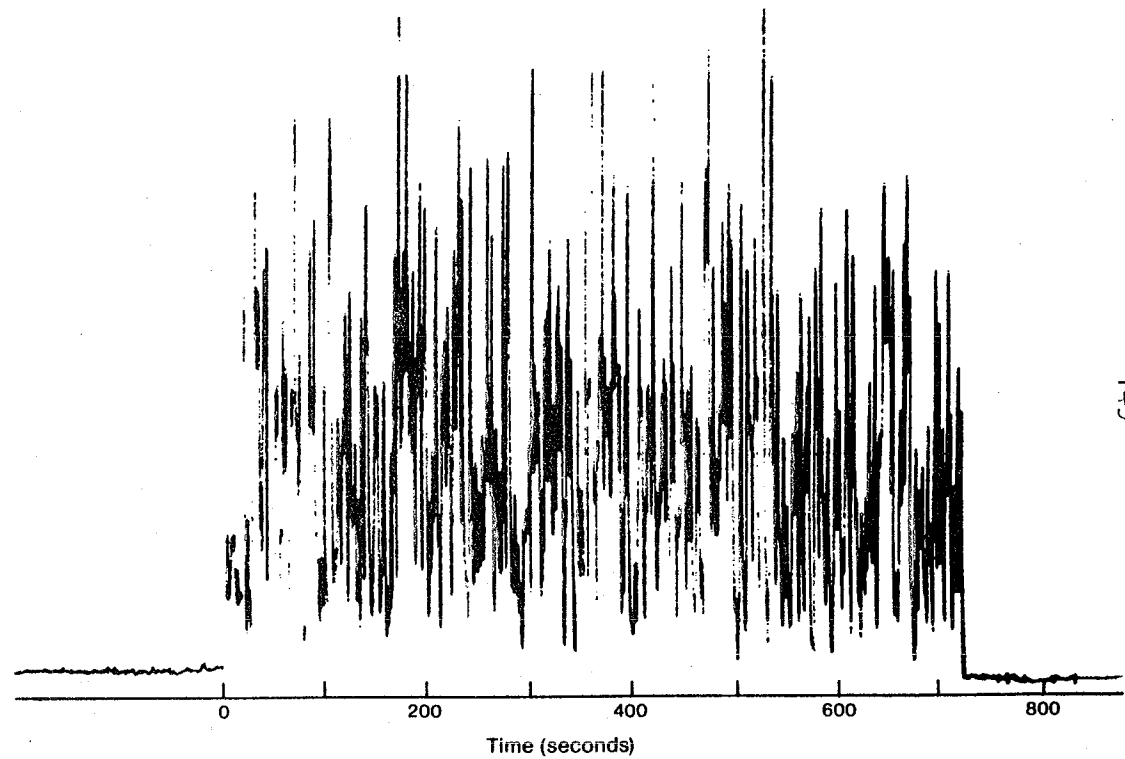
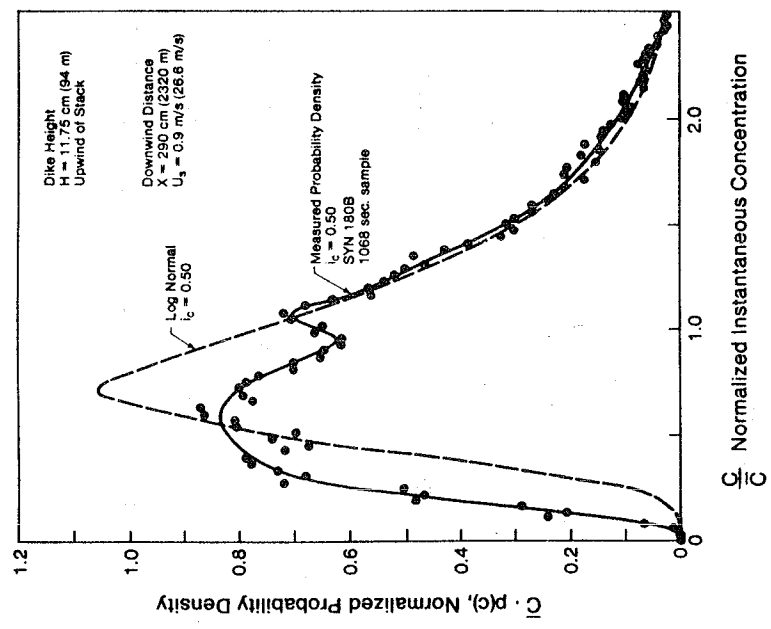


Figure 7-2. Probability Density and Observed Concentration Fluctuations from Main Stack Plume with 94 m High Dike Upwind

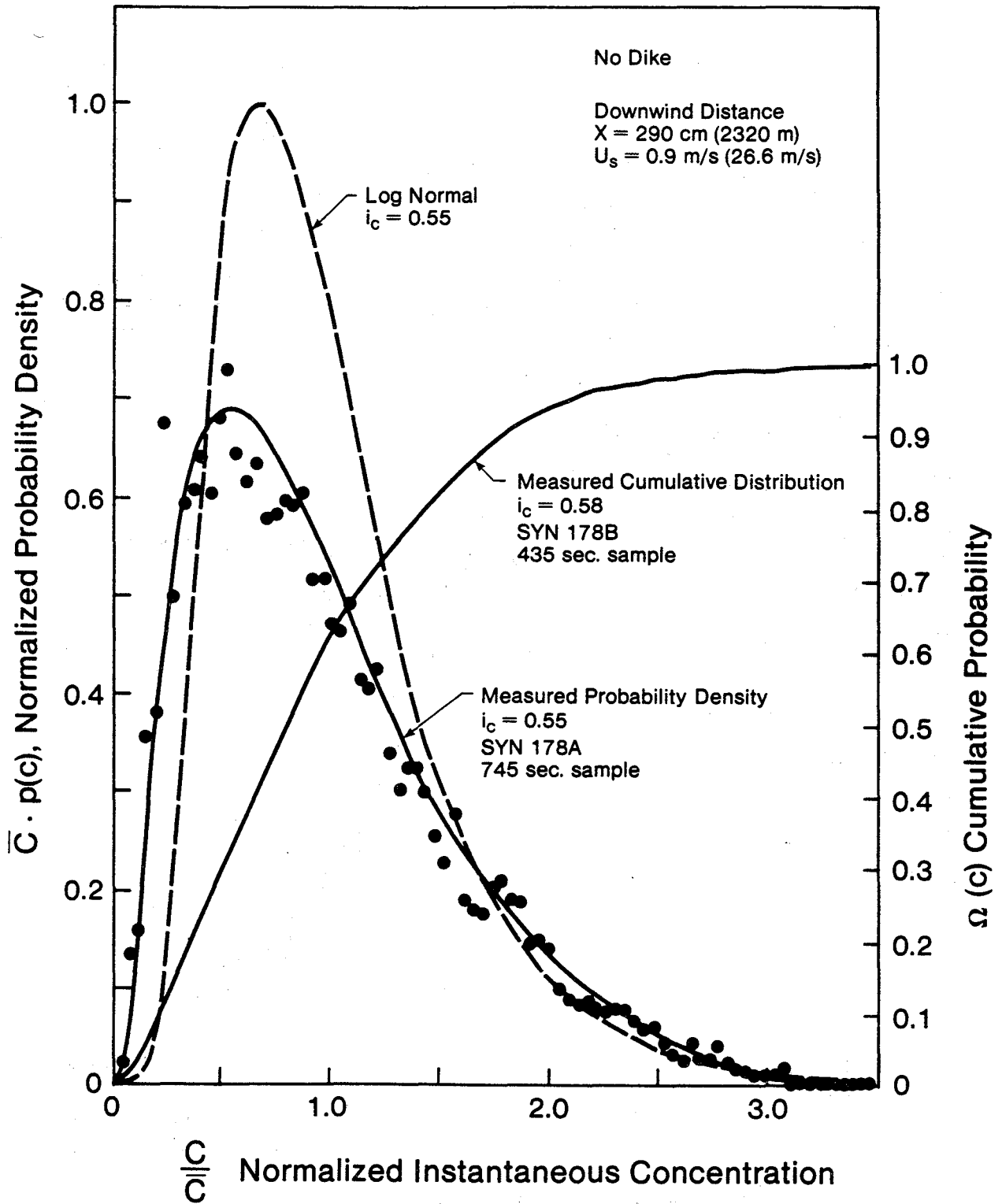


Figure 7-3. Ground Level Concentration pdf for Main Stack Plume with Flat Terrain

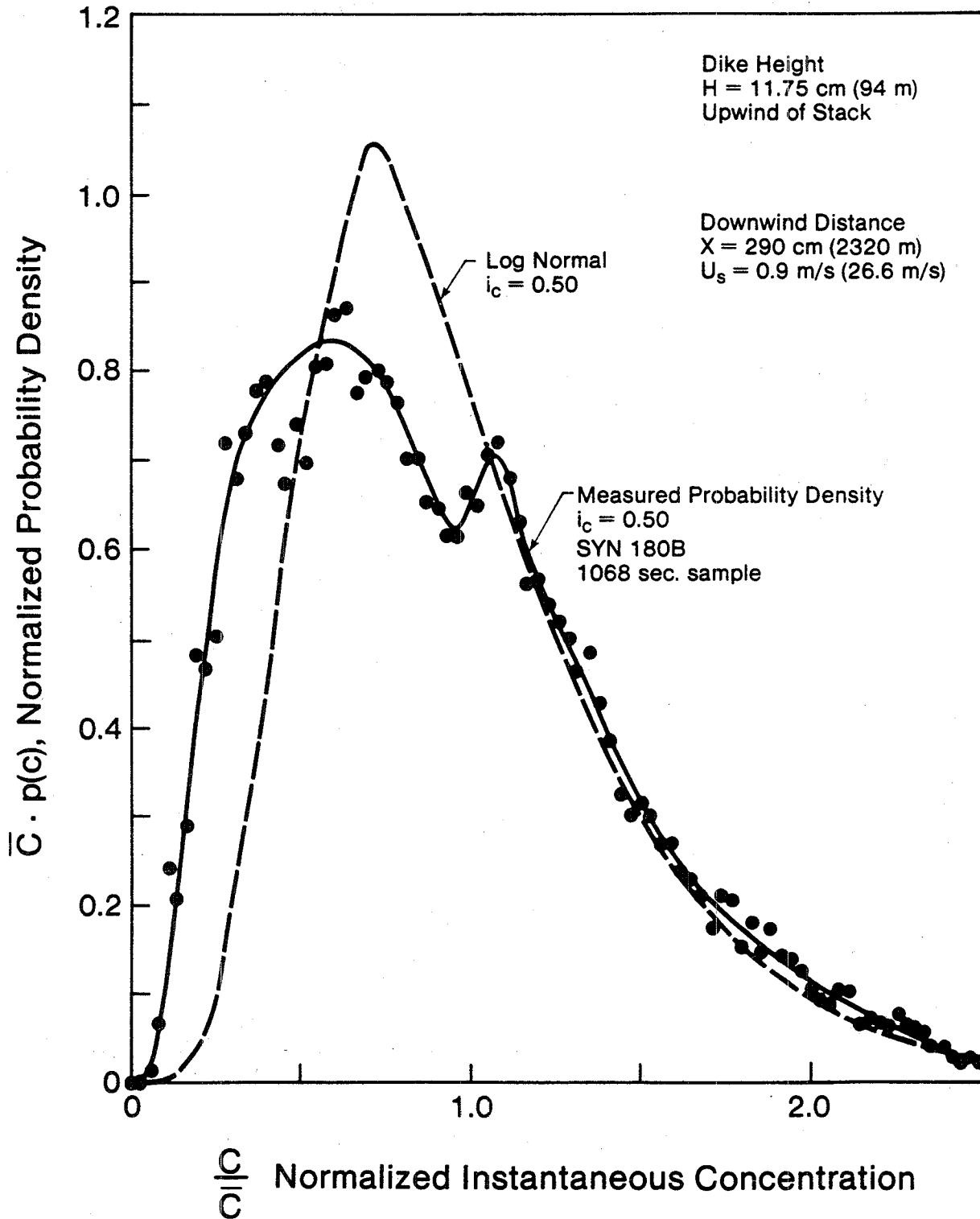


Figure 7-4. Ground Level Concentration pdf for Main Stack Plume with 94 m High Dike Upwind

TABLE 7-1
CONCENTRATION FLUCTUATION AND PEAK TO MEANS AT GROUND LEVEL

DIKE CONFIGURATION**	WIND SPEED U_s	RUN NUMBER SYN-	MODEL DOWNWIND DISTANCE X , cm	MODEL CONCENTRATION, ppm			FLUCTUATION INTENSITY i_c	5% PEAK TO MEAN RATIO* $\frac{C_5}{\bar{C}}$	10% PEAK TO MEAN RATIO* $\frac{C_{10}}{\bar{C}}$	RATIO OF LOG NORMAL TO MEASURED PEAK-TO-MEAN	
				MEAN \bar{C}	RMS $\sqrt{\frac{C^2}{T^2}}$	MEDIAN* C_{50}				10% PEAKS	5% PEAKS
NO DIKE	0.45 m/s (13.4)	177A	290	25	25	20	1.06	3.55	2.63	0.79	0.81
		177B	290	20	14	17	0.80	2.70	2.04	0.94	0.92
		177C	200	17	15	9	1.34	2.68	2.04	1.07	1.19
H = 5.72 cm (45.7 m) DOWNWIND @ $X = 152.4$ cm	0.45 m/s (13.4)	179A	290	33	21	43	0.60	2.10	1.80	0.97	1.02
		179B	290	41	33	39	0.76	2.52	1.89	1.00	0.96
		179C	200	17	12	13	0.90	2.93	2.37	0.84	0.90
NO DIKE	0.90 m/s (26.8)	178A	290	60	58	-	0.55	-	-	-	-
		178B	290	65	59	83	0.64	2.18	1.87	0.95	1.01
		178C	200	62	62	54	0.77	2.93	2.36	0.80	0.83
		178D	150	50	45	14	1.40	3.60	2.49	0.89	0.90
H = 11.75 cm (94 m) UPWIND @ $X = -152.4$ cm	0.90 m/s (26.8)	180A	290	78	55	140	0.50	2.01	1.67	0.98	0.97
		180C	220	78	62	108	0.61	2.16	1.79	0.98	1.00
		180D	150	72	63	56	0.84	2.79	2.19	0.89	0.91
		180E	150	76	69	-	0.85	-	-	-	-

* From measured cumulative distribution function

** Full scale values shown in brackets

152

probability density function is not log-normal at low concentrations, that peak-to-mean concentrations are very well predicted using a log-normal distribution. The theoretical log-normal peak-to-mean values are typically 10% less than those measured. This trend is expected because some Gaussian noise undoubtedly was present in the measured distribution functions, while the noise signal was removed in computing the theoretical log-normal peak-to-means. On the whole, these are very encouraging results, and indicate that a log-normal distribution is adequate for predicting peak-to-mean values at ground level.

Dike Effects on Fluctuation Intensity

In order to apply the log-normal cumulative distribution function to predict peak concentrations it is necessary to specify the mean concentration \bar{C} and the fluctuation intensity i_c defined in equation 7-4. Measured values of the fluctuation intensity are shown in Fig. 7-5. From these measurements we can conclude:

1. The fluctuation intensity decreases with downwind distance. This behavior is expected, because as downwind distance increases the ground level receptor lies a smaller number of standard deviations off the plume center line. Because fluctuation intensity increases with distance off the plume center line, it should decrease at ground level with increasing downwind distance.
2. Higher fluctuation intensities were observed at the lower wind speed. At this lower speed, plume rise causes the same downwind receptor point to lie further off the plume center line, thus increasing fluctuation intensity. Fig. 7-6 shows that when the downwind distance is normalized with

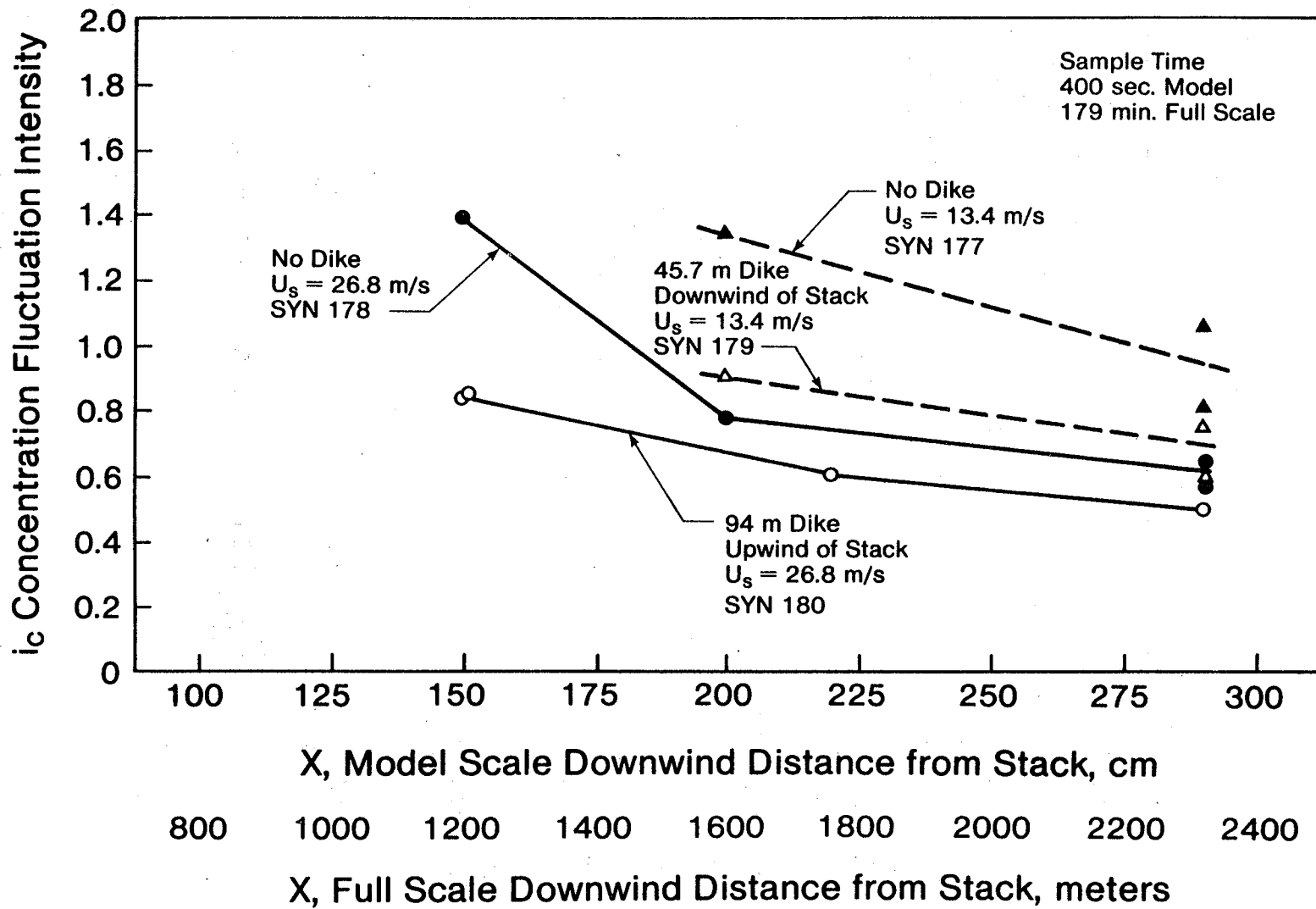


Figure 7-5. Variation of Concentration Fluctuation Intensity with Wind Speed and Dike Configuration

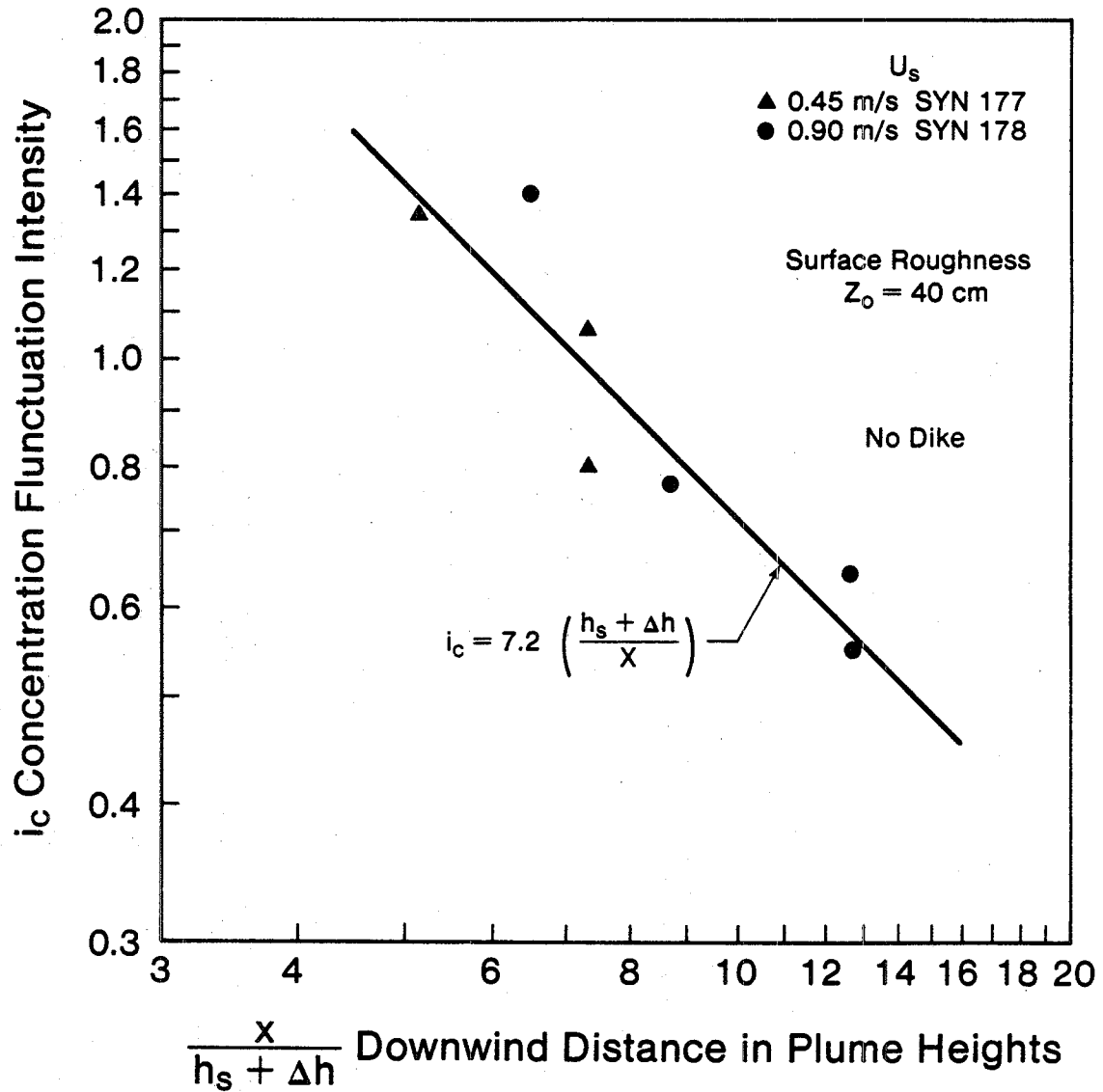


Figure 7-6. Decay of Fluctuation Intensity at Ground Level with Normalized Downwind Distance for Flat Terrain

effective source height, fluctuation intensities at the two wind speeds fall on the same line. In the absence of turbulence from the tailings pond dike this decay of fluctuation intensity with downwind distance is given by the empirical relation

$$i_c = 7.2 \left(\frac{h_s + \Delta h}{x} \right) \quad (7-9)$$

The values from this equation are consistent with the recommendations of Csanady (1973) who recommends $i_c = 0.35$ for "smooth" terrain and $i_c = 0.80$ for "rough" terrain with neutral atmospheric stability.

3. The influence of turbulence from the two different tailings pond dike configurations is to reduce the fluctuation intensity as shown on Fig. 7-5. The turbulence in the dike wake causes the mean concentration to increase more than the fluctuating concentration variance, and therefore decrease the fluctuation intensity. As a rough estimate for design purposes, it is suggested that the fluctuation intensities predicted by equation 7-9 be reduced by about 20 percent to account for the influence of the tailings pond dike wake. It should be kept in mind that while the peak-to-mean concentration ratio will decrease due to the influence of the tailings pond dike, the magnitude of the peak concentration will in fact increase because of the increased mean concentration level.

It should be kept in mind that the present study was unable to investigate the effect of concentration intermittancy due to the limitations of detector time response. In the full-scale large periods of zero concentration are expected because of crosswind meandering of the plume. In predicting peak-to-mean concentrations, wind statistics would be used to estimate the periods when a given receptor will have zero concentration. In addition to plume meandering, intermittent concentrations are found in all diffusion plumes. However, it is expected that the zero concentration readings will mostly result from plume meandering, and not from these short time zero periods due to inherent intermittancy.

REFERENCES

- Alberta Environment (1978) "Guidelines for Plume Dispersion Calculations"
Standards and Approvals Division, Dept. of Environment, Edmonton,
Alberta, Canada.
- Baines, W.D. and Peterson, E.G. (1951), "An Investigation of Flow Through
Screens" Trans. A.S.M.E. 73 pp. 467-480.
- Bradshaw, P. and Wong, F.Y.F. (1972), "The Reattachment and Relaxation of
Turbulent Shear Layer", J. Fluid Mech. 52, 113-135. Part 1.
- Briggs, G.A. (1969), Plume Rise, U.S. Atomic Energy Commission.
- Briggs, G.A. (1970), "Some Recent Analyses of Plume Rise Observations",
- Briggs, G.A. (1975) "Plume Rise Predictions" in Lectures on Air Pollution and
Environmental Impact Analyses American Met. Soc. Workshop, Sept.
1975, Boston, Mass.
- Cermak, J.E. (1975), "Applications of Fluid Mechanics to Wind Engineering--
A Freeman Scholar Lecture", Jour. Fluids Eng., Trans. ASME 97,
pp. 9-38.
- Counihan, J. (1969), "An Improved Method of Simulating an Atmospheric
Boundary Layer in a Wind Tunnel", Atmospheric Environment 3,
pp. 197-214.
- Counihan, J., Hunt, J.C.R. and Jackson, P.S. (1974), "Wakes Behind Two-
Dimensional Surface Obstacles in Turbulent Boundary Layer", J.
Fluid Mech. 64, 529-563. Part 3.
- Counihan, J. (1975), "Adiabatic Atmospheric Boundary Layers: A Review
and Analysis of Data from the Period 1880-1972", Atmospheric
Environment 9, pp. 871-905.
- Csanady, G.T. (1973), Turbulent Diffusion in the Environment, Reidel.
Proc. Second Int. Clean Air Congress, Washington D.C.

- Djurfors, S. and Netterville, D. (1978) "Buoyant Plume Rise in Nonuniform Wind Conditions" Jour. of Air Pollution Control. Assn. 28 pp. 780-784.
- Eliseev, V.S. (1973), "Stereophotogrammetric Investigation of the Air Flow in the Boundary Layer of the Atmosphere Above a Hill", from Berlyand, M. (ed.) Air Pollution and Atmospheric Diffusion, John Wiley and Sons, pp. 95-108.
- Gifford, F.A. (1968), "An Outline of Theories of Diffusion in the Lower Layers of the Atmosphere, Chap. 3 in Slade, D.H. (ed.) Meteorology and Atomic Energy 1968, U.S. Atomic Energy Comm., pp. 65-116.
- Golden, J. (1961), "Scale Model Techniques", M.S. Thesis, College of Engineering, New York University.
- Good, M.C. and Joubert, P.N. (1968), "The Form Drag of Two Dimensional Bluff Plates Immersed in a Turbulent Boundary Layer" Jour. Fluid Mechanics 31 part 3, pp. 547-582.
- Hay, J.S. and Pasquill, F. (1959), "Diffusion from a Continuous Source in Relation to the Spectrum and Scale of Turbulence", Advances in Geophysics 6, Frenkiel and Sheppard (eds.), Academic Press, pp. 345-365.
- Hinze, J.O. (1975), Turbulence, 2nd ed., McGraw Hill, pp. 48-55 and pp. 427-459.
- Hoult, D.P. and Weil, J.C. (1972), "Turbulent Plume in a Laminar Cross Flow", Atmospheric Environment 6, pp. 513-531.
- Hoult, D.P., O'Dea, S.R., Touchton, G.L. and Ketterer, R.J. (1977), "Turbulent Plume in a Turbulent Cross Flow: Comparison of Wind Tunnel Tests with Field Observations", Jour. Air Poll. Control Assn. 27, pp. 56-60.

- Huber, A.H. and Snyder, W.H. (1976), "Building Wake Effects on Short Stack Effluents", Proc. Third Symposium on Atmospheric Turbulence, Diffusion and Air Quality; Raleigh, N.C., Oct. 1976, American Meteorological Soc., Boston.
- Huber, A.H., Snyder, W.H., Thompson, R.S. and Lawson, R.E. (1976), "Stack Placement in the Lee of a Mountain Ridge", U.S. EPA Rept.: EPA-600/4-76-047, Research Triangle Park, N.C.
- Isumov, N., Jandali, T. and Davenport, A.G. (1976), "Model Studies and the Prediction of Full Scale Levels of Stack Gas Concentration", Jour. Air Poll. Control Assn. 26, pp. 956-964.
- Isumov, N. and Tanaka, H. (1979) "Wind Tunnel Modelling of Stack Gas Dispersion - Difficulties and Approximations" Proc. Fifth Int. Conf. on Wind Engineering, Colorado State University, Fort Collins, U.S.A. July 1979.
- Ludwig, G.R. and Skinner, G.T. (1976), "Wind Tunnel Modeling Study of the Dispersion of Sulphur Dioxide in Southern Allegheny County, Pennsylvania", U.S. Environmental Protection Agency Report EPA 903/9-75-019, pp. 3-16.
- Mueller, T.J. and Robertson, J.M. (1963), "Modern Developments in Theoretical Applied Mechanics", 1, 326.
- Murphy, C.R. (1970), "On the Mean Path of a Buoyant Chimney Plume in a Non-Uniform Wind", Jour. Applied Meteorology 9, pp. 603-611.
- Murray, W. and Morrow, M. (1977), "The Vertical Wind Profile at Mildred Lake, Alberta", Syncrude Professional Paper 1977-1.
- Nagabhushanaiah, H.S. (1962), "Separation Flow Downstream of a Plate Set Normal to a Plane Boundary", Ph.D. Dissertation, Colorado State University, Fort Collins, Color.

- Ogawa, Y. (1976), "The Effects of a Single Building on Diffusion--A Combined Laboratory and Field Study", ASME Paper 76-WA/FE-27, Jour. of Fluids Engineering, in Press.
- Panofsky, H.A. (1973), "The Boundary Layer Above 30M", Boundary-Layer Met. 4, pp. 251-264.
- Pasquill, F. (1961), "The Estimation of the Dispersion of Windborne Material", Meteorological Magazine 90, pp. 33-49.
- Pasquill, F. (1975), Atmospheric Diffusion, Halsted Press, pp. 365-378.
- Pasquill, F. (1976), "Atmospheric Dispersion Parameters in Gaussian Plume Modeling, Part II: Possible Requirements for Change in the Turner Workbook Values", U.S. Environmental Protection Agency Rept. EPA-60014-76-030b.
- Petryk, S. and Brundrett, E. (1967), Department of Mechanical Engineering, University of Waterloo, Research Report No. 4.
- Plate, E.J. and Lin, C.M. (1964), "The Velocity Field Downstream from a Two-Dimensional Model Hill", Part 1. Colorado State University, Fort Collins, Colo., Technical Report No. CER65EJP-CWL41.
- Ricou, F.P. and Spalding, D.B. (1961), "Measurements of Entrainment by Axisymmetrical Turbulent Jets", Jour. Fluid Mechanics 11, pp. 21-32.
- Robins, A.G. (1977a), "The Development and Structure of Simulated Neutrally Stable Atmospheric Boundary Layers", Central Electricity Generating Board, Marchwood Engineering Laboratories, Southampton, Report R/M/R246.
- Robins, A.G. (1977b), "Plume Dispersion from Ground Level Sources in Simulated Atmospheric Boundary Layers", CERL Report R/M/R245.
- Robins, A.G. (1977c), "Wind Tunnel Modelling of Plume Dispersion", CERL Report R/M/R247.

- Robins, A.G. and Castro, I.P. (1977), "A Wind Tunnel Investigation of Plume Dispersion in the Vicinity of a Surface Mounted Cube--II. The Concentration Field", *Atmospheric Environment* 11, pp. 299-311.
- Roshko, A. (1961) "Experiments on the Flow Past a Circular Cylinder at Very High Reynolds Number" *Jour. Fluid Mechanics* 10 pp. 345-356.
- Rouse, H., Yih, C.S. and Humphreys, H.W. (1952), "Gravitational Convection from a Boundary Source", *Tellus* 4, pp. 201-210.
- Sachs, P. (1972), Wind Forces in Engineering, Pergamon Press, Chap. 3, pp. 59-94.
- Singer, I.A. and Smith, M.E. (1966), "Atmospheric Dispersion at Brookhaven National Laboratory", *Int. J. Air and Water Pollution* 10, pp. 125-135.
- Slawson, P.R. (1978) "Observations and Predictions of Natural Draft Cooling Tower Plumes at Paradise Steam Plant: *Atmospheric Environment* 12 pp. 1713-1724.
- Slawson, P.R. and Csanady, G.T. (1971) "The Effect of Atmospheric Conditions on Plume Rise: *Jour. Fluid Mechanics* 47 part 1 pp. 33-49.
- Smith, M. (ed.) (1973), Recommended Guide for the Prediction of the Dispersion of Airborne Effluents, Am. Soc. of Mech. Eng., 2nd ed.
- Snyder, W.H. (1972), "Similarity Criteria for the Application of Fluid Models to the Study of Air Pollution Meteorology", *Boundary-Layer Met.* 3, pp. 113-134.
- Snyder, W.H. and Lawson, R.E. (1976), "Determination of a Necessary Height for a Stack Close to a Building--A Wind Tunnel Study", *Atmos. Environment* 10, pp. 683-691.
- Tani, I., Iuchi, M. and Komoda, H. (1961), Aeronautical Research Institute, Tokyo, Japan, Report No. 364.

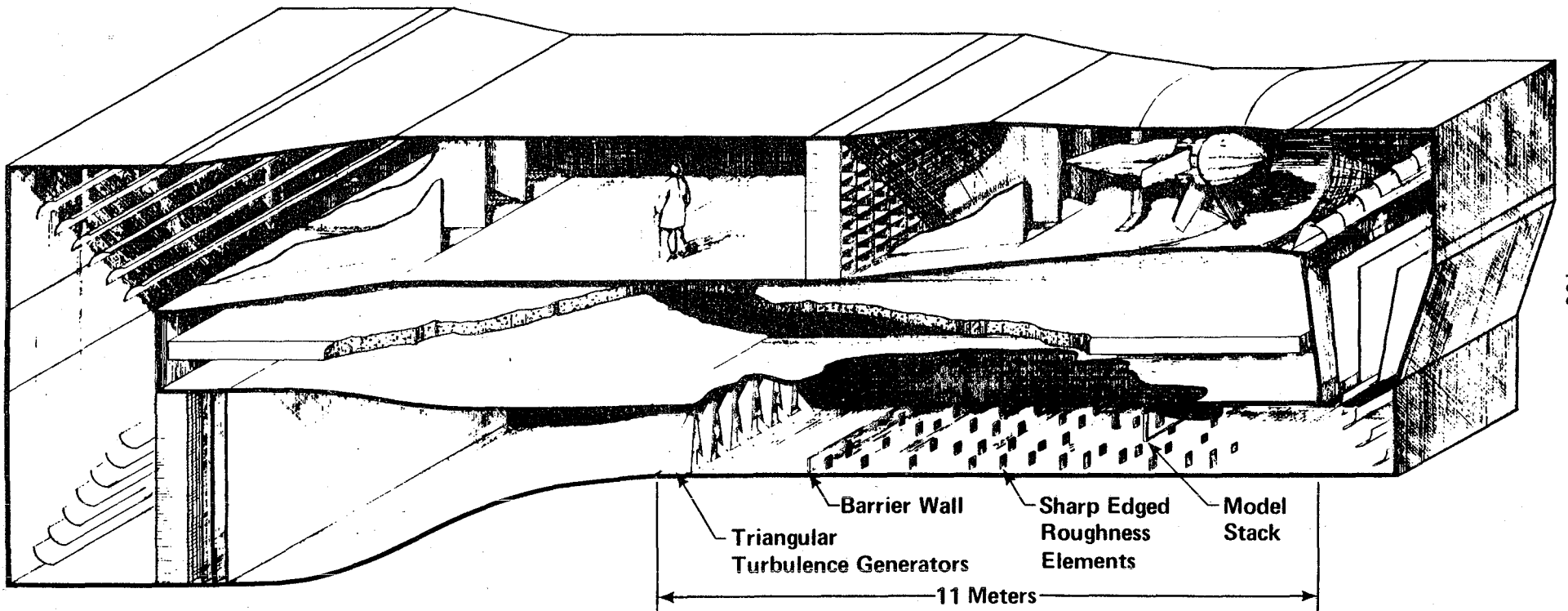
- Taylor, G.I. (1953) "Dispersion of Soluble Matter in a Solvent Flowing Slowly Through a Tube" Proc. Roy. Soc. London Ser. A 219 pp. 186-203.
- Teunissen, H.W. (1970), "Characteristics of the Mean Wind and Turbulence in the Planetary Boundary Layer", U. of Toronto, Inst. for Aerospace Studies, Review No. 32.
- Tillman, W. (1945), Volkenrode Translation MAP-VG34-45T. British Ministry of Aircraft Production, London, England.
- Weil, J.C. and Jepsen, A.F. (1977), "Evaluation of the Gaussian Plume Model at the Dickerson Power Plant", Atmos. Environment 11, pp. 901-910.
- Wilson, D.J. (1976), "Contamination of Air Intakes from Roof Exhaust Vents", ASHRAE Trans. 82, Part 1, pp. 1024-1038.
- Wilson, D.J. (1977), "Effect of Vent Stack Height and Exit Velocity on Exhaust Gas Dilution", ASHRAE Trans. 83, Part 1, pp. 157-166.
- Wilson, D.J. and Netterville, D.D.J. (1977), "Interaction of a Roof Level Plume with a Downwind Building", Atmospheric Environment 11, in Press.
- Wilson, D.J., Winkel, G., and Neiman, O. "Reynolds Number Effects on Flow Recirculation Behind Two-Dimensional Obstacles in a Turbulent Boundary Layer" Proc. Fifth Int. Conf. on Wind Engineering, Colorado State University, Fort Collins, U.S.A. July 1979.

APPENDIX A

WIND TUNNEL FACILITY

The large wind tunnel at the University of Alberta occupies two floors of the Mechanical Engineering Building and is designed to be suitable for both aerodynamic measurements and for the simulation of atmospheric boundary layers. The cut-away view shows the closed circuit configuration and the upper and lower wind tunnel test sections.

The wind tunnel fan is of a fixed pitch design driven by a variable speed 200 hp DC electric motor. The combination of a variable speed motor drive and a closed return design, which allows the airstream to be shielded from outside influences, makes this tunnel particularly suitable for stable low speed operation. The lower test section is 1.2 m high, 2.4 m wide and 11 m long, providing a sufficient size to accurately simulate atmospheric shear flows over model terrain. A maximum speed of 35 m/s may be attained in this section. At this maximum speed the motor drive system generates a heat input of approximately 150 kw which is dissipated by bleeding a few percent of the air flow out of the tunnel before the screens, and introducing an equivalent amount by aspirating fresh outside air through a duct immediately in front of the fan. With this means of temperature control the tunnel will operate at maximum speed at a temperature approximately 20°C above ambient. When operating at very low tunnel speeds heat generation from the motor drive system is no longer significant, and the intake and exhaust bleed ducts are sealed to allow more stable operation. It is the low speed operating characteristics of this wind tunnel which make it particularly suitable for use in air pollution studies. In order to correctly model buoyant stack gases in a wind tunnel it is necessary to operate the tunnel at speeds which are typically 10 to 20 times less than the full-scale wind speed. With the air bleed ducts sealed the tunnel will operate at speeds in the range from 0.15 m/s to 2.0 m/s



U. of A. Wind Tunnel Facility

with ± 0.01 m/s speed regulation over time intervals of at least half a day in length.

The atmospheric wind is stimulated by using a row of triangular spikes and a low barrier on the floor of the tunnel to generate turbulence, as shown in the cut-away drawing. This row of triangular turbulence generators and barrier is followed by distributed roughness of the proper shape and height to match the wind velocity profile and turbulence to the required terrain type. When properly adjusted these turbulence generators produce a fully developed simulated atmospheric shear layer up to 1 m thick in about one-half of the test section's 11 m length. Experiments using scale models of terrain, structures and pollution emission sources are carried out in the downstream half of the 11 m test section. Because of the absence of any surface heating or cooling in the wind tunnel, only neutrally stable adiabatic boundary layers may be simulated. Atmospheric conditions with varying stability with height are beyond the capability of this facility. The one exception to this is the presence of a strong elevated inversion which forms an impenetrable barrier to upward diffusion of air pollution. This situation may be simulated using a solid barrier fixed at some suitable height in the wind tunnel test section to reflect any pollution which strikes it downward. In contrast to atmospheric simulation where turbulence is purposely introduced into the wind tunnel air stream, it is often useful to carry out tests in a uniform wind with low turbulence levels. By the use of a glass fibre filter, flow straighteners, and three turbulence control screens, the free stream turbulence level in the lower test section may be reduced to values of about 0.1%, and a spatial uniformity of mean flow velocity across the test section area of $\pm 1\%$.

Generating Simulated Atmospheric Boundary Layers

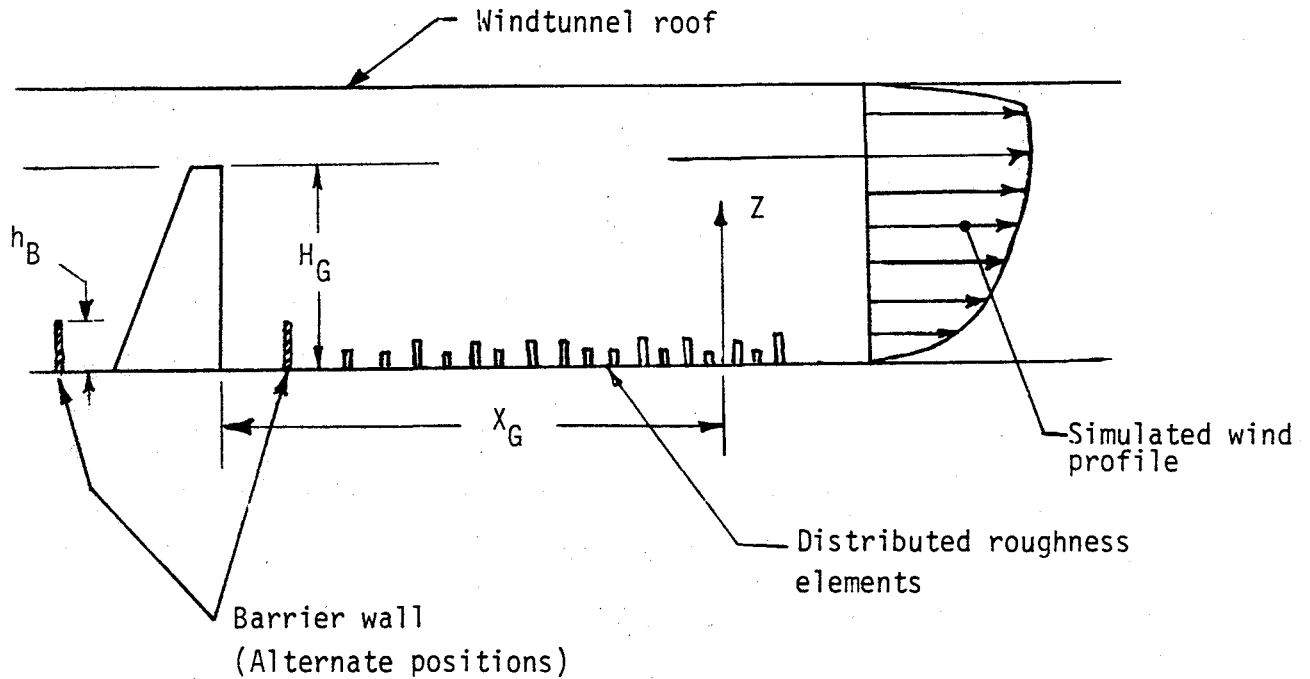
As discussed in the previous section the large wind tunnel facility makes use of artificial stimulation methods for generating thick simulated atmospheric boundary layers within the short 11 meter test section length. Because of the importance of accurate atmospheric simulation to the validity of wind tunnel testing, a detailed assessment of the accuracy and limitations of these flow generation methods will be considered here.

The large number of laboratories now engaged in atmospheric wind tunnel modelling have generated as many (or more) different methods for atmospheric boundary layer generation as there are wind tunnels engaged in this work. The artificial stimulation systems are of two types. The first are active systems which depend on injection of air jets across the flow or close to the wall to generate an initial distribution of turbulence. These active jets are always followed by distributed surface roughness to maintain the turbulence. In contrast to this the second type is passive in nature, and consists of a series of flow obstructions which generate turbulence in their wakes.

The advantage claimed for active systems is that they are easier to adjust to provide a specific turbulence distribution. At the same time, proponents of passive systems point out that once the geometrically configuration has been developed to generate a particular level of turbulence, it can then be easily reproduced at a later time, and is less likely to slip out of adjustment.

A passive generation system was chosen for the University of Alberta large wind tunnel facility because of its mechanical simplicity,

and its stability of operation. Like most other successful passive systems it is based on the pioneering work of Counihan (1969), whose method is generally referred to as the "spike and barrier system". All such and spike barrier systems make use of the following three elements to generate turbulence:



1. A row of tapered turbulence generator spikes extending to the upper edge of the stimulated boundary layer provides a source of vortex motions whose axis of rotation is perpendicular to the tunnel floor. In addition, their height allows them to generate turbulence in the outer regions of the boundary layer, and thus avoid the long delay during which natural production of turbulent energy near the wall is diffused outward. The turbulence generator spikes used in the present system are in the shape of truncated triangles with streamlined forebodies, as illustrated in Figure A1.

By varying the spacing of these generators and the angle of attack of the streamlined forebodies some control can be exerted on the crosswind uniformity of the generated flow field.

2. A low barrier wall mounted on the floor of the wind tunnel section is used to generate crosswind vortex motions. The drag of this barrier produces the high turbulence levels and mean flow momentum loss near the surface necessary to quickly develop a thick turbulent boundary layer. This barrier wall may be located either upstream or downstream from the row of spikes. The barrier height is adjusted to provide the correct turbulent shear stress and velocity profile in the lower region of the simulated atmospheric boundary layer. In the system used at the University of Alberta the upper half (approximately) of this barrier wall is fabricated from perforated metal sheet, while the lower portion of the wall is solid. This perforated upper wall generates small scale turbulence to allow a more gradual transition between the barrier and the outer flow. In addition, the small scale turbulence generated in this way hastens the reattachment of the separation cavity downwind of the barrier, and promotes a more rapid approach to equilibrium of the simulated shear flow.
3. Surface roughness elements are distributed on the wind tunnel floor downwind from the spikes and barrier. This roughness provides a source of turbulence generation to maintain the downwind equilibrium of the flow. The University of Alberta

system uses a pseudorandom roughness distribution. This distribution assigns the same number of roughness elements to each square in a grid pattern. The side of each grid square is one-half the overall test section width, and the roughness elements are distributed at random within each of these grid squares. In order to minimize Reynolds number sensitivity the roughness elements used are flat sharp edged plates of varying height. This concern for Reynolds number sensitivity is required because wind loading and dispersion tests are usually carried out at Reynolds numbers from 1000 to 20,000 times smaller than their full scale values. As an additional means of eliminating the Reynolds number sensitivity the upper half of the turbulence generating spikes have a sharp edged ridge at the trailing edge to assure an abrupt flow separation.

All of the above devices generate turbulence from wakes behind obstacles. Some settling length must be provided to allow this wake turbulence to decay and mix with wall generated turbulence to provide a structure typical of a surface shear flow. Some investigators have objected to the use of turbulence generator spikes because of the wake-like nature of the turbulent structure generated in this way. Unfortunately, turbulent boundary layers generated with only a barrier and surface roughness require several times more downwind distance to develop the same thickness as one using spikes.

Regardless of the particular combination chosen, it is generally agreed that the selection of a particular barrier-spike-roughness com-

mination is more of an art than a science. In carrying out the trial and error process of adjustment for a passive system it is essential to recognize that the turbulence levels in the outer portion of the boundary layer as well as the crosswind uniformity are influenced mostly by the spacing and orientation of the generator spikes. The barrier wall generates a free shear layer and recirculation region which has its major influence in the lower half of the boundary layer, while the surface roughness influences the shape of the boundary layer profile near the wall, and maintains longitudinal uniformity of the mean velocity and turbulence levels.

The method used in adjusting the present system is to install generators with a height H_G approximately the thickness of the desired boundary layer. A barrier with a height of approximately $h_B \approx 0.15 H_G$ is installed downwind from the generators as shown in the schematic diagram. A first approximation to the required surface roughness density is placed on the tunnel floor downwind of the barrier. The generator spacing and angles of attack are then adjusted to obtain crosswind uniformity at a downwind position of about $X_G \approx 7 H_G$ and $Z \approx 0.5 H_G$. The barrier height is then adjusted to obtain the desired vertical velocity profile shape in the central portion of the boundary layer at this same location. Finally, the surface roughness density is altered to obtain longitudinal flow uniformity. This process of adjusting the generators, the barrier and the surface roughness is then repeated until the desired mean flow profile, turbulence intensity and flow uniformity is achieved.

A few remarks are in order regarding the position of the barrier wall. The diagram shows that the barrier wall may be located either upwind or downwind of the turbulence generators. Both configurations have

been tested, and the University of Alberta system has adopted the downwind location for several reasons. For an upwind barrier, the recirculation zone from the barrier wall covers the lower portion of the generator spikes rendering them ineffective. A downwind barrier does not have this disadvantage. In addition, turbulence from the row of upwind generators assists in causing rapid reattachment of the flow recirculation zone, and a more rapid development of the desired boundary layer profile.

Distance Required for Flow Development

Robins (1977a) carried out a comprehensive investigation into the downwind development of artificially stimulated boundary layers. His investigations were all for a spike-barrier-roughness system in which the barrier was located upwind of the spikes. Studies in the University of Alberta Low Speed Wind Tunnel have confirmed Robins' observations, and if anything show a somewhat quicker approach to flow equilibrium for barrier walls located downwind of the generator spikes.

Because it is the outer part of the boundary layer that is slowest to develop, the relevant distance for development X_G is measured from the trailing edge of the turbulence generator spikes, where this outer layer begins its growth.

In following the downstream development of these artificially generated shear flows Robins obtained the following results:

1. The production and dissipation of turbulent energy do not approach equilibrium values typical of natural boundary layers for a distance of about $X_G \approx 11 H_G$. In all cases the dissipation exceeds production during the development phase of these artificially stimulated flows, and the turbulence intensity decays

from high values close to the generators to its final equilibrium intensity.

2. The flow becomes useful for testing purposes long before this final equilibrium is reached. Crosswind uniformity of the flow, and longitudinal uniformity of both mean velocity, turbulence intensity and turbulent shear stress occur at about $X_G \approx 5 H_G$ to $6 H_G$.
3. For wind loading studies the downwind region of interest is small, and minor variations in longitudinal flow uniformity are not the major factor. Fully developed turbulence appropriate for loading studies is fully developed for $X_G \approx 6 H_G$.
4. Plume dispersion from elevated sources whose height is 10% or more of the generator height H_G will have their spreading rates independent ($\pm 5\%$) of source location for $X_G > 6H_G$. Ground level sources are much less sensitive to flow development because the boundary layer near ground level is dominated by surface roughness. Ground level sources, and elevated sources whose height is $Z < 0.1 H_G$ will be insensitive to source position for $X > 4H_G$ approximately. Sources which are located too close to the spikes and barrier will spread more rapidly than in the fully developed flow because the high turbulence intensity in the wakes behind the generators and barrier wall have not had the opportunity to decay to the lower equilibrium values in the fully developed flow.

Both Robins (1977a) and the University of Alberta Large Wind Tunnel test sections employ a constant cross-section area, with a flat wind tunnel roof. This causes the flow to develop a stream-wise pressure

gradient much like pipe flow. However, Robins demonstrated that this gradient causes only a negligibly small effect on the turbulent shear stress in the simulated atmospheric boundary layer.

In addition, Robins (1977a) studied several different boundary layer thicknesses and determined that the wind tunnel roof has only a small effect on the structure of turbulence in the simulated shear flow, even when the generator height H_G was 83% of the total wind tunnel test section height. The only effect of the close proximity of the roof to the top of the generators was to prevent the development of a completely non-turbulent free stream above the boundary layer. This effect slightly increased the fraction of time the flow was turbulent in the outer part of the boundary layer.

In conclusion, it may be stated that for tests carried out at a distance of more than six times the generator height downwind, the artificially stimulated shear flow will provide an accurate model of the atmospheric boundary layer. In practice, the basic limitation to wind tunnel simulation of atmospheric boundary layers does not lie in the means used to generate these shear flows, but rather in the inability of wind tunnel systems to model the Coriolis force effects which cause turning of the wind direction with height. For example, the wind direction close to the surface in a full scale neutrally stable atmospheric boundary layer may have its direction 10° to 50° different than that at the outer edge of the layer. This turning of the wind with height causes a crosswind shear which can significantly affect both the mean trajectory and the crosswind dispersion of a plume, as well as influence the angle of attack of flow over high structures.

APPENDIX B

SCALE MODELING TECHNIQUES

In order for the scale model tests to exhibit the same behaviour as the full-scale system, it is necessary that certain non-dimensional parameters be matched between model and full-scale. Unfortunately, because of the small size of the scale models used, even in a large wind tunnel facility such as the one employed in the present study it is never possible to match all of the relevant dimensionless parameters. In practice, only a few of these parameters are matched between model and full-scale, and we rely on the insensitivity of the physical processes to wide mismatches in most of the others.

In modeling the atmospheric wind, one parameter which can never be correctly matched is the Reynolds number, which represents the ratio of inertial to viscous effects. In the large wind tunnel facility used in the present study, structures and terrain are typically modeled in scales ranging from 400:1 to 1000:1. This large size reduction places the impossible condition that the wind tunnel be operated at supersonic speeds in order to obtain a match between full-scale and model Reynolds numbers. A further difficulty occurs when buoyant plumes must be modeled in the wind tunnel. In this situation, a correct scaling of the buoyant rise of a stack gas plume requires a wind tunnel speed 10 to 20 times less than the full-scale atmospheric wind. Combined with the model scales used in the present study, this decrease in model speed forces the Reynolds number in the wind tunnel model to be 5000 to 20,000 times smaller than its full-scale counterpart. Snyder (1972), in a review of similarity criteria for scale modeling, pointed out that most of the differences in turbulence structure and transport coefficients between model and full-scale can be traced to their difference in Reynolds numbers. A detailed consideration must be given to the sensitivity of

the various processes governing flow and diffusion to determine their sensitivity to Reynolds number variations.

Streamline Patterns and Flow Separation

In order for the streamline patterns to be the same in model and full-scale, the mean flow velocity profile and turbulence structure must be scaled. In addition, the ratio of momentum flux from the stack and the atmospheric wind must be matched to assure similar trajectories of stack gas effluents.

In the facility used in the present study the atmospheric wind structure including mean flow velocity profiles, turbulence intensity, and spectra are matched to the correct atmospheric condition for vertical, along-wind and crosswind fluctuations. Integral scale and microscale of turbulence are also matched to assure the correct distribution of eddy sizes. To match the trajectory of stack gas effluents caused by momentum effects consider the momentum rise Δh_M which in non-dimensional terms is a function of the momentum flux

$$\frac{\Delta h_M}{d} = f\left(\frac{\alpha \rho_s W_s^2}{\rho_a U_s^2}, \frac{x}{d}\right) \quad (B1)$$

Assuming that the stack diameter d and the terrain distances x are modeled in the same length scale, the second parameter x/d will be the same from model and full-scale. The only requirement for obtaining the correct stack gas momentum induced plume trajectory is to maintain a constant value between model and full-scale of the momentum parameter

$$\sqrt{\phi_M} = \left(\alpha \frac{\rho_s}{\rho_a}\right)^{0.5} \frac{W_s}{U_s} \quad (B2)$$

The kinetic energy correction factor α is the ratio of the integrated mean kinetic energy in the velocity profile exiting from the stack, and the kinetic energy of the mean velocity W_s . It is defined by

$$\alpha = \frac{1}{A} \int_A \left(\frac{W}{W_s} \right)^3 dA$$

where A is the cross sectional area of the stack, W is the local velocity in the stack and W_s is the mean velocity. For laminar flow in a circular tube, $\alpha = 2.0$. For turbulent velocity profiles α ranges from about 1.02 to 1.10. Because most model stacks have laminar flow while their full scale counterparts always have turbulent flow this kinetic energy factor is important in matching model to full scale conditions. Wilson (1977) in a wind tunnel study of roof mounted stacks with varying effluent density ρ_s , verified that this momentum ratio ϕ_M , rather than the velocity ratio W_s/U_s governs plume trajectory.

Correct scale modeling also requires that the flow patterns around terrain obstacles such as buildings and hills be correctly simulated. For sharp edged bodies such as buildings, Ogawa (1977) found that the flow patterns would be correctly simulated if a Reynolds number based on turbulent quantities is maintained constant. Assuming that the lower regions of the atmosphere where terrain obstacles occur may be correctly represented by a logarithmic velocity profile, this turbulent Reynolds number for similarity is proportional to $Re_{\text{turb}} \propto \log(H/Z_0)$, where H is the height of the sharp edged terrain obstacle, and Z_0 is the logarithmic equivalent surface roughness parameter. The significance of this similarity requirement is that even though the mean flow Reynolds number is much different between model and full-scale, if the mean flow velocity pro-

file and turbulence in the approach wind which determine z_0 are correctly modeled, the flow patterns around sharp edged obstacles will also be correctly simulated. In addition, Ogawa showed that the logarithmic form of this similarity parameter makes the flow patterns around obstacles quite insensitive to considerable variations in approach flow characteristics.

On the other hand, gently curved surfaces where there are no sharp edges to fix the point of flow separation are much more sensitive to Reynolds number variations. While the freestream turbulence in the atmospheric wind helps to generate a stable separation point typical of high Reynolds numbers, even when the model is tested at low wind tunnel Reynolds number, considerable difficulties still occur. For example, buildings with gently rounded corners and circular cylinders, such as stacks, require a Reynolds number greater than about $Re_d \equiv Ud/\nu > 3 \times 10^5$ for stable positions for flow separation, and constant values of the surface pressure coefficients. In general, the more gentle the surface curvature of the body shape, the higher the Reynolds number that will be required to develop a stable flow separation point. For a gently curved hill, the wind may not find a stable separation location until the Reynolds number based on hill height has exceeded a critical value somewhere in the range from 10^6 to 10^7 . Because of these relatively high values of critical Reynolds number for the flow to develop a similar structure, it is often found that the full-scale situation lies above the critical Reynolds number, and the model test operates at Reynolds numbers below this critical value. In order to induce stable flow separation points on curved surfaces some special adjustments of the wind tunnel model are usually necessary. For gently curved surfaces flow separation often occurs in the wind tunnel where none exists in full scale. Flow deflectors or suction through slots in the model may be used to keep the wind tunnel flow attached to the

surface. Other studies of cooling tower models have used exaggerated surface roughness in the form of coarse grit glued to the model surface to induce stable separation at the low wind tunnel Reynolds numbers.

In modeling flow around curved surfaces in atmospheric diffusion, one system of particular interest is the determination of stack gas downwash in the low pressure zone on the downwind side of a cylindrical stack. Because of the small stack diameter in the model scale, the Reynolds number for the flow around the stack is almost always less than the critical value for stable turbulent separation. The data compiled by Roshko (1961) for pressure coefficients on the downwind side of a circular cylinder indicate that the effect of this lower Reynolds number may be to cause higher suction pressures on the downwind side of the model stack, thus exaggerating the effects of stack wake downwash in the model, relative to the full-scale. For Reynolds number $U_s d/\nu$ below 3×10^4 and above 3×10^6 the pressure coefficient remains approximately constant at a value of $C_p = -0.9$. Between these limits the pressure coefficient rises and falls to extremes of -1.2 to -0.2 , with the largest changes near the separation transition point of $U_s d/\nu = 2 \times 10^5$. Fortunately, many model studies have wind tunnel Reynolds number below 3×10^4 and full scale values above 3×10^6 , which avoids the critical range where pressure coefficient varies. In this way model and full scale stacks have the same pressure coefficient.

Modeling Atmospheric Diffusion

Diffusion from emission sources is modeled in the wind tunnel by emitting a tracer gas which can be readily detected at various downwind locations. Because turbulent diffusion dominates plume spreading in both

the model and full-scale, it is not necessary to match the molecular diffusion properties of the tracer gas to the actual contaminant in the full-scale system. Helium is used as a tracer gas in the present study to simulate full-scale diffusion of sulphur oxides, particulates and water vapor. While the use of helium with its much higher coefficient of molecular diffusion tends to smear out very small scale eddies which would contribute to full-scale fluctuations of a few seconds or less, the overall plume dispersion and mean concentration will be correctly modeled.

In order to increase the measured concentration levels in the model, and so improve the signal to noise ratio of the detection equipment, tracer gases are emitted from the model stack at concentrations ranging from several hundred to several thousand times greater than the full-scale values. For correct scaling of the measured model concentrations the dispersion process for a passive contaminant must be examined. If we characterize the crosswind and vertical width of a plume at any x location by the parameters σ_y and σ_z the concentration field is given by

$$\chi = \frac{\dot{m}_s}{U_s \sigma_y \sigma_z} f\left(\frac{y}{\sigma_y}, \frac{z}{\sigma_z}\right) \quad (B3)$$

$$\sigma_y = \sigma_y(x), \quad \sigma_z = \sigma_z(x)$$

where $\chi \text{ kg/m}^3$ is the mass concentration of a passive contaminant which is emitted at a rate $\dot{m}_s \text{ kg/s}$ from the stack. This contaminant emission rate is simply

$$\dot{m}_s = \chi_s \frac{\pi d^2}{4} W_s \quad (B4)$$

By combining equations B3 and B4, and noting that the plume widths σ_y and σ_z will be represented in the same scale as the stack diameter d so that

$\sigma_y \sigma_z / d^2$ remains constant at any equivalent x location between model and full-scale, we obtain the non-dimensional concentration parameter

$$\phi_c = \frac{\chi U_s}{\chi_s W_s} \quad (B5)$$

For correct modeling of the diffusion process this concentration parameter will remain constant between model and full-scale at equivalent x positions. Then, we can write the relationship between model (m) and full-scale (f), as

$$\frac{\chi_m U_{sm}}{\chi_{sm} W_{sm}} = \frac{\chi_f U_{sf}}{\chi_{sf} W_{sf}} \quad (B6)$$

From which the concentration scaling factor is

$$\boxed{\frac{\chi_f}{\chi_{sf}} = \frac{\chi_m}{\chi_{sm}} \left(\frac{U_{sm}}{U_{sf}} \right) \left(\frac{W_{sf}}{W_{sm}} \right)} \quad (B7)$$

Using the conversion from mass concentration, χ kg/m³, to volume concentration, C , developed in Appendix C,

$$\boxed{\frac{C_f}{C_{sf}} = \frac{C_m}{C_{sm}} \cdot \left(\frac{U_{sm}}{U_{sf}} \right) \cdot \left(\frac{W_{sf}}{W_{sm}} \right) \left(\frac{T_{af}}{T_{sf}} \right)} \quad (C9)$$

Ludwig and Skinner (1976) obtained the same form for this concentration scaling factor by examining plume transport through a fixed plane in space for model and full-scale.

The essential requirement for correct atmospheric diffusion modeling is that the turbulence intensities in the vertical, crosswind and along wind direction be correctly modeled in the wind tunnel. In addition, because plume spread is influenced by the scale of turbulent eddies that participate in the diffusion process, it is also necessary to simulate the correct range of eddy sizes through a proper match of fluctuation velocity spectra and integral and microscales of turbulence. In neutrally stable atmospheric shear flow, all boundary layers which are generated by a natural interaction between flow and surface roughness are similar in structure. This is true

whether the boundary layer is 1 km thick in the atmosphere or 1 cm thick in the wind tunnel. Unfortunately this inherent similarity can not be exploited in the laboratory because, to create a thick shear flow in a short length of wind tunnel test section, artificial stimulation of turbulence generation is used. In addition, the Coriolis forces in the full-scale atmosphere which contribute to turning of wind direction with height are not present in the laboratory model. The technique used in the present study to circumvent these difficulties is to artificially generate turbulence in the wind tunnel boundary layer in order to meet the intensity and scale criteria set by full-scale atmospheric measurements. This matching process between the model and full-scale boundary layers inevitably results in some difficulties, due to two factors. The first of these is that there is a large Reynolds number difference between the model and full-scale. The second difficulty is that full-scale measurements of turbulence intensity scale and spectrum are not adequate to define the required model turbulence structure for large variations in surface roughness and height above ground.

Fortunately, large differences between model and full-scale Reynolds numbers are tolerable because they introduce only small effects on the processes that govern turbulent plume diffusion even though the model Reynolds number may be 10,000 times smaller than its full-scale counterpart. The reason why this large discrepancy in Reynolds number does not significantly effect plume dispersion may be seen by considering the range of eddy sizes which will be available in model and full-scale. Using the Eulerian integral scale of turbulence Λ_x as typical of the energy containing eddies, and the Kolmogorov microscale η as the smallest active scale, the range of eddy sizes is given by the ratio, Hinze (1975)

$$\frac{\Lambda_x}{\eta} \sim \text{Re}_\Lambda^{0.75} \left[\frac{\sqrt{u'^2}}{U_\delta} \right]^{0.5} \quad (\text{B8})$$

Using this, and a wind tunnel Reynolds number 10,000 times less than the full-scale, the range of eddy sizes in the model is approximately 1,000 times less than in the full-scale. However, the reason for the smaller range is due to viscous dissipation of the smallest eddies in the model due to its lower Reynolds number. Because it is the small eddies which will disappear first, it can be shown using B9 that for a typical model boundary layer with the characteristics $\Lambda_x = 0.20$ m, $\delta = 1$ m, $U = 1.0$ m/s, $\sqrt{u'^2} = 0.1$ m/s, that the wind tunnel model will be incapable of reproducing full-scale eddies smaller than about 0.5 m in size. This will not cause a significant departure from similarity, because eddies smaller than this size are not expected to participate actively in the diffusion of a continuous point source plume in the atmosphere. It can be concluded from this analysis that the large difference in Reynolds number between model and full-scale will not have a significant effect as long as the turbulence intensity and overall integral scale of turbulence are correctly modeled.

In attempting to accurately match intensity and turbulence scale in the model boundary layer we must be aware of the sensitivity of the turbulent diffusion process to these parameters. To see the effect of scale and intensity of turbulence on diffusion, consider the crosswind y direction spread of a continuous plume in homogeneous turbulence. Here the only length scale is the Lagrangian scale of turbulence \mathcal{L}_y . Following the suggestion first made by Hay and Pasquill (1959) we may assume

that the Lagrangian scale following the flow may be related to the Eulerian scale measured by a fixed anemometer by the simple relation, $L_y = \beta \Lambda_y$. It has been established that β is weakly dependent on the turbulence intensity, but is often taken as a constant approximately equal to 4.0. Then, by dimensional analysis the plume spread should depend on the turbulence intensity and scale according to

$$\sigma_y \approx \frac{\sqrt{v'^2}}{U} (\beta \Lambda_y)^{1-p} x^p \quad (B9)$$

where p is a power which may vary slowly with x . The statistical theory of turbulent diffusion of a single puff in homogeneous turbulence, eg. Hinze (1975), provides an exact solution for σ_y in terms of the turbulence intensity and the Lagrangian time scale. Noting that for homogeneous turbulence the spread σ_y of a continuous plume at distance x is the same as for a puff whose travel time is x/U , it can be shown that the exact solution takes the same form as (B9) with

$$p = 1.0 \text{ for } x \ll \beta \Lambda_y$$

$$p = 0.5 \text{ for } x \gg \beta \Lambda_y$$

The region of interest for atmospheric diffusion usually lies between these two asymptotic limits. In this intermediate zone $0.5 \leq p \leq 1.0$, and typical observations indicate that $p \approx 0.75$. For this case, the plume spread at a given downwind location depends linearly on the turbulence intensity, but only on $\Lambda_y^{0.25}$.

Thus, it is apparent that more attention must be given to correct modeling of the turbulence intensity than to the scale Λ_y , where a factor of 2 mismatch in modeling will cause only about a 15% change in plume spread σ_y , all else being equal. We conclude then, that because in the lower regions of the atmosphere the turbulence intensity is not much affected by the choice

of model scale, that variations in model scale a factor of 2 above and below that indicated by matching of the integral scales should still give reasonable results.

The preceding analysis provides general guidelines for estimating the effects of intensity, scale and Reynolds number on turbulent diffusion. To verify the applicability of these criteria Wilson (1976), (1977) carried out a series of tests of diffusion of a non-buoyant plume in an artificially generated boundary layer similar to the one used in the large wind tunnel facility. It was found that there was no significant effect on mean concentration fields as long as Reynolds number exceeded $\frac{U_\delta \delta}{\nu} > 1.8 \times 10^5$. For $\delta = 1.0$ m this would require a gradient wind speed $U_\delta > 2.7$ m/s, which is considerably above the values of 0.5 to 1.0 m/s actually used. However, as long as turbulence intensities and scales are matched at speeds close to the experimentally used values, Reynolds number effects will not be significant. Thus, for all wind tunnel speeds below this critical value of $U_\delta > 2.7$ m/s turbulence structure must be measured and adjusted over the range of wind tunnel speeds anticipated for the model test.

Because plume diffusion is influenced by locally generated turbulence from upwind obstacles as well as atmospheric turbulence, the Reynolds number of obstacles such as buildings, hills and dikes, must also be considered for similarity. As discussed previously, Reynolds number effects are expected to be insignificant for sharp edged obstacles. For gently curved surfaces Synyder's (1972) review suggests that atmospheric diffusion processes should be insensitive to Reynolds number effects as long as separation points are properly fixed on the model, and the Reynolds number based on obstacle height exceeds approximately 11,000, based on Golden's (1961) data.

Modeling Buoyant Plumes

The upward rise of a buoyant plume may be modeled in the wind tunnel by using a helium-air mixture to simulate the hot stack gases. Because we can adjust the quantity of buoyant efflux by setting the stack exit velocity W_s , and independently can set the tunnel speed U_s it is possible to find a combination of these two speeds in order to obtain a perfect match of both buoyancy and momentum effects of the stack gases. In this section two different approaches will be discussed which lead to dimensionless ratios for matching both stack gas buoyancy and momentum effects simultaneously.

The diffusion of a buoyant plume is caused not only by atmospheric turbulence, but also by self-generated turbulence generated by buoyant mixing. This self-generated turbulent mixing is particularly effective in dispersing the plume close to the source where the buoyancy effects are strongest, before large quantities of ambient air are entrained in the plume. The relative contribution of buoyancy induced turbulence to plume dispersion is also enhanced in the initial stages of plume growth by the fact that these self-generated eddies are approximately the same size as the plume width, and it is exactly this size range of eddies that is most effective in dispersing a plume.

As distance from the source increases the dispersion of a buoyant plume is dominated by atmospheric turbulence. As atmospheric turbulence comes to dominate the plume entrainment process, buoyancy rise is also inhibited, and the plume levels off in its final rise phase. Briggs (1969), (1975) has reviewed existing data to estimate the relative importance of atmospheric turbulence on plume rise, from which he concludes that it is eddies in the inertial subrange of atmospheric turbulence that contribute to ambient air entrainment into the buoyant plume. For a wind tunnel model

to provide a correct simulation of this final rise phase, it is essential that the correct turbulence structure of the atmospheric wind be simulated.

There are two basic approaches to modeling the buoyancy of a stack gas plume. The first, which we call "Froude Number Modeling" requires that the buoyant forces on an individual parcel of stack gas be correctly simulated. An alternate similarity requirement, called "Flux Modeling" requires only that the total buoyancy flux, F , be matched for model and full-scale. An excellent review of different modeling criteria for stack gas dispersion has been carried out by Isumov and Tanaka (1979).

In order to illustrate the similarities and differences between these two modeling requirements, let us first consider Froude number modeling. For an individual parcel of stack gas, the relevant dimensionless parameter which relates buoyancy forces to the inertial effects of the approach wind is the densimetric Froude number. The most convenient form for model scaling is to express this Froude number, Fr in terms of the bulk Richardson number, Ri

$$Ri = \frac{1}{Fr^2} = \frac{g \left(\frac{\Delta \rho}{\rho_a} \right) d}{U_s^2} \quad (B10)$$

where $\Delta \rho \equiv \rho_a - \rho_s$. By equating the Richardson number for the model to that of the full-scale, designating the model by a subscript m and the full-scale by a subscript f , equation B10 may be used to obtain the wind speed velocity scale as

$$\boxed{\frac{U_{sf}}{U_{sm}} \Big|_{\text{Froude}} = \left(\frac{d_f}{d_m} \right)^{0.5} \left[\frac{\left(\frac{\Delta \rho}{\rho_a} \right)_f}{\left(\frac{\Delta \rho}{\rho_a} \right)_m} \right]^{0.5}} \quad (B11)$$

In the same way using the momentum parameter from equation B2 combined with equation B11 the stack gas exit velocity scale is

$$\frac{W_{sf}}{W_{sm}} \left| \begin{array}{c} \text{Froude} \\ + \\ \text{Momentum} \end{array} \right. = \left(\frac{d_f}{d_m} \right)^{0.5} \left[\frac{\alpha_m \left(\frac{\Delta \rho}{\rho_a} \right) f \left(\frac{\rho_s}{\rho_a} \right)}{\alpha_f \left(\frac{\Delta \rho}{\rho_a} \right) m \left(\frac{\rho_s}{\rho_a} \right) f} \right]^{0.5} \quad (\text{B12})$$

By maintaining the two scales for wind speed and stack exit velocity we are guaranteed that each individual parcel of stack gas will experience the same accelerations due to buoyancy and momentum effects as it interacts with the approach wind. In the above equations the ratio d_f/d_m is simply the terrain and stack geometric scale factor which is chosen for convenience, and usually ranges from 400:1 to 1000:1.

Flux modeling represents an alternate method of setting similarity criteria. In this approach, we start with the observation that most successful theoretical and empirical models of buoyant plume rise indicate that the only three parameters which influence the plume trajectory in a neutrally stable atmosphere are the buoyancy flux F , the wind speed U_s and the downwind distance x . For all of these theoretical and empirical models the general functional relationship for plume rise may be represented by

$$\frac{\Delta h_B}{x} = f \left(\frac{F}{x U_s^3} \right) \quad (\text{B13})$$

where

$$F \equiv g \left(\frac{\Delta \rho}{\rho_a} \right) \frac{d^2 W_s^2}{4} \quad (\text{B14})$$

The combination F/U_s^3 is called the buoyancy length scale, L_B . For flux modeling the non-dimensional parameter F/xU_s^3 must be matched between

model and full-scale. Using the definition for F in equation B14 this non-dimensional group may be used to define the buoyancy flux parameter

$$\phi_B = \left[\frac{g \left(\frac{\Delta \rho}{\rho_a} \right) d}{U_s^2} \right] \left(\frac{d}{x} \right) \left(\frac{W_s}{U_s} \right) \quad (\text{B15})$$

The first bracketed term in this buoyancy flux parameter is simply the bulk Richardson number Ri defined in equation B10 and used for Froude number modeling. If we assume that the stack diameter d and terrain distances x are in the same model scale, the buoyancy flux parameter from equation B15 may be combined with the momentum scaling parameter from equation B2 to obtain the wind speed and stack gas exit velocity scales. After some manipulation of these two equations these scales may be written, denoting the model by subscript m and the full-scale by subscript f as,

$$\left. \frac{U_{sf}}{U_{sm}} \right|_{\substack{\text{Flux} \\ + \\ \text{Momentum}}} = \left(\frac{d_f}{d_m} \right)^{0.5} \left[\frac{\alpha_m \left(\frac{\rho_s}{\rho_a} \right)_m}{\alpha_f \left(\frac{\rho_s}{\rho_a} \right)_f} \right]^{0.25} \left[\frac{\left(\frac{\Delta \rho}{\rho_a} \right)_f}{\left(\frac{\Delta \rho}{\rho_a} \right)_m} \right]^{0.5} \quad (\text{B16})$$

$$\left. \frac{W_{sf}}{W_{sm}} \right|_{\substack{\text{Flux} \\ + \\ \text{Momentum}}} = \left(\frac{d_f}{d_m} \right)^{0.5} \left[\frac{\alpha_m \left(\frac{\rho_s}{\rho_a} \right)_m}{\alpha_f \left(\frac{\rho_s}{\rho_a} \right)_f} \right]^{0.75} \left[\frac{\left(\frac{\Delta \rho}{\rho_a} \right)_f}{\left(\frac{\Delta \rho}{\rho_a} \right)_m} \right]^{0.5} \quad (\text{B17})$$

Because the stack exit velocity W_s appears in both the momentum and buoyancy flux parameters, these wind speed and velocity scales each contain elements of momentum and buoyancy similarity. In contrast, the wind speed scaling

criteria in equation B11 from Froude number modeling set by buoyancy criteria alone. The question which must be answered is which of these two different buoyancy modeling criteria should be used for wind tunnel modeling. Froude number modeling of buoyancy effects guarantees that individual parcels of stack gas will experience the same forces in model and full-scale, but does not necessarily provide a correct match of the important buoyancy flux parameter F . On the other hand, buoyancy flux modeling guarantees a similarity in buoyancy flux parameter F , but does not necessarily provide a correct scaling of buoyancy and momentum forces on an individual parcel of stack gases. Both types of modeling criteria have been used with apparent success. Isumov et al. (1976) and Cermak (1975) have carried out wind tunnel studies using Froude number modeling, while Ludwig and Skinner (1976) have used flux modeling. Unfortunately, no study has been carried out of the relative merits of each of these two different similarity modeling methods, and in fact in selecting a particular method previous investigators have simply ignored the existence of the alternate possibility.

In a recent review of wind tunnel modeling methods Cermak (1975) suggests that the density of the effluent gas is in itself an important parameter, and that the ratio ρ_s/ρ_a must be matched between model and full-scale to obtain complete similarity. This suggestion is interesting because, if the ratio of stack gas to ambient density is maintained constant in model and full-scale, it is easy to show that the wind speed and stack gas exit velocity scales for Froude and Flux modeling become equivalent if $\alpha_m = \alpha_f$. While this would represent a convenient solution to the dilemma of choosing an appropriate modeling criteria, in order to maintain reasonably large wind tunnel velocities it is usually necessary to select a larger density difference in the model than in the full-scale.

An alternate technique for obtaining equivalence of both Froude number and flux modeling was used by Hoult et al. (1977) in a recent wind tunnel study. With this investigation the stack gas density ratio ρ_s/ρ_a was maintained at a considerably smaller value in the model than the full-scale, but Buoyancy Flux and Froude number modeling criteria were both satisfied by maintaining only the exit velocity ratio W_s/U_s constant, rather than the complete momentum parameter ϕ_M from equation B2. While this relaxation of momentum similarity may result in some differences in initial momentum rise and stack wake downwash, it does allow correct modeling of all of the relevant buoyancy parameters, which are usually far more important than momentum in determining overall plume rise. In order to apply this approximate modeling procedure, equation B11 is used for the wind speed velocity scale, and the stack exit velocity scale becomes simply

$$\frac{W_{sf}}{W_{sm}} \Big|_{\substack{\text{Froude} \\ + \\ \text{Flux}}} = \frac{U_{sf}}{U_{sm}} \Big|_{\text{Froude}} \quad (\text{B18})$$

This approach to scale modeling should only be used when buoyancy effects are certain to dominate the plume trajectory, and when stack wake downwash effects are not important.

Hoult and Weil (1972) discuss the sensitivity of scale modeling to the stack gas density ratio ρ_s/ρ_a and to the Reynolds number of the stack gases. For stack gas density ratios which were varied over the range $0.6 \leq \rho_s/\rho_a \leq 0.9$ no measurable effect could be observed on the rate of entrainment into a buoyancy dominated plume. Some small effect must undoubtedly be present, but was obscured by the $\pm 20\%$ scatter of the observed trajectories. This weak density dependence is consistent with the observations of Ricou

and Spalding (1961), who found the rate of entrainment to be proportional to the ratio $(\rho_c/\rho_a)^{0.5}$ where ρ_c is the plume centerline density. Due to entrainment, ρ_c/ρ_a approaches unity after a travel distance of only 10 to 20 stack diameters.

In their experiments in a towing tank, Hoult and Weil also found that a fully turbulent plume developed as long as the stack exit Reynolds number is greater than about 300.

$$Re_s \equiv \frac{\rho_s W_s d}{\mu_s} > 300 \quad (B19)$$

This result is consistent with the observations of Rouse, Yih and Humphreys (1952) who state that if the Reynolds number based on the local rise velocity and plume width exceeds about 600 turbulent flow will exist. The Reynolds number criteria in equation B19 is usually satisfied for most stacks tested in the wind tunnel facility. When this criteria can not be met directly, surface roughness may be introduced in the stack interior to assure fully turbulent flow at the stack exit, allowing proper simulation of the growth of the turbulent plume in spite of large differences of Reynolds number between the model and full-scale stacks.

Finally, Isumov and Tanaka (1979) carried out wind tunnel measurements to determine the sensitivity of stack gas rise and dispersion to a mismatch between model and full-scale density ratio ρ_s/ρ_a . They found that using a model stack gas density ratio less than the full-scale value tended to overestimate plume rise by a significant amount. This causes the model ground level concentration to be much too low. Their findings are in direct contradiction to the observations of Hoult and Weil (1972) discussed previously, and leads us to conclude that the sensitivity of modeling to a mismatch in density ratio is still a question for further investigation.

APPENDIX CGAUSSIAN PLUME DISPERSION EQUATIONS

For a continuous point source emitting a chemically inert pollutant at an effective height h above ground level, with a completely reflecting boundary, the concentration at any point downwind is given by

$$X = \frac{\dot{m}}{2\pi U \sigma_y \sigma_z} \left[\exp\left(-\frac{y^2}{2\sigma_y^2} - \frac{(z-h)^2}{2\sigma_z^2}\right) + \exp\left(-\frac{y^2}{2\sigma_y^2} + \frac{(z+h)^2}{2\sigma_z^2}\right) \right] \quad (C1)$$

The concentration at ground level where $z = 0$ and along the plume centerline where $y = 0$ is

$$X_0 = \frac{\dot{m}}{\pi U \sigma_y \sigma_z} \exp\left(-\frac{h^2}{2\sigma_z^2}\right) \quad (C2)$$

For the special case where σ_y is assumed proportional to σ_z , we can determine the maximum concentration as

$$X_{0\max} = \frac{2\dot{m}}{\pi e h^2 U} \left(\frac{\sigma_z}{\sigma_y}\right) \quad (C3)$$

At $x = x_{\max}$ it can be shown that

$$\sigma_z^2 = \frac{h^2}{2} \quad (C4)$$

Both of the preceding results require that the source height be independent of downwind distance x , that is, that final rise has occurred. Equation (C2) and (C3) may be combined to write a normalized concentration profile

$$\frac{X_0}{X_{0\max}} = \frac{h^2}{2\sigma_z^2} \exp\left(1 - \frac{h^2}{2\sigma_z^2}\right) \quad (C5)$$

Using Ground Level Concentrations to Estimate σ_z

Because the assumption of constant diffusivity is not valid near the ground where turbulence levels change rapidly with height, Gaussian profiles may fail to match real concentration profiles. To avoid this difficulty we will use (C5) to define a vertical spread σ_{z0} which exactly matches an observed ground level concentration profile.

In practice, σ_{z0} is evaluated by generating the curve of $x_0/x_{0\max}$ from the experimental data with x , and then at each desired x location inserting this value into equation (C6) and determining by iteration the appropriate value of σ_{z0} for the given value of source height h . By this method, the vertical plume dispersion σ_{z0} is forced to provide a perfect agreement with the observed ground level concentration profiles. It should be kept in mind that the values of σ_{z0} obtained in this way usually do not give good agreement when used to generate the entire vertical concentration profile. For this reason, σ_{z0} should not be interpreted as an actual vertical plume dimension.

Crosswind Spread σ_y

The previous analysis required a constant value for the ratio σ_y/σ_z . To determine this ratio equation (C3) may be written as

$$\frac{\sigma_{z0}}{\sigma_{y0}} = \frac{\pi e}{2} \left[\frac{x_{0\max} U h_o^2}{\dot{m}} \right] \quad (C3a)$$

The observed experimental value of the bracketed term may be used in this equation to find the crosswind to vertical spread ratio.

In applying equations (C3a) and (C5) it must be kept in mind that h is an effective source height, which must include buoyancy rise and upward or downward drift induced by wind shear or terrain effects. This effective height must be selected with care because σ_{z0}/σ_{y0} depends on h^2 .

Relationship Between Mass and Volume Concentration

The previous relations are computed for mass concentration, simply because the mass flux \dot{m} kg/sec and the mass concentration χ kg/m³ are used.

It is also popular to express the concentration of gaseous pollutants in terms of volume concentration C or in $C \times 10^6$ which is ppm by volume.

By using the law of partial volumes a relation between C and χ may be found. For the partial volume V_i occupied by the i^{th} component of a gaseous mixture, (in our case the i^{th} component is sulphur dioxide) the ideal gas law is

$$PV_i = \frac{m_i \bar{R} T}{M_i}$$

where P and T are the mixture pressure and temperature, \bar{R} is the universal gas constant, M_i is the molecular weight and m_i is the mass component i .

If we then consider a total mixture volume of one cubic meter, V_i is the volume fraction C_i and m_i is the mass fraction χ_i , so that

$$P C_i = \chi_i \frac{\bar{R} T}{M_i}$$

or

$$\boxed{C_i = \chi_i \frac{\bar{R} T}{M_i P}} \quad (C6)$$

This equation may be used to determine the concentration ratio between any two conditions. For example, between stack and ground level, noting that the pressure P is the same at both points

$$\frac{C}{C_s} = \frac{\chi}{\chi_s} \left(\frac{T_a}{T_s} \right) \quad (C7)$$

Also, the modeling criteria in Appendix B, equation B6 may be written, for the model values (m) and the full scale values (f),

$$\frac{C_m U_{sm} T_{sm}}{C_{sm} W_{sm} T_{am}} = \frac{C_f U_{sf} T_{sf}}{C_{sf} W_{sf} T_{af}} \quad (C8)$$

But, the temperature at stack and in the air is constant for the model, which relies on molecular weight differences to produce the plume buoyancy; so the above equation simplifies to

$$\frac{C_f}{C_{sf}} = \frac{C_m}{C_{sm}} \cdot \left(\frac{U_{sm}}{U_{sf}} \right) \cdot \left(\frac{W_{sf}}{W_{sm}} \right) \left(\frac{T_{af}}{T_{sf}} \right) \quad (C9)$$

which shows that the use of helium - air mixtures for modeling hot gas discharges can only be used if a correction is applied to the measured concentrations.

If it is convenient to use volume fluxes and concentrations directly in the Gaussian plume equation, the volume flux may be written,

$$\begin{aligned} m_i &= \rho_{is} Q \\ &= \frac{PM_i}{RT_s} Q \end{aligned}$$

Using this and the relation between χ and C in the diffusion equation results in

$$C = \frac{Q \cdot \left(\frac{T_a}{T_s} \right)}{2\pi U_s \sigma_y \sigma_z} \left[\exp \left(\frac{-y^2}{2\sigma_y^2} - \frac{(z-h)^2}{2\sigma_z^2} \right) + \exp \left(\frac{-y^2}{2\sigma_y^2} + \frac{(z+h)^2}{2\sigma_z^2} \right) \right] \quad (C10)$$

This shows that the stack volume flux $Q \text{ m}^3/\text{s}$ must be corrected by cooling it at constant pressure from the stack temperature T_s to ambient conditions T_a .

Vertical and Crosswind Spreads Not Proportional

The above analysis does not require any specific functional form for σ_y or σ_z , only that σ_y/σ_z has a constant value. Alternately, we can propose specific forms for the crosswind and vertical spread, and remove the restriction of $\sigma_y/\sigma_z = \text{constant}$. Following Pasquill (1975) and Weil and Jepsen (1977) we assume a power law form

$$\sigma_y = D_y X^{a_y} \quad (\text{C11})$$

$$\sigma_z = D_z X^{a_z} \quad (\text{C12})$$

where a_y and a_x may have different values. Using (C11) and (C12) in (C2) and differentiating to find the maximum results in, for $h \equiv \text{constant}$,

$$x_{o \max} = \frac{\dot{m}}{\pi \exp\left(\frac{\alpha}{2}\right) U h^\alpha} \cdot \frac{(D_z \sqrt{\alpha})^\alpha}{D_z D_y} \quad (\text{C13})$$

$$\text{where } \alpha \equiv 1 + \frac{a_y}{a_z}$$

This maximum concentration occurs at x_{\max} , at which point

$$\sigma_z^2 = \frac{h^2}{\alpha} \quad (\text{C14})$$

using (C12), we obtain

$$x_{\max} = \left[\frac{h}{D_z \sqrt{\alpha}} \right]^{\frac{1}{a_z}} \quad (\text{C15})$$

For the case of a plume whose effective source height, h , is constant with x , the normalized ground level concentration varies with distance according to

$$\frac{X}{X_{\max}} = \frac{1}{(x/x_{\max})^{\alpha a_z}} \exp \left[-\frac{\alpha}{2} \left((x/x_{\max})^{-2a_z} - 1 \right) \right] \quad (C16)$$

Conditions of Use

Wilson, D.J., 1979. Wind tunnel simulation of plume dispersion at Syncrude Mildred Lake site. Syncrude Canada Ltd., Edmonton, Alberta. Environmental Research Monograph 1979-1. 198 pp.

Permission for non-commercial use, publication or presentation of excerpts or figures is granted, provided appropriate attribution (as above) is cited. Commercial reproduction, in whole or in part, is not permitted without prior written consent.

The use of these materials by the end user is done without any affiliation with or endorsement by Syncrude Canada Ltd. Reliance upon the end user's use of these materials is at the sole risk of the end user.